Rebuilding Cytokinesis One Molecule at a Time

Baldauf, L.

DOI
10.4233/uuid:412a4272-9ec2-4aba-852d-981e392d64d0

Publication date
2022

Document Version
Final published version

Citation (APA)
Baldauf, L. (2022). *Rebuilding Cytokinesis One Molecule at a Time*. [Dissertation (TU Delft), Delft University of Technology]. https://doi.org/10.4233/uuid:412a4272-9ec2-4aba-852d-981e392d64d0

Rebuilding Cytokinesis One Molecule at a Time

Rebuilding Cytokinesis One Molecule at a Time

Dissertation

for the purpose of obtaining the degree of doctor
at Delft University of Technology
by the authority of the Rector Magnificus, prof. dr. ir. T.H.J.J. van der Hagen,
chair of the Board for Doctorates
to be defended publicly on Thursday 22 December 2022 at 12:30 o'clock.

by

Lucia BALDAUF

Master of Science in Technische Physik,
Technische Universität Ilmenau, Germany,
born in Freiburg, Germany.

This dissertation has been approved by the promotors.

Composition of the doctoral committee:

Rector Magnificus	chairperson
Prof. dr. G. H. Koenderink	Delft University of Technology, promotor
Dr. T. Idema	Delft University of Technology, copromotor
Independent members:	
Prof. dr. C. Dekker	Delft University of Technology
Dr. K. Ganzinger	AMOLF
Dr. D. V. Köster	University of Warwick (United Kingdom)
Dr. G. Romet-Lemonne	Institut Jacques Monod (France)
Dr. H. Geertsema	Delft University of Technology
Prof. dr. C. Joo	Delft University of Technology, reserve member

The research presented in this thesis was performed at AMOLF and TU Delft. It is part of the research programme *BaSyC - Building A Synthetic Cell* of the Netherlands Organisation for Scientific Research (NWO).

Cover design	Lucia Baldauf
Printed by	Gildeprint

Casimir PhD Series, Delft-Leiden 2022-36

ISBN/EAN: 978-90-8593-545-2

It's still magic even if you know how it's done.

Terry Pratchett, A Hat Full of Sky

Summary

Cells are the fundamental units of life. They make up all living things, from bacteria that live in the soil, to archea that give thermal springs their bright colors, to trees and humans. All of these cells share some common functions: they build themselves from basic building blocks, following the instructions of their genetic blueprint, and procreate by growing and dividing. The building blocks must be taken up from the environment and metabolized, and cell division requires the cell to be able to control its own shape. While these basic tasks are shared across the tree of life, different types of organisms have evolved distinct molecular machineries to complete them. In this thesis, we take a close look at animal cells, and ask how they control their shape as they must do in order to move, eat, sense, and divide.

In animal cells, shape is controlled by the cytoskeleton, and in particular by the actin cortex. This cortex is a thin layer of actin filaments that sit underneath the plasma membrane, supporting the cell surface. The filaments are highly dynamic: they are constantly growing, shrinking and being remodeled, with well over 100 different proteins regulating their length and architecture. This molecular complexity, combined with the small size and high density of filaments and their rapid remodeling, makes it extremely difficult to disentangle different functions performed by the actin cortex in living cells.

To better understand what fundamental principles govern cortex-based shape control of animal cells, we thus pursue a different approach: instead of studying living cells directly, we build minimal versions, so-called 'synthetic cells', from the bottom up. In such a bottom-up reconstitution approach, we isolate proteins (for instance actin) from their native environment, purify them, and bring them back together *in vitro*, following rational design principles. Consequently, we drastically reduce the complexity of the system, giving us a chance to actually understand what is going on. This allows us to test our assumptions about how cellular processes work *in vivo*, and discover new functions that are normally hidden in the complexity of the living cell. In this thesis, we use bottom-up reconstitution to ask how animal cells control their shape, with the ultimate aim to build a minimal actin-based cell division machinery.

We first introduce important concepts and molecular players in the introductory **Chapter 1**, and delineate what makes a system a good candidate for bottom-up reconstitution. **Chapter 2** then lays out a roadmap towards reconstituting cell division *in vitro*. Based on theoretical models of animal cell division, we identify minimal functional requirements for cytokinesis. We review the state of the art in reconstitution of actin-based cellular machineries, and recent developments in the cell biology of the actin cortex, and emphasize the so far under-appreciated importance of the cell membrane for cytokinesis. Finally, we propose solutions to some of the technical roadblocks on the path to actin-based synthetic cell division.

In **Chapter 3**, we zoom in on one of the key molecular players in the actin cortex: the molecular motor myosin. Myosin-2 motors self-assemble into bipolar motor filaments that

remodel the actin cortex, mediating cell division but also conferring tension to the cell surface. Here we study how two different forms of myosin-2, one from muscle and one from non-muscle cells, self-assemble into filaments, and how those filaments then run on actin race tracks. We find that skeletal muscle myosin-2 assembly is robust over a wide range of ionic strengths, whereas *C. elegans* nonmuslce myosin assembly is more sensitive to small buffer changes. Surprisingly, our motility measurements reveal that filaments of skeletal muscle myosin-2 in particular can switch between faster and slower running speeds, likely depending on whether the trailing end of the myosin filament binds to the underlying actin structure and acts as a built-in molecular break.

Chapter 4 zooms out from single cortical components to a more holistic view of synthetic cells: we establish a robust and versatile protocol for reconstituting actin cortices in giant unilamellar vesicles (GUVs), cell-sized containers surrounded by a simplified plasma membrane. Surprisingly, we find that the same protocol also produces dumbbell-shaped GUVs as a result of partial membrane fusion. We find that Arp2/3-nucleated actin cortices have a strong preference for assembling at the highly curved necks of these dumbbells, showing that actin cortices can intrinsically sense membrane curvature. This raises fundamental questions such as what mediates this curvature sensing, and to what extent cells use it to control targeted actin assembly at curved membranes, for instance during early cell division.

In **Chapter 5**, we ask more broadly how the interplay between a membrane and an actin cortex plays out, when the cortex is stiff and thus inhibits membrane deformation, but at the same time exerts polymerization forces on the membrane, which can actively change the membrane shape. We show that branched actin cortices can trap GUV shapes two orders of magnitude longer than the actin turnover time in the cortex. Using a combination of *in vitro* experiments and theoretical modelling, we show that branched cortices induce finger-like membrane protrusions when polymerization forces accumulate locally due to a force-curvature feedback mechanism.

Cell division can only happen if the synthetic cell possesses enough membrane area to cover two daughter cells. Since enzymatic production of lipids is currently too slow and inefficient to fulfill this task, we implement in a technical shortcut **Chapter 6**: we feed small vesicles to large GUVs via a DNA-mediated membrane fusion protocol. Our experiments reveal that such a process tends to make GUVs leaky, a factor which will have to be considered in membrane design for synthetic cells. Nonetheless, our results also indicate that GUVs are growing as a result of DNA-mediated membrane fusion, presenting a path towards delivering membrane area and complex membrane components to synthetic cells.

Finally, we conclude in **Chapter 7** with a look into the future of synthetic cells. We present preliminary data on how cytokinetic rings could be controlled in synthetic cells, and discuss the next steps in integrating cytoskeletal activity with other functional modules that synthetic cells will need to live.

Samenvatting

Cellen zijn de kleinste eenheid van het leven. Ze zijn als het ware de Legoblokjes waarvan alle levende wezens gemaakt zijn, van de kleinste bacteriën in de aarde, de kleurrijke microorganismen in hete bronnen, tot bomen en zelfs mensen. Alle cellen hebben een aantal overeenkomstige functies: ze moeten zichzelf bouwen volgens hun genetische blauwdruk, zich vermenigvuldigen en groeien. Hiervoor is het noodzakelijk dat ze moleculaire bouwstenen uit hun omgeving kunnen opnemen en verwerken, en ook dat ze hun eigen vorm kunnen bepalen. Verschillende organismen hebben hiervoor verschillende moleculaire machines ontwikkeld. In dit proefschrift onderzoek ik hoe dierlijke cellen hun vorm bepalen, zoals ze dat moeten doen om te eten, te bewegen, hun omgeving te verkennen, en zich te delen.

De vorm van dierlijke cellen wordt bepaald door hun cytoskelet, vooral door de zogenoemde *actine cortex*. Dit is een dun laagje van eiwitten in de vorm van lange draden die het celmembraan verstevigen. Deze draden zijn erg dynamisch: ze groeien en krimpen continu. Meer dan 100 andere eiwitten reguleren waar en hoe lang ze groeien, en ook hoe ze aan elkaar plakken. De actine cortex van een levende cel is dus een klein maar enorm complex systeem, dat ook nog eens snel verandert. Dit maakt het lastig om precies uit te pluizen wat een specifiek eiwit in een levende cel doet.

Om deze redenen bestuderen we niet de levende cellen zelf, maar vereenvoudigde 'nepcelletjes', zogenoemde *synthetische cellen*, die gebouwd worden uit levenloze bouwstenen. Dit doen we door eiwitten (zoals bijvoorbeeld actine) uit hun cellulaire omgeving te halen en op te zuiveren, om ze vervolgens in een gecontroleerde omgeving *in vitro* weer bij elkaar te brengen. Hierdoor wordt het systeem veel minder complex, en dit biedt de kans om beter te begrijpen wat er in onze cellen gebeurt. Zo kunnen we hypotheses testen over de werking van processen in levende cellen, en functies van eiwitten ontdekken die normaal gesproken door de complexiteit van een cel niet zichtbaar zijn. In dit proefschrift onderzoek ik door middel van *in vitro* reconstitutie hoe dierlijke cellen hun vorm veranderen, om uiteindelijk een eiwit-machine te bouwen die een synthetische cel kan delen.

In **hoofdstuk 1** geven we eerst een overzicht van de moleculaire bouwstenen en concepten die in de celdeling een belangrijke rol spelen. Daarnaast laten we zien dat we het proces van celdeling beter kunnen begrijpen door het bouwen van synthetische cellen. **hoofdstuk 2** is een *roadmap*, die de weg naar synthetische celdeling beschrijft. We presenteren een literatuurstudie over de huidige kennis van de celbiologie van de actine cortex, en over de status van reconstitutie daarvan. Ook laten we zien hoe belangrijk het is om meer aandacht aan het celmembraan te geven, en we geven suggesties voor het oplossen van de technische problemen die reconstitutie in de weg staan.

In **hoofdstuk 3** kijken we in detail naar een van de belangrijkste spelers in de actine cortex: het motoreiwit myosine. Myosine-2 motoren vormen staafachtige structuren, die de actine cortex herschikken en samentrekken, zoals bijvoorbeeld tijdens de celdeling, maar ze kunnen ook op actine draden lopen. Wij gebruiken twee soorten myosine-2

eiwitten, één uit spiercellen van konijnen en één uit lichaamscellen van een worm, om te bestuderen hoe de myosine staafjes ontstaan en hoe ze vervolgens op actine 'racebanen' lopen. We laten zien dat myosine uit spiercellen in verschillende bufferoplossingen staafjes van nagenoeg constante massa maakt, terwijl myosine uit worm-cellen gevoeliger is voor veranderingen in de zoutconcentratie van de omgeving. Tot onze verrassing zien we dat vooral spiercel-myosine tijdens het lopen van snelheid kan veranderen, waarschijnlijk omdat motoreiwitten in het achterste deel van het staafje als moleculaire rem werken.

In **hoofdstuk 4** kijken we naar volledige (maar wel simpele) synthetische cellen in plaats van enkele moleculen. We ontwikkelen eerst een robuuste methode om actine laagjes te bouwen in zogenoemde *giant unilamellar vesicles* (GUVs), membraanblaasjes met het formaat van een cel. Naast bolvormige cellens produceren we ook GUVs met een sneeuwpop-achtige vorm, die ontstaan door gedeeltelijke membraanfusie. In deze sneeuwpoppen hebben actine cortices een voorkeur voor de nek, waar de kromming van het membraan het grootst is. Dit laat zien dat actine niet alleen membranen kan krommen, maar ook de membraankromming in een cel kan meten. Dit roept nieuwe vragen op: hoe detecteert actine membraankromming? En gebruiken levende cellen deze intrinsieke eigenschap om robuust actine netwerken te bouwen op plaatsen waar het membraan gekromd is, bijvoorbeeld als een cel begint te delen?

Hierna stellen we een algemenere vraag in **hoofdstuk 5**: wat gebeurt er als een actine cortex een celmembraan verstevigt, maar tegelijkertijd continu tegen dat membraan aangroeit en daardoor krachten uitoefent? We laten zien dat actine cortices membranen over lange tijden verstijven, tot wel 100 keer langer dan de *turnover* tijd van actine in de cortex. We gebruiken naast *in vitro* experimenten ook een nieuw theoretisch model om te laten zien dat soortgelijke cortices dunne membraan uitsteeksels laten groeien, als er locaal genoeg actinedraden tegen het membraan aangroeien, en daardoor een *force-curvature-feedback* ontstaat.

Wannneer een cel zich in tweeën deelt, moet er genoeg membraan beschikbaar zijn voor beide dochtercellen. De productie van vetzuren *in vitro* is op dit moment nog te inefficiënt en traag om hiervoor genoeg membraan beschikbaar te stellen. Daarom ontwikkelen we in **hoofdstuk 6** een systeem waarin we membraanmateriaal van buiten toevoegen aan GUVs. Dit doen we door GUVs met kleinere vesicles te fuseren door middel van membraangebonden DNA linkers. Helaas zien we dat GUVs lek raken tijdens dit proces; een ontdekking die zeker belangrijk zal zijn voor het ontwerpen van membranen voor synthetische cellen in de toekomst. Desondanks vinden we ook aanwijzingen dat het protocol werkt om de GUVs te laten groeien. Het kan dus een manier zijn om in de toekomst, na optimalisatie, synthetische cellen te voorzien van extra membraanmateriaal.

We sluiten af met een blik richting de toekomst van synthetische cellen. In **hoofdstuk 7** laten we experimenteel zien hoe celdeling *in vitro* kan worden controleerd met behulp van licht, en we geven aanbevelingen voor het combineren van het cytoskelet met andere cellulaire systemen, om de volgende stap te zetten naar een kunstmatige cel.

Zusammenfassung

Die fundamentale Einheit des Lebens ist die Zelle. Alles Leben besteht aus Zellen, angefangen von Bakterien im Boden über die bunten Mikroorganismen in heißen Quellen, bis hin zu Bäumen und Menschen. All diesen Zellen sind einige Grundfunktionen gemein: Sie bauen sich selbst anhand ihres genetischen Bauplans aus leblosen Grundstoffen, die sie aus ihrer Umgebung aufnehmen, und pflanzen sich fort indem sie wachsen und sich teilen. Zur erfolgreichen Zellteilung muss die Zelle Kontrolle über ihre eigene Form ausüben können. Diese Basisfunktionen müssen zwar alle Zellen beherrschen, jedoch haben unterschiedliche Organismen hierfür verschiedene molekulare Maschinen entwickelt.

In Tierzellen wird die Zellgestalt durch das Zytoskelett, und vor allem durch den *Aktinkortex*, kontrolliert. Der Aktinkortex ist ein dünnes Gewebe aus Protein-Filamenten, die die Plasmamembran versteifen. Die Filamente sind extrem dynamisch, sie wachsen und schrumpfen kontinuierlich und werden von zahlreichen anderen Proteinen umstrukturiert. Es sind weit über 100 solcher Proteine bekannt, die Länge, Position und Netzwerkarchitektur des Aktins im Kortex bestimmen. Diese molekulare Komplexität, sowie die hohe Proteindichte und schnelle Dynamik machen den Aktinkortex zu einer Herausforderung für die klassische Zellbiologie: In lebenden Zellen ist es nahezu unmöglich herauszuarbeiten, welche Funktionsprinzipien dem Aktinkortex seine Funktion geben.

In dieser Arbeit nähern wir uns dem Problem daher auf einem anderen Weg: Statt lebende Zellen zu untersuchen, bauen wir vereinfachte ‘synthetische Zellen’ in einem ‘bottom-up’ Verfahren nach. Hierfür werden Proteine aus ihrem natürlichen Umfeld genommen, gesäubert und in einer kontrollierten Umgebung *in vitro* wieder zusammengesetzt. Dies ermöglicht es uns, die Komplexität des Systems drastisch zu reduzieren, und macht es so möglich, Hypothesen über zelluläre Prozesse gezielt zu testen. Darüber hinaus kann ein solches vereinfachtes System Funktionen zu Tage bringen, die in lebenden Zellen meist von anderen Effekten überlagert werden. Im Rahmen dieser Arbeit nutzen wir *in vitro* rekonstituierte Systeme um zu untersuchen, wie Tierzellen ihre Gestalt kontrollieren, und um letztendlich eine Aktin-basierte Zellteilungsmaschinerie in synthetischen Zellen zu entwickeln.

Zuerst geben wir in **Kapitel 1** einen Überblick über die wichtigsten Konzepte und molekularen Bestandteile im Aktinkortex, und legen dar warum dieser sich besonders gut zur *in vitro* Rekonstitution eignet. In **Kapitel 2** entwickeln wir einen Strategieplan zur Rekonstitution von Aktin-basierter Zellteilung *in vitro*. Auf Basis theoretischer Studien arbeiten wir heraus, was die minimalen Voraussetzungen für Aktin-basierte Zellteilung sind. Des Weiteren fassen wir den Stand der Technik in der Zellbiologie des Aktin-Kortex und dessen Rekonstruktion *in vitro* zusammen, und heben die bisher vernachlässigte Rolle der Zellmembran für die Zellteilung hervor. Schlussendlich schlagen wir Lösungsansätze für die technischen Hürden vor, die derzeit der erfolgreichen *in vitro* Zellteilung im Wege stehen.

In **Kapitel 3** untersuchen wir einen der wichtigsten Spieler des Aktin-Kortex im Detail: den molekularen Motor Myosin. Myosin-2 Motorproteine lagern sich in bipolaren Filamenten zusammen, die den Zellkortex modellieren, in Spannung halten, und die Zellteilung vorantreiben. Wir untersuchen zwei Isoformen dieses Motorproteins, eine aus Kaninchen-Muskelzellen und eine aus Zellen des Wurms *C. elegans*. Das *self assembly* von Motorfilamenten aus Muskelzellen ist robust in einer Reihe verschiedener Pufferlösungen, während Wurm-Myosin sensibler auf Ionen in seiner Umgebung reagiert. Wir entdecken eine überraschende Eigenschaft beider Motorproteine bezüglich ihrer Motilität auf Aktin-'Rennstrecken': Motorfilamente können zwischen langsameren und schnelleren Laufgeschwindigkeiten hin- und herwechseln, wahrscheinlich aufgrund von bremsenden Interaktionen des rückwärtigen Motorfilament-Endes mit dem Aktinsubstrat.

Für **Kapitel 4** weiten wir den Blick und untersuchen nicht einzelne Zellkomponenten, sondern ganze 'synthetische Zellen'. Wir entwickeln eine robuste und vielfältig einsetzbare Methode zum Herstellen von Aktinkortizes in sogenannten *Giant Unilamellar Vesicles* (GUVs), Lipidmembran-Kompartmenten mit zellähnlichen Ausmaßen. Überraschenderweise produziert diese Methode nicht nur sphärische, sondern auch hantelförmige GUVs, die durch teilweise Membranfusion entstehen. Wir stellen fest, dass Aktinkortizes die durch den Arp2/3-Proteinkomplex aufgebaut werden, vorzugsweise an der Verengung dieser hantelförmigen GUVs wachsen. Dies zeigt, dass Aktinnetzwerke nicht nur wie bisher bekannt Lipidmembranen verformen können, sondern auch auf deren Krümmung reagieren. Dies wirft fundamentale Fragen auf: Auf welchen molekularen Eigenschaften beruht die Krümmungsmessfähigkeit der Kortizes? Und inwieweit nutzen Zellen diese intrinsische Fähigkeit, um gezielt Aktin auf gekrümmten Membranen wachsen zu lassen, wie etwa in den frühen Stadien der Zellteilung?

In **Kapitel 5** stellen wir die allgemeinere Frage, wie das Zusammenspiel von Dynamik und passiver Festigkeit des Aktinkortex der Zellmembran ihre Form gibt. Aktinnetzwerke sind mechanisch steif und sollten daher Zelldeformationen entgegenwirken, generieren aber gleichzeitig kontinuierlich Polymerisationskräfte, die die Membran biegen können. Wir zeigen, dass verzweigte Aktinkortizes über lange Zeiträume die Form von GUVs einfrieren können, zwei Größenordnungen länger als die Residenzzeit eines einzelnen Aktinfilaments im Kortex. Durch eine Kombination aus *in vitro* Experimenten und mathematischer Modellierung zeigen wir, dass Aktin schlanke Membranausstülpungen produziert, wenn Polymerisationskräfte durch ein Kraft-Krümmungs-Feedback lokal akkumuliert werden.

Um eine Zelle in zwei zu teilen, muss genug Zelloberfläche vorhanden sein. Da enzymatische Produktion von Lipiden derzeit zu langsam und ineffizient ist, um solches Oberflächenwachstum bereitzustellen, entwickeln wir in **Kapitel 6** eine technische Abkürzung: Wir füttern GUVs über einen DNA-induzierten Membranfusionsmechanismus von außen kleine Vesikel zu. Bei GUVs, an die mithilfe von DNA Vesikel gebunden sind, stellen wir fest, dass viele GUVs durchlässig werden; ein Umstand, der in Zukunft für das Membrandesign von synthetischen Zellen von hoher Wichtigkeit sein wird. Dennoch finden wir starke Anzeichen daür, dass Membranfusion in unserem System stattfindet und die GUVs wachsen. Dies macht DNA-induzierte Membranfusion zu einem attraktiven System, mit dem Membranoberfläche und potentiell auch komplexere Membranbestandteile synthetischen Zellen zugeführt werden können.

Zuletzt schließen wir in **Kapitel 7** mit einem Blick in die Zukunft der synthetischen

Zellen ab. Wir zeigen erste Daten zur Kontrolle von synthetischer Zellteilung, und diskutieren, wie ein synthetisches Zytoskelett mit den komplexeren funktionalen Modulen vereint werden kann, um synthetischen Zellen Leben einzuhauchen.

Contents

1

Introduction

Abstract

Cells are the fundamental unit of life, and all cells across the evolutionary tree must perform common basic functions like growing and dividing. Yet, basic questions remain about how these tasks are accomplished. To address these questions, many researchers use a bottom-up reconstitution approach in which cellular components are taken out of their complex environment and re-assembled in a simpler and more controlled system, ultimately culminating in the creation of a life-like synthetic cell. In this thesis, we take steps towards building such a synthetic cell that can divide, inspired by the machinery that drives cell division in animal cells. This chapter serves as an introduction to bottom-up biology, and to membranes and actin cortices, the key players that shape the surface of animal cells. It also lays out the overall motivation and aim of this thesis, and provides an outline of the following chapters.

1.1 Synthetic cells and bottom-up biology

The simplest unit of any organism we consider alive is a single cell. Cells come in many different shapes and sizes: from tiny, rod-like bacterial cells, through long and spikey neuronal cells and blob-like immune cells that crawl around our tissues hunting for invaders, to human egg cells, which are so large as to be visible with the naked eye. Yet, all of these cells share a few characteristics that make them 'alive': They all take up and metabolize nutrients from their environment, build their own components according to a DNA blueprint they carry and process, and crucially, they grow and divide to produce copies of themselves.

How do cells perform these basic functions? Surprisingly, this largely remains an open question despite decades of intense cell biological research. To find out how different cellular processes work, the classical biologist's approach is to isolate a living cell, perturb it in some way (for instance using a drug to block the function of a protein), and observe how the cell reacts. However, since living cells across the tree of life have evolved for billions of years to survive, they tend to have built-in redundancies that make their basic cellular functions robust. This means that especially the functions that are crucial to life

1

itself (and not just to some specialized cellular function) are driven by complex systems, where loss of function in one protein may be compensated for by another, making it difficult to disentangle precisely what each molecular player does in a cell. Some scientists have consequently embarked on a quest to discover the key to life's essential functions by stripping non-essential components away from cells one by one, using genetic engineering tools. In the remaining minimal cell, removal of any other component will produce an unviable cell and lead to death. Great strides have been made in this field of so-called **'top-down synthetic biology'**, and in 2016, a bacterium was stripped down to live with just 473 genes, less than any other living organism ever found [1]. However, even in this genome where every component is essential for life, the function of almost one third of all genes is still unknown. Top-down manipulation of living cells can thus plainly not reveal all the secrets of cellular life.

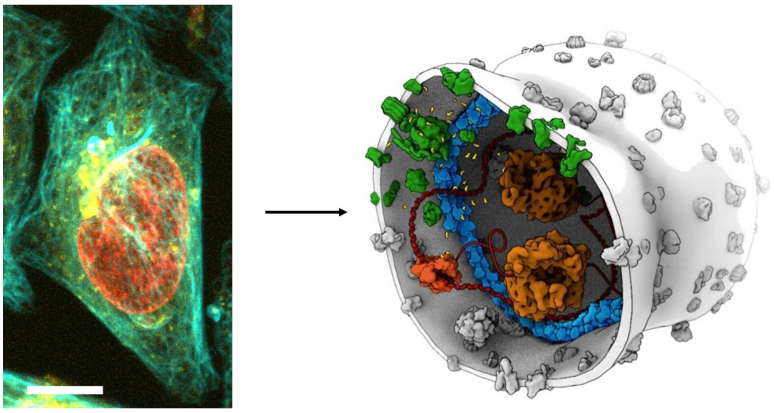

Figure 1.1: **Reducing complexity in synthetic cells.** The key functional modules in living cells (genetic processing, metabolism, growth and division) are mediated by intricate machineries: A microscopy image of a human cell* with fluorescently labeled DNA (red), endoplasmatic reticulum (ER, yellow) and microtubule cytoskeleton (cyan) hints at its complexity. Scale bar: 10 µm. In synthetic cells, we aim to build the simplest possible versions of these functional models. The sketch (artist's impression by Graham Johnson, basyc.nl) allows us to peak inside a synthetic cell, where components responsible for nutrient uptake and metabolism are highlighted in green, those involved in processing genetic material are shown in orange, and a cytoskeletal element that divides the cell appears in blue. Such a cell will likely be extremely simple, and more closely resemble prokaryotic cells, which do not posess membrane-bound organelles like the ER or nucleus in eukaryotic cells. The sketch is not drawn to scale.

Thus, a growing community of researchers has been turning turn to an alternative approach: **'bottom-up biology'**, or cell-free reconstitution, where cells are assembled from their fundamental molecular building blocks [2]. Ultimately, many of these researchers envision that fully autonomous synthetic cells may emerge from these efforts. The hope is that such custom-built synthetic cells can help us tackle challenges in a variety of

*The fluorescence micrograph shows a maximum intensity projection of a living HeLa cell, which is a cultured human cervical cancer cell line. It was acquired at the Marine Biological Laboratory in Woods Hole using an Olympus spinning disk microscope with a 60x water immersion objective and SoRa superresolution module. The cell constitutively expressed the ER-marker Ergic3, and DNA and microtubules were stained using the live cell dyes Hoechst and SiR-tubulin, respectively.

applications, from personalized medicine to environmental engineering [3], and in fact industrial players are also starting to take an interest [4]. However, as introduced above, synthetic cells can also be viewed as the ultimate arena for basic biological science.

To build synthetic cells, we remove individual components from their complex cellular environment, and put them back together following rational design principles. Reconstituted systems often contain no more than a few purified proteins, making it easier to hone in on the precise function of each one, and conceptualize what is really going on in the system. Just because an effect is observed in reconstituted systems, does not necessarily mean that it plays a significant role in living cells, so the biological relevance must always be critically evaluated. However, we can use reconstitution to test hypotheses which originate from the study of living cells: if we understand a cellular process well enough, we should be able to reverse engineer it and build it from its key components. Physicist Richard Feynman summarized this sentiment in one sentence, which has since become the unofficial motto of bottom-up biology: *"What I cannot create, I do not understand."*

I believe that to use the full power of bottom-up reconstitution as a tool for basic research, any problem to which we apply it should fit a set of criteria:

- **Complexity:** Reconstituting a system is only worth the effort if studying it in living cells is severely hampered by cellular complexity. Otherwise, probing it inside cells directly is often simpler and more likely to yield biological understanding.
- **Prior knowledge:** To reconstitute a structure or process, one should at least have some idea what molecular players are involved in its construction in the living cell.
- **Universality:** Reconstitution is particularly attractive when it can address 'big questions'. Due to its reductive nature, reconstitution does not cover all aspects of a system precisely. Glossing over molecular detail allows the researcher to zoom out and identify the key principles that are relevant in molecularly distinct systems, such as different cell types, species, or even domains of life.
- **Context:** Any reconstitution efforts must match in scale and context the question they are addressing. When probing the precise nature of an interaction between two molecules, it does not make sense to place them in the context of a vast network. On the other hand, when two cellular sub-systems compete for the same building block in cells, we cannot understand their functioning by reconstituting them in a test tube with an unlimited supply of molecules.

1.2 What shapes a cell?

The shape (and shape changes) of cells are fundamental properties that have fascinated scientists since the first microscopes were developed that were powerful enough to resolve single cells [5], making it a 'big question' that lends itself particularly well to bottom-up reconstitution. We know that cellular shape control is mediated by different molecular players depending on where in the tree of life we look: bacteria and most archea use rigid cell walls made from sugar molecules to control their shape, as do plants and yeast cells. By contrast, animal cells lack cell walls and instead regulate their shape through an internal fibrous structure called the cytoskeleton. This cytoskeleton of animal cells has long been

subject of intense study, and researchers have identified several hundred components that are associated with it [6, 7], so cellular shape regulation is both well-characterized and extremely complex. It has also been established that some key components of the actin cortex (see section 1.4), that part of the cytoskeleton that is most involved in shaping animal cells, are highly conserved across all animals, and often also across plants and yeasts [8–10].

Yet, to understand what shapes cells, it is not enough to study the cytoskeleton: we must also consider what defines the boundary between a cell and its environment. For animal cells, this boundary is set by the plasma membrane, a thin double-layer of lipids that acts as a physical barrier for containing the cellular lumen, but also actively contributes to trafficking of molecules, templating of cortical structures, and regulating tension at the cell surface (see section 1.3). Finding out what shapes animal cells by reconstitution thus means that we must bring membranes and cytoskeletal networks together to create a context in which cell shape can be meaningfully studied. By varying the molecular makeup of either component, we can then tease out how the cytoskeleton and lipid membrane shape each other.

1.3 Cell-like containers

The plasma membrane has remarkable properties: it is extremely thin compared to its lateral dimensions (~ 4 nm compared to several micrometers), and its components can move around within the layer as in a fluid, while only very small molecules can pass from one side of a membrane to the other. This is a result of the structure of membranes: they are built up of lipids, small molecules that have a hydrophilic headgroup attached to two hydrophobic acyl chains or 'tails' (Fig. 1.2 A, left). Due to this amphiphilic molecular structure, hydrophobic interactions drive lipids in aqueous solution to self-assemble into structures where the headgroups are exposed to the surrounding water, but the tails cluster together and are concealed from the solvent. Such structures are called lipid bilayers, and they are the basic unit of the plasma membrane. The two opposite-facing layers of lipids are called the leaflets of a membrane. Note that a flat lipid bilayer as drawn in the middle panel of Fig. 1.2 A would be surrounded by a region where the hydrophobic lipid tails are exposed to the solvent on the sides. To avoid these energetically costly border regions, lipid bilayers can close up into spherical vesicles, which separate the inside solution from the outside world, like the plasma membrane separates a cell from its environment (Fig. 1.2 A, right). Such a container is called a Small, Large or Giant Unilamellar Vesicle (SUV, LUV or GUV), depending on its size ($\lesssim$ 100 nm, ~ 100 nm - 1 µm and $\gtrsim$ 1 µm, respectively), and GUVs are particularly relevant as synthetic plasma membrane compartments, as they most closely match the sizes of typical animal cells.

Natural lipids can have many different headgroups (varying in size, charge and chemical composition) and tails (varying in length and unsaturation of the chain of carbon-carbon bonds), which may drive the lipids to form bilayers with different properties (fluidity, porosity, thickness and lipid order), or even to form supramolecular structures that are altogether different from bilayers. Natural animal cell plasma membranes contain an enormous diversity of lipids [11, 12] as well as a high density of proteins that are either partially or fully embedded in the membrane [13]. For simplicity, we will focus in this work on very simple lipid bilayers with only a few basic phospholipids, mimicking the

main classes of lipids in animal cell plasma membranes [11].

Free-standing lipid membranes like those of vesicles can be deformed by external forces. Due to the strong hydrophobic forces that hold lipid bilayers together, high forces are required to stretch a lipid bilayer in-plane (Fig. 1.2 B), and bilayers generally rupture when stretched by more than 5 % [14, 15]. By contrast, bending a lipid bilayer is much easier: thermal energy alone is enough to induce undulations in membranes, and pico- to Nanonewton forces generated by the actin cytoskeleton [16] can easily deform them (Fig. 1.2 C). Lipid membranes are also semipermeable: water and some other small molecules can pass across them (Fig. 1.2 D) [14], while large ions and proteins are confined to one side of the bilayer (Fig. 1.2 E) [17]. This allows cells to use their plasma membrane as a barrier against transport: no macromolecules get in or out of a cell unless membrane pores or specific transporter proteins allow them through.

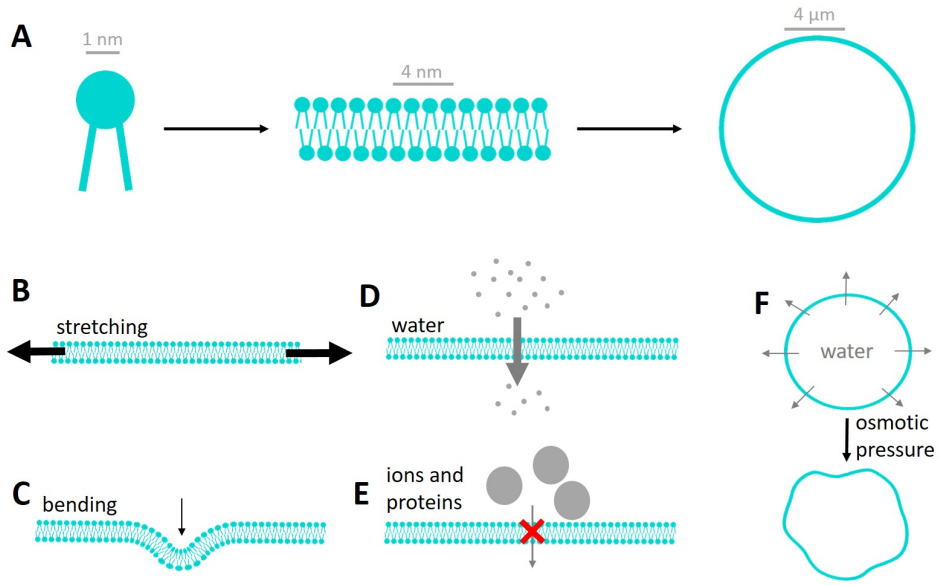

Figure 1.2: **Key properties of lipid membranes.** (A) Amphiphilic lipid molecules self-assemble into bilayers, where their tails cluster together in a hydrophobic core that is concealed from the surrounding aqueous medium by the hydrophilic lipid heads. Such bilayers can close up to form spherical vesicles. (B) Stretching or compressing lipid bilayrs in-plane requires high forces and quickly leads to membrane rupture. (C) Bending membranes is easy by comparison, allowing even thermal motion to produce out-of-plane fluctuations in a lipid membrane. (D) Lipid membranes are water-permeable, allowing water to pass from one side to the other through the membrane. (E) Ions and large macromolecules, by contrast, cannot pass from one side of a membrane to the other as they are blocked by the hydrophobic core of the bilayer. (F) An osmotic mismatch between the inside and outside of a spherical vesicle triggers the release of water from the vesicle, deflating it and inducing large-amplitude deformations in the membrane, which undulate over time due to thermal motion.

The principles described in Fig. 1.2 B-D combined also allow us to introduce a final concept that will be important for this thesis: excess membrane area. When a spherical lipid vesicle has a lower concentration of solutes on its inside than in the surrounding medium,

osmotic pressure works towards equilibrating this difference. Since the solutes cannot pass the lipid membrane, osmotic pressure instead drives expulsion of water from the vesicle until the osmolarities inside and outside the vesicle are balanced. Meanwhile, the total area of the lipid membrane has not changed, since the bilayer is close to incompressible in-plane (Fig. 1.2 B). The same membrane area now surrounds a smaller volume, so the newly formed 'excess membrane area' must induce a deviation of the vesicle from its spherical shape. This deformation is not static, but instead shows up as membrane fluctuations around a spherical shape, as the membrane bends just by thermal energy (Fig. 1.2 F). Cells control the amount of excess membrane area by many different mechanisms including vesicle trafficking, lipid synthesis and pumping ions across membranes, but we will use osmotic deflation in this work to produce synthetic cells with some excess membrane area.

1.4 The actin cortex

The actin cortex is an important part of the cytoskeleton of all animal cells. It is a thin layer of filamentous proteins that lays underneath the plasma membrane, giving the cell surface mechanical strength, but also the ability to remodel and change its shape. While more than 150 proteins are associated with the actin cortex [6], we will focus on only a few key players in this thesis.

Monomeric actin is a globular protein ('G-actin') that can polymerize into filaments with a double-helix structure ('F-actin'). Polymerization proceeds via a nucleation-and-growth pathway, where monomers must first form a stable seed complex of four monomers, from which a filament can then grow (Fig. 1.3 A) [18, 19]. Smaller seeds are energetically disfavourable compared to the monomer, so nucleation is the rate limiting step in the process and is used by cells to control when and where actin polymerizes. Once a seed is formed, it has two distinct ends: the pointed end (also called minus-end) and the barbed end (plus-end). New monomers can in principle be added to both ends, but with different affinities. This means that, in the presence of the chemical fuel adenosine triphosphate (ATP), the concentration above which addition of monomers to a filament is energetically favourable ('critical concentration') is higher for the pointed end than the barbed end. Consequently, as seeds grow into filaments and bind the available actin monomers from solution, the pointed end eventually stops growing and instead starts to depolymerize, while the barbed end is still growing. When the speed of pointed-end depolymerization matches the speed of barbed-end polymerization, net actin polymerization is zero and filaments treadmill, growing from one end while shrinking from the other. Such effective movement of the filament in the direction of the barbed end generates forces, which cells use to for instance drive lamellipodial cell motility [20].

In vitro, actin polymerization as described above can be induced by changing the environment around monomeric actin: when G-actin is dissolved in a low-ionic-strength buffer ('G-buffer'), it is stabilized in solution by a charged hydration layer. When salt is added to the solution ('F-buffer'), ions disrupt these charge-based repulsive forces and monomers can approach each other closely enough in solution for stable seeds to form, triggering filament formation [21]. The cytoplasm of animal cells contains a high salt concentration and could easily induce spontaneous actin polymerization throughout the cell. To inhibit this and trigger actin polymerization when, where and how it is needed, almost all monomeric actin in cells is sequestered by profilin and other proteins that bind

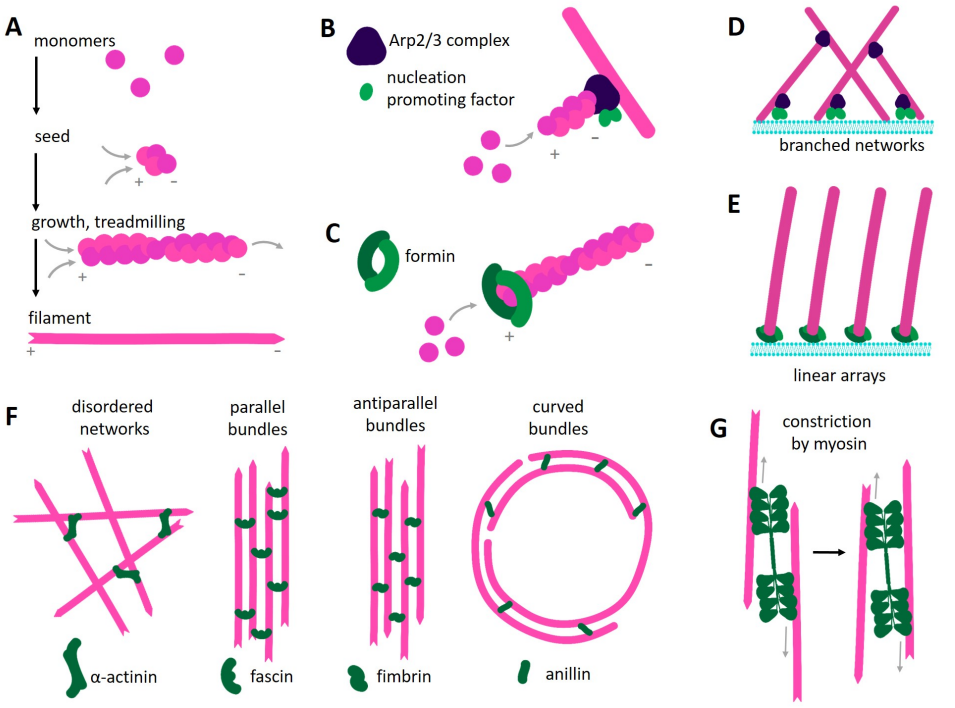

Figure 1.3: **The actin cortex.** (A) Actin is a globular protein that polymerizes by first forming a stable seed of 4 actin monomer subunits, that subsequently grows by addition of monomers. Polymerization is an equilibrium reaction, where both ends of the filament can grow as long as the concentration of monomers is higher than their critical concentration, but will otherwise shrink. In the presence of ATP, the pointed (or minus) end of an actin filament has a higher critical concentration and will thus start depolymerizing while the barbed (or plus) end is still growing. Thus, polymerization eventually reaches a steady state, where there is no more net change in the amount of filamentous actin. (B) The Arp2/3 complex drives the polymerization of actin in the cortex by binding to the side of an existing filament and mimicking an actin seed, from which a new filament can grow. Arp2/3 must be activated by a nucleation promoting factor, which is itself activated by plasma membrane components and signaling proteins. (C) A large pool of cortical actin is polymerized with the help of formins. Formins are homodimeric proteins that cap the barbed end of actin filaments and rapidly elongate it by integrating profilin-actin monomers. (D) Since the Arp2/3 complex nucleates new actin filaments from the side of existing filaments at a 70° angle, it forms branched networks of short filaments. (E) Formin, by contrast, forms long linear filaments. (F) Crosslinking proteins further shape the architecture of actin networks, producing random networks, aligned bundles, or even rings of actin. Note that many crosslinkers can produce several different structures depending on the circumstances. (G) Actin networks can be remodeled by the motor protein myosin-2, which self-assembles into rod-like bipolar filaments with motor domains on both sides, and can thus hold on to two different actin filaments at the same time, moving them relative to one another.

the monomer in such a way that it can not spontaneously bind other monomers [22–25]. Instead, specific actin nucleating proteins are used to induce the growth of actin filaments and networks. In the cortex of animal cells, most F-actin is produced by two nucleators: the Arp2/3 complex and formin Dia1 [26]. Other actin nucleators have been recently identified (see Chapter 2) but will not be discussed in detail in this thesis.

The Arp2/3 complex binds to the sides of existing actin filaments and nucleates a

daughter filament from there (Fig. 1.3 B). It consists of 7 subunits, where the two Arp subunits (Arp2 and Arp3) act as a pseudo-actin-dimer that mimicks an actin seed, and the other five subunits (ArpC1 to ArpC5) mediate binding with the mother filament [27–31]. Arp2/3 must be activated by membrane-bound Nucleation Promoting Factors (NPFs), a class of proteins including the Wiskott-Aldrich syndrome family proteins such as WASP and N-WASP [32–34]. Activation of Arp2/3 in this family of proteins is mediated by the VCA domain (Verprolin-rich, Central and Acidic regions) that, together with an actin monomer, associates with the Arp2/3 complex to create the nucleation core [35]. Since the NPFs are bound to and regulated at the plasma membrane, Arp2/3-mediated assembly of actin in the cortex can be precisely steered by the cell. Furthermore, the presence of Arp2/3 on the new filament's pointed end means that this filament is protected from rapid depolymerization until the branch dissociates from the mother filament [36, 37].

Diaphanous1 (Dia1) and other members of the formin family nucleate actin filaments from the barbed end: Dia1 is a homodimeric protein that envelops the actin barbed end, where it prevents depolymerization and promotes polymerization by incorporating actin monomers underneath itself in a ladder-climbing motion [19, 38]. This leads to rapid elongation of actin filaments from profilin-actin [39]. To induce actin polymerization, formins must be activated by a range of membrane associated factors including Rho-GTP, again giving the cell control over where and when actin polymerization happens.

Which protein nucleates actin determines the architecture of the resulting structure: Arp2/3-nucleated actin (Fig. 1.3 D) forms branched networks made up of short filaments (60-120 nm on average in living cells [40]). Formin, on the other hand, nucleates linear arrays of much longer actin filaments (600-1200 nm on average in living cells [40]) (Fig. 1.3 E).

In addition to the nucleating proteins, a myriad of other actin binding proteins determine the architecture of actin networks (Fig. 1.3 F). Depending on the binding partner and its concentration, actin may form disordered networks (e.g. α-actinin [41, 42]), bundles of parallel or antiparallel filaments (e.g. fascin, filamin or fimbrin [41, 43–45]) or even curved bundles and rings (septin, IQGAP, anillin [46–48]). Beyond that, filament lengths are regulated by countless other proteins such as capping protein, tropomyosin, and severing proteins like cofilin and gelsolin [7, 45].

Finally, actin networks are actively remodeled by molecular motor proteins like myosin-2 (Fig. 1.3 G). Myosin-2 forms bipolar filaments composed of tens to hundreds of individual motors, depending on the isoform. These bipolar filaments have motor domains on both ends, allowing myosin to not only move along actin filaments in a directional manner, but also slide actin filaments past one another and thus rearrange actin networks. Muscle myosin-2 is responsible for the macroscopic contraction of muscle cells, and nonmuscle myosin-2 similarly allows nonmuscle cells to contract their cell surface during cell division, or build up tension in stress fibres to withstand forces from the environment. These functions are in turn regulated by the density and architecture of the actin cortex [49, 50].

During cytokinesis, where a cell constricts its equatorial plane (the cytokinetic furrow) to physically split into two daughter cells, the actin cortex as a whole remodels under the influence of motor proteins and regulatory molecules. Actin and myosin are recruited separately to the cytokinetic furrow [51] and are maintained there at tightly regulated levels [52, 53]. At the same time, actin filaments in the furrow gradually align [54–56] and become more tightly anchored to the plasma membrane [57]. The furrow region thus

stiffens, while cortical tension is relaxed at the poles to ensure stable furrow contraction [58–60].

1.5 Outline of this thesis

The previous sections only scratch the surface of the wealth of knowledge that biologists and biophysicists have accumulated about the cell over the past decades. We now have a **detailed list of components** that play a role in shaping the surface of animal cells, giving us a good foundation of knowledge on which we can design reconstitution studies. This vast list also highlights the **complexity** of the cell surface, suggesting that reconstitution can provide valuable insights into how it functions. Since all animal cells must divide to proliferate, and other types of shape changes (like the formation of protrusions, or cell shape adaptation to physical constraints) are also shared among many different cell types and animal species, principles behind the actin-driven shaping of membranes are likely to be **universally applicable**. However, reconstituting actin-driven cytokinesis and other shape changes in the proper **context**, i.e. in a system where actin can deform membranes with enough excess area, poses some significant challenges.

First, we must choose the right components for our minimal actin cortices, and learn how to control their activity. Second, we must find a way to reliably enclose the cortical components in a membrane that can be deformed like the cell surface, and induce preferential assembly of an actin cortex on that membrane. Finally, to change the shape of such a cell-like container from one sphere to a constricted dumbbell-like shape - like during cell division - we must supply it with new membrane area on demand.

In this thesis, we address these three challenges with the ultimate aim of designing an actin-based machinery that can mechanically support and change the shape of the surface of synthetic cells.

In **Chapter 2**, we review in more detail what is known about cytokinesis in animal cells, and summarize the state of the art in reconstituting aspects of animal cell cytokinesis. We identify what the key functional requirements are for driving the constriction of a cell-like container by an actomyosin cortex, and point out which factors have so far hindered progress towards reconstituting productive cellular deformations. Based on the state of the art in actin reconstitution, and taking inspiration from related fields of study, we propose a roadmap towards overcoming the current challenges and achieving sustained constriction of synthetic cells driven by an actin-based machinery.

A central factor in driving the contraction of actin networks is the motor protein myosin. **Chapter 3** focuses on the self-assembly and motility of myosin depending on isoform and buffer conditions, with the aim of understanding how myosin assembly can be controlled for synthetic cell applications. We use high resolution microscopy techniques to compare how both rabbit muscle myosin-2 and *C. elegans* nonmuscle myosin-2 motors self-assemble *in vitro*, and develop a microscopy assay that allows us to study the motility of the resulting myosin filaments on actin bundles. Surprisingly, we find that both large and small myosin assemblies are able to switch between fast and slow motility regimes when moving along stationary actin bundles.

Besides precise control over the behaviour of single cortical components such as myosin, another long-standing challenge in the field of synthetic biology is robust encapsulation of cellular components inside synthetic lipid membrane containers. We address this problem

in **Chapter 4**, where we develop a simplified emulsion-transfer method for encapsulating proteins, in particular actin, in GUVs. The method is broadly applicable, fast and efficient, and allows us to study actin cortex formation in detail. Using quantitative imaging, we quantify the actin encapsulation efficiency, and find that GUVs not only contain a broad distribution of solute concentrations, but can also be significantly enriched in solutes compared to the solution that was originally encapsulated. As a byproduct of our GUV formation technique, we also find that dumbbell-shaped GUVs are produced. Using a combination of experiments and mathematical modeling we show that these dumbbells form as a result of partial GUV-GUV fusion events. Consequently, we are able to use them as a convenient template on which to study how actin cortices respond to curved membranes. We find that Arp2/3-generated actin networks can generate concave patches of plasma membrane, and also preferentially assemble on inwardly bent membranes, apparently sensing micron-scale membrane curvatures. This raises the intriguing question whether such intrinsic curvature sensing also plays a role in sites of micron-scale membrane curvature in living cells, and presents a potential way to simplify actin recruitment to a cytokinetic furrow in synthetic cells.

In **Chapter 5**, we then use our newly established GUV formation method to study how dynamic but rigid actin cortices shape model cell membranes. We demonstrate that the formation of dynamic actin cortices requires less molecular complexity than previously thought, showing that Arp2/3 and membrane-bound VCA alone can nucleate thin actin cortices that turn over on similar timescales as the cortex in living cells. Intriguingly, we show that the reconstituted cortices stiffen the GUV surface and impart on it a shape memory that many times longer than the actin turnover time. Furthermore, we find that the same actin cortices can induce finger-like membrane protrusions in a nucleator-dependent manner. By combining *in vitro* experiments and mathematical modeling, we show that protrusion formation relies on local enrichment of actin nucleators. We also find that several protrusions can originate in close spatial proximity, giving rise to bouquets of membrane protrusions. Our findings demonstrate that dynamic actin cortices can be used to stiffen synthetic cell membranes, and raise the question how living cells avoid trapping of their shape by dendritic cortical actin networks.

Chapter 6 zooms out from the cell cortex and addresses one of the main stumbling blocks we point out in the roadmap towards synthetic cell division laid out in Chapter 2: how can membrane growth in a synthetic cell keep pace with any cell division machinery? We present a protocol for 'feeding' GUV membranes with smaller vesicles (LUVs), which we bind to the GUVs using membrane-anchored DNA zippers. Using population-level quantitative image analysis, we establish that binding of both DNA and LUVs to GUVs happens rapidly and in a DNA-concentration dependent manner. We use a previously reported content mixing assay [61] based on photo-quenching of molecules encapsulated separately in GUVs and LUVs to assess whether the membrane binding we observe also results in LUV-GUV fusion, which is our ultimate goal. Our findings in this matter are inconclusive, as we find that membrane porosity induced by DNA-mediated binding of LUVs to GUVs dominates our results. However, we note that GUV-LUV binding correlates consistently with a population-level size increase of the GUVs, suggesting that membrane fusion likely does occur. This raises several questions for follow-up research: How reliable is the well-established dye-unquenching assay for assessing membrane fusion in other

systems? What drives the large increase in membrane porosity we observe in our assay? What could be done to mitigate this, given that membrane fusion appears to be an important technology for growing membranes in synthetic cells, and delivering lumen and membrane contents more generally?

Finally, we present an outlook (**Chapter 7**) in which we highlight other methods of manipulating synthetic actin cortices. We show how charge-mediated interactions can be exploited for targeted actin-membrane binding, and present two methods of templating cytokinetic furrows: Firstly by controlling myosin motor activity by light, and secondly by incorporating other curvature-generating proteins. We conclude by discussing how the machineries developed in this thesis can be integrated with other functional modules such as metabolism and DNA segregation, and propose next steps towards building a synthetic cell.

2

Actin-Based Synthetic Cell Division

Abstract

One of the major challenges of bottom-up synthetic biology is rebuilding a minimal division machinery. The animal cell division apparatus is mechanically the simplest, in which an actin ring constricts the membrane, as compared to microbes and plant cells, where a cell wall is involved. Furthermore, reconstitution of the actin-based division machinery helps to understand the physical and molecular mechanisms of cytokinesis in animal cells and thus our own cells. In this chapter, we describe the state-of-the-art research on reconstitution of minimal actin-mediated cytokinetic machineries. Based on the conceptual requirements that we obtained from the physical models of shape changes involved in cell division, we propose two major routes for building a minimal actin apparatus capable of division. Importantly, we acknowledge both the passive and active roles that the confining lipid membrane can play in synthetic cytokinesis. We conclude this chapter by identifying the most pressing challenges for future reconstitution work, thereby laying out a roadmap for building a synthetic cell equipped with a minimal actin-based division machinery.

2.1 Introduction

Bottom-up synthetic biology is an emerging field at the interface of cell biology, chemistry and physics. Several national and international initiatives have been founded recently, which are aimed at reconstituting synthetic cells that can autonomously grow and divide [2, 62]. As a chassis, usually giant unilamellar vesicles (GUVs) are used, which are cell-sized (5-50 µm) containers enveloped in a lipid bilayer [63–66]. One of the key functions that a synthetic cell must be able to perform in order to be considered life-like is cytokinesis [67], a process in which a cell physically splits into two daughter cells. To reconstitute cytokinesis, various strategies are being pursued, inspired by biological strategies employed by prokaryotic, archaeal or eukaryotic cells [67, 68]. These biological systems have in

This chapter was co-written by Lucia Baldauf, Lennard van Buren, Federico Fanalista and Gijsje Koenderink and is published as a Review of the same name in ACS Synthetic Biology (2022).

common that cell division is accomplished by a cytoskeletal protein machinery, often ring-shaped, that assembles at the cell equator. In microbial cells (bacteria and yeast), this protein machinery collaborates with a complex cell wall synthesis machinery [69, 70]. By contrast, animal cells lack a cell wall and cytokinesis is entirely driven by the actin cytoskeleton. Actin-based cell division could thus be an ideal basis for engineering synthetic cell division.

Bottom-up reconstitution of actin-based cell division is interesting not only from an engineering perspective, but also as a means to understand how cytokinesis works at the molecular level in animal cells. Although cytokinesis is a well-studied cellular process, surprisingly many fundamental questions about its working principles remain unanswered [71]: What are the relative roles of molecular motors and other components and cellular processes in force generation? How much molecular complexity is needed to ensure that the actin cortex retains its structural integrity during cytokinesis? What are the requirements for cortex-membrane interactions to promote furrow ingression? These questions are difficult to address in cell-based studies because of the enormous molecular complexity of cells, combined with inbuilt redundancies and substantial variation between cytokinetic mechanisms employed by different species and cell types [72–74].

In this review, we propose a roadmap towards the bottom-up reconstitution of actin-driven cytokinesis in minimal cells. For brevity, we consider only the process of furrow ingression, neglecting other aspects such as membrane abscission and chromosome and cytoplasmic segregation, which are reviewed elsewhere [75–78]. Based on theoretical models of cytokinesis in animal cells, we first identify four central biophysical requirements for actin-driven furrow ingression. Next we review experimental insights obtained from recent efforts to reconstitute minimal actin systems. We also emphasize the importance of controlling the surface area of the synthetic plasma membrane to enable cell division. Finally we propose a roadmap towards building a molecular machinery that can successfully deform a minimal cell-like container.

2.2 Biophysical requirements for making a cell divide

Cytokinesis in animal cells is a complicated process that involves many different molecular components (lipids and proteins) whose interactions and localization are tightly regulated. At a coarse-grained level, however, it is possible to formulate general biophysical requirements for cell division based on a consideration of the mechanical forces at play. Pioneering experimental work from the 1950s onward has demonstrated that cytokinesis is accompanied by membrane furrowing [79], cortical stiffening [58, 80] and the appearance of ordered filamentous structures in the cytokinetic ring [54, 81]. These observations have served as input for coarse-grained theoretical and computational models that describe cytokinesis as the shape evolution of a thin, viscoelastic and active shell around a (nearly) constant volume of cytoplasm. From the models, we can infer several key requirements that a cell, living or synthetic, must fulfil in order to successfully divide (Fig. 2.1).

1. Cortical activity. The actin cortex driving cytokinesis in animal cells must be active. This means that it should include elements that hydrolyse adenosine triphosphate (ATP), an energy-carrying nucleotide, to generate contractile forces that produce cellular shape changes. The viscoelastic and active nature of the cortex can be described using the

framework of active gel theory as proposed by Kruse et al. [82]. This formalism is usually applied in the viscous limit [55, 83–85], as cytokinesis is slow (minutes) compared to the fluidization time scale (10 s) of the actin cortex [83]. This effectively implies that the cortex flows on the time scale of cytokinesis, which can result from different microscopic origins such as crosslinker or filament turnover [86, 87]. The molecular origins of active force production are complex and depend on molecular detail, as discussed below.

2. Cortical thickness. Active gel theory predicts that cortex activity, at least when mediated by myosin motors, is roughly proportional to cortical thickness [83–85]. To maintain cortical activity, the cortex must consequently be of a controlled thickness. Cortical thickness is regulated by a balance of actin polymerization and depolymerization, or turnover, and cortical flows: cortical flows accumulate material in the cytokinetic furrow, whereas turnover redistributes actin throughout the cell. This suggests two requirements for synthetic cell division. Firstly, components of the cortex must be laterally mobile to be effectively redistributed by cortical flows [83, 85, 88]. Secondly, actin turnover rates must be low enough to allow local actin accumulation and therefore increased contractility in the furrow region. If actin is removed too rapidly, furrow constriction slows down significantly and may be halted altogether [85]. On the other hand, complete lack of filament turnover in a 2D actomyosin cortex is theoretically predicted to lead to irreversible clustering of actin, inhibiting effective stress generation [89]. While active gel theory has been useful to capture various aspects of the actin cortex, recent studies show that other models might be required to describe the mitotic region, where cortex thinning due to protein alignment is accompanied not be decreased, but by an increased cortical tension [56]. This prediction has yet to be reconciled with experimental evidence from yeast cells, which suggests that the persistent presence of filamentous actin, rather than turnover, is key for successful contraction of the cytokinetic ring [90]. The difference might be explained by the fact that in yeast, the ring is an isolated one-dimensional object, where theoretical models predict sustained contraction both at slow and rapid turnover speeds [91].

3. Cortical symmetry breaking. From the 1930s onwards, various models have been proposed to explain the mechanical basis of cytokinesis. The early models range from active expansion of the cell poles [92], through active pushing by the mitotic spindle [93], to spindle-mediated relaxation of the cell poles [88, 94] and finally active constriction of the cytokinetic furrow [54, 85, 95, 96]. While details vary widely between these models, they share a key characteristic: they all posit that there must be a difference in activity between the polar and equatorial regions to drive furrow ingression. After decades of research it is now widely accepted (reviewed e.g. in [97]) that the main driving factor of animal cell cytokinesis is actin-based constriction at the cleavage furrow. However, *in vitro* reconstitution may be the ideal tool to understand actin's role in molecular detail, and to assess to which extent other mechanisms, such as polar expansion [98] or interaction with astral microtubules (reviewed in [99]) also contribute.

4. Cell surface area and volume regulation. Consistent with observations in cells, models have generally assumed that the cytoplasm is very weakly, if at all, compressible [85, 88]. The apparent cell surface-to-volume ratio, however, changes dramatically during cytokinesis [100]. It follows that the cell's (visible) surface area must be changing. In theoretical works this change in surface area is generally assumed to be energetically 'free', as living cells can regulate the available membrane area through a variety of processes like

blebbing [60], or caveolae disassembly and membrane trafficking [101, 102]. This supply of membrane on demand is probably one of the most challenging aspects to recapitulate in a reconstituted system.

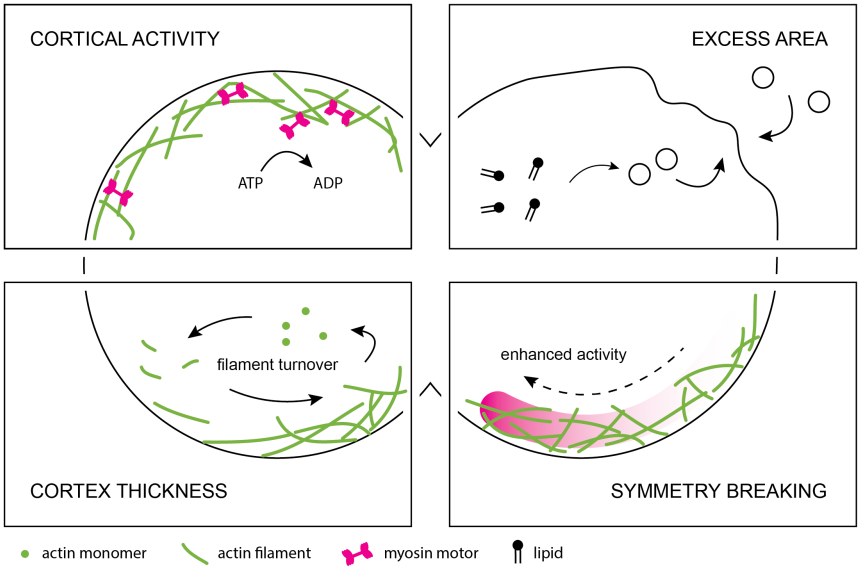

Figure 2.1: **Four key biophysical requirements for reconstituting synthetic cell division.** For cell deformation to occur, cortical activity driven by ATP hydrolysis is required (top left), which can for example be generated by myosin activity. Regulation of cortex thickness (bottom left) is essential for control of cortical activity and is determined by the rate of actin filament turnover versus cortical flows. For cortical activity to lead to cell deformation, the symmetry of the system needs to be broken (bottom right). Finally, to accommodate the drastic change in surface-to-volume ratio during cell division, excess membrane area needs to be generated prior to or during cytokinesis (top right).

2.3 Roadmap towards actin-driven synthetic cell division

Cytokinesis of animal cells is a highly complex and tightly regulated process. Yet, as discussed earlier, fairly minimal computational models are able to recapitulate aspects of cytokinesis, suggesting that the underlying mechanisms may be recreated with simplified molecular mechanisms. Here, we propose a roadmap towards reconstituting actin-driven cell division by considering lessons from recent cell and *in vitro* (i.e. cell-free reconstitution) studies. Basically, there are two routes for reconstitution of actin-driven cytokinesis (see Fig. 2.2). First, cell division can be recreated via reconstitution of an actin cortex that, upon symmetry breaking, is more contractile at the cell equator as compared to the poles. This route is closest to cytokinesis in mammalian cells, and we therefore name it the 'naturalistic route'. The second route is by construction of a cytokinetic ring that anchors and contracts at the cell equator, coined the 'engineering route'. We will first discuss the design of an actin-based machinery fit for driving cytokinesis in both scenarios, and in the next section

consider the design of the lipid membrane envelope.

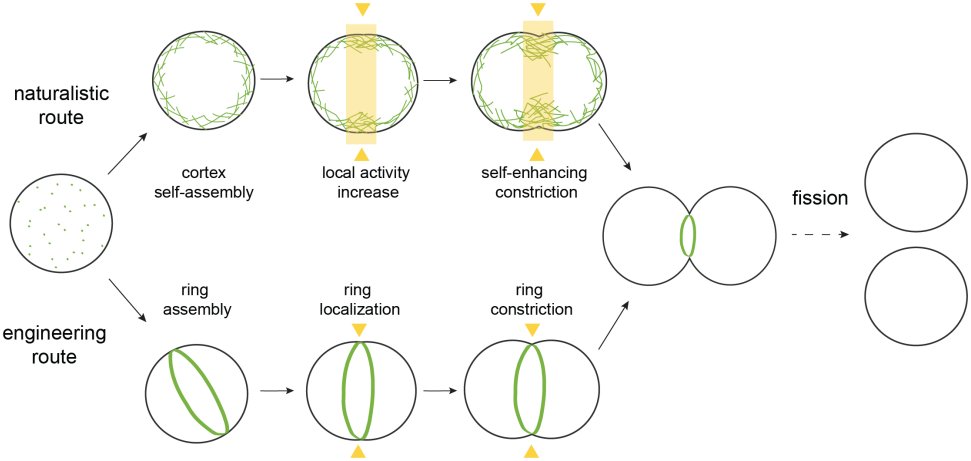

Figure 2.2: **Routes to actin-based synthetic cell division.** There are two main routes to achieve actin-driven division of a synthetic cell: by symmetry breaking of a reconstituted actin cortex, triggered by external or biochemical cues, which leads to self-enhanced furrow constriction (the 'naturalistic' route, top), or by construction of a contractile ring at the cell equator (the 'engineering' route, bottom). Yellow arrowheads indicate where contractile activity is concentrated. The final fission step is outside the scope of this review.

2.3.1 Naturalistic route: Building a self-assembling cytokinetic ring

During interphase, mammalian cells have a continuous actin cortex that lines the plasma membrane [6]. When cells enter mitosis, the cortex is remodelled and self-assembles into a contractile ring at the cell equator. Symmetry breaking and midplane localization of the cytokinetic furrow is initiated by biochemical signalling, which includes Rho-dependent myosin phosphorylation in the furrow region [85, 103]. The locally enhanced activation of myosin is thought to lead to cortical flows from the poles to the equator [88, 104], which further accumulate and organize contractile elements in the furrow [105] that drive furrow ingression [85]. Such a complex self-assembling system has not been built to date, but steps have been taken along the road (Fig. 2.3).

Reconstitution of active actin networks

Both cell-free experiments and theoretical models of cortex-like disordered actin networks have been used to elucidate why disordered actomyosin networks are contractile in the first place. The detailed mechanisms are reviewed elsewhere [50, 106, 107], but they broadly comprise two scenarios. Actin filaments are semiflexible polymers with a thermal persistence length of 10-15 µm, of the same order as their contour length [108] in *in vitro* studies. Note that cortical actin filaments are much shorter *in vivo*, ranging from 120 to 1200 nm depending on the nucleator and cell type [40]. The first contraction scenario, relevant for well-connected networks of long filaments, is that the anisotropic mechanical force-extension response of actin filaments causes them to buckle and break under motor-induced compressive stress [109, 110]. The second scenario, relevant for networks with

short actin filaments, is that the structural polarity of actin filaments in combination with the tendency of myosin-2 motors to dwell at the filament plus end before detachment causes contraction via polarity sorting [84, 111, 112]. In the actin cortex of mammalian cells both mechanisms may contribute to contractility, since distinct populations of short and long filaments are present there [40].

Notably, the combined effect of contractile motor activity and actin turnover remains poorly explored. Theoretical models generally assume that the cytokinetic cortex does undergo actin turnover [83, 85, 113], and have even indicated that turnover is key for sustained stress generation during furrow ingression [89]. Experimentally, besides one study with a cell extract [114], only one minimal *in vitro* study has so far combined actin turnover and myosin activity [115]. This work showed that myosin activity alone can be sufficient to induce turnover in minimal actin networks (see Fig. 2.3, purple). Myosin-driven compaction and fragmentation of Arp2/3-nucleated actin led to the removal of actin from the network, and subsequent redistribution and re-incorporation of network components, creating a cortex in dynamic steady state. Strikingly, actin turnover rates were observed to be much slower here than typical rates in cells, with actin turning over within tens of minutes rather than tens of seconds, respectively [116, 117]. This discrepancy is likely due to the absence of dedicated actin severing proteins in the minimal system. More rapid turnover has been observed *in vitro* in volume-spanning entangled actin networks where filaments were severed by cofilin and polymerization was driven by formin [87]. Combining more rapid turnover with motor activity *in vitro* may open a rich field of network behaviours, with complex implications for both the regulation of cortical thickness and of stress propagation and relaxation [118].

To build and control a system that allows actin to turn over, we can turn to the growing body of work studying the functions of various actin regulators on the single molecule or filament level. Research into the two key nucleators of cortical actin, Arp2/3 and formins [26, 40, 121] has uncovered new complexities in recent years. Both the processivity and the actin filament elongation rate of different formins have been shown to be regulated by the physicochemical environment, the presence of profilin, and mechanical stress [122–124]. Even more complex co-regulation of formin with other barbed-end binding proteins is emerging [125]. Regulation of Arp2/3 by profilin [126, 127] as well as by actin filament curvature [128] has been known for a number of years. However, the true diversity and complexity of the various isoforms of Arp2/3, which itself is a protein complex consisting of seven protein subunits, is only just emerging [129]. In addition, there are regulating factors that control cortex architecture by controlling both formin and Arp2/3 activity [121]. Besides formin and Arp2/3, other actin nucleators such as the recently identified spire [130] have barely been used in reconstitution experiments and may offer yet other routes towards reconstituting a minimal dynamic cortex. Actin depolymerization can equally be controlled by various factors. Disassembly of filamentous actin *in vitro* is usually mediated by proteins of the ADF/cofilin family [131]. The activity of ADF/cofilin proteins has been shown to depend on cooperation with other proteins [132, 133] and on actin crosslinking [134]. ADF/cofilin also facilitates debranching in actin networks nucleated by Arp2/3 [131], which is furthermore sensitive to force and actin filament age [135].

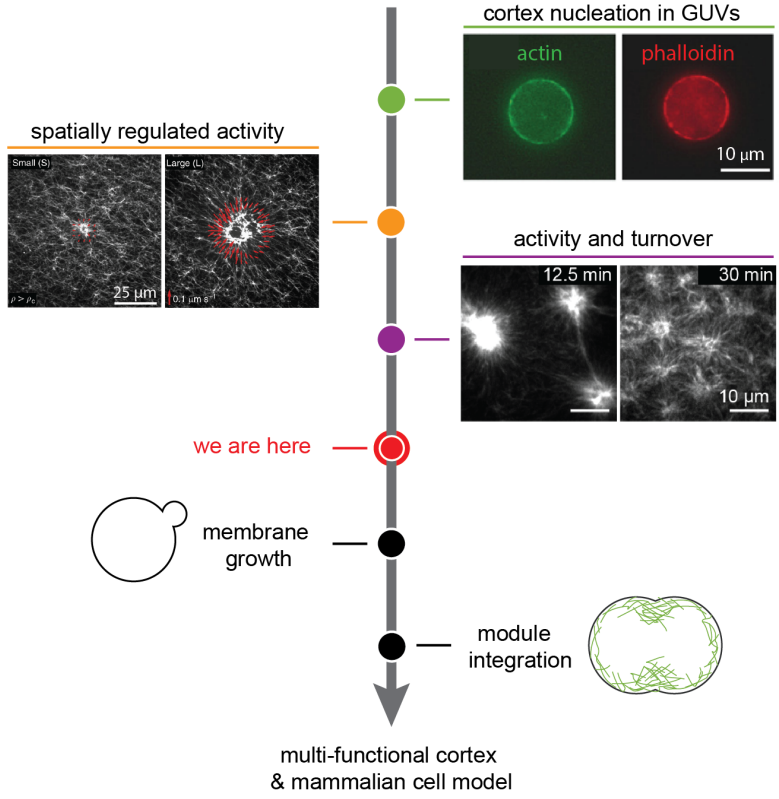

Figure 2.3: **Roadmap to division with an actin cortex.** Green: successful nucleation of an actin cortex inside GUVs [119]. Filament formation of actin (green) is confirmed by co-localization of the filament-binding peptide phalloidin (red). Orange: spatiotemporal control of myosin activity by light-induced inactivation of the myosin inhibitor blebbistatin was used to generate network contraction over different length scales, from small (left) to large (right) [120]. Purple: combination of myosin activity with actin filament turnover generates sustained network contraction [115]. In the coming time, steps need to be taken to engineer membrane growth, and finally to integrate the different modules inside a GUV.

Reconstitution of actin cortices inside GUVs

Controlled actin encapsulation in GUVs has proven to be a challenge. Over the years, many different methods have been explored for protein encapsulation, either based on lipid swelling [136] or on emulsion transfer [119, 137–139] (reviewed in [63]). Of these, methods based on emulsion transfer are currently most successful, although the encapsulation efficiency and the ability to upscale the number of encapsulates remain to be characterized [138]. Most prior GUV studies focused on the effect of crosslinking proteins and myosin motors on bulk-nucleated actin. By contrast, membrane-nucleated actin networks with turnover in GUVs remain poorly explored. Early works from the Sykes lab [119, 140] demonstrated that Arp2/3 nucleated cortices can be reconstituted at the inner leaflet of GUVs (Fig. 2.3, green), and that such cortex-bearing vesicles reproduce aspects of the mechanics of living cells. More recently, Dürre et al. demonstrated that Arp2/3 nucleated

cortices can induce local deformations of the GUV membrane by either polymerization forces alone or in combination with contractility induced by non-muscle myosin-II [141]. New work from the Liu lab shows that membrane-bound Arp2/3 in combination fascin and α-actinin is sufficient to yield ring-like membrane-bound actin networks [142]. Myosin-initiated contraction of these networks resulted in membrane constriction, thus getting one step closer to cell division.

More extensive work, especially with myosin-driven cortices, has been performed with stable actin filaments anchored to the membrane by streptavidin or actin-binding membrane proteins. In such systems, cortical tension was shown to depend on the ratio of active versus passive crosslinkers [143] and excessive cortical tension was shown to cause full or partial detachment of the cortex from the membrane [143, 144]. Recently, Litschel et al. demonstrated the formation of actomyosin rings in GUVs [137]. However, these structures were unable to deform the GUV membrane on large length scales because they slipped on the membrane. Based on our understanding of cell division, this is likely due to (at least) three missing factors: cortex turnover, symmetry breaking between the poles and equator of the synthetic cell, and a severely limited supply of extra membrane area. Symmetry breaking is likely necessary for productive and sustained membrane deformations. There are several artificial means by which symmetry breaking could be triggered in synthetic cells. Myosin activity could, for instance, be locally light-activated by targeting either the light-sensitive myosin inhibitor blebbistatin [120, 145, 146] (see Fig. 2.3, orange) or myosin-II directly [147]. Similar approaches could be used to locally modulate the crosslink density of the actin cortex or the interaction strength of the cortex with the synthetic cell membrane. Finally, it would likely help to make GUVs shape-asymmetric, for instance by using microfluidic channels [148].

Conceptually, building a dynamic actin cortex and pushing it towards self-assembly of a cytokinetic furrow is very attractive. Such a system would mimic many core attributes of the cortex of living animal cells. Further, the continuous nature of such a cortex would allow it take on a triple function: as a mechanoprotective module for the synthetic cell, as a dynamic controller of cortical and membrane tension, and as a division apparatus. Its versatility sets the actin cortex apart from other cytoskeletal systems such as FtsZ [149]. A life-like actin cortex offers the opportunity to test existing theoretical models of cell division and to tease out the essential functions needed for cytokinesis in living cells. On the other hand, a dynamic actin cortex will necessarily comprise more proteins and hence a higher level of complexity than one composed of stable actin filaments. From an experimental perspective, reconstituting sustained actin turnover in combination with motor activity will in particular be challenging, as it requires fine control over both stoichiometry and activity of cytoskeletal components. In addition, timing self-assembly in concert with other cellular events, such as chromosome segregation, cell size doubling, and fission, remains a challenge to date.

2.3.2 Engineering route: Building an isolated contractile ring

A more engineering-type approach to synthetic cell division may also be interesting: instead of building a cortex that self-organizes into a ring, one could build an isolated ring directly (Fig. 2.2, bottom). This would inherently fulfil the requirement for different activities in

polar and equatorial contractility, as by definition the poles are not contractile in such a case. If a sufficient supply of long actin filaments throughout furrow ingression can be ensured, the need for controlled turnover may be diminished and the complexities of such regulated filament assembly and disassembly may be avoidable. This approach will need to address three key challenges: 1) to build an actin ring, 2) to make it contractile, and 3) to maintain the ring's mid-center position during contraction such that membrane invagination rather than ring slippage occurs.

How to build an isolated ring?

Actin filaments can be bundled and bent into ringlike structures in various ways (Fig. 2.4, green). Most simply, ring formation can be induced by entropic effects through macromolecular crowding [150] or by cross-linking with multivalent ions [151]. Alternatively, proteins can be used to bend actin into rings. Septins spontaneously bend actin into ringlike structures [46] and are recruited to the cytokinetic furrow, where they cooperate with anillin in actin-membrane binding [152–156]. Anillin itself also promotes the formation of actin rings by promoting overlap between filaments [48]. Further, the IQGAP fragment 'curly' has recently been shown to bend actin into rings on model membranes by bending single actin filaments [47]. The fact that all three of these proteins are enriched in the cytokinetic furrow [157] suggests that these ring-forming capabilities may provide a cellular mechanism to promote successful cytokinesis.

Confinement of actin filaments inside spherical droplets or vesicles tends to promote the formation of actin rings because the confinement forces the semiflexible filaments to minimize the filament bending energy [161]. Entangled or crosslinked actin networks inside emulsion droplets and inside lipid vesicles form peripheral cortex-like networks [142, 162–166], while bundled actin forms one or more closed rings [136, 142, 158, 164, 165]. Single rings form when the container size is smaller than the persistence length of the actin filament or bundle [142, 165]. Recent theoretical [167] and experimental work [137] has shown that ring formation can be further enhanced by introducing actin-membrane adhesion. It should be noted, however, that ring formation requires a subtle balance of filament-filament and filament-wall adhesion, as well as size and stiffness of the confinement, and is not trivial to precisely control experimentally.

How to contract an isolated ring?

Contracting a once-formed actin ring can again proceed in different ways (Fig. 2.4, orange). The classical purse-string model posits a well-organized cytokinetic ring that closes by myosin-mediated translocation of actin filaments [54, 168]. Although this model does not appear to hold in all cell types [169–171], recent superresolution and electron microscopy showed convincing evidence that it does apply at least in some cell types [172, 173]. Contracting actin-myosin rings have been succesfully reconstituted on supported lipid bilayers [47] and inside water-in-oil droplets [158] and GUVs [137]. The efficiency of ring closure is likely determined by the orientation and arrangement of the actin filaments in the ring, which can be tuned by crosslinker composition and concentration [49, 110, 165, 174, 175].

Alternatively, ring contraction may be driven by mechanisms that do not require molecular motors. For instance, anillin was recently shown to drive actin bundle contraction even though it is a passive crosslinker [48]. Contraction was attributed to an energetically

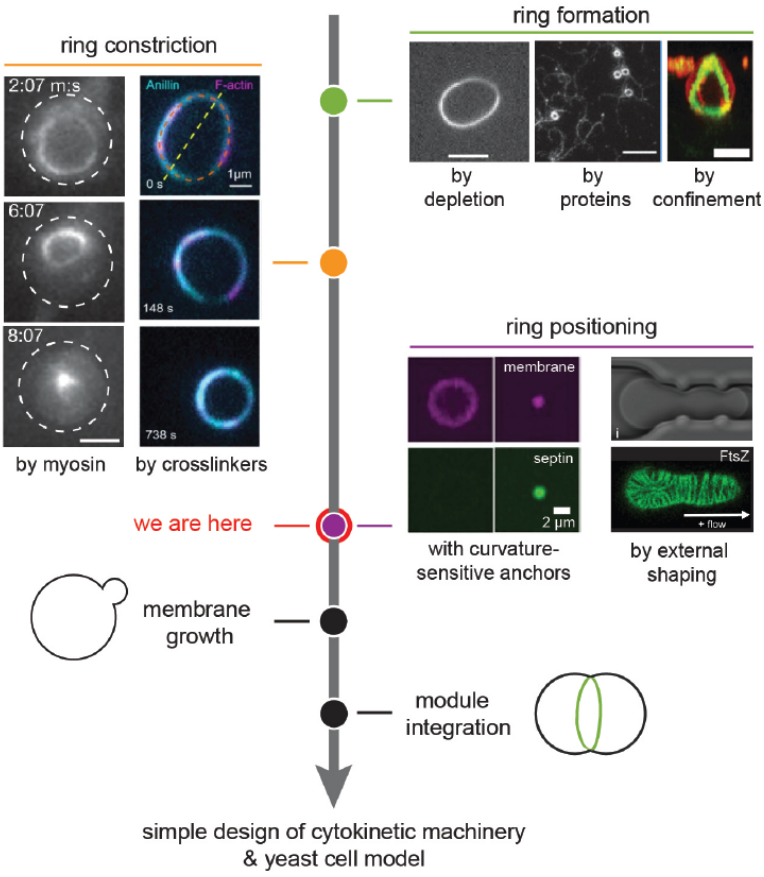

Figure 2.4: **Roadmap for division with contractile actin ring.** Roadmap towards synthetic cell division using a contractile actin ring. Green: actin rings can be formed by depletion interactions using macromolecular crowders [150], by proteins that combine actin binding with curvature generation such as curly [47] or simply by confinement of actin bundles [136]. Orange: constriction of actin rings can be executed using myosin motors [158] or using actin crosslinkers like anillin [48]. Purple: the actin ring can be positioned using curvature-sensing anchors (left: septin binds preferentially to membranes of higher curvatures as shown with membrane-coated beads [159]) or by mechanical deformation (right: microfluidic traps deform GUVs leading to rearrangement of FtsZ rings [160]). In the next steps towards achieving synthetic cell division, membrane growth needs to be reconstituted, and all separate modules have to be integrated.

driven process whereby actin filaments increase their overlap as long as energy can be gained by accumulating diffusible crosslinkers in the overlap region [48]. This mechanism was enhanced when anillin was combined with actin depolymerization. Since contraction driven by passive crosslinkers does not consume energy from an external energy source such as ATP, it can only bring the system into a configuration of minimal free energy, at which point rearrangement will stop [176]. Intriguingly, recent theoretical modelling [177] suggests that a crosslinker that consumes ATP to unbind from actin filaments, but does not actively translocate them like myosin, could in principle induce contraction indefinitely.

In this case, the consumption of an energy carrier breaks detailed balance in the system, and in combination with the asymmetric mechanical properties of actin, overall contractile forces can arise.

How to keep an isolated ring in place?

Although contractile actin rings have been successfully reconstituted inside GUVs, so far none of these efforts have yielded anything close to furrow-like membrane invaginations. The rings either detached or slipped along the membrane upon myosin activation [137, 143, 144, 158], at best producing rare instances of slight membrane deformation [137]. In cells, positioning of the cytokinetic ring is ensured by a complex and poorly understood interplay between the actin and microtubule cytoskeleton, local changes in lipid composition, and soluble signalling molecules [178, 179]. Reconstituting this interplay in GUVs seems too technically challenging to be expected in the coming years. We therefore expect that simpler, if less biological, solutions may be more promising. To the best of our knowledge, no such efforts have been reported so far. However a few options present themselves (Fig. 2.4, purple): curvature-sensing or –inducing scaffolding proteins such as septins [159] or I-BAR-domain proteins [180, 181] may help in templating a furrow and inhibiting slippage of contractile actin rings. These proteins may have to be combined with more engineering-type solutions designed to deform GUVs from the outside, either by confinement in traps [148, 160] or by membrane-binding complexes [182–184].

Building an isolated contractile actin ring in principle offers an elegant way to drive synthetic cytokinesis. Formation of such a ring requires only few components and tuning ring contractility is certainly subtle, but most likely achievable. The biggest technical challenge in this approach is to localize the ring at the equator and keep it in place during contraction so as to foster productive membrane deformation. On a more conceptual level, reconstituting isolated contractile rings likely will not bring us much insight into the mechanisms of cytokinesis in animal cells. It may however be a valid strategy for understanding mechanisms in yeast cytokinesis, in tandem with top-down work on yeast cell ghosts [53].

2.4 Involving the membrane

So far, we have largely ignored an important assumption in the key requirements that we set out earlier, which is that the GUV membrane and actin cortex are intrinsically coupled. However, it is far from trivial that actomyosin contraction is followed by deformation of the cellular membrane. While actomyosin networks and membranes have separately been thoroughly investigated by biophysicists, their interplay has received much less attention and presents a crucial challenge to address in the coming years.

2.4.1 Membrane-cortex anchoring

In vivo, a multitude of cytoplasmic proteins is known to be involved in actin-membrane adhesion, many of which have binding sites for both actin and membrane lipids. These proteins include ERM (ezrin, radixin, moesin)-proteins, myosin-1b, anillin and septins [188–191]. How these proteins cooperate in adhesion and how they are spatially organized at the membrane remains elusive. Electron microscopy and superresolution microscopy have revealed that the distance between the filamentous actin and the plasma membrane is

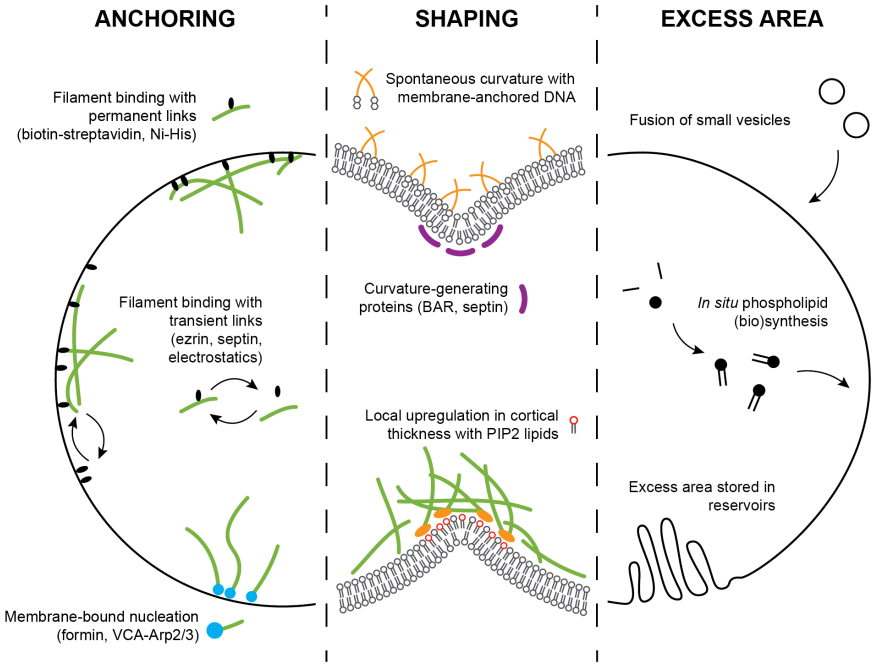

Figure 2.5: **Membrane engineering for synthetic cell division.** Schematic overview of possibilities for membrane design. Anchoring of the actin cortex (left) can be done either via filament nucleation from the membrane, or via filament binding to the membrane. Binding can be done using strong permanent linkers, or using weaker transient links. Membrane shaping (middle) can be done by generating spontaneous curvature, for example with membrane-bound DNA nanostars [185] or by physiological curvature-generating proteins such as BAR proteins [186] or septin [187]. Otherwise, when lipids can be spatially separated, local elevation of PIP_2 levels can increase cortical thickness via regulating actin nucleation and severing proteins. To provide excess area during cytokinesis (right), new membrane area can be added by fusion of small vesicles or by *in situ* synthesis of phospholipids. Alternatively, membrane area could be stored in reservoirs that become accessible upon furrow ingression.

surprisingly large, ranging from 10 to 20 nm in the cell cortex of animal cells [192] and from 60 to 160 nm in the cytokinetic ring of fission yeast [193, 194]. It is unclear how this large gap, which is often wider than the distance that known linker proteins span, arises. There is evidence that the actin cortex itself is stratified, with myosin filaments being restricted towards the cytoplasmic side of the cortex due to steric exclusion from the dense cortex [195]. Interestingly, a recent *in vitro* reconstitution study showed that actin-myosin networks on supported lipid bilayers spontaneously self-organize into radial actin structures (asters) with myosin at the core and layered atop to relieve steric constraints [196].

Mechanical measurements on cells indicate that the cortex adheres to the membrane via a high density of weak links. With optical tweezers, one can pull membrane tubes from cells with membrane-bound beads. These tubes can easily be moved over the cell

surface [197], indicating that the membrane easily zips off the cortex and quickly rebinds. Various tube pulling experiments have shown that the force required for tube extrusion is dependent on the levels of ezrin [198] and phosphatidylinositol-4,5-bisphosphate (PIP_2) lipids [199]. PIP_2 lipids specifically interact with many actin-binding proteins including ezrin (reviewed in [200]). In *S. Pombe* cells, PIP_2 depletion causes sliding of the cytokinetic ring, indicating that PIP_2-dependent actin-membrane adhesion is essential for anchoring of the ring [201]. Although PIP_2-protein interactions are individually weak, their high density collectively causes a tight yet dynamic seam between bilayer and cytoskeleton.

In stark contrast to the reversible actin-membrane binding observed *in vivo*, *in vitro* reconstitution efforts have mostly relied on anchoring interactions with unphysiologically high binding affinity (Fig. 2.5, left). Many studies used either direct coupling of biotinylated actin filaments to biotinylated lipids via streptavidin [137, 143, 202] or indirect coupling using His-tagged actin-binding proteins coupled to Ni-NTA lipids [144, 203]. These bonds are virtually permanent and unbreakable [204–206]. As described above, actin-myosin cortices anchored in this manner typically detach from the membrane upon myosin activation [143, 144] as a result of anchor slippage [207] or pulling out of lipids [143]. In two studies with high anchor density, the acto-myosin cortex did remain attached to the membrane upon contraction, but it slid towards one side so the membrane was only minimally deformed [137, 143]. Cortex slippage is likely due to the fluid nature of the lipid bilayer membrane. Actin and microtubule gliding assays with motors proteins anchored onto supported lipid bilayers have shown that motor activity is accompanied by lipid slippage [208, 209]. The interplay between the dynamics of the actin cortex and the dynamics of the lipids is complicated. Adhesion to the actin cortex slows down lipid diffusion [210, 211], while myosin-driven actin cortex contraction can actively cluster lipids into microdomains [212–217]. Altogether, it remains poorly understood what conditions are necessary for the actin cortex to remain stably anchored and cause sustained membrane deformation.

Dynamic actin-membrane linkage has so far been reconstituted only on supported lipid bilayers. Using ezrin recruited to the bilayer via PIP_2 lipids, a dynamic actin network was created that could be remodelled by passive filament cross-linkers [218]. Bead tracking microrheology showed that ezrin serves as a dynamic cross-linker for the membrane-attached actin layer with the network stiffness being controlled by the pinning point density [219]. Ezrin-anchored actin filaments could diffuse over the membrane but longer filaments were immobilized, being pinned by a larger number of actin-membrane links [220]. This indicates that collective binding with transient links can fix cytoskeletal structures in place on top of a fluid membrane. Other promising candidates for *in vitro* transient actin binding are septins and anillin. Septins themselves can bind to membranes and self-assemble into filamentous scaffolds [221]. Membrane binding is curvature-sensitive [187, 222], which renders septins interesting candidates for spatially controlling actin organization in synthetic cells. In solution, septins can bind and crosslink actin filaments into curved bundles [46]. This could explain the role of septins in the formation and stabilization of contractile actomyosin rings observed *in vivo* [46]. However, the simultaneous interplay of septins with lipid membranes and actin has yet to be reconstituted *in vitro*. Like septins, also anillin possesses both actin-binding and membrane-binding domains. Anillin has been shown by reconstitution to be able to anchor actin filaments to lipid membranes in a RhoA-dependent manner [223]. In combination with anillin's ability to bundle and

constrict actin rings via condensation forces [48], it would be interesting to explore anillin's ability to promote synthetic cell division. Besides protein-based binding, actin filaments can also be bound to lipid membranes by electrostatic interactions that can be tuned by the choice of ions, offering an alternative route for studying and modulating transient actin-membrane binding [224].

Besides actin-membrane linkers, also membrane-localized actin nucleation contributes to cortex-membrane adhesion. The main nucleators of cortical actin filaments *in vivo* are Arp2/3 and formin [26]. Arp2/3 in combination with membrane-bound nucleation promoting factors such as WASP are responsible for the formation of branched actin filament arrays, whereas formins nucleate linear filaments. Actin nucleation has been successfully reconstituted *in vitro* both with formins, often for simplicity with constitutively active mutants [225], and with Arp2/3, often activated by WASP fragments such as VCA [39, 119, 226]. Actin turnover can be introduced by addition of severing proteins such as ADF/cofilin [227].

It is unknown how filament nucleation in conjunction with actin-membrane anchoring by dynamic linker proteins such as ezrin will influence the ensemble mechanics of the actin-membrane composite. Tailoring actin-based division machineries towards synthetic cell division will require careful tuning of the cortex itself, the anchoring strategy, and also the membrane physico-chemical properties.

2.4.2 Membrane engineering

The membrane should not be considered just a passive player in cytokinesis. In contrast, membrane properties can be exploited to aid cytokinesis, for example by shaping the contractile network (Fig. 2.5, middle). *In vivo*, the plasma membrane in the cleavage furrow has a distinct lipid composition that is thought to contribute to cytokinesis by biochemical signalling and perhaps also by induction of spontaneous curvature [228]. Elevated PIP_2 levels at the cleavage furrow probably contribute to furrow ingression by recruiting anillin, septins and ERM-proteins [229]. Furthermore, PIP_2-mediated signalling promotes the formation and maintenance of a stable actin cortex by promoting actin nucleation and slowing down actin filament severing via actin regulatory proteins [230]. Other membrane components such as gangliosides and cholesterol also accumulate in the cleavage furrow, where they regulate and bind the cortex [229]. In addition, the distribution of phosphatidylethanolamine (PE) lipids over the two bilayer leaflets changes significantly during cell division: while PE lipids reside in the inner leaflet during interphase, they are exposed in the outer leaflet of the cleavage furrow during cytokinesis [231]. This asymmetric distribution of PE lipids has been shown to be important for disassembly of the contractile ring after cytokinesis [231]. It is possible that the specialized lipid composition of the cleavage furrow also directly affects cytokinesis by changing the mechanical properties of the membrane, but this remains to be shown.

For engineering artificial cell division, it could be useful to exploit known mechanical effects of lipids. An important characteristic of lipid bilayers is that asymmetries between the two membrane leaflets give rise to spontaneous membrane curvature. Asymmetries can be generated in many different ways (reviewed in [232]), such as by different lipid compositions or different numbers of lipids in the two leaflets [233], proteins binding to one leaflet[184], membrane-anchored DNA oligos inserting into one leaflet[185], or

different solutes on both sides of the membrane [234]. In the context of actomyosin-based synthetic cell division, spontaneous curvature effects could be exploited for spatial control and symmetry breaking. Binding of proteins to the outer leaflet of vesicles can be used to make vesicles dumbbell-shaped and to constrict and even split the neck [184]. Generation of negative membrane curvature could be used to locally recruit septins, which selectively bind to membrane areas with micrometric curvature [159, 187]. In addition, membrane-binding proteins that not only sense, but also generate curvature could be used, such as BAR-domain proteins. I-BAR proteins were shown to directly bind to actin in fission yeast [181] and are therefore interesting candidates for promoting actomyosin-driven membrane invagination. Interestingly, I-BAR domain proteins promote ezrin enrichment in negatively curved membrane protrusions [180], providing further prospects for boosting membrane invagination *in vitro*.

2.4.3 Addition of new membrane area

To create two daughter cells from a single mother cell, assuming spherical geometry, the cell surface area has to increase by 28% [100]. *In vivo*, this extra membrane area is delivered to the cleavage furrow by targeted endosomal transport [235]. This mechanism does not only lead to a local area increase, but also allows fast and localized delivery of specific lipids and regulatory proteins (reviewed in [236]). For reconstitution of cell division, various strategies can be followed to increase the membrane area (Fig. 2.5, right). First, GUV membranes can be grown by external addition of small unilamellar vesicles (SUVs) that can be forced to fuse with the GUV using fusogenic peptides, DNA, or charge-based interactions [237–240]. Second, lipid membranes can be grown by *in situ* synthesis of lipids from their precursors. Examples are non-enzymatic reactions from synthetic reactive precursors [241] or enzyme-catalysed biosynthesis using either purified proteins [242] or *in vitro* transcription-translation [243]. Although there is evidence that mammalian cells do not use area reservoirs, such as microvilli, to supply extra membrane area for division [244, 245], this mechanism could be exploited for engineering division in a synthetic cells. Asymmetries between the two leaflets of the bilayer generated by different means (see preceding section) can be used to store excess area in membrane tubes and buds [184, 234, 246, 247]. Low forces suffice to access these reservoirs [234, 247]. To achieve synthetic cell division, it will be important to match timing of membrane areal growth with the timing of actin-driven constriction. To achieve multiple cycles of division, it will moreover be important to build in a mechanism to maintain lipid homeostasis.

2.5 Challenges ahead

In the past decades, our knowledge of cell division and its molecular actors has increased tremendously. To understand the physical mechanisms governing actomyosin-driven cell division, focus is put increasingly on bottom-up reconstitution experiments. Bulk and SLB experiments have helped us to understand mechanics of active actomyosin networks in 3D and 2D. However, translating these insights to the process of cell division is not trivial. To summarise, we list here the critical challenges that need to be overcome before we can reconstitute a minimal version of actin-driven cell division.

First, we need to understand how actin network contraction is sustained to drive

division all the way. This will require myosin activity working in concert with actin turnover. While activity and turnover have been studied to great extent individually, we still have minimal understanding how they together govern actin network mechanics and contractility. Not only is this a challenging system to understand from a physical and biological perspective, also from an experimental perspective it is difficult to recapitulate, as it involves a large number of components whose concentration and activity need to be tightly controlled. More *in vitro* work in this direction, both in 3D and 2D, will be essential to explore the parameter space.

Second, it remains elusive how the actomyosin network should be anchored onto the membrane in order to achieve membrane deformations. A multitude of anchoring strategies has been developed and investigated, but only minimally in combination with a deformable membrane. Combined with our limited understanding of cortex-membrane molecular organization *in vivo*, this may prove one of the most important challenges. Future studies need to focus on understanding the influence of linker density and strength, as well as membrane composition and organization. In addition, the individual contributions of actin-membrane linkers and membrane-bound filament nucleators need to be delineated. After successful deformation, size stability between the two forming daughter cells, driven by Laplace pressure, needs to be ensured [248].

Third, attention must be paid to the supplying of extra membrane area during constriction. Additional area can be present in membrane reservoirs, be synthesized, or be added by fusion of small vesicles. However, none of these approaches have to our knowledge been co-reconstituted with actin-driven contraction and resulting membrane deformation.

Fourth, there is to date only a minimal body of work on contractile actomyosin networks in GUVs. Confining the system in GUVs requires that all components are encapsulated in the right concentration and stoichiometric ratio, while preserving functionality. Although there are numerous GUV formation techniques, they have been minimally characterized for their potential to encapsulate complex mixtures of biochemically active components. More work in this direction is crucial to perform controlled reconstitution in GUVs, but also to be able to extrapolate findings from bulk and SLB experiments to vesicle systems.

Fifth, spatial and temporal control of the components and their activity is crucial. On the short term, some of the involved challenges may be by-passed by taking a semi-autonomous approach to synthetic cell division. For example, optogenetics, external mechanical or chemical cues, or fusion-based delivery of components with small vesicles provide handles to control the system even after encapsulation of the components inside GUVs. However, if the goal is to create a synthetic cell that divides fully autonomously, reconstitution will be more complicated, requiring for example feedback loops, signalling molecules and internal clocks.

As a concluding remark, we note that the most pressing challenges to achieve *in vitro* actin-driven cell division require integration of modules. Only when actomyosin studies meet membrane biophysics, when myosin motor activity is combined with actin turnover, and when protein biochemistry becomes integrated in GUV formation, we can start thinking about reconstituting cell division. In the coming years, perspectives from experimental work, theoretical studies and simulations need to be combined to guide future work with the ultimate goal to develop a full understanding of actin-driven synthetic cell division.

2.6 Acknowledgements

We thank Ilina Bareja, Gerard Castro-Linares and Fred MacKintosh for useful discussions about actin cross-linkers. We acknowledge financial support from The Netherlands Organization of Scientific Research (NWO/OCW) Gravitation program Building A Synthetic Cell (BaSyC) (024.003.019).

3

Role of myosin-2 filament assembly in its motility on actin tracks

Abstract

Class 2 myosins are motor proteins that play a crucial role in a range of cellular functions such as cytokinesis, cell migration, and wound healing. To fulfill these functions, these non-processive motor proteins need to self-assemble into bipolar filaments that are able to rearrange actin filaments. However, the relation between the size of myosin filaments and their motility, and its dependence on myosin isoform and species are unclear. Here, we reconstitute myosin-2 filaments from rabbit skeletal muscle myosin as well as *C. elegans* nonmuscle myosin *in vitro* and characterize their self-assembly using high-resolution mass sensitive electron microscopy and interferometric scattering microscopy. We find that the skeletal muscle myosin filaments are large and consistent in size over a range of physiological buffer conditions, while *C. elegans* nonmuscle myosin filaments consist of only 8-10 monomers with some dependence of size on ionic strength. We furthermore develop a motility assay where the self-assembled myosin filaments move along actin racetracks made of thin bundles of parallel actin filaments. We measure the myosin run speeds in the presence of physiological levels of ATP, and find that *C. elegans* nonmuscle myosin-2 filaments are surprisingly fast-moving. Moreover, both the nonmuscle myosin-2 and the skeletal muscle myosin-2 filaments switch between fast and slow running segments on the same actin racetrack. We propose that this surprising behaviour originates from different binding modes of the bipolar myosin filament with the underlying race track.

This chapter includes STEM data that was acquired and analyzed by Viktoria Wollrab (AMOLF). Lutz Vogeley, Tina Wiegand and Stephan Grill (MPI-CBG) purified and biochemically characterized the *C. elegans* nonmuscle myosin.

3.1 Introduction

Myosin-2 motor proteins are key players in the actin cytoskeleton, fulfilling a range of functions, from regulating cortical tension [147] to contracting the cytokinetic ring [249], facilitating wound closure by constricting supracellular actin cables [250], to actuating contraction of muscles [251]. All of these functions rely on the ability of myosin-2 motors to form filaments that bind actin filaments for prolonged periods of time, walk along them, and rearrange actin filament networks. Class 2 myosins, often referred to as 'conventional' myosins, form filaments in different types of muscle cells (e.g. striated and smooth muscle), as well as in non-muscle cells [252–254]. All class 2 myosins are heterohexameric proteins that consist of a pair of identical heavy chains (HCs, green) and two sets of light chains (essential light chain (eLC, orange) and regulatory light chain (rLC, purple)) (Fig. 3.1 A). The HCs are further subdivided into an N-terminal head or motor domain, which facilitates actin binding and ATPase activity, and a C-terminal tail domain, which mediates assembly of myosin filaments [255, 256]. The light chains stiffen the neck region, which undergoes conformational changes as ATP is hydrolyzed during the myosin power stroke, allowing the motor domain to translocate along actin filaments in a barbed-end-directed manner (Fig. 3.1 B). For simplicity, we will refer to the full hexameric protein as a 'myosin monomer' from now on.

The overall protein domain structure is consistent among all the members of the myosin-2 family, but the domains have slightly different functions depending on the isoform of myosin-2. In skeletal muscle myosin-2, the motor domain is constitutively active [257], whereas nonmuscle myosin-2 is inactive and folded in an autoinhibitory state until the rLC is phosphorylated [258]. For *in vitro* reconstitution experiments, rLC phosphorylation can be mimicked by phosphomimetic point mutations, yielding a constitutively active form of nonmuscle myosin-2.

Since the myosin-2 motor domain has a low duty ratio, i.e., it spends the majority of its ATPase cycle not strongly bound to an actin filament ($\lesssim 0.05$ for skeletal muscle, compared to up to 0.8 for nonmuscle myosin-2, depending on the isoform [259]), a single myosin monomer cannot processively walk along actin filaments like other myosin family members such as myosin V or myosin X [260–262]. Instead, myosin-2 motors must first assemble into bipolar filaments. In skeletal muscle cells, myosin is arranged in symmetric bipolar thick filaments of ~ 1.5 µm in length, with motor domains protruding along both sides in a regularly spaced pattern [251, 263, 264]. This arrangement also emerges when myosin-2 motors self-assemble *in vitro*: The rod-like myosin tail domains drive filament formation by association of their alpha-helical coiled-coil domains, forming the central bare zone [265–267]. Note that the bare zone may also be decorated with motor domains, depending the assembly protocol [268]. Nonmuscle myosin-2 forms small filaments *in vitro*, with typically a few tens of motor domains per rod [267, 269], whereas muscle myosin-2 forms much larger bipolar filaments comprising several hundred monomers [268, 270, 271]. *In vitro,* filament assembly is triggered when myosin is transferred from a high ionic strength buffer (> 300 mM KCl) to a low ionic strength buffer (<200 mM KCl, typically 50-100 mM [265, 272]). Monomers are thought to first assemble into parallel dimers via charge-mediated interactions between highly charged regions in the tail domain [255, 273–275], which go on to associate with each other into a spiral structure [276] both in a parallel and antiparallel orientation to form bipolar filaments [255, 277].

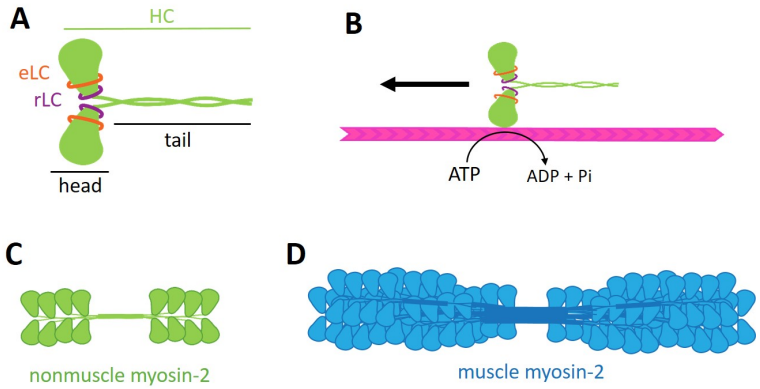

Figure 3.1: **Structure and self-assembly of myosin-2 motors.** (A) Class 2 myosins are two-headed motor proteins comprised of two sets of three distinct domains: the two heavy chains, subdivided into head and tail (green), the two essential light chains (eLC, orange) and the two regulatory light chains (rLC, purple). (B) Myosin-2 binds to actin filaments via its motor domain, which also hydrolyzes ATP to fuel the myosin power stroke that drives translocation towards the barbed end of the actin filament. To become processive, myosin-2 monomers must self-assemble into bipolar filaments of <30 monomers in the case of nonmuscle myosin-2 (C), or several hundred monomers in the case of skeletal muscle myosin-2 (D).

The size of filaments formed by skeletal muscle myosin-2 is known to depend on ionic strength and pH. Acidic conditions (pH ~ 6.0 – 7.0) promote the formation of long and thick filaments, compared to shorter filaments ($\lesssim$ 0.5 µm) formed in a more alkaline buffer (pH ~ 7.0 – 8.0) [278]. Furthermore, the filament size is influenced by kinetic effects: rapid dilution into the final buffer leads to the formation of relatively short filaments (~ 1 µm) while slow dialysis into the final buffer favours the formation of long and thick filaments that can reach up to 5 µm in length with a large polydispersity [265].

Nonmuscle myosin-2 assembly is known to be specific to both species and tissue [277]. The formation of nonmuscle myosin-2 filaments *in vitro* has been studied for human platelet myosin-2 [267] as well as for nonmuscle myosin-2A and 2B [269, 279], revealing that even myosin filaments from the same species can differ by a factor of 2 in size (28 monomers per filament for platelet myosin versus 60 for nonmuscle myosin-2B). *Acanthamoeba* myosin-2 [272] and Drosophila [280] nonmuscle myosin filaments show the same overall structure, but both form filaments with fewer constituent monomers, also depending on the assembly buffer pH and ionic strength [272]. The filament sizes and morphologies formed by nonmuscle myosin-2 in the widely used model organism *Caenorhabitis elegans (C. elegans)* have so far not been characterized.

While skeletal muscle myosin-2 in particular has been known since the 1860s [281], we still lack a full understanding how assembly and motility of myosin filaments are connected. Classically, the motor activity of myosin is assessed in a so-called actin sliding assay, where myosin monomers are adhered randomly to a flat nitrocellulose-coated substrate, and the motion of fluorescently labeled actin filaments atop these motors is monitored by fluorescence microscopy [282–284]. This is an extremely elegant biochemical assay which has yielded insights into many aspects of myosin function, such as what part of the protein is responsible for motility and ATPase activity [285], myosin step size and actin

translocation speed [286], and the effect of environmental conditions [282] and disease-related mutations [287]. However, it is unclear to what extent the assay can capture the role of the spatial organization of myosin monomers within bipolar filaments [283]. In sliding assays with surface-immobilized myosin filaments [285], the actin sliding speeds were only slightly higher than for single immobilized motors. However, protein adsorption to sticky surfaces can induce flattening or unfolding of protein structures, so it remains unclear whether the monomer organization in immobilized filaments is the same as for filaments in solution. Possible interactions between actin and the trailing end of the myosin filament are also inhibited. Furthermore, to observe processive sliding of actin filaments by nonprocessive motors like myosin-2, it is generally necessary to add high concentrations of methylcellulose in the buffer, which changes interaction strengths between actin and myosin and can qualitatively change the motile behaviour of myosin filaments [279]: It was reported that nonmuscle myosin-2 A filaments were not motile in conditions where the monomers did produce actin filament motion in gliding assays, further suggesting that myosin filament assembly is important for its motility [279].

To study myosin motility in a context which is more relevant to myosin's role in cellular processes, we thus need a well-characterized experimental system in which myosin motility can be studied in a high-throughput fashion. Early studies demonstrated such a system in the form of actin 'railroad tracks' isolated from *Nitella axillaris* algae [288], on which the motion of fluorescent beads coated with heavy meromyosin, a truncated version of myosin-2, was tracked. However, this system is challenging to set up, requiring algeal culturing and dissection, and introduces the complex biological context of a native structure from plant cells. Recently, similar assays built bottom-up from purified components have been developed, to demonstrate myosin movement in dense, membrane-tethered actin networks a few actin layers in height [220] or on actin bundles crosslinked by different actin binding proteins [289].

Here, we build an experimental system to allow for straightforward tracking of many hundreds of self-assembled myosin filaments over long actin bundles, allowing us to follow processive myosin motion without being limited by the length of individual actin filaments. Moreover, bundles are representative of actin structures that myosin interacts with in cells (e.g. stress fibres and dense cortical actin networks). We first characterize the assembly of myosin-2 derived from rabbit skeletal muscle as well as recombinant *C. elegans* nonmuscle myosin-2. We show that assembly of *C. elegans* nonmuscle myosin-2 is salt-sensitive, whereas rabbit skeletal muscle myosin filament size and packing density remains unchanged over a wide range of ionic strengths. High-throughput automated particle tracking reveals that both muscle and non-muscle myosin-2 motor filaments exhibit an unexpected switching behaviour between a slow-moving or quasi-stationary, and a fast-moving state. Further, motility is salt-dependent: Muscle myosin filaments can walk faster at higher ionic strength, but spend less time doing so.

3.2 Results

3.2.1 Self-assembly of C. elegans nonmuscle myosin-2

We characterized nonmuscle myosin-2 from the nematode worm *C. elegans* because it is a genetically tractable model system [290] that has been extensively studied for its function

in cytokinesis and morphogenesis *in vivo* [105, 291–294]. Nonmuscle myosins from various different species have been characterized, and their protein sequences are highly conserved [254]. However, it remains unclear to what extent filament assembly is consistent across species.

We found in negative stain transmission electron microscopy (ns-TEM) that the filaments had the expected rod-like structure which broadens towards the ends, where motor domains protrude (Fig. 3.2 A and B, white arrows). However, we also often found a protruding mass of protein in the middle of the filament (Fig. 3.2 A, yellow arrow), the bare zone where we would ordinarily not expect any protruding motor domains [267]. We attributed this mass to the protein (mGFP and FLAG) tag at the C-terminus of our myosin construct, and hence at the end of the rod domain [295]. The clustering of these fluorescent proteins can hence explain the extra protein mass in the center of the filament. Many of the filaments were slightly curved, either in the same direction along the entire filament (Fig. 3.2 B, green arrow) or with the two ends bent in opposite directions (Fig. 3.2 B, white arrows). This bent shape indicates that the nonmuscle myosin filaments are more flexible than those formed by muscle myosin under the same conditions, consistent with the much lower number of constitutent molecules (see section 3.2.2). From ns-TEM images, we measured the contour length of nm-myosin-2 filaments. Median filament lengths decreased from 260 to 189 nm in filaments assembled at 80 mM compared to 50 mM KCl (Fig. 3.2 C). This suggests that fewer myosin monomers assemble into one filament at higher ionic strength, consistent with proposed mechanisms of myosin-2 assembly, which is thought to rely on electrostatic interactions between adjacent rod domains [255, 274, 295]. To directly measure the filament size in terms of the number of monomers, we turned to mass photometry based on interferometric scattering microscopy (iSCAT). iSCAT relies on the interference of light reflected by a coverslip surface with that reflected by particles adsorbing to that interface (see Supp. Fig. 3.19). The interference contrast is proportional to the particle size. For proteins, the contrast is therefore directly proportional to their mass, assuming a constant mass density of 1.41 g/cm^3, which is valid for proteins above ~ 25 kDa [296]. The mass distribution of protein samples can be measured with a resolution down to around 20 kDa.

Nonmuscle myosin-2 monomers appeared as dark circular spots on a grey background in iSCAT, while filaments featured an additional white rim whose intensity varied with filament mass (Fig. 3.2 D). We first determined the mass of a nonmuscle myosin-2 monomer in a myosin monomer buffer at 300 mM KCl (Fig. 3.2 E). The mass distribution revealed a clear Gaussian monomer peak centered around 548 kDa (inset) as well as a small peak around 100 kDa due to buffer components (Supp. Fig. 3.19 C) and a low shoulder around 400 kDa, likely from a proteolytic myosin fragment or some protein contaminant. Since this contamination was minor, we did not study its origins further.

We next proceeded to perform iSCAT measurements on the filaments formed in the 50 and 80 mM KCl buffers after 30 minutes assembly time at room temperature. We normalized the masses to the monomer mass, to obtain the number of constituent monomers per filament. In Fig. 3.2 F, we weighted the mass histogram by the mass in the bin, and normalized the entire histogram so that the sum of all bin heights was one. Consequently, the height of a bin at mass m_{bin} represents the likelihood for a myosin monomer to be part of an assembly with mass m_{bin}. Both at 50 mM KCl and at 80 mM KCl, we saw that a

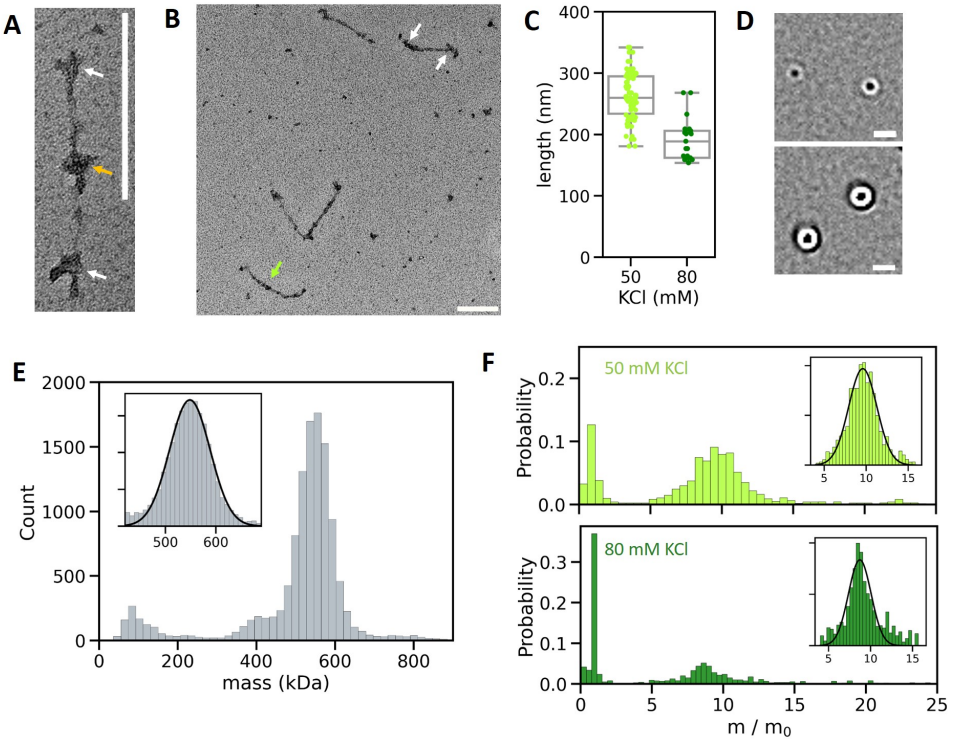

Figure 3.2: **Assembly of C. elegans nonmuscle myosin-2.** (A) Negative stain TEM image of a typical filament. The elongated structure broadens at the ends where the head domains protrude outwards (white arrows), and has a visible blob in the center (yellow arrow), likely representing the C-terminal mGFP- and FLAG-tags in the tail domain. (B) Overview image showing that the nonmuscle myosin-2 filaments were consistent in appearance and often were slightly curved in one direction (green arrow) or two opposite directions (white arrows). (C) Box plot of filament lengths assembled at either 50 mM or 80 mM KCl from the TEM images of N = 102 and 26 from 2 separate experiments each. (D) Ratiometric iSCAT images of nonmuscle myosin-2 monomers (top) and filaments (bottom). Due to their small size, both appeared as diffraction-limited circular spots, with the contrast was proportional to the mass. (E) Histogram of the myosin monomer masses from iSCAT. The main peak follows a Gaussian distribution (inset, black line) centered around 548 kDa with a standard deviation of 40 kDa, consistent with the expected monomer mass. The peak below 100 kDa originates from buffer components (Supp. Fig. 3.19), and the low shoulder around 400 kDa comes from an unidentified contaminant. N = 12287 events from 3 independent samples. (F) Histogram of masses (normalized to the measured monomer mass m_0 = 548 kDa) for filaments assembled at 50 (top, light green) and 80 mM KCl (bottom, dark green), respectively. The histograms were weighted by the mass and normalized, so that the height of each bar represents the probability of finding a myosin monomer in a myosin assembly of mass m/m_0. N = 6580 and 5684 events from 2 samples in each condition. In addition to the monomer peak at m/m_0 = 1, both histograms show a broad peak at higher masses, which represents myosin filaments. At 50 mM KCl, this peak follows a Gaussian function centered around 9.6 monomers with a standard deviation of 1.7 (black line, inset in top panel). At 80 mM KCl, the filament peak is centered around 8.7 monomers with a standard deviation of 1.3 (black line, inset in bottom panel). TEM images were convolved with a median filter of 2 px kernel size for clearer visualization. Scale bars: 0.2 µm.

filament peak emerged next to the monomer peak, which continued to be present at low ionic strength. We fitted Gaussian functions to the monomer ($0 < m/m_0 < 2.5$) and filament ($5 < m/m_0 < 16$) peaks and integrated over both peaks to measure the fraction of myosin monomers incorporated in filaments. At 50 mM KCl, 96 % of all myosin monomers were contained in filament assemblies between 5 and 15 monomers in size, with an average of 9.6 ± 1.7 monomers per filament (Fig. 3.2 F, top). At 80 mM KCl, by contrast, the filament peak was smaller in size, but still contained 82 % of all myosin monomers. Individual assemblies were also smaller on average, with the peak at 8.7 ± 1.3 monomers, consistent with the reduced filament length seen in TEM images.

3.2.2 Self-assembly of rabbit skeletal muscle myosin-2

Skeletal muscle myosin-2 is well-known to self-assemble into much larger filaments than nonmuscle myosin-2 [297]. Since the assembly is known to be sensitive to many parameters including protein concentration and buffer composition, we used electron microscopy to study rabbit skeletal muscle myosin-2 self-assembly in conditions compatible with our motility assays. We confirmed that the protein indeed formed rod-like structures which were both longer and thicker than those formed by nonmuscle myosin-2 (Fig. 3.3 A, B). While we did not observe broadening of the filament ends, there were small protrusions visible along the length of the filament, representing myosin motor domains protruding from the central rod (Fig. 3.3 A, white arrows). The filaments all appeared straight and with slightly tapered ends, and varied considerably in length (Fig. 3.3 B). From ns-TEM images, we determined that the median filament length was 503 nm for skeletal muscle myosin-2 assembled at 50 mM KCl (N=71, Fig. 3.3 C).

To determine how many monomers make up a filament, we were not able to use iSCAT: most filaments appeared as elongated structures in iSCAT images (Fig. 3.3 D) since their length was larger than the diffraction limit for green light, so that we could not treat them as point scatterers. The appearance of several diffraction rings (black, white, black going from the inside out) was also an indication of the large particle mass, and signals the breakdown of the assumption that mass is proportional to interferometric scattering contrast. Instead, we therefore turned to scanning transmission electron microscopy (STEM) for mass mapping. Here, unstained myosin filaments adsorbed to a thin EM grid are scanned by a convergent electron beam, and the transmitted electrons are recorded in High-Angle Annular Dark-Field mode (HAADF) at a high angle relative to the incident beam. At these high angles, the image intensity is directly proportional to the local mass [298, 299] and can be calibrated using specimens of known and constant mass-per-length, typically virus particles like the Tobacco Mosaic Virus (TMV) [300]. Since STEM is based on darkfield imaging, it provides information about the total mass of a given particle (like iSCAT) but also resolves its spatial structure, in principle down to the Ångstrom lengthscale [298]. In practise, we could clearly distinguish structures down to ~ 20 nm, enough to resolve individual myosin motor domains.

Automated analysis of the STEM images provided the length- and mass distributions of the filaments assembled at different ionic strengths (Fig. 3.3 F, G). Total filament masses were extracted by integrating the mass-per-length along the length of each filament. We found that filaments assembled at 50 to 100 mM KCl did not statistically differ in length (774 ± 312 nm for 50 mM KCl, 871 ± 411 nm for 75 mM KCl and 810 ± 369 nm for 100 mM

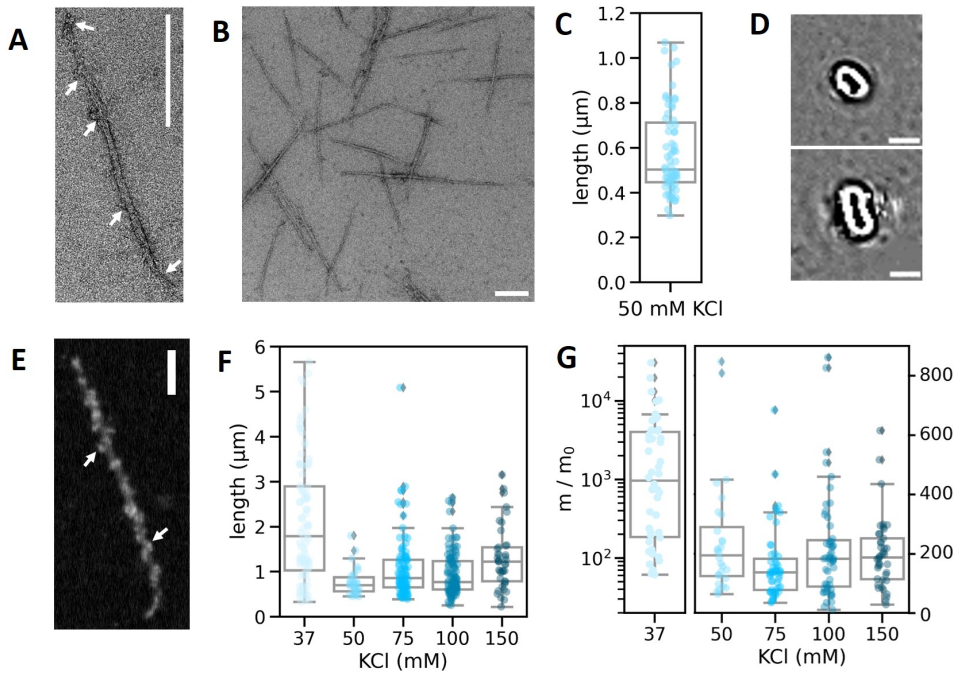

Figure 3.3: **Assembly of rabbit skeletal muscle myosin-2.** (A) ns-TEM image of a typical filament. White arrows indicate blob-like protrusions, which represent the myosin motor domains protruding from the straight, rod-like structure. (B) Overview ns-TEM image showing that filaments assembled at 50 mM KCl appeared rod-like, straight, and slightly tapered towards the ends. (C) Length distribution of muscle myosin-2 filaments assembled at 50 mM KCl from ns-TEM showed an average length of around 500 nm (N=71 from 2 separate experiments). (D) iSCAT images confirmed that the skeletal muscle myosin filaments were larger than the diffraction limit, clearly looking elongated. (E) STEM image of a skeletal muscle myosin-2 filament assembled at 50 mM KCl. Compared to ns-TEM, the STEM image showed a much clearer signature of blobs along the rod (white arrows), representing the myosin motor domains. Note that the intensity is proportional to mass density. (F) Box plot of filament lengths from STEM analysis for muscle myosin-2 assembled at different KCl concentrations. (G) Box plot of corresponding total filament masses. Myosin filaments assembled at 37 mM KCl were much larger than those assembled at higher KCl concentrations. (F) and (G) are based on N = 46, 52, 52, 51 and 41 filaments from at least two independent samples for 37, 50, 75, 100 and 150 mM KCl, respectively. ns-TEM images were convolved with a 4 px median filter for clearer visualization. Scale bars: 1 µm in panel D, otherwise 200 nm.

KCl, p=0.60 by one-sided ANOVA test). At 150 mM KCl, the filaments became longer (mean length of 1294 nm, $p < 10^{-5}$ comparing 50, 75, 100 and 150 mM KCl by one-sided ANOVA test, Fig. 3.3 G). Filaments did not statistically differ in their total mass at KCl concentrations between 50 and 150 mM KCl (p=0.10 by one-sided ANOVA text), with filament masses averaging between 843 and 1274 MDa, corresponding to a range of 162 - 245 monomers per filament (assuming a myosin monomer mass of 480 kDa [301]). By contrast, filament assembly changed dramatically at 37 mM KCl (Fig. 3.3 F, G). Under this condition, filaments were significantly longer, with average lengths around 1951 nm, and much more massive, with an average mass of 1720 MDa or 3308 myosin monomers, up to masses as high as 30500 myosin monomers. Similarly, the mass per length was comparable among samples

assembled at 50 - 150 mM KCl, but was significantly higher for filaments assembled at 37 mM KCl (Supp. Fig. 3.10 A). A drastic change in filament morphology was also evident in the STEM images: instead of the slender myosin filaments with a pronounced bare zone at higher KCl concentrations (Supp. Fig. 3.22 B, bottom panels), myosin filaments assembled at 37 mM KCl were very thick, decorated along the entire length of the filament with motor domains, and tapered towards the ends (Supp. Fig. 3.22 B, top panel). Surprisingly, even though the means of the mass-per-length distributions at 50, 75, 100 and 150 mM KCl were statistically different ($p < 10^{-5}$ by ANOVA test), we did not observe any clear trends.

3.2.3 Building actin racetracks to test myosin filament motility

To form actin racetracks on which to monitor myosin motility, we first pre-polymerized actin in bulk solution at 15 μM at room temperature in the absence of any methylcellulose or actin binding proteins. We included small amounts of fluorescently labeled actin monomers to facilitate fluorescence microscopy, and biotin-tagged actin monomers to mediate sparse binding to the coverslip. To stabilize the filaments, unlabeled phalloidin was added to the filaments after 30 min at a 1:1 molar ratio. An image of such pre-polymerized actin filaments is shown in Fig. 3.4 A. To create actin racetracks, we were inspired by the method reported in [302], where actin was deposited in a flow channel and subsequently bundled by methylcellulose. We adapted the method to include a pre-bundling step at higher actin concentration, which in our hands led to significantly more reliable bundle formation. We first mixed 6 μM actin filaments with methylcellulose at high concentrations (0.5 % w/V), to induce bundling driven by macromolecular crowding [303]. After at least 30 min incubation at room temperature, the viscous solution of F-actin and polymer was diluted to 2 μM actin, keeping the concentrations of other buffer components constant, and subsequently flushed into flow channels. The flow channels were then kept at room temperature for at least 30 min to allow time for actin to be crowded towards the channel walls. At this stage, we found large, often curly bundles of actin, which were primarily aligned in the direction of flow in the flow channel owing to the high viscosity of the solution (Fig. 3.4 B). Such large, disordered actin bundles were unsuitable substrates for myosin running, as myosin filaments tended to get trapped in them (Supp. Fig. 3.12). We thus needed to straighten and order the bundles, as well as remove excess methylcellulose. This was done in a two-step process: First, the flow channel was flushed with 3 chamber volumes of the same buffer containing 0.5 % methylcellulose as well as 0.25 μM fascin. Fascin selectively cross-linked parallel actin filaments in the bundles [41] and fixed them in place, while flushing with high methylcellulose concentrations removed large parts of the non-crosslinked actin and helped to straighten and further align the bundles (Fig. 3.4 C). In the second step, excess methylcellulose was removed by flushing with 5 chamber volumes of buffer containing 0.25 μM fascin and 0.1 % methylcellulose. This yielded arrays of long, largely parallel and sparsely connected actin bundles (Fig. 3.4 D). All buffers were supplemented with 0.1 mg/mL κ-casein to ensure good surface passivation at all times, and any further flushing steps were performed in the presence of 0.25 μM fascin to avoid destabilization of the actin bundles [304, 305].

To test whether our assumptions about the bundle formation process were justified, we first analyzed whether the actin bundle sizes at different stages of the assembly process

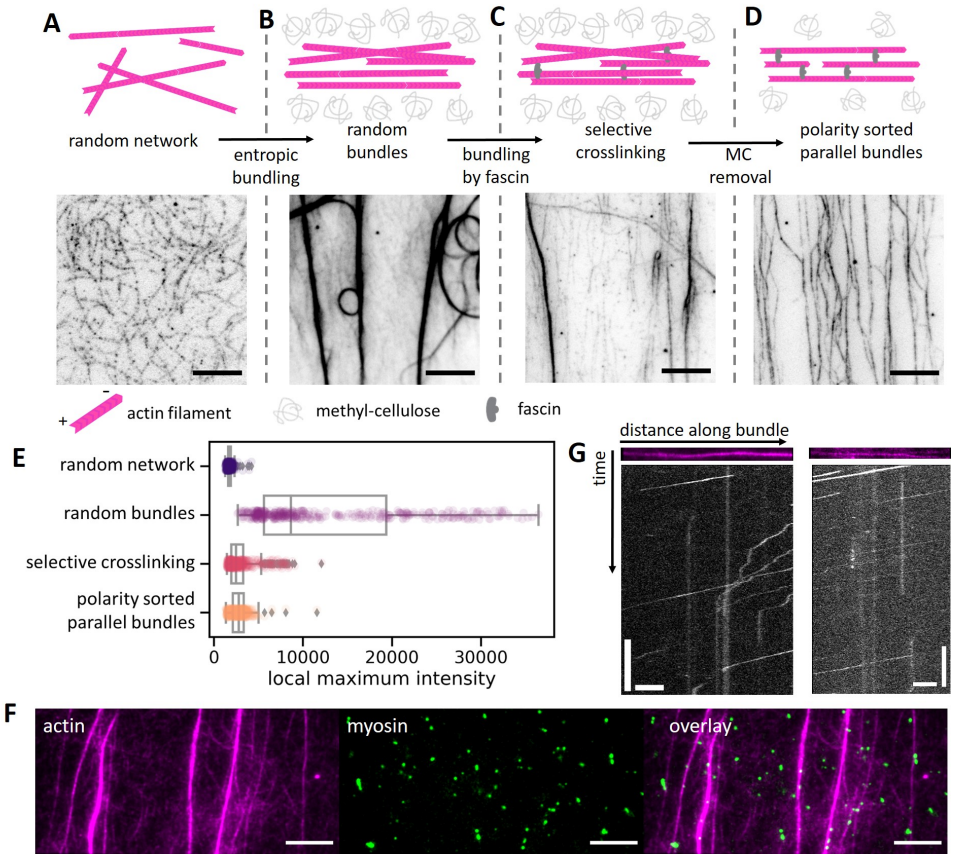

Figure 3.4: **Assembly of fascin-stabilized actin racetracks.** Top panels illustrate the process while bottom panels show TIRF images of actin at each step. Scale bars: 10 µm. For clarity, an inverted grey colorscheme is used such that actin shows up as dark filaments on a bright background. (A) Actin filaments in solution were first separate and oriented randomly. The TIRF image was taken in a 2 µM actin filament solution, so individual filaments can be distinguished. (B) Upon addition of methylcellulose, excluded volume interactions promoted the formation of thick bundles aligned in the direction of flow due to the sparse attachment of filaments to the coverslip. (C) Flushing with a buffer of containing methylcellulose and fascin led to selective crosslinking of parallel actin filaments. Filaments of the opposite polarity were gradually removed. (D) Finally, methylcellulose was completely replaced by fascin. This yielded thinner bundles that were well-aligned and only sparsely connected with each other. (E) Box plot of the local maxima in actin fluorescence intensity at different stages of the track formation process. Each datapoint represents the maximum actin intensity in 20x20 pixel sections of each image as a proxy for the local actin density. n=400 sections from one field of view for each distribution (images shown in A-D). (F) TIRF images of a typical field of view in a running assay with skeletal muscle myosin (green). Actin bundles (magenta) were usually up to ~ 40 µm long with their length limited by the field of view. Scale bars: 10 µm. (G) Example kymographs of myosin running along actin bundles. The horizontal axis represents the distance along an actin bundle, and the vertical axis represents time. Scale bars: 5 µm (horizontal) and 10 s (vertical). Vertical white lines show immobile motors. White lines represent myosin filaments moving along the bundle from the upper right towards the lower left, i.e. from right to left along the bundle (top panel, magenta). This confirmed that the actin bundles were polar.

matched our expectations. We measured the maximum in actin fluorescence intensity in every 20x20 pixel section of the images shown in Fig. 3.4 A-D and used this as a proxy for local actin density (Fig. 3.4 E). As expected, single actin filaments yielded a narrow intensity distribution with one peak (1742 ± 214 a.u.). After actin bundling by methylcellulose, the intensity distribution shifted to much higher values and broadened significantly (12702 ± 8909 a.u.), reflecting the coexistence of larger and smaller bundles observed in the microscopy image (Fig. 3.4 B). Note that the very thick bundles were most likely so large that they protruded out of the evanescent field illuminated by TIRF, so our analysis probably underestimated the amount of actin present in these bundles. After flushing with methylcellulose and crosslinking with fascin, the intensity distribution once again became narrower and shifted to lower values (3042 ± 1715 a.u.) but continued to be much broader than the single filament intensity distribution. More flushing left the average intensity only very slightly changed, but made the distribution narrower and removed the high-intensity population altogether (2802 ± 991 a.u.). Thus, it seems likely that by flushing we indeed selectively removed loosely crosslinked actin filaments. To assess the typical bundle size, we fitted the entire intensity distributions for the random network and parallel bundles with Gaussian functions. This revealed that the local maximum intensity was on average just 1.7-fold higher in the final bundled sample compared to the single filaments. During the track preparation process, we found much thicker bundles, consisting of an average of 13 filaments and often up to 18 filaments upon random bundling, and around 4 filaments after the first methylcellulose flushing step. The final bundles had a distribution of lengths that usually surpassed the 30-40 µm we could visualize in one field of view, and significantly longer bundles were sometimes visible ($\lesssim$ 70 µm for bundles crossing the field of view diagonally) (Fig. 3.4 F).

Due to the preferred binding geometry of fascin, we expect the bundles to be unipolar after extensive flushing. In principle, it is possible to specifically label actin barbed ends using fluorescent capping protein [112]. However, we could not resolve individual actin filaments within a bundle using fluorescence microscopy, so even if we could locate a specific end, we would be unable to reliably deduce the filament's orientation from it. We therefore used myosin-2 as an indirect reporter for bundle polarity. Myosin-2 walks in a barbed-end-directed manner [306], so bundles can be assumed to be polar if all myosin filaments move in the same direction. Indeed, kymographs revealed that on any given bundle, different myosin filaments all consistently walked in the same direction (leftward in Fig. 3.4 F).

We investigated whether the protocol could be simplified by skipping the methylcellulose-bundling-step, either bundling actin by fascin directly in an Eppendorf tube, or bundling actin by fascin in the flow channel. However, we found that this yielded either well-separated bundles that were much shorter than the dimensions of our field of view (*ex situ* bundling by fascin, Supp. Fig. 3.13 A) or highly inhomogeneous and often tightly interconnected actin networks (*in situ* bundling by fascin, Supp. Fig. 3.13 B). Both outcomes were undesirable, as the short bundles limited the maximum observable run lengths, while highly interconnected bundles tended to actively contract upon myosin addition (Supp. Fig. 3.14). Similarly, bundling outcomes were poorer when we performed the step-wise protocol with shorter actin filaments formed in the presence of capping protein (molar ratio 100:1 G-actin:capping protein, Supp. Fig. 3.13 C and D).

3.2.4 Tracking myosin motility on actin bundles

To analyze myosin motility, we acquired TIRF videos (~ 7 fps for two-color imaging) and extracted motility data by automated image analysis. In TIRF images, myosin-2 filaments appeared as bright dots (spherical or, in the case of skeletal muscle myosin, sometimes slightly elongated) on a dark background (Fig. 3.5 A). We located these bright blobs at subpixel resolution using the python package *trackpy* [307] (Fig. 3.5 B). After detecting the myosin blobs in each frame of the video, tracks were linked into trajectories using the *trackpy*-implementation of the Crocker-Grier algorithm [308]. Trajectories could be either stationary, where a myosin filament was stuck in one place and underwent diffusive motion around that location (blue track highlighted in circle, Fig. 3.5 C), or elongated, where a myosin filament migrated along an actin bundle (brown track highlighted in rectangle, Fig. 3.5 C).

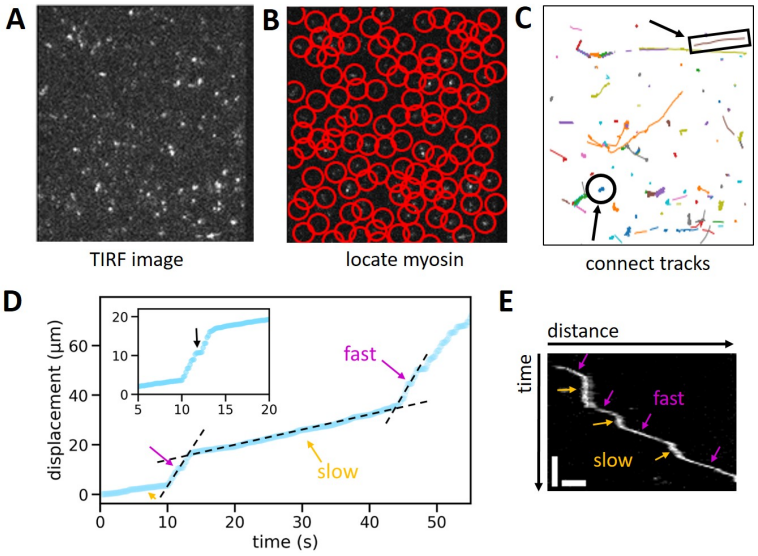

Figure 3.5: **Analysis of myosin-2 motility data.** (A) Typical TIRF image of muscle myosin-2 filaments (bright blobs on dark background) bound to an array of actin bundles (not shown). The buffer contained 50 mM KCl and 2 mM ATP. (B) We tracked myosin filaments using the Python package *Trackpy* [307], which locates the center of mass position of filaments in each frame at sub-pixel resolution (red circles). (C) Blobs are linked into trajectories over time using the *Trackpy* implementation of the Crocker-Grier algorithm [308]. The different colours indicate tracks of different particles. Highlighted tracks are discussed in the main text. (D) Finally, we calculate the particle displacements between frames. Individual particle tracks (blue datapoints) often consisted of different segments where run time and displacement were linearly related. Segments of constant velocity ('runs') were identified based on sliding linear fits (black dashed lines). The inset zooms in on a section in which the myosin filament moves quickly but briefly slowed down (black arrow). These short segments of altered velocity are not picked up by our segmentation algorithm, so we count the entire segment from ~ 10 to ~ 14 s as one run with a single effective speed. (E) Myosin filament motion can also be tracked using kymographs. Each horizontal line represents the fluorescence intensity profile along a line in one frame of the movie, and profiles from each time point are stacked underneath each other. The horizontal direction thus represents distance and the vertical direction time. Kymographs confirm that a single muscle myosin filament can switch between running slowly (segments with a steep slope, yellow arrows) and quickly (segments with a shallow slope, magenta arrows). Scale bars: 2 µm (horizontal) and 3 s (vertical).

To analyze how individual myosin filaments moved, we then computed filament displacements from the tracking data. Interestingly, we observed that a large fraction of rabbit skeletal muscle myosin-2 filaments (~ 47 % of 29371 tracked particles) had tracks like the one shown in Fig. 3.5 D, where the filament switched between a faster and slower running regime, signified by the sections of steeper and shallower slopes in the time-displacement diagram. We also found this behaviour in *C. elegans* nonmuscle myosin-2 filaments, but in a much smaller fraction of the trajectories (~ 8 % of 9690 particles). The switching behaviour was confirmed by kymographs, in which we also observed sections of faster and slower movement in the trajectory of single skeletal muscle myosin filaments (Fig. 3.5 E) [1]. This behaviour is striking, as it has not been reported before for skeletal muscle myosin to the best of our knowledge, although myosin motility on similar arrays of actin bundles was investigated in a recent study [289].

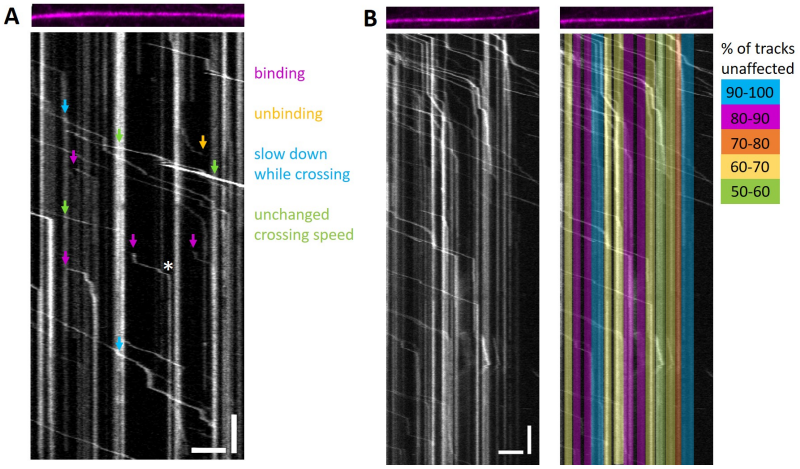

Figure 3.6: **Analysis of rabbit skeletal muscle myosin-2 motility data to test for effects of the actin bundle structure.** (A) Kymograph of myosin-2 filaments running along an actin bundle (magenta, top panel) in a 100 mM KCl buffer. Bright diagonal trajectories represent individual myosin filaments running. Bright vertical lines indicatean immobile myosin filament (or cluster of filaments) that is either stuck to the bundle or to the underlying coverslip. The white asterisk indicates a point where a myosin filament is first motile, and then gets stuck for the rest of the observation time. Colored arrows indicate other types of events: Where a bright spot appears and a track starts somewhere along the bundle, myosin is binding from solution (magenta arrows). Where a track stops and the bright spot disappears abruptly, myosin is unbinding (yellow arrow, extremely rare for muscle myosin-2). Some myosin filament slow down as they cross a piece of actin bundle which is already decorated with another myosin filament (blue arrows). Usually, however, myosin speed remains unaffected by the presence of another filament on the track (green arrows). (B) Kymograph of a different myosin running along a different actin bundle (magenta, top panels) where many myosin assemblies are stuck (i.e. high density of bright vertical lines). For each section of bundle where a myosin was stuck, we counted how the trajectories of other myosins were affected when they crossed. The right panel shows the same kymograph, with each 'stuck myosin' segment highlighted with a colored bar representing the fraction of crossings where the running myosin's characteristics were unchanged by the presence of the stuck myosin. Overall, 80 % of myosins were unaffected when they crossed a 'sticky' section of racetrack, 14 % slowed down, and 6 % remained stuck (N = 265 crossing events on 15 separate sections of track). Scale bars: 5 µm (horizontal) and 3 s (vertical).

[1] Note that in contrast to the time-displacement diagram, steeper slopes in the kymograph indicate slower movement, as distance is generally plotted along the x-axis and time progresses from top to bottom.

Prompted by this observation, we thus asked whether some structure in the underlying actin bundles could induce the switching behaviour. The locations where a switch occurred were not visibly distinct from other stretches of actin bundles (Fig. 3.6 A and B, top panels), although we note that, being diffraction limited, TIRF imaging may be insensitive to subtle structural changes in the bundle. Besides filaments that switched between fast and slow running, we also observed myosin filaments that were first motile and subsequently stopped moving (Fig. 3.6 A, white asterisk), and others that were immobile from the start of our timelapse videos and remained so throughout the observation time (vertical white lines spanning the entire height of the kymograph in Fig. 3.6 A). Such stopping is arguably the most drastic change in motility on actin bundles, so if the underlying actin bundle is responsible for the change in motility, then we should expect a particularly great likelihood for myosin to slow down at locations where another myosin filament has gotten stuck. We thus analyzed in an example kymograph what proportion of running myosin filaments changed in motility as they passed a location on an actin bundle where a myosin filament was either already stuck or got stuck later in the same video (Fig. 3.6 B). For each location of a stuck myosin on the kymograph, we counted how many passing myosins slowed down or stopped entirely at that location. Out of the 265 crossing events analyzed, 13 % showed the running myosin filament slowing down briefly as it passed the stuck filament. Note that these events typically lasted no more than 3 frames, which means that they were not detected as separate running segments in our run segmentation algorithm. They did, however, slightly decrease the overall speed measured for that segment of the run (Supp. Fig. 3.15). In 7 % of crossing events, the running myosin became stuck at the spot where another myosin was already adhering, and did not resume running again within our observation time. The vast majority (80 %) of crossing events, however, proceeded without any change to the running myosin's motility behaviour (Fig. 3.6 B). Thus, we conclude that structural features in the actin bundles do influence the motility of some particles, but this effect is too small to dominate the tracking results. We do note however that the velocity distributions we extract from the tracking analysis are likely broadened as a result of short periods where filaments slow down when crossing a defect in the bundle.

Since our assay measured myosin motility in close proximity to a coverslip surface, we also tested whether this spatially confined geometry changed myosin motility. We performed imaging in TIRF mode, where fluorophores get excited by an evanescent field at the site where the laser hits the coverslip at an angle. This evanescent field decays exponentially from the coverslip surface, so fluorophores appear brighter as they come closer to the coverslip surface (Fig. 3.7 A). If a myosin filament gets trapped between an actin bundle and the surface, or unspecifically adheres to the coverslip, and is slowed down as a consequence, we should see that the same myosin filament appears brighter in the slower-moving sections of its trajectory. Note that we had to limit ourselves to comparing different sections of the same trajectory, rather than correlating myosin signal and running speed globally, since the different myosin filaments varied widely in brightness, consistent with the broad range of sizes we observed in TEM and mass mapping experiments (Fig. 3.3). We also considered only trajectories of at least 15 frames, so that any change in brightness would be obvious despite the significant level of noise in the intensity data. We indeed observed that occasionally, the same myosin filament appeared brighter when it was moving fast than when it was moving slowly (Fig. 3.7 B). However, we also found trajectories in

which the myosin signal changed suddenly, but that change did not correlate with the filament's running speed (Fig. 3.7 C). In almost 90 % of all trajectories the intensity of a particle stayed consistent throughout the trajectory (Fig. 3.7 D). Furthermore, we observed some signal changes uncorrelated with running speed in 9 % of trajectories, and potentially surface-induced switching was observed in only 2 % of trajectories (Fig. 3.7 E). We thus conclude that, while proximity to the surface may play some part in myosin motility, it is not a major factor that can explain motility switching.

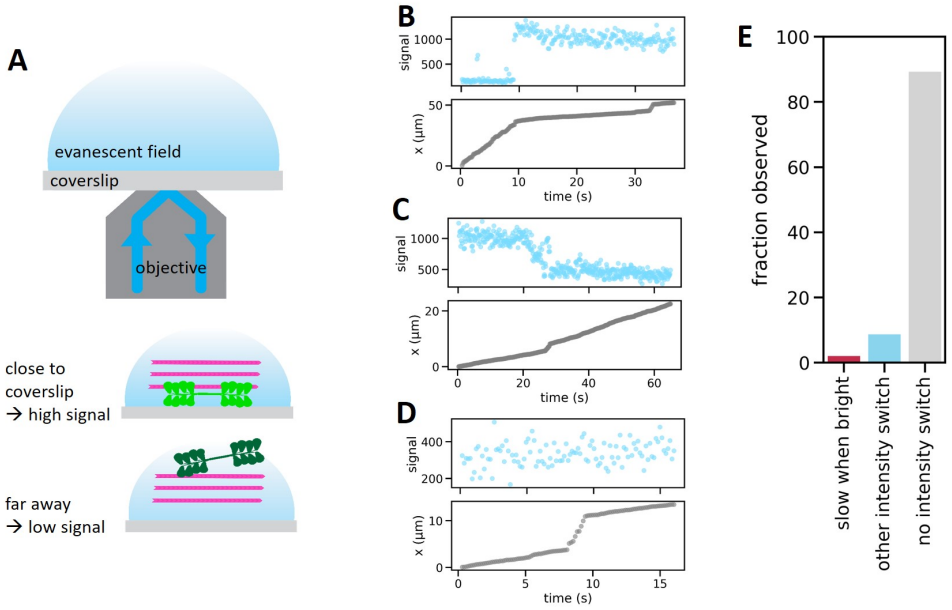

Figure 3.7: **Proximity to the coverslip only rarely affects myosin filament motility.** (A) Top panel: in TIRF, the laser is directed at the coverslip at an angle above the critical angle for total internal reflection so an exponentially decaying evanescent field reaches a few tens of nanometres (up to ~ 200 nm) into the sample. Bottom panels: the closer a myosin filament (green) is to the coverslip, the brighter it thus appears. If the coverslip strongly influences myosin motility, we should expect run segments of slower speeds to correlate with brighter signals. (B - D) Examples of individual skeletal muscle myosin-2 trajectories, showing a time-displacement-curve (bottom panel, grey datapoints) and the fluorescence signal of myosin at the same time (top panel, blue datapoints). (B) Example of a myosin trajectory where the myosin signal is brighter in the slow-running than the fast-running segment, possibly indicating an influence from the coverslip surface. (C) Example of a trajectory in which the signal intensity changes abruptly, but high signal is not correlated with slow running speed. (D) Example trajectory in which myosin switches between different running regimes, but the signal stays consistent throughout. (E) Bar plot of the fraction of trajectories where slower segments coincided with higher brightness (red, 2 %), where the intensity changed abruptly but did not coincide with any changes in running speed (blue, 9 %), and where running speed changed but signal intensity stayed consistent throughout (grey, 89 %). We analyzed 345 trajectories of muscle myosin filaments running in a buffer containing 50 mM KCl, each at least 2.2 s (= 15 frames) long.

3.2.5 Motility of *C. elegans* nonmuscle myosin-2 filaments on actin racetracks

Confident that running behaviour was not dominated by surface- or bundling-induced artefacts, we went on to examine myosin motility behaviour on a population level. We evaluated the motility patterns of several thousand myosin trajectories and fit their individual runs as segments of constant velocity using the image and data analysis pipeline laid out in Fig. 3.5.

We first studied the speed distributions of *C. elegans* nonmuscle myosin-2. Histograms revealed two very different run speed distributions for myosin filaments assembled at 50 mM versus 100 mM KCl (Fig. 3.8 A). Filaments assembled at 100 mM showed three distinct peaks: one at apparent speeds around 200 nm/s, corresponding to filaments that were stationary (see below for details). The two other peaks were centered around 395 ± 174 nm/s and 836 ± 234 nm/s (see Supp. Fig. 3.16 A for peak fits). Plotting the same data, but weighting them by the time spent in each running state, did not yield any qualitative changes and only shifted the distributions towards slower speeds (Fig. 3.8 B), indicating that the motor filaments spent less time on average in fast-running segments. For 50 mM KCl, we observed the same 'stationary filament' peak around 0.2 µm/s, but the distribution was otherwise broad with a long tail extending up to ~ 1.5 µm/s speeds (Fig. 3.8 A) and no clear additional peaks. We could therefore not calculate a characteristic running speed for these filaments. Plotting the distance covered by a myosin filament as a function of the run lifetime confirmed that nonmuscle myosin-2 assembled at 100 mM KCl was observed mainly in three separate running regimes: one fast-moving one (Fig. 3.8 C, orange dashed line), one slow-moving one (Fig. 3.8 C, yellow dashed line) and one quasi-stationary one (red dashed line). For motor filaments assembled at 50 mM KCl, we did not observe such a clearly structured point cloud, although the data points appeared to cluster at high speeds and at run lengths below ~ 20 µm (Fig. 3.8 D).

Note that for both 50 mM and 100 mM KCl, there was a line at low run lengths below which we did not observe any data points, while there was a sizeable population of myosin filaments which by eye appeared completely stuck in the kymographs, showing up as vertical white stripes as exemplified Fig. 3.6. Since stuck filaments sometimes showed tethered rotation, and the TIRF data was noisy, even stationary myosins showed some apparent motion upon tracking their centroid position in TIRF images. The run lengths were computed as the sum of all frame-to-frame displacements throughout the run, which were always positive. Therefore, the slow-moving population with running speeds below ~ 0.3 µm/s should really be interpreted as not moving in a directional manner. This population is reflected in the first peak in the run speed histograms (Fig. 3.8 A), which is centered around 0.2 µm/s but extends up to ~ 0.3 µm/s.

To test whether the bundle architecture of the racetrack changed the motility of the nonmuscle myosin filaments, we performed the same experiment on single surface-adhered actin filaments. We found that the running speeds on actin filaments matched those on bundles, with a peak at ~ 1.3 µm/s along with a smaller peak around 0.4 µm/s for 100 mM KCl, and a peak of 'stationary' myosin filaments observed at both 50 mM and 100 mM KCl (Supp. Fig. 3.17 A). For filaments running at 100 mM KCl, the fast-moving population became more prominent on single actin filaments compared to bundles. At 50 mM KCl, a small population of myosin filaments moving at around 0.4 µm/s emerged. (Fig. 3.17 A-C).

We regularly observed myosin filaments residing at one end of actin filaments for the duration of the video (~ 3 min, see Supp. Fig. 3.17 D), consistent with the barbed end-dwelling that was previously reported for rabbit skeletal muscle myosin [112] and human nonmuscle myosin [279].

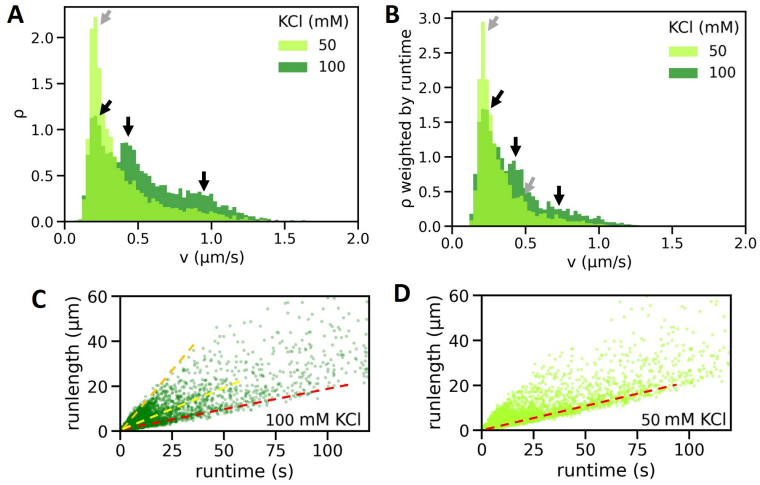

Figure 3.8: **Nonmuscle myosin-2 motility on actin bundles.** (A) Histograms of running speeds of nonmuscle myosin-2 filaments assembled at 50 and 100 mM KCl (light and dark green, respectively). The data was normalized to make the area of each histogram equal to one, so that $\rho(v)$ denotes the probability density of finding a myosin in a track segment of speed v. The histogram show a peak (grey arrow) with a long tail for myosin assembled at 50 mM KCl, and three distinct peaks for 100 mM KCl (black arrows). (B) Histogram of the same data weighted by the time spent running at that speed. Here, the tail of the distribution at 50 mM is shortened slightly and the two peaks at higher speeds are shifted slightly to the left in 100 mM KCl. (C) Scatter plot of distances versus run times for nonmuscle myosin-2 assembled and running at 100 mK KCl. Each data point represents one run segment, and the slope of the line connecting the point and the origin corresponds to the running speed of that segment. This again revealed a trimodal distribution where myosins either remained stationary (red dashed lines), or ran at one of two characteristic speeds (yellow and orange dashed lines to guide the eye). (D) For 50 mM KCl, we similarly observed a distinct population of quasi-stationary myosins KCl (red dashed line to guide the eye), but the remaining distribution was much less structured than at 100 mM KCl A small population of data points clustered at high speeds, reaching up to run lengths of around 20 μm. Sample sizes: N (50 mM KCl) = 3891 run segments from a total of 3551 particles. N (100 mM KCl) = 4536 run segments from a total of 4207 particles. Both datasets come from two independent experiments.

3.2.6 Motility of rabbit skeletal myosin-2 filaments on actin racetracks

Finally, we analyzed the motility patterns of skeletal muscle myosin-2 in the same manner. At 50 mM KCl, we found a bimodal velocity distribution with a fast-running peak centered around 3.69 μm/s and a standard deviation of 2.41 μm/s, and a peak due to stationary myosin filaments (Fig. 3.9 A). We note that there was also a long shoulder towards larger speeds, reaching up to around 8 μm/s. Surprisingly, at 100 mM KCl we found a broader distribution with two distinct high-speed peaks. One peak matched the one we observed for myosin running at 50 mM KCl, with a mean speed of 3.94 μm/s and a standard deviation

of 2.41 µm/s. The second high-speed peak was located at almost twice this speed, with 6.83 ± 0.67 µm/s (Fig. 3.9 A, distribution fits in Supp. Fig. 3.16 B). Strikingly, when we weighted the histogram with the time spent in each running state, both the first and especially the second high-speed peak in 100 mM KCl were reduced in height, indicating that myosin filaments spent less time on average in a fast-running state (Fig. 3.9 B). At 50 mM KCl, the high-speed peak was also reduced in height, but much less so than at 100 mM KCl (Fig. 3.9 B). Displacement-run time plots again confirmed a clear distinction between a slow-moving population (Fig. 3.9 C, red dashed lines) - largely resulting from diffusion and tracking artefacts - and a fast-moving population (yellow dashed lines). In the case of 100 mM KCl, two separate sub-populations of the fast-moving population were visible (two dashed yellow lines, Fig. 3.9 D). Almost all segments for the faster of the two subpopulation lasted less than 10 s (Fig. 3.9 D, inset). This low average lifetime explained why weighting by run time reduced the fast-moving peak so significantly.

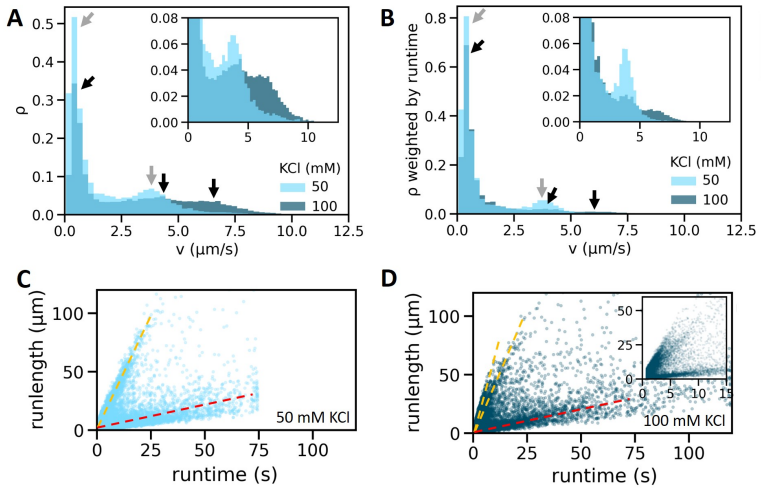

Figure 3.9: **Skeletal muscle myosin-2 motility on actin bundles.** (A) Histograms of running speeds of skeletal muscle myosin-2 filaments assembled at 50 and 100 mM KCl (light and dark blue, respectively). The inset shows the same data but zoomed in on the smaller peaks in the fast-running regime. The histogram reveals two peaks for 50 mM KCl (grey arrows), and three broad but distinct peaks for 100 mM KCl (black arrows). (B) The same data weighted by the time spent running at that speed. Here, the high-speed regime was dis-favoured for both KCl concentrations, especially for the higher ionic strength. (C, D) Scatter plot of distances versus run times for skeletal muscle myosin-2 assembled and running at 50 (C) and 100 mM KCl (D). The slope of a line which crosses any given point in the plot and the origin is the running speed of the segment represented by the point. Both sets of data was largely bimodally distributed: myosins either remained almost stationary (red dashed lines to guide the eye), or ran rapidly, covering long distances in a short time (yellow dashed lines). Note that there are no datapoints beyond ~ 70 s, as this was the length of each timelapse taken for these experiments. At 100 mM KCl, the fast-running population comprised a large population running at similar speeds as the fast-running population at 50 mM KCl, and a smaller population running at higher speeds. The faster sub-population covered hardly any run lengths exceeding 50 µm, or about 10 s. The inset shows a zoomed-in view of the two fast-moving populations for clarity. Sample sizes: N (50 mM KCl) = 18632 run segments from a total of 15711 particles. N (100 mM KCl) = 15526 run segments from a total of 13660 particles. Both datasets come from two independent experiments.

3.3 Discussion

In this chapter we studied the self-assembly and motility of skeletal muscle and nonmuscle myosin-2 filaments in vitro. The characterization of the assembly of *C. elegans* nonmuscle myosin-2 is, to the best of our knowledge, the first one reported in the literature. Similar to other nonmuscle myosins, *C. elegans* myosin self-assembled into bipolar filaments with motor domains protruding from both sides and a long and slender bare zone in between. The filaments were compact and often bent at the ends of the bare zone, similar to unphosphorylated human nonmuscle myosin-2B and 2C [269] and *Drosophila* nonmuscle myosin [280]. The filaments were slightly shorter than human and *Drosophila* nonmuscle myosin-2 filaments (~ 200 – 300 nm for *C. elegans* versus ~ 300 nm for both *Drosophila* nonmuscle myosin and human myosin-2A and 2B [279, 280]), consistent with the lower number of constituent motors we measured in iSCAT (~ 10 versus ~ 15 in *Drosophila* and up to 60 for human nonmuscle myosin-2 [279, 280]). We observed a large protein mass in the center of the bare zone, which originated from protein tags used to purify and visualize the protein. We note that the tag does not give rise to significant changes in cytoskeletal organization or dynamics in the early *C. elegans* embryo compared to wild type embryos (S. Grill, personal communication, 2021). We found that filament formation was efficient both at 50 and 80 mM KCl, with more than 82 % of myosin monomers incorporated into filaments, and supporting the notion that the tag does not interfere with filament assembly. However, we were surprised to find that the assembly of *C. elegans* nonmuscle myosin-2 was quite sensitive to the ionic strength of the buffer, with a doubling of the fraction of free monomers going from 50 mM to 80 mM KCl, although the filament mass did not change much. This raises the question how self-assembly proceeds in *C. elegans*, where ionic strength is significantly higher, likely equivalent to > 100 mM KCl [309]. Myosin filament assembly may be regulated by environmental viscosity and crowding [279], or by specific proteins such as the chaperone UNC-45A that regulates stress fibres and myosin folding [310, 311], or proteins of the S100 protein family that can co-assemble into mixed filaments with nonmuscle myosin-2 [312]. Further study of the assembly process of *C. elegans* nonmuscle myosin-2, for instance in cytoplasmic extracts, could shed light on this, and we suggest that iSCAT would be an excellent tool to study the dependence of filament self-assembly on both buffer conditions and assembly time.

Next, we studied the assembly and motility of rabbit skeletal muscle myosin-2. Synthetic muscle myosin filaments were much larger than the nonmuscle filaments, consistent with the large body of literature for skeletal muscle myosin. Filament sizes were rather insensitive to the final ionic strength of the buffer, with no statistically significant differences in average filament lengths and masses for myosin assembled in the range of 50-150 mM KCl, which is a range commonly used for in vitro assays. At 37 mM KCl, by contrast, we saw both filament length and thickness increase dramatically, consistent with the formation of thick filaments, in which several smaller myosin filaments associate with each other [313, 314]. In fact, muscle myosin filaments assembled at 37 mM KCl often appeared to consist of smaller sub-filaments that frayed apart on the EM grid (Supp. Fig. 3.11). Notably, we did not observe significant asymmetries in the motor distribution in our filaments by STEM, as a previous study showed by correlative TIRF and AFM for synthetic muscle myosin filaments [315]. This discrepancy may be due to the fact that our buffers were slightly more basic than those used in the earlier study (pH 7.4 compared to pH 7.0), which is known to

influence myosin filament assembly [278].

Turning from myosin assembly to motility, we first set up a high-throughput myosin motility assay from purified proteins. We established a step-wise protocol in which actin was first assembled into random bundles by entropically induced bundling, and subsequently crosslinked by fascin in a polarity-specific manner. After removal of excess actin and crowding agents, this protocol yielded arrays of long, aligned actin bundles. The bundles were at most a few filaments thick, and thus well below the geometrically limited bundle thickness of around 20 filaments reported for fascin-bundled actin in vitro [316]. This clearly indicated that the stepwise process of bundle formation has a strong influence on the final bundle organization. Using myosin motility as a reporter, we found that the bundles were polar, as expected for fascin-stabilized structures. Since the bundles were generally longer than our field of view, and therefore also much longer than individual actin filaments (> 30 μm versus < 25 μm [317]), they made an effective substrate for observing processive myosin-2 motility over long distances. A more detailed characterization of bundle thicknesses could be performed using atomic force microscopy [318], or cryo-electron-tomography [319], to get access to the internal bundle structure.

Using our assay, we measured the motility of *C. elegans* nonmuscle myosin-2 on thin actin bundles in the presence of physiological concentrations of ATP (2 mM). At 100 mM KCl, we found two characteristic run speeds of ~ 400 nm/s and ~ 800 nm/s, both on thin actin bundles and on single actin filaments. The run speed of 400 nm/s is comparable to the velocity of actin filaments in classical sliding assays with heavy meromyosin cleaved from the same myosin construct, which was measured at around 100 nm/s in the presence of 0.1 mM ATP (L. Vogeley, personal communication, 2022). This run speed is also consistent with the speed of tropomyosin-decorated actin filaments in sliding assays on human heavy meromyosin from phosphorylated nonmuscle myosin-2A (~ 300 nm/s) [320]. We were, however, surprised to see a peak of myosin filaments with run speeds around 800 nm/s. To the best of our knowledge, this is the fastest nonmuscle myosin run speed observed so far. Although we have observed some nonmuscle myosin-2 filaments running at such high speeds, we suspect that some of these fast-moving myosins may be due to tracking artefacts, where neighbouring myosin filaments may sometimes be linked into tracks, rather than the same myosin in two consecutive frames. Extensive manual analysis of kymographs will be necessary to identify what proportion of these very fast runners are 'real', and to what degree they originate from tracking artefacts. For nonmuscle myosin at 50 mM KCl, the run speeds were not distributed in distinct peaks as for 100 mM KCl. It is unclear why this was so, but we suspect that the surface passivation in these samples was suboptimal, inducing unspecific binding to the surface and inhibiting myosin motion. It would thus be beneficial to gather more data, ensuring that surface stickiness does not limit mobility of myosin filaments.

We found that skeletal muscle myosin-2 filaments were also motile on actin bundles, with charcteristic running speeds around 3.8 μm/s for both 50 mM and 100 mM KCl, consistent with actin gliding speeds of around 3-4 μm/s that have been reported for ATP concentrations above ~ 1 mM [282]. Surprisingly, we also observed myosin running at significantly higher speeds: particularly, but not exclusively, at 100 mM KCl, a second distinct running population appeared, with average running speeds around 6.8 μm/s, almost twice as fast as the slower 'runner' population. This speed matches closely the ~ 7 μm/s

reported in assays where actin filaments were sliding over surfaces densely packed with heavy meromyosin [321], suggesting that in our assays myosin motility happens in the limit where no additional motor domains can productively bind actin to propel the filament forwards. It is also consistent with the ~ 5 μm/s predicited for skeletal muscle myosin filaments at high ATP and low load in a theoretical study, where both the details of the myosin-2 motor cycle and the effects of myosin self-assembly were taken into account. In previous experimental studies, strikingly different velocities have been reported in for motile rabbit skeletal muscle myosin-2 filaments on actin. Speeds ranged from 200 nm/s on single actin filaments tethered to supported lipid bilayers [220], through speeds between 38 and 620 nm/s on actin bundles of different architectures [289], and up to 2-3 μm/s for myosin on untethered actin filaments [112]. These widely spread literature values may be due to differences in load experienced by myosin in the different systems, which has a great influence on the motor domain binding kinetics in myosin [277]. It should also be noted that these speeds were all measured in different buffer conditions of different, but always low, ATP concentrations (≤ 300 μM).

We observed that individual myosin filaments could even switch between faster- and slower-running regimes. We found some examples of speed-switching in nonmuscle myosin filaments, but observed it much more frequently for skeletal muscle myosin-2 filaments. This switching is reminiscent of the quantized actin velocities in sliding assays on surfaces covered with very low motor densities [286]. In that study, it was observed that the number of strongly bound motor domains determined the speed of actin sliding, with the actin displacements generated additively by each motor domain's power stroke. If the speed of our myosin filaments is determined by the number of strongly bound heads that contribute to forward motion at any given time, then we should expect myosin motility to shift to lower speeds on average when we lower the binding affinity of the myosin heads for actin by increasing the ionic strenth [322]. However, we observed the opposite trend: at 100 mM KCl, the myosin filaments were more likely to be running at faster speeds. This indicates that rather than helping to propel the myosin filament, decreased ionic strength, and thus increased binding, in fact hindered motility. This observation is consistent with earlier work showing that, as a bipolar filament of rabbit skeletal muscle myosin walks on a single actin filament, motor domains in its trailing end can also bind the actin track, effectively acting as a 'break' for the motile filament, and even leading to fragmentation of actin [323]. On actin bundles, the myosin filament trailing end can bind not just the same actin filament, but also different actin filaments in the same bundle. A similar effect has indeed been observed in motility measurements on human nonmuscle myosin-2 filaments, which showed that the motors can switch between two binding modes previously identified in electron microscopy [269], with the trailing end either free or bound to the same actin filament as the leading end [279]. The same study reported that human nonmuscle myosin filaments intermittently stopped walking when they encountered an intersection between two actin filaments and engaged with both at the same time [279]. In fact, this study even showed an example of a human nonmuscle-myosin-2A filament switching between a faster and slower walking pace, although this was not explored further by the authors. It thus seems that the switching phenomenon we observed here is feature of myosin-2 filament motility that can occur for both muscle and nonmuscle myosin filaments across different species, and is likely induced by trailing end binding of the myosin filament to its

track. The broad distributions of running speeds are also consistent with this hypothesis: skeletal muscle myosin filaments contain several hundred motor domains, so the number of heads bound both at the leading and trailing end, and therefore the number of heads contributing to movement (or the inhibition thereof) at any one time should be variable. We thus propose that the fastest running speeds we measured occurred when only the leading end of the myosin filament was engaged with the actin track, and slower running speeds were induced by engagement of the trailing end with the actin track. This also explains why such switching is not seen in classical sliding assays, where the myosin heads are either not assembled into filaments at all [286, 321, 324, 325] or filaments are adhered on a surface, most likely preventing the trailing end from interacting with the sliding actin filaments [285].

Our proposed mechanism can be tested by measuring the angular distribution of myosin orientations on the track, which should narrow when both ends of the filament engage with the underlying actin track. This analysis could in principle be done on our data, but would benefit strongly from using myosin filaments with a higher degree of fluorescent labeling to achieve better signal to noise ratios and thus better localization of the blobs. Alternatively, higher resolution microscopy techniques, such as structured illumination [326], would also better resolve the elongated structure of the myosin filaments, and make measuring the angular distribution significantly more precise.

Importantly, high-speed myosin runs were rare and short compared to slower-running segments, so they may easily be missed or discarded as outliers unless large numbers of motile myosin filaments are observed. Since studies to date generally reported analyzing no more than a few tens to hundreds of trajectories [286, 289, 320], it is thus not surprising that this striking behaviour, which is unlikely to be specific to our experimental system, has not been reported before. Recently, new tracking software tailored to analyzing motility of molecular motors has been published [327], which also allows for automated analysis of, for instance, the precise orientation of motor filaments with respect to their direction of motion. Such developments, in combination with high-throughput motility assays like ours, will make the analysis of large populations of motors easier and more accessible in the coming years, possibly revealing yet more surprises in the behaviour of a well-studied motor.

3.4 Materials and Methods

3.4.1 Chemicals

The following chemicals were purchased from Sigma-Aldrich: Tris(hydroxy-methyl)amino-methane hydrochloride (Tris-HCl), potassium chloride (KCl), calcium chloride ($CaCl_2$), magnesium chloride ($MgCl_2$), DL-dithiothreitol (DTT), Adenosine 5'-triphosphate magnesium salt (MgATP), Adenosine 5'-triphosphate disodium salt (Na_2ATP), proto-catechuic acid (PCA), proto-catechuate-3,4-dioxygenase (PCD), glycerol, κ-casein, methyl cellulose (Cat. # M0512), ammonium hydroxide solution (Cat. # 221228), hydrogen peroxide solution (Cat. # 95299) streptavidin (Cat. # S4762), and phalloidin from Ammanita phalloides (Cat. # P2141). PLL(20)-g[3.5]-PEG(2)/PEG(3.4)-biotin(20%) was purchased from SuSoS Surface Technology.

3.4.2 Proteins

Rabbit skeletal muscle myosin-2 Skeletal muscle myosin-2 was purified in-house from *psoas* rabbit leg and back muscle tissue following a classical protocol [328]. Fresh meat was kept on ice throughout. Any remaining connective tissue was removed from the muscle tissue, and the dissected muscle was minced using a meat grinder. Myosin was extracted from the mince through mechanical agitation in a high-ionic-strength phosphate buffer (150 mM KH_2PO_4 pH 6.5, 300 mM KCl, 20 mM EDTA, 5 mM $MgCl_2$, 1 mM ATP) for 15 min, and separated from the rest of the tissue by filtration through cheese cloth. Myosin was precipitated by dilution in MilliQ water approximately ten-fold to reach 30 mM KCl in the buffer, and further purified of actin and other actin-binding proteins by sequential dialysis steps against buffers of decreasing KCl molarity, alternating with precipitation in water, where we use the ability of myosin to form filaments at KCl concentrations below ~ 300 mM. Finally, myosin was stored at -20° C in a buffer containing 25 mM KH_2PO_4 (pH 6.5), 300 mM KCl, 0.5 mM DTT, and 50 % v/v glycerol. Myosin monomers were fluorescently labeled using N-hydroxysuccinimide (NHS) ester amine reactive dyes, either AlexaFluor488 or DyLight550 (ThermoFisher Scientific), according to the supplier protocol, with typical labeling ratios (determined by UV/VIS spectroscopy) ranging from 1-2 dye molecules per motor. Both labeled and unlabeled myosin monomers were stored at -20° C in a 50 % glycerol buffer to avoid freezing the protein.

Skeletal muscle myosin was prepared as follows for experiments: Unlabeled myosin doped with labeled monomers (typically 50 µL, 5 mole % fluorescently labeled) was dialyzed overnight or for at least 2 hours at 4° C against a high ionic strength Tris-based myosin buffer (20 mM TrisHCl pH 7.4, 300 mM KCl, 4 mM $MgCl_2$, 1 mM DTT) using a 0.5 mL Slide-A-Lyzer dialysis cup with a 20 kDa molecular weight cutoff (Sigma Aldrich). This step was used to remove the glycerol from the myosin buffer. The dialyzed protein was subsequently centrifuged for 20 min at 148,000 g, to pellet any aggregated protein. This step yielded a soft transparent pellet (which was discarded) and a supernatant containing a typical myosin concentration of 2-3 µM as determined by UV absorption at 280 nm (ϵ_{280} = 0.249 µMcm^{-1}, [328, 329]). For running experiments, skeletal muscle myosin was further cleaned of dead heads, which are ATP-hydrolysis incompetent and generally arise during the purification process [330]. The cleaning procedure and its limitations are illustrated in Supp. Fig. 3.20. In brief, 1.5 µM myosin was bound to 7.5 µM actin (pre-polymerized at room temperature for 30 min) in the absence of ATP (binding buffer: 20 mM Tris pH 7.4, 300 mM KCl, 4 mM $MgCl_2$, 1 mM DTT). After 5 min, MgATP was added to a final concentration of 3 mM, and the sample was incubated for a further 5 min, to allow functional motors to unbind from the actin filaments. 50 µL of this actin-myosin-mix were then centrifuged at 148,000 g for 30 min, and the bottom 10 µL of the sample were discarded as they contained the pellet (not large enough to be visible) of actin and dead myosin heads. The 40 µL supernatant were dialyzed for 2 hrs against ATP-free myosin buffer to remove the residual ATP, and then used for myosin running assays. Note that the concentration of myosin in these samples could not be determined precisely by Nanodrop, since the adsorbance at 280 nm was still dominated by residual actin fragments in the sample. We therefore assumed that the total mass of myosin in solution did not change throughout the cleaning procedure, and measured the volume after the last dialysis step to determine an approximate final concentration of myosin.

***C. elegans* nonmuscle myosin-2** Expression and purification of recombinant *C. elegans* nonmuscle myosin-2 was performed by Lutz Vogeley at the Max Planck Institute of Molecular Cell Biology and Genetics, Dresden.

Genes encoding the main and light chains of *C. elegans* non-muscle myosin (nmy-2, mlc-4 and mlc-5) were codon-optimized for expression in Spodoptera frugiperda and synthesized by Genscript. The genes were cloned into a single baculovirus expression vector system (BEVS) transfer vector with separate expression cassettes for each gene [331]. Mlc-4 (wild type amino acid sequence with two phosphomimetic mutations) and mlc-5 (wild-type sequence) were under the control of the p10 promoter. Nmy-2 (wild type sequence and C-terminal mGFP+FLAG-tag) was under the control of the polh promotor. Recombinant virus was prepared by standard methods using the BVES co-transfection method (https://tools.thermofisher.com/content/sfs/manuals/bevtest.pdf). Proteins were expressed in High Five (*Trichoplusia ni*) insect cells using standard protocols. Insect cells at a cell density of 10^6 cells/mL were infected with 0.1 - 1 % v/v of P2 virus, cultured at 27° C and harvested 48 h after infection. Insect cells were harvested 48 h after infection, washed with PBS and freezing buffer, and stored at -80° C. The protein was purified in a two-step protocol, purifying first by Anti-FLAG affinity purification using 2 mL resin suspension (Anti-FLAG M2 Affinity Gel, Cat. # A2220-5ML, Sigma Aldrich) per 1 L of culture, through a gravity column (Glass Econo-Column, Bio-Rad). Protein concentration was determined by Bradford assay, and elution fractions with high protein content were pooled and concentrated to a buffer volume of 800 µL, and incubated with 20 units/mL hexokinase (Cat. # 11426362001, Roche) to remove any ATP from solution. Secondly, F-actin binding-competent myosin was purified by actin affinity purification. Myosin was bound to pre-polymerized rabbit skeletal muscle actin (87 µL, 2 µM) at room temperature for 10 min, and subsequently ultracentrifuged for 20 min to pellet all actin and actin-bound myosin. The supernatant contained only actin binding incompetent myosin and was discarded. The pellet was washed twice to remove any remaining hexokinase, and myosin was eluted from the actin in an ATP-rich elution buffer (20 mM imidazole pH 7.5, 500 mM KCl, 5 mM MgCl2, 1 mM EDTA, 1 mM EGTA, 3 mM DTT, 5 mM MgATP) for 10 min at room temperature. Actin and ATP hydrolysis-incompetent myosin was pelleted and removed by another centrifugation step at 156,000 g. The myosin in the supernatant was washed (20 mM imidazole pH 7.5, 5 mM $MgCl_2$, 500 mM KCl, 1 mM EGTA, 1 mM EDTA, 5 mM ATP, 3 mM DTT) using a desalting column (PD-25, GE Healthcare) and concentrated into ~ 30 µL using a centrifuge filter (UFC510024, Merck Millipore). After determining the protein concentration by Bradford assay, the protein was diluted 1:1 v/v in glycerol-rich buffer, to final buffer conditions of 25 mM imidazole pH 7.5, 300 mM KCl, 5 mM $MgCl_2$, 1 mM EDTA, 3 mM EGTA, 2 mM DTT, 0.1 mM ATP and 38 % glycerol, and stored at -20 ° C to avoid freezing.

For experiments, *C. elegans* myosin was used as is, since the small sample volumes made any further cleaning impossible.

Other proteins. Rabbit skeletal muscle actin was purchased from Hypermol (Cat. # 8101-03). The lyophilized powder was dissolved to 23.8 µM (= 1 mg/mL) according to supplier instructions, resulting in a storage buffer composed of 2 mM Tris-Cl pH 8.2, 0.4 mM ATP, 0.1 mM DTT, 0.08 mM $CaCl_2$ and 0.2% unspecified disaccharides. The G-actin

solution was left to rest on ice for 2 hours and cleared by centrifugation at 148,000 g for 1 hour. We confirmed by UV absorption measurements at 290 nm using a Nanodrop 2000c spectrophotometer that clearing did not result in a measurable loss of protein concentration. Unlike most other proteins, actin concentration is determined at 290 nm rather than 280 nm to avoid artefacts from absorbance by ATP in the actin storage buffer. The extinction coefficient is $\epsilon_{290} = 0.617^{\text{mg/mL}}$ [332]. The actin solution was subsequently aliquoted, snap-frozen and stored at -80° C. Monomeric (G)-actin was fluorescently labeled with AlexaFluor 594 NHS Ester (Invitrogen, through Thermo Fisher Scientific, Cat. # A20004) or AlexaFluor 647 NHS Ester (Invitrogen, through Thermo Fisher Scientific, Cat. # A37573) following [329]. Free dye was separated from the protein after labeling by size exclusion chromatography using a PD MiniTrap G-25 desalting column (Sigma Aldrich, Cat. # GE28-9180-07). Actin was typically labeled with 1 dye molecule per protein as determined by UV/VIS absorbance measurements. G-actin aliquots were thawed quickly and stored on ice for no more than one week. They were left on ice for at least 2 hours before use, to allow for depolymerization of any filamentous (F-)actin [333].

SNAP-tagged murine capping protein was purified according to a published protocol [334]. The plasmid was a kind gift from David Kovar (University of Chicago) In brief, the protein was expressed in E. coli BL21 Codon Plus (DE3)-RP (Agilent Technologies) and purified via a Talon cobalt affinity resin (Cytiva Life Sciences). From the elution buffer, the protein was dialyzed overnight at 4° C (14 kDa MWCO cellulose membrane, Sigma Aldrich Cat. # D9527-100FT) into storage buffer (10 mM Tris-HCl pH 7.5, 40 mM KCl, 0.5 mM DTT), protein concentration was determined by UV absorbance at 280 nm on a Nanodrop2000 spectrometer, and aliquots were snap-frozen and stored at -80° C.

Murine fascin was purified following a published protocol [335]. In short, GST-tagged recombinant murine fascin was expressed in T7 E. coli and purified by GST affinity chromatography. The GST tag was cleaved off during protein elution, and the untagged protein was further purified on an anion exchange column (MonoQ 5/50 GL, Cat. # 17-5166-01, GE Healthcare). Protein concentration was determined by UV absorbance at 280 nm on a Nanodrop2000 spectrometer. The purified protein was then aliquoted and snap-frozen in liquid N_2 and stored at -80° C. Thawed protein was used within a day.

3.4.3 Imaging chambers and surface passivation

Fluorescence imaging was performed in flow chambers (Supp. Fig. 3.21 A) which consisted of strips of parafilm sandwiched between a standard microscopy slide (26x76 mm, Cat. # AA00000102E01FST20, ThermoFisher) and a # 1 coverslip (24x60 mm, Cat. # BB02400600A113FST0, ThermoFisher) as described in [329].

Glass cleaning. Glass slides and coverslips were cleaned by submerging them in hot base piranha solution (5:1:1 volumetric ratio of MilliQ water, ammonium hydroxide solution and hydrogen peroxide solution, heated to > 70°). After 10 min cleaning, the glasses were removed from the piranha solution and thoroughly rinsed with MilliQ water, and stored in MilliQ water for up to 4 days.

Chamber assembly. Strips of around 3 cm long and 2 mm wide were cut from parafilm and placed onto the glass slide at ~ 2 mm intervals, perpendicular to the long side of the

glass. A coverslip was then placed on top and gently pressed down with gloved fingers. Any parafilm protruding from the sides of the glass slide by more than 1 mm was cut off using a scalpel. The parafilm was fused to the glass by heating the chamber on a hotplate until the parafilm softened (and thus went transparent), and gently pressing down on it to remove any air bubbles trapped in the parafilm. The chambers were then removed from the heat and any rolled-up parafilm on the side was secured down onto the glass. The chambers were left on the bench to cool down for ~ 2 min, until the parafilm solidified and went opaque again.

Surface passivation. Imaging chambers were passivated immediately after assembly to avoid protein sticking to the surfaces (Supp. Fig. 3.21 B). To this end, we prepared three passivating solutions, all in F-buffer: PLL-PEG-biotin at 0.1 mg/mL, streptavidin at 0.25 mg/mL, and κ-casein at 0.5 mg/mL. The chambers were incubated sequentially for at least 10 min with 10 µL of each solution, followed by flushing with 30 µL of F-buffer to remove any unbound polymers (Supp. Fig. 3.21 B). To this end, buffer was added from one end of the chamber while a tissue was used to wick away excess buffer from the other side, generating a flow through the chamber. After the last incubation step, the chambers were flushed once more with 50 µL of F-buffer and subsequently stored in a humid environment until use (no longer than one day).

3.4.4 Myosin motility assay

Assembly of racetracks

Factors influencing racetrack formation are detailed in the main text (section 3.2.3). In short, actin filaments for racetracks were assembled by co-polymerizing 89 % unlabeled monomers, 10 % G-actin labeled with either AlexaFluor 647 (for assays with nonmuscle myosin) or AlexaFluor 594 (for assays with muscle myosin), and 0.5 % biotin-actin monomers. After pre-bundling in an Eppendorf tube, the actin bundles were diluted to 2 µM actin and flushed into the flow chambers, where the sparse biotin-tagging of the filaments mediated tethering of the bundles to the streptavidin-functionalized PEG polymer brush on the coverslip (Supp. Fig. 3.21 C). After extensively flushing the bundles as detailed in section 3.2.3, the bundles were inspected in TIRF. Flow channels that still contained significant amounts of large, curly bundles, an indication that methylcellulose was still present, were discarded. Channels with thin and straight bundles were then flushed with at least 3 chamber volumes of the final buffer (i.e., the target concentration of KCl), to ensure that the running assay was performed in the correct buffer conditions. Everything was prepared for imaging (finding the appropriate focus height and TIRF angle, defining timelapse parameters etc.) before myosin was added to the channel.

Myosin filament assembly and running assay

Myosin filaments were assembled separately from the actin bundles. Both *C. elegans* nonmuscle myosin-2 and rabbit skeletal muscle myosin-2 were assembled by rapidly diluting into ATP-free assembly buffer, and incubating at room temperature $(24 \pm 1)^\circ$ C for 30 min. *C. elegans* nonmuscle myosin was assembled at 10 nM and rabbit skeletal muscle was assembled at 166 nM. Myosin assembly buffers contained 20 mM Tris pH 7.4, 2 mM $MgCl_2$, 1 mM DTT, and either 50 or 100 mM KCl. Myosin running buffers also

contained 20 mM Tris pH 7.4, 2 mM $MgCl_2$, 1 mM DTT, and either 50 or 100 mM KCl, and were furthermore supplemented with 2 mM MgATP, 0.1 mg/mL κ-casein for surface passivation, 0.25 μM fascin to stabilize the racetracks, 1 mM PCA and 0.05 μM PCD to prevent photobleaching, as well as 10 mM creatine phosphate and 0.1 mg/mL creatine kinase as an ATP-replenishing system. Myosin was always assembled in the same concentration of KCl that was used in the running assay.

After assembly, myosin filaments were stored on ice until use (1 hr at most), and we did not observe any changes in the appearance or motility of the myosin filaments during this time. Immediately before adding the myosin filaments to the actin racetracks, they were diluted in running buffer (with 2 mM ATP). Nonmuscle myosin filaments were added to the channels at a final concentration of 3.5 nM, skeletal muscle myosin was added at 70 nM. This yielded a good coverage of the racetracks with myosin, so that many (> 100) filaments were visible in each field of view, but they were far enough apart to be easily distinguishable by our automated tracking software. 15 μL of myosin was flushed into the chamber, and imaging was started immediately.

Statistics

We imaged every batch of assembled myosin in at least three different flow channels, diluting a new sample of pre-assembled myosin with MgATP each time, and we typically acquired data from 3-4 fields of view per channel. All data shown in this chapter encompasses measurements from at least two independent experiments (for nm-myosin running on single actin filaments), and at least four for all experiments studying myosin running on bundles of actin. Note that we inspected all data before performing automated analysis, and discarded any fields of view in which actin filaments moved during the video.

Automated analysis

The procedure for myosin tracking in motility assays is laid out in the main text; we performed all the analysis using a custom-written Python [336] script based on the following packages: *pims* for handling 16-bit multichannel timelapses, *trackpy* for locating and linking blobs [307], *pandas* for data handling [337, 338], and *scikit-learn* for fitting [339].

We chose tracking parameters as follows, based on visual inspection of the blob finding results:

Parameter	muscle myosin	nonmuscle myosin
blob size estimate	11 px	11 px
blob mass lower threshold	2000	2000
blob mass upper threshold	15000	15000
band pass filter lower threshold	50	50
band pass filter upper threshold	default	default
minimum track length	8 frames	8 frames
maximum step range	15 px	3 px
maximum allowed hole in track	2 frames	1 frame

Table 3.1: *Trackpy* segmentation and tracking parameters for muscle and nonmuscle myosin filaments. Note that while nonmuscle myosin-2 filaments were much smaller than skeletal muscle myosin filaments, they were also much more intensely fluorescent and could thus be segmented with the same settings.

From the *trackpy* results, frame-by-frame filament displacements and velocities were calculated using a custom written python script. Many trajectories comprised more than one linear segment, i.e. the myosin filament switched between different running speeds (Fig. 3.5 D). To separate the trajectories into these individual segments, we used a python script that was kindly provided by Cristina Martinez Torres. Linear parts in the displacement-time-curves were segmented by a sliding linear fit with variable window size. The best fit was defined as the fit that required the smallest possible number of linear segments, where each segment fit was better than $R^2 > 0.95$. Note that we did not impose limits on the number or length of individual segments, but the R^2-criterion effectively means that segments with fewer than ~ 8 frames did not get picked up by this segmentation. For further analysis, we discarded any tracks where the fit quality was worse than $R^2 = 0.98$

Segment speed distributions were visualized using the *seaborn* 'histplot' function with the 'density' statistic, so that histograms of segment speeds were normalized to a total area of 1 ($\int_{-\infty}^{\infty} \rho dv = 1$). Weighting the segments by their lengths was performed using the *seaborn* 'weights' function.

We also confirmed that the automated analysis was yielding correct results by re-analyzing a small portion of our data by hand, extracting myosin running speeds from kymographs, which indeed yielded consistent results (Supp. Fig. 3.23). Kymographs were generated using the ImageJ plugin 'MultiKymograph' with a 5 pixel linewidth, and myosin speeds were extracted manually by measuring the slopes of myosin run segments in ImageJ [340].

For both muscle and nonmuscle myosin-2, we tried to extract bond lifetimes with the actin racetracks. If our tracks were dominated by myosin unbinding, we should expect to see an exponential distribution in lifetimes [279]. However, we found that short tracks were overrepresented in all our measurements compared to an exponential decay (Supp. Fig. 3.18). The duration of myosin runs must therefore be dominated by an effect other than myosin filament unbinding. Indeed, visual inspection confirmed that myosin filaments very often ran out of the field of view, effectively cutting tracks short. We thus conclude that our data is not suitable for determining the binding lifetimes of myosin-2 filaments to actin tracks.

3.4.5 TIRF Microscopy

For all myosin running assays, total internal reflection fluorescence (TIRF) microscopy was performed on an inverted Nikon Ti-2 microscope equipped with an azimuthal TIRF/FRAP illumination module (Ilas^2, GATACA Systems), a 100x Apo TIRF 1.49 NA oil immersion objective and an EM-CCD Andor iXon Ultra 897 camera, as well as a Perfect Focus System. Dual-color imaging was performed using a Cairn Research Optosplit II Split module, which allowed for rapid two-colour image acquisition. Samples were illuminated at 488 nm with a 100 ms exposure time, gain of 250 and 15.3 % laser power, and at 561 nm with a 100 ms exposure time, gain of 250 and 8.2 % laser power. The TIRF angle was adjusted to yield a 189 nm TIRF penetration depth as determined by the instrument control software for all wavelengths. The exact TIRF angle did not qualitatively change the outcome much, but we kept it consistent to allow for comparable fluorescence intensities between experiments.

TIRF imaging in experiments aimed at optimizing bundling conditions was performed on an inverted Nikon Eclipse Ti-E microscope equipped with an Apo TIRF 100 x 1.49 N.A.

oil immersion objective and QuantEM 512SC EM-CCD camera (Photometrics). Samples were illuminated with a 635 nm Nelles Griot laser (CVI Laser Optics) using a motorized TIRF illuminator (Roper Scientific) and with a variable TIRF angle chosen to give the best signal-to-background ratio on any given day.

Imaging was performed at room temperature (24 ± 1° C). Registration of two-color images was performed separately for each day of experiments, to align the two channel images produced by the Optosplit setup. Reference images for registration were acquired using 200 nm multifluorescent beads mounted on a microscope slide (Cat. # 10505593, Invitrogen), and registration was performed using the ImageJ plugin *2D descriptor based registration* [341].

3.4.6 Interferometric Scattering Microscopy

Interferometric Scattering Microscopy (iSCAT) mass photometry was performed on a OneMP Mass Photometer (Refeyn) equipped with a 525 nm laser. iSCAT measurements were performed in CultureWell gaskets (Cat. # GBL103250, Grace Biolabs) mounted on # 1.5 coverslips (Cat. # 13296788, Corning). The coverslips were first cleaned by stepwise sonication in MilliQ water, 50 % isopropanol and again MilliQ water for 5 min each. To ensure good protein adhesion, the coverslips were then incubated with poly-L-lysine solution (PLL, Cat. # P4832, Merck) for 30 s, rinsed with MilliQ water and dried under N_2 flow. Treated coverslips were stored upright in a Teflon rack in air in a covered beaker to protect them from dust, and used within a week. iSCAT videos were acquired using a 10x10 µm field of view and measuring between 6000 and 15000 frames at 300 fps to ensure that at least 1000 particles were counted per video. iSCAT requires a dilute solution of proteins, so that individual events where a protein lands on the surface are well-separated and no overlap exists between their scattering patterns. We chose the protein concentrations (typically ~10 nM myosin monomers or 25 nM myosin assembled in filaments) such that landing events were well-separated most of the time, but high enough that we could collect good statistics within no more than 15000 frames to limit data volume. Analysis of iSCAT videos was performed using the commercial DiscoverMP software (Refeyn), and the analysis workflow is illustrated in Supp. Fig. 3.19 A and B.

3.4.7 Negative stain transmission electron microscopy

Electron microscopy was performed on Cu400 carbon support grids (Quantifoil, Cat. # N1-C73nCu40-01) on a JEM-1400Plus transmission electron microscope (JEOL) with an acceleration voltage of 120 kV and a TemCam-F416 CMOS camera with 4kx4k pixels (TVIPS). Negative stain EM samples were prepared by first glow discharging the grids in an oxygen plasma (GloQube-D, Quorum Technologies Ltd.), then depositing a 3 µL drop of sample on the grid and incubating for 1 min to allow the protein to adsorb to the grid. To remove excess protein and salt, samples were blot-dried and washed in MilliQ water three times before blot-drying again. Finally, samples were stained with a aqueous solution of 2 % uranyl acetate (Electron Microscopy Sciences) for 2 min, and blot dried completely. For each condition, we measured at least 26 filaments from 2 independent samples, analyzing between 7 and 14 different fields of view at at least 25,000x magnification

3.4.8 Scanning transmission electron microscopy

Scanning Transmission Electron Microscopy (STEM) was performed on a Verios 460 electron microscope (FEI) in Hig-Angle Annular Dark-Field mode with a working distance of 4.4 mm. Imaging was done with a beam current of 100 pA and a pixel dwell time of 3 µs and a convergence half-angle of 2 mrad. Masses were calibrated using Tobacco Mosaic Virus rods (TMV), which were a kind gift from Jean-Luc Pellequer. TMV rods were deposited on each grid before sample deposition, by allowing a 2 µL drop of 25 µg/mL solution of TMV rods in PBS to adsorb to the grid for 1 min at room temperature, washing three times with MilliQ water and blot drying. Myosin filaments were first assembled by rapidly diluting monomeric skeletal muscle myosin-2 to 30 nM into assembly buffer (20 mM imidazole, 2 mM $MgCl_2$, 1 mM DTT and between 37 and 150 mM KCl). After a 30 min assembly time, filaments were mounted on pure carbon on 300 mesh copper grids (Ted Pella Inc., Cat. # 01843-F) by first incubating the grid with 5 µL sample buffer for 5 min to make the grid surface hydrophilic, and then replacing 2 µL of buffer with the assembled protein. After allowing the protein (final concentration 20 nM) to adsorb for 1 min, the grids were washed three times in MilliQ water and blotted completely dry. Images were analyzed by Viktoria Wollrab using published Python-based software by Cristina Martinez-Torres, which was designed specifically to analyze mass-mapping data on filamentous protein structures [299]. The molecular mass of a rabbit skeletal muscle myosin monomer was assumed to be 480 kDa [301]. The analysis procedure is explained in Supp. Fig. 3.22 and the reader is referred to Ref. [299] for the precise implementation details. Note that the analysis measures mass-per-length. To arrive at total filament masses, the mass per length was thus integrated along the length of each filament.

Code availability

All python code to analyze the data reported in this chapter is available on Github: github.com/BioSoftMatterGroup/myosin-assembly-and-motility.

Acknowledgements

We thank Cristina Martinez-Torres for sharing her software for track segmentation and fitting. Jeffrey den Haan, Marjolein Vinkenoog, and Nils Liebe (U Göttingen) are thanked for their help with purification of muscle myosin-2, and Kabir Razack and Irene Isturiz Petitjean are thanked for their help with myosin labeling. We thank Lutz Vogeley, Tina Wiegand and Stephan Grill (all Max Planck Institute for Molecular Cell Biology and Genetics, Dresden) for purification of *C. elegans* nonmuscle myosin-2 and helpful and inspiring discussions. David Kovar (U Chicago) is acknowledged for his kind gift of the capping protein plasmid. Thanks to Celine Alkemade for sharing her insights into actin bundling, to Daniel Ramirez Montero for helpful discussions on surface artefacts, and to Jérémie Capoulade for his support setting up the TIRF microscopy assay. We acknowledge financial support from The Netherlands Organization of Scientific Research (NWO/OCW) Gravitation program Building A Synthetic Cell (BaSyC) (024.003.019).

3.5 Supplementary Figures

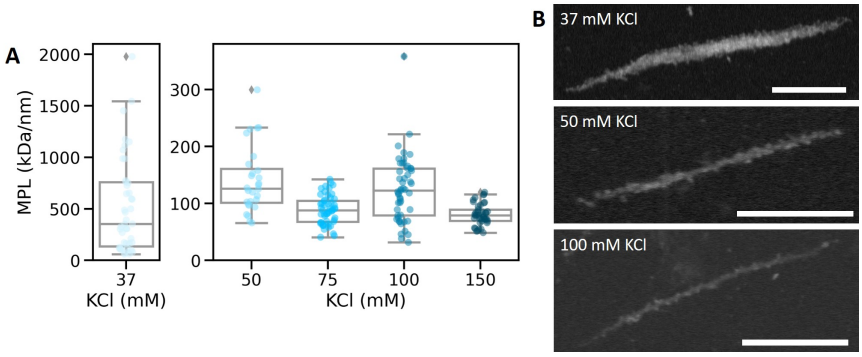

Figure 3.10: **Mass mapping of skeletal muscle myosin-2 filaments.** (A) Box plots of the mass per length of myosin filaments assembled at different concentrations of KCl. Each data point represents the mean mass per length of one filament. There was no consistent trend in the change of mass per length between 50 mM to 150 mM KCl, but average filament masses per length were much higher at 37 mM KCl than in any other condition. (B) STEM images of typical myosin filaments confirmed that filaments were much thicker at 37 mM KCl than at 50 mM or 100 mM KCl. The filament morphology also changed: while filaments at higher ionic strength had a bare zone in the center of the filament and tapered only slightly at the very ends, filaments at 37 mM KCl tended to be thickest in the center, tapering significantly towards the ends, and the bare zone was completely absent. Scale bars: 500 nm.

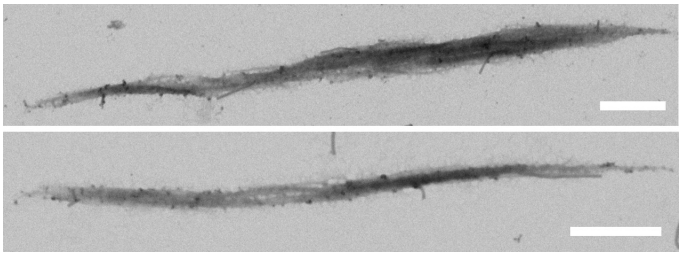

Figure 3.11: **Large skeletal muscle myosin-2 filaments may consist of multiple subfilaments.** STEM images of myosin filaments assembled at 37 mM KCl that appeared to come apart on the grid, with individual sub-filaments fraying from the main filament. Scale bars: 500 nm.

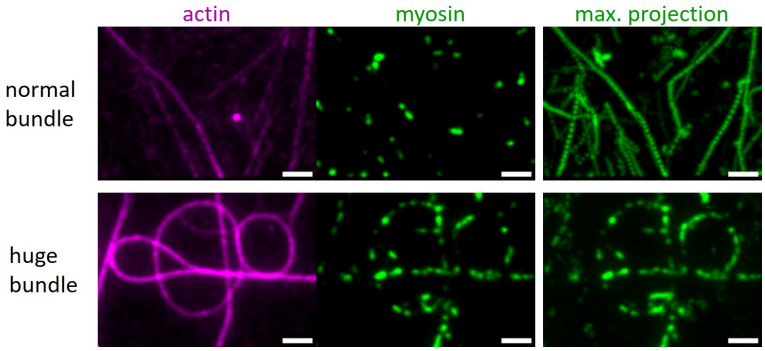

Figure 3.12: **Skeletal muscle myosin-2 filaments get trapped in large actin bundles.** TIRF image of 'normal' actin bundles (top) compared to huge, curly actin bundles (bottom). Myosin (green) decorated both normal and huge actin bundles (magenta), but maximum intensity projections show that myosin filaments ran over normal bundles, while they got stuck on huge ones. These images show the same batch of skeletal muscle myosin-2 filaments assembled at 50 mM KCl. Maximum intensity projections were generated from 100 frames at 5.75 fps. Scale bars: 3 µm.

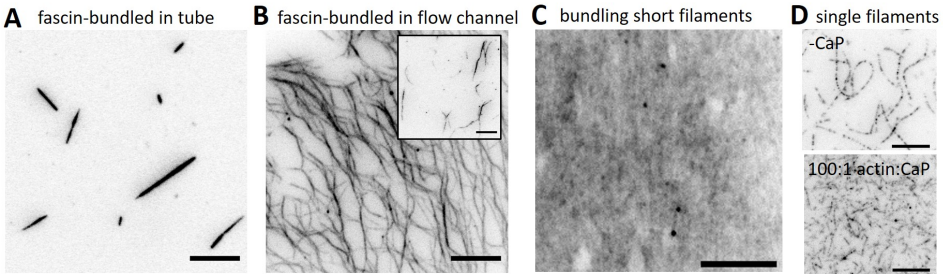

Figure 3.13: **Actin bundle assembly depends on filament lengths and bundling conditions.** TIRF microscopy images of actin; LUT is inverted for clarity, so actin-rich regions are shown as dark features on a bright background. (A) Incubating actin overnight at 4 ° with fascin (molar ratio 1:8) yielded straight bundles of relatively well-defined thickness. However, bundles were short ($\lesssim$ 15 µm), relatively sparse, and poorly aligned with respect to the flow direction. (B) Incubating actin at 1 µM with fascin (1:25 molar ratio) in the flow channel directly yields networks of bundles which are very sparse in some regions (inset) and highly interconnected in others (main panel). (C) Using shorter actin filaments inhibited effective bundling by the standard protocol. Filaments were straightened in the direction of flow, but not significantly bundled. The right panel shows actin filaments before bundling in the absence of capping protein (top) and after polymerization at a 100:1 molar ratio of actin:capping protein (bottom), which yielded significantly shorter filaments. Scale bars: 10 µm.

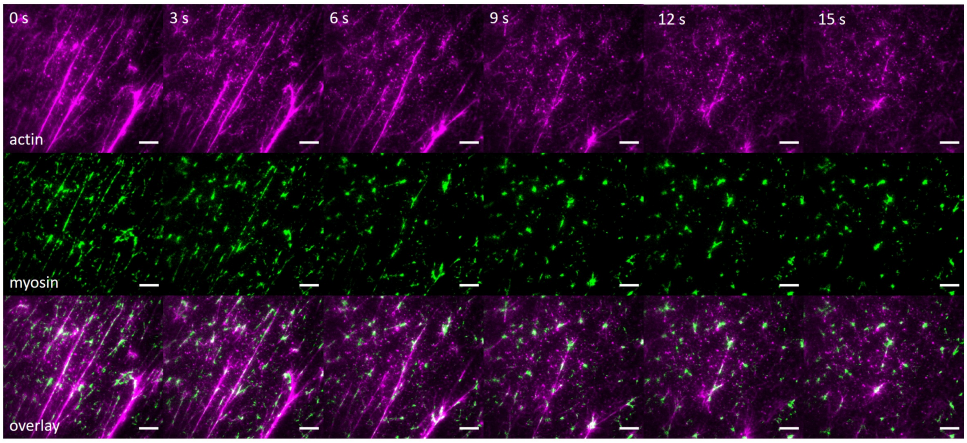

Figure 3.14: **Myosin filaments contract interconnected actin bundle networks.** TIRF images of a highly connected network of actin bundles (magenta) and rabbit skeletal muscle myosin-2 (green). The network contracts rapidly due to the high connectivity between the actin bundles. Bundles are removed, fragmented, and re-arranged into asters with myosin at their center. This assay was performed at 50 mM KCl and 1 mM MgATP. Images are 3 s apart and scale bars are 10 µm.

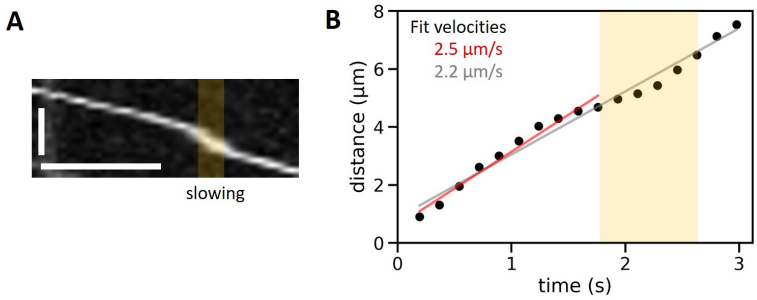

Figure 3.15: **Effect of transient reduction in myosin running speed on the velocity distribution from the automated tracking analysis.** (A) Kymograph of a myosin filament running on an actin bundle. The yellow shaded area denotes the location where a different myosin filament gets stuck later in the same video. When passing this section of the actin bundle, the myosin filament briefly slows down (steeper section of the kymograph). Scale bars: 2 s (vertical) and 3 µm (horizontal). (B) The time-distance-graph of the same run (black circles) confirms that myosin briefly slows down (yellow shaded region). Since the slow-moving period only lasts for a few time points, and the difference in velocities is not very large, our sectioning algorithm does not pick up on these subtle changes in running speed and will thus measure a slightly reduced speed for this segment. Consequently, we measure a running speed of 2.2 µm/s along the entire run segment (grey fit line), compared to 2.5 µm/s up to the point where the myosin filament slows down (red fit line).

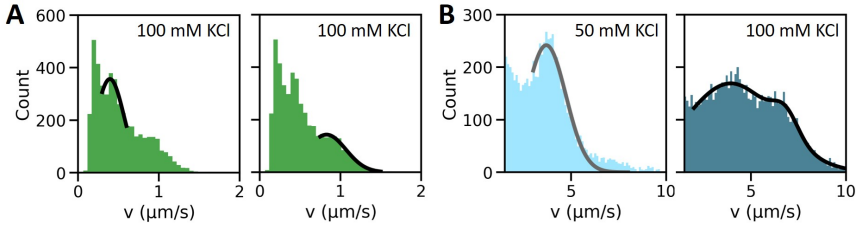

Figure 3.16: **Peak fitting in running histograms by Gaussian functions for the high-speed running peaks.** (A) Gaussian fits to the two peaks in the 100 mM KCl running histograms for nonmuscle myosin-2. Peaks are centered around 395 nm/s (left) and 835 nm/s (right) and with standard deviations of 174 and 234 nm/s. (B) Gaussian fit (grey) to histogram of muscle myosin running at 50 mM KCl, and fit of a sum of two Gaussians to data taken at 100 mM KCl (black). At 50 mM KCl (left), we find a single Gaussian centered around 3.69 μm/s and with a standard deviation of 1.03 μm/s, wheras the two distributions at 100 mM KCl (right) are centered around 3.94 ± 2.41 and 6.83 ± 0.67 μm/s, respectively.

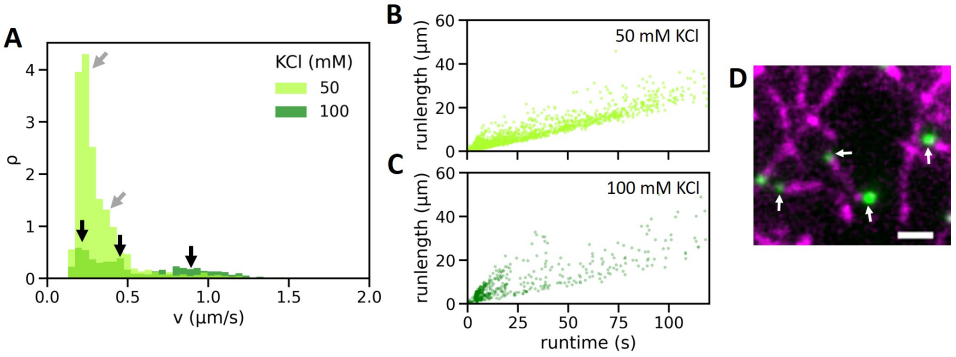

Figure 3.17: **Nonmuscle myosin-2 motility on single actin filaments.** (A) Unweighted histograms of nonmuscle myosin-2 segment running speeds on single actin filaments. The histogram at 100 mM KCl shows the same three peaks as that in Fig. 3.8 A (black arrows), where the first corresponds to stationary filaments and the other two correspond to motile filaments. At 50 mM KCl, we observe the same peak for stationary filaments as well as a shoulder around 0.4 μm/s (grey arrows) and a tail with run speeds up to ~ 1 μm/s. (B, C) Scatter plot of run lengths against run times at 50 mM KCl (B) and 100 mM KCl (C) further confirm that the data are consistent with data acquired on actin bundles (Fig. 3.8). Sample sizes: N (50 mM KCl) = 1487 run segments from a total of 1725 particles. N (100 mM KCl) = 469 run segments from a total of 542 particles. Both datasets are from two samples measured on the same day. The samples came from the same batch of myosin, but were assembled into filaments independently from each other (D) TIRF image of nonmuscle myosin-2 filaments (green) at 50 mM KCl on single actin filaments. Many motors reside at the ends (white arrows) of actin filaments (magenta). Scale bar: 2 μm.

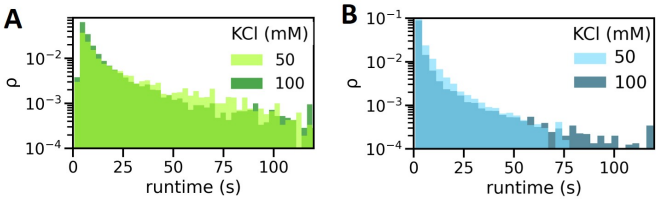

Figure 3.18: **Track lifetimes of muscle and nonmuscle myosin-2 on actin racetracks.** Track lifetimes measured by automated image analysis for *C. elegans* nonmuscle myosin-2 (A) and rabbit skeletal muscle myosin (B) at 50 and 100 mM KCl, respectively (light and dark colours). If the lifetimes were exponentially distributed, we would expect them to decrease linearly in this diagram. However, short lifetimes are overrepresented, indicating that binding times are not determined by myosin unbinding.

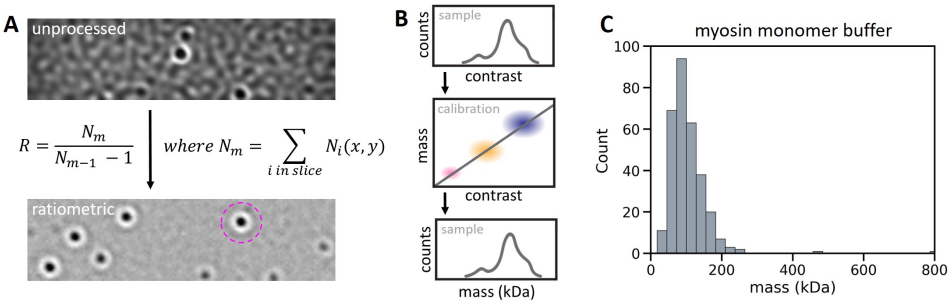

Figure 3.19: **Analysis of iSCAT mass photometry data.** (A) In iSCAT, raw images (top) are acquired that show the interference contrast between the incident light reflected off the coverslip surface, and that scattered by the sample. For mass photometry, we typically record series of several 1000 such images in rapid succession, to observe molecules landing on the coverslip surface. The raw data is then processed to remove the static scattering contribution from the coverslip's rough surface in a pixel-by-pixel manner. In essence, each frame is divided by the sum of the previous few frames ($i \approx 5$ is suitable to obtain good contrast), yielding the corresponding 'ratiometric' image (bottom). In contrast to the static coverslip, proteins landing from solution have a scattering pattern that changes from frame to frame as they approach the coverslip, thus becoming visible in the ratiometric image, where they can then be tracked (magenta dashed circle) and the total scattering contrast can be extracted for each particle. The iSCAT images show rabbit skeletal muscle myosin monomers and show a 10 µm wide field of view. (B) A histogram of particle interference contrasts is converted to a histogram of molecular masses by means of a separately recorded calibration curve, where a series of proteins of known mass are used as mass references. (C) Some buffer components, in particular reducing agents like DTT, form particles that are detected in iSCAT at an apparent mass around 100 kDa (T. de Garay, Refeyn, personal communication, 2021). The diagram shows the buffer signature of myosin monomer buffer. Note that the particle count stemming from buffer components ($\lesssim 500$ counts) was much smaller than that of myosin monomers ($\gtrsim 10000$ counts) in our experiments.

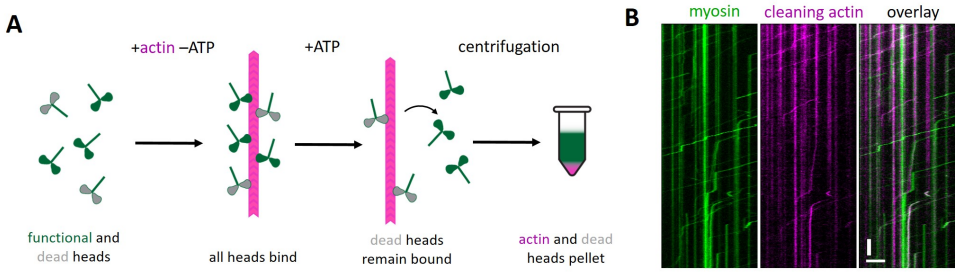

Figure 3.20: **Actin-affinity purification leaves actin fragments bound to myosin.** (A) Working principle of actin-affinity purification of myosin. Myosin samples contain a mixture of functional and 'dead' heads, which are unable to hydrolyse ATP. When such a sample is mixed with actin filaments in the absence of ATP, all myosin heads will bind in the rigor state. Adding high concentrations of MgATP (typically 5 mM) elutes those heads with intact ATPase activity, while the dead heads remain bound to the actin filaments and can thus be removed from the sample, as they pellet with filamentous actin upon ultracentrifugation. (B) Kymograph of a TIRF video showing rabbit skeletal muscle myosin-2 filaments (green) at 50 mM KCl and 2 mM ATP, walking on an actin bundle (not labeled). A number of myosin tracks, both from stationary and motile myosin filaments, colocalize with fluorescence signal from sacrificial cleaning actin. We found that such actin was always detectable unless the sampe was centrifuged for at least 30 min at 148,000 g.

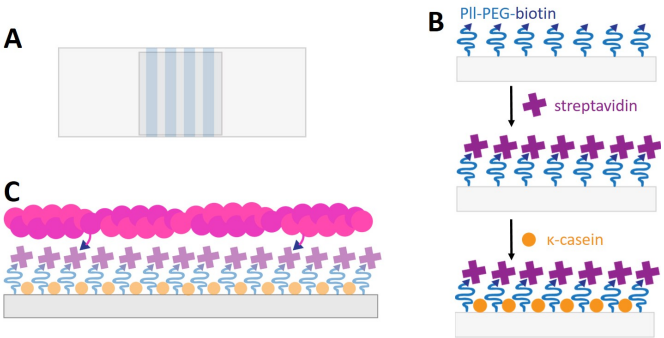

Figure 3.21: **Flow channel assembly and surface passivation** (A) Schematic representation of a slide with flow chambers. Parafilm (blue strips) acts as a spacer between the glass slide and coverslip (light grey), forming rectangular flow channels. (B) Stepwise incubation with Pll-PEG-biotin (blue), streptavidin (purple) and κ-casein (orange) produces passivated glass surfaces to which unspecific protein adhesion is minimized. (C) Actin filaments are loosely adhered to the flow chamber wall by doping the filaments with biotinylated monomers (blue triangles), which can bind to the surface-grafted streptavidin.

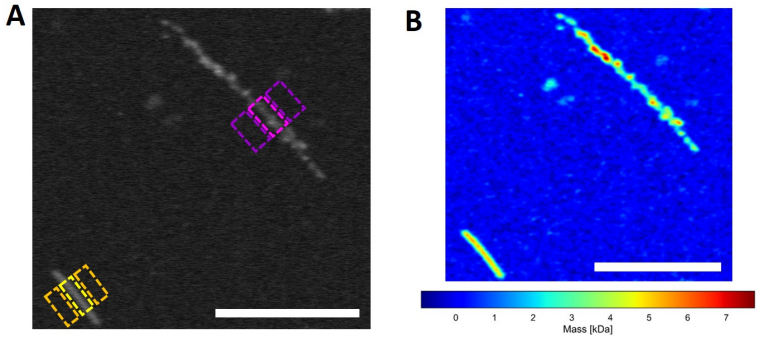

Figure 3.22: **Extraction of filament mass by automated analysis and calibration of STEM images.** (A) STEM image of a myosin filament (skeletal muscle myosin-2, assembled at 50 mM KCl) and a tobacco mosaic virus rod (bottom left corner). With the dark field detector, both protein and virus appear as bright structures on a dark background. The mass per length was extracted for both the virus particle and myosin filament in small sections along the filament (dashed rectangles encompassing the virus (yellow) and myosin filament (magenta)). To correct for the contribution of the underlying carbon support, a local background correction was first performed on the sides of the filaments (dashed orange and purple rectangles). (B) The virus has a known mass per length, which was extracted and used as an internal mass calibration in order to convert the entire image to a mass map. Scale bars: 500 nm.

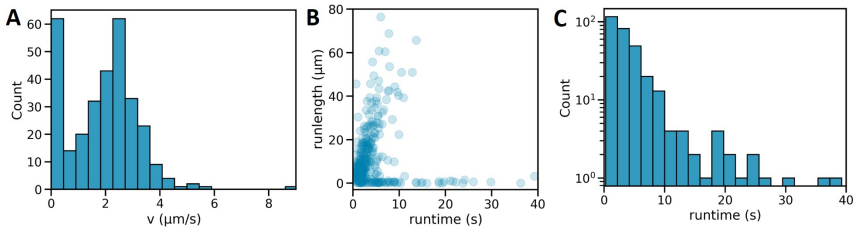

Figure 3.23: **Kymograph-based analysis of myosin motility confirms the results of our automated analysis.** To confirm that our automated analysis correctly identified myosin running speeds, we manually analyzed kymographs of running skeletal muscle myosin-2 filaments. We first generated kymographs from three separate actin bundles in two separate fields of view, all showing skeletal muscle myosin-2 assembled at 100 mM KCl. We then manually identified all myosin track segments (310 in total) on these kymographs and traced them with the ImageJ 'line' tool to measure their length and slope. These values were then converted into run lengths, times and speeds in python. (A) A histogram of run speeds confirmed that there was an immobile population as well as a large population of myosin filaments running at around 3 μm/s, and a small number of filaments with almost double that speed. (B) Scatter plot of run lengths against run times confirmed the same observation. Note that the immobile myosins, represented in the nearly horizontal population in the population at low run lengths, had a slope of nearly zero, while this population had a non-zero slope in the data produced by automated track analysis. This was a result of the difference in how speeds are calculated: here, we fitted a line to a kymograph, effectively averaging over any fluctuations of the myosin filament's center-of-mass position, and thus measured no net displacement. In the automated analysis, detector noise and thermal motion of the filament invariably led to some shifts in the center-of-mass position from frame to frame, which were recorded by automated tracking. This resulted in a finite frame-to-frame displacements that accumulated over time, rather than being averaged out. Consequently, the speeds calculated in the automated analysis were all slightly higher than those measured in kymograph analysis. (C) Run times measured on kymographs were roughly exponentially distributed.

4

Branched actin cortices reconstituted in vesicles sense membrane curvature

Abstract

The actin cortex is a complex cytoskeletal machinery which drives and responds to changes in cell shape. It must generate or adapt to plasma membrane curvature to facilitate diverse functions such as cell division, migration and phagocytosis. Due to the complex molecular makeup of the actin cortex, it remains unclear whether actin networks are inherently able to sense and generate membrane curvature, or whether they rely on their diverse binding partners to accomplish this. Here, we show that curvature sensing is an inherent capability of branched actin networks nucleated by Arp2/3 and VCA. We develop a robust method to encapsulate actin inside giant unilamellar vesicles (GUVs) and assemble an actin cortex at the inner surface of the GUV membrane. We show that actin forms a uniform and thin cortical layer when present at high concentration and distinct patches associated with negative membrane curvature at low concentration. Serendipitously, we find that the GUV production method also produces dumbbell-shaped GUVs, which we explain using mathematical modelling in terms of membrane hemifusion of nested GUVs. We find that branched actin networks preferentially assemble at the neck of the dumbbells, which possess a micron-range convex curvature comparable to the curvature of the actin patches found in spherical GUVs. Minimal branched actin networks can thus both generate and sense membrane curvatures, which may help mammalian cells to robustly recruit actin to curved membranes in order to facilitate diverse cellular functions such as cytokinesis and migration.

This chapter is based on a manuscript of the same name by Lucia Baldauf*, Felix Frey*, Marcos Arribas Perez, Timon Idema and Gijsje Koenderink, which is in revision for publication in Biophysical Journal. Lucia Baldauf led the experimental effort and analyzed the data. Felix Frey and Timon Idema (TU Delft) developed the model for hemifusion-driven dumbbell shapes of GUVs. Marcos Arribas Perez performed the experiments with fluorescent VCA and contributed to actin polymerization measurements. Lennard van Buren performed tensiometry

4.1 Introduction

The actin cortex is a thin but dense meshwork of cytoskeletal actin filaments that lines the plasma membrane of animal cells. It provides mechanical stability to the cell surface, yet also actively drives cellular shape changes necessary for cell division, cell migration, and tissue morphogenesis. The main structural component of the cortex is filamentous actin. More than 100 actin-binding proteins, including nucleators, membrane-anchoring proteins, crosslinkers and motors control the organization, turnover dynamics, thickness, and mechanical properties of the cortical actin meshwork [6]. Proteomic and functional studies have shown that cortical actin filaments are nucleated primarily by the formin Dia1 and the Arp2/3 complex [26, 342]. Dia1 generates linear actin filaments and associates with their fast-growing (barbed) end [39], whereas the Arp2/3 complex binds to the side of a pre-existing actin filament and nucleates a new actin filament from its slow-growing (pointed) end upon activation by a nucleation promoting factor such as N-WASP [34]. As a consequence of this mechanism, Arp2/3-mediated actin network growth is autocatalytic and results in dendritic arrays [126, 343, 344].

Cortical actin networks accumulate at various curved plasma membrane structures, for instance in the cytokinetic ring [54, 81] and and tunnel-like wounds [345], in phagocytic cups [346], or in cells that grow confined to micropatterned environments [347] or migrate through tight spaces [348]. However, it remains unknown whether cortical actin networks have any intrinsic ability to sense and respond to membrane curvature. Any such abilities are difficult to observe in living cells, as cortical actin interacts with a multitude of curvature-sensitive actin-binding partners, including membrane-bending BAR-domain proteins [180, 349–351], curvature-sensitive septins [46, 159], and IQGAP proteins [47], possibly obscuring any intrinsic curvature sensitivity of the actin network itself. Conversely, it is also unknown how cortical actin affects the generation of membrane curvature. On the one hand, polymerizing actin can generate membrane curvature by exerting pushing forces [141, 352], but on the other hand the high rigidity of the cortex may counteract membrane deformation [86, 353].

To study how simple actin networks intrinsically interact with curved membranes, we pursue a bottom-up reconstitution approach. Reconstitution of actin inside cell-sized, deformable membrane compartments has been gaining traction recently, with several studies exploring how actin networks self-organize in and shape giant unilamellar vesicles (GUVs) [119, 136, 137, 140, 141, 143, 144, 165, 354]. However, systematic *in vitro* characterization of the interplay between the membrane and a dynamic actin cortex in GUV assays has been challenging due to difficulties with reproducible actin encapsulation.

In principle, various approaches are available for GUV formation, ranging from methods based on swelling dried lipid films [355–362] through picoinjection of droplet-templated GUVs [363, 364] to emulsion-based approaches [139, 365–373]. However, most of these approaches are incompatible with actin encapsulation, as their yield drops dramatically when encapsulating proteins in physiological buffers. The most successful strategies

measurements and contributed to the analysis of encapsulation efficiencies. Iris Lambert performed actin encapsulation experiments by cDICE and started the development of eDICE under the supervision of Lucia Baldauf. GUVs containing cardiolipin and PIP_2 in their membranes were produced by Britta Bor (supervised by Gerard Castro-Linares and Lennard van Buren) and Marcos Arribaz-Perez. Tom Aarts (supervised by Lucia Baldauf and Lennard van Buren) and Federico Fanalista acquired images of dumbbell-shaped GUVs in samples produced by gel-assisted swelling and cDICE.

for reconstituting actin in GUVs have been emulsion-transfer methods, where droplets of protein-containing aqueous solution are formed in an oil phase, stabilized by a self-assembled lipid monolayer, and transformed into GUVs by passing through a second lipid monolayer. One version of this type of GUV preparation is 'continuous Droplet Interface Crossing Encapsulation' (cDICE), a method where droplets are created by injecting a continuous stream of inner protein containing solution into the oil phase by means of a thin glass capillary. The inner aqueous phase is supplemented with a density medium, and the oil phase is placed atop an aqueous subphase inside a rotating chamber, so GUVs can be created on a single compact device [370]. While cDICE has been used for actin encapsulation in several studies [119, 137, 140, 141, 144, 165, 374, 375], recent optimization efforts have made it significantly more robust [138], and attempts at simplifying the method have also been made [139]. Nonetheless, the technique remains relatively slow and cumbersome, and a full characterization of the produced GUVs is lacking.

Here, we establish a robust and fast variant of the cDICE method which we term "emulsion Droplet Interface Crossing Encapsulation" (eDICE) to reconstitute biomimetic actin cortices inside GUVs, and characterize the resulting GUVs. We show that Arp2/3-mediated assembly generates either cortical actin patches or continuous cortices, depending on the concentration of actin and its nucleation factors. Interestingly, these cortical patches are associated with membrane curvature. Serendipitously, we discovered that cortical actin patches recognize membrane curvature because our GUV formation protocol produces a small fraction of dumbbell-shaped GUVs that likely originate from nested GUVs. We use these dumbbell-shaped GUVs as a model system in which the membrane provides a substrate with fixed and spatially varying curvature, and find that actin networks have a strong preference for assembling at regions of concave membrane curvatures on the micron-scale.

4.2 Results

4.2.1 A robust protocol for actin encapsulation

To study the interactions between cortical actin and lipid bilayer membranes, we reconstituted membrane-anchored actin cortices inside giant unilamellar vesicles (GUVs). We used a modified emulsion transfer method adapted from a recently optimized cDICE procedure [138] (Fig. 4.1 A). We used the same optimized spinning chamber setup reported in [138] and took care to maintain low humidity conditions during the procedure to enhance the GUV yield. However, rather than forming the droplets by injection of the Inner Aqueous Solution (IAS) through a capillary, we pipetted pre-formed emulsion droplets into the spinning chamber. Using pre-formed droplets has several important advantages. First, it avoids problems that can arise from clogging of the capillary that is needed to produce droplets with cDICE. Second, it speeds up the encapsulation step, reducing the time during which the G-actin monomers are at room temperature from several minutes to under 15 s, hence preventing premature actin polymerization [376]. Third, it allows downscaling of the amount of IAS required to generate samples from > 100 µL for cDICE to $\lesssim$ 25 µL in the case of eDICE, important when working with recombinant proteins that are available only in small amounts. eDICE robustly produced a high number of GUVs that were polydisperse in size and in encapsulated protein concentration. In addition to the GUVs, of which a

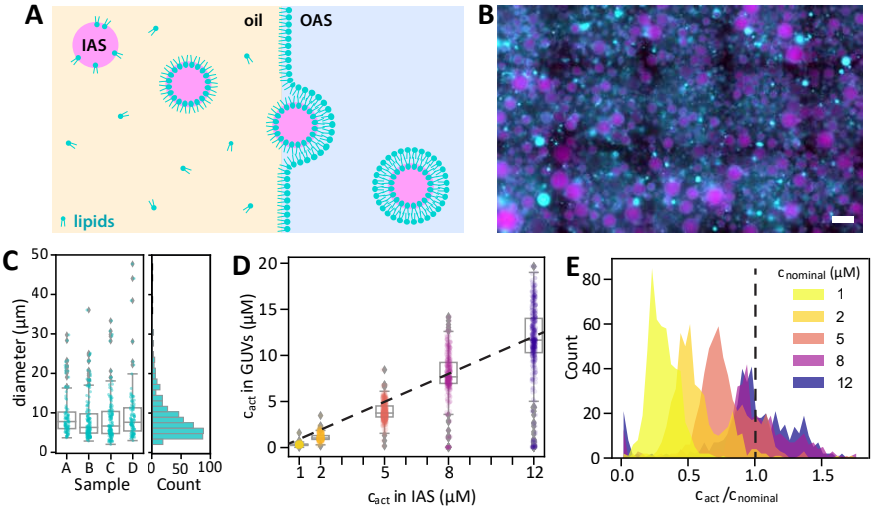

Figure 4.1: **Robust actin encapsulation by eDICE.** (A) Schematic of the eDICE process. Preformed lipid-stabilized emulsion droplets containing the Inner Aqueous Solution (IAS) with G-actin are injected into a spinning chamber. Centrifugal forces created by rotation of the spinning chamber establish concentric layers of the oil phase and an Outer Aqueous Solution (OAS) and push the droplets through the oil/OAS interface, where they acquire a second lipid leaflet and thus transform into GUVs. (B) Typical widefield image of GUVs formed by eDICE. F-actin is shown in magenta, lipids in cyan. Scale bar: 50 µm. (C) Diameter distributions of GUVs from four independent experiments (left) and the aggregated histogram of GUV sizes (right). N per sample: 98, 149, 137, 110. (D) Actin concentrations in eDICE GUVs measured by quantitative fluorescence microscopy, as a function of the nominal actin concentration in the IAS. Individual data points indicate single GUVs, boxplots indicate medians and quartiles. (E) Histogram of encapsulation efficiency, $c_{rel} = c_{act}/c_{nominal}$, for different nominal actin concentrations. The dashed line represents $c_{rel} = 1$. $N_c = 515, 468, 536, 368$ and 447 GUVs for $c = 1, 2, 5, 8$ and 12 µM actin, respectively.

small fraction typically had one or more small lipid pockets attached, we also usually found some large lipid aggregates (bright cyan spots in Fig. 4.1 B) that were not physically attached to GUVs. The average GUV diameter (9 µm) was comparable to that obtained with optimized cDICE (12 µm [138]), and reproducible across independent experiments (Fig. 4.1 C, $p = 0.39$ by one-sided ANOVA test for four independent GUV samples). In rare cases, GUV diameters could be as large as ~ 40 µm. In the Supplementary Information (section 4.5.3), we expand on the optimization of the eDICE method and demonstrate its broad applicability for cytoskeletal reconstitution.

To quantify the encapsulation efficiency, we analyzed confocal fluorescence images of actin inside the GUVs and converted intensities to concentrations using calibration measurements on bulk actin solutions. We found that the mean actin concentration inside the GUVs increased linearly with the concentration of actin in the IAS, and that the mean value was close to the nominal (input) actin concentration (Fig. 4.1 D). However, the distribution of actin concentrations broadened as the nominal actin concentration increased. Interestingly, at high actin concentrations ($c_{nominal} \geq 8$ µM), a substantial fraction of the GUVs was supersaturated with actin, containing up to 1.7× the nominal actin concentration, while a small fraction of the GUVs showed no measurable actin content at all (Fig. 4.1 E). By

contrast, a large fraction of GUVs contained substantially less actin than expected at low concentrations of actin in the IAS ($c_{\text{nominal}} \leq 2$ μM, Fig. 4.1 E). In Supp. Fig. 4.22, we show extended quantification of these results, along with FCS measurements that confirmed our conclusions and demonstrated that encapsulation efficiency varied significantly from day to day. We also showed that F-actin was proportionally co-encapsulated with other proteins. Note that in the following, we assume that membrane-binding proteins like VCA follow the same co-encapsulation characteristic as proteins that do not interact with the membrane (i.e. formin in the absence of a receptor lipid in the membrane, Supp. Fig. 4.20 F, G). This is a reasonable assumption, given that doplet formation and thus protein encapsulation happens rapidly and should be faster than protein-lipid binding at the interface. However, directly quantifying the encapsulation efficiency of membrane-bound proteins is more challenging than quantifying the encapsulation of soluble proteins, and was not performed as part of this study. While it is widely known that GUV formation yields a polydispersity in solute concentrations, our results highlight that this polydispersity is in fact nontrivially dependent on the initial solute concentration.

4.2.2 Actin cortex formation proceeds by nucleation and fusion of patches

In order to form a membrane-nucleated actin cortex, we encapsulated actin along with the nucleating protein Arp2/3 and the Arp2/3-activating protein fragment VCA from murine N-WASP (Fig. 4.2 A). Nucleation was constrained to the membrane by using a 10×-His tag on VCA in order to recruit it to the GUV membrane via Ni-NTA lipids present at a small density within the membrane.

At low actin concentrations (4.4 μM), actin cortices formed with 50 nM Arp2/3 and 0.65 μM VCA exhibited three distinct types of structures. Cortices were either continuous, being enriched all around the GUV (Fig. 4.2 B), or they were made up of distinct small (1-2 μm sized) cortical actin patches (Fig. 4.2 C), or a combination of both. We note that the prevalence of the three cortex phenotypes varied widely from day to day, likely due to variations in protein encapsulation efficiency. Kymographs of the actin signal along the membrane revealed that the actin patches diffused over the surface on a timescale of seconds (Fig. 4.2 D, white rectangle) and could also split (Fig. 4.2 D, white arrow) or merge (Fig. 4.2 D, black arrow).

When we increased the nominal actin concentration to 8 μM, observations varied much less from day to day. Furthermore, we no longer found any GUVs with small cortical actin patches. Instead, we observed four different cortical phenotypes whose prevalence varied with VCA concentration. Actin either formed bright patches inside the GUV lumen (Fig. 4.2 E), patches that were localized to deformed sections of the membrane (Fig. 4.2 F), large flat patches of cortical actin (Fig. 4.2 G), or continuous actin cortices (Fig. 4.2 H). To test the role of the nucleator density, we varied the VCA concentration, which determines both the rate of actin nucleation and the interaction strength of actin with the membrane, between 0.65 and 6.5 μM while maintaining a constant actin concentration of 8 μM (Fig. 4.2 I). Bright foci in the GUV lumen arose in ~ 23 % of GUVs with 0.65 or 1.3 μM VCA (Fig. 4.2 I) and in a few cases at 2 μM (example in Fig. 4.2 E), whereas actin was always localized at the cortex at higher VCA concentrations. The large cortical patches were immobile over a 50 s timespan (Fig. 4.2 J), in contrast to the small mobile patches formed at 4.4 μM actin.

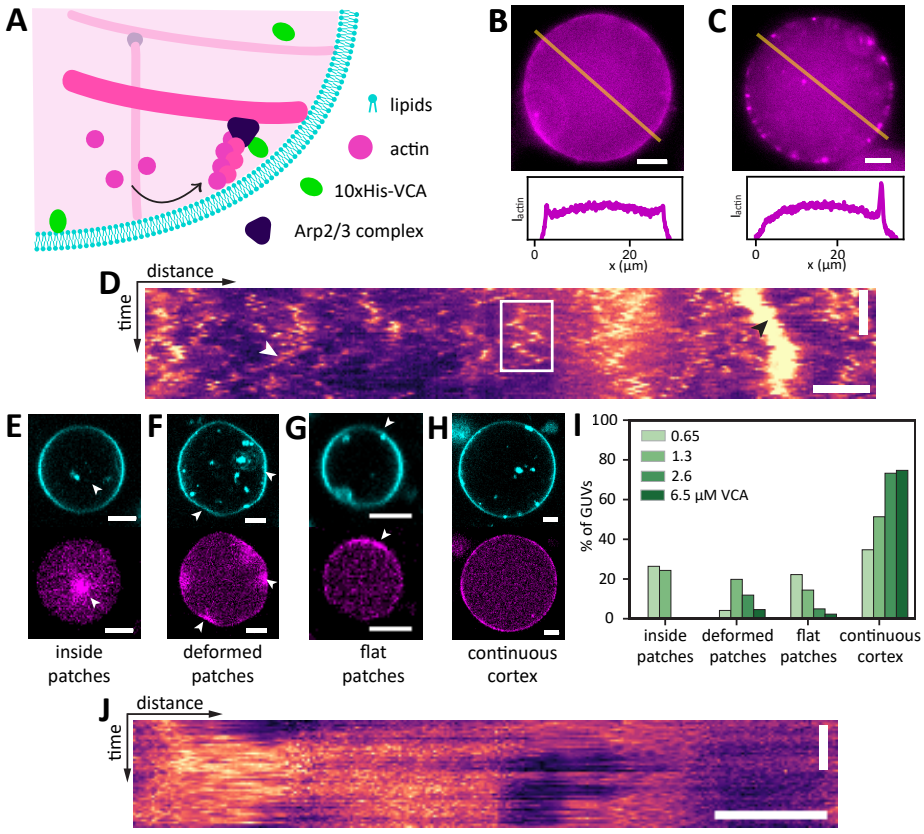

Figure 4.2: **Formation of membrane-nucleated actin cortices inside GUVs.** (A) Actin filaments (magenta) were nucleated using the Arp2/3 complex, which was activated near the inner leaflet of the GUV membrane (cyan) by membrane-bound VCA (green). (B, C) Top row: At low actin concentration (4.4 µM), actin formed either a continuous cortex (B), or small bright patches (C), or a combination of both. Bottom row: Line profiles of actin fluorescence intensity along the yellow lines in the epifluorescence images. (D) Kymograph of a patchy actin cortex from a line drawn along the circumference of a GUV in a time lapse of 50 frames recorded at a frame rate of 1 fps. Scale bars: 10 µm (horizontal), 20 s (vertical). Actin patches could diffuse along the cortex (white rectangle), split (white arrow) or merge (black arrow). (E - H) At high actin concentration (8 µM), we found bright actin foci inside the lumen (E, white arrow), bright deformed actin patches (F, white arrows), extended flat membrane patches (G, white arrow), or a continuous flat cortex (H). All examples show GUVs with 2 µM VCA and 50 nM Arp2/3. Lipids are shown in cyan, actin in magenta. Scale bars: 5 µm. (I) Quantification of cortical phenotypes for 8 µM actin and 50 nM Arp2/3 as a function of the density of VCA activator. Actin patches in the GUV lumen occurred only at low VCA concentrations, bent patches were most prevalent at intermediate VCA concentrations, continuous cortices were most prevalent at high VCA concentrations. GUVs were all produced on the same day and statistics are based on N = 72, 111, 101 and 87 GUVs for VCA concentrations of 0.65, 1.3, 2.6 and 6.5 µM, respectively. (J) Kymograph of an actin cortex (8 µM actin) with large flat patches that were immobile. Scale bars: 5 µm (horizontal), 20 s (vertical).

Flat patches strongly declined in frequency from 22 to 2 % of GUVs when the VCA concentration was raised from 0.65 to 6.5 µM, while the fraction of GUVs with a continuous cortex rose from 35 % to 75 % over this VCA concentration range (Fig. 4.2 I). Since patches

tend to become larger compared to the GUV perimeter as VCA concentration increases, we eventually classify them as a continuous cortex. Deformed membrane sections were observed both in the presence and absence of a continuous cortex. Their prevalence peaked at a 1.3 μM VCA concentration and dropped to around 4 % of GUVs at both ends of the studied VCA concentration range.

4.2.3 eDICE produces some dumbbell-shaped GUVs due to membrane hemifusion

In all GUV samples produced by eDICE, we found some GUVs with a striking dumbbell shape (Fig. 4.3 A). The prevalence of such dumbbell-shaped GUVs varied from experiment to experiment, but they usually made up a few percent of all observed GUVs. These GUVs consisted of two spherical caps connected by an open neck (Fig. 4.3 A). They could be easily distinguished from GUV doublets, created when two vesicles stick to one another (Fig. 4.3 B), by the fact that they lack a membrane septum. Strikingly, one lobe of the dumbbell appeared as a normal unilamellar vesicle membrane (right lobe in Fig. 4.3 A), whereas the other appeared either as one bright membrane (left lobe in Fig. 4.3 A) or as two separate membranes (Fig. 4.3 C), which could be close together (left panel) or, in rare cases (3 out of 85 dumbbells), far apart (right panel). Line intensity profiles along the membrane contours revealed that the brighter lobe had on average twice the membrane intensity of the dimmer lobe (Fig. 4.3 D, E). Thus, dumbbell-shaped GUVs appeared to be made up of one lipid bilayer on the dim side and two on the bright side, consistent with the observation of dumbbells with two well-separated membranes in the bright lobe (Fig. 4.3 C).

We characterized the shapes of dumbbell vesicles by fitting circles to both lobes in the equatorial plane and measuring the distance between the two membranes at the neck (Fig. 4.3 F). When the two membranes of the bright lobe were visibly separated as in the example in Fig. 3 C, we defined the bright lobe size as that of the inner membrane. This analysis revealed that dumbbell shapes were diverse but followed general overall trends. First, the two lobes were usually similar in size, with the dim lobe being slightly larger than the bright lobe in most GUVs (64 % of N = 85 GUVs), although there were occasional outliers where the bright lobe was more than twice the size of the dim lobe (Fig. 4.3 G, Supp. Fig. 4.21). The neck diameter was usually quite wide, ranging from 0.4 to 0.9 times the average lobe diameter (Fig. 4.3 H). Only ~ 5 % of dumbbells had a neck narrower than 0.4 times the average lobe size.

How could these dumbbell-shaped GUVs arise? Motivated by the observation that a small fraction of GUVs contain another GUV within their lumen (Fig. 4.4 A and Fig. 4.7 A), we hypothesized that dumbbells might originate from bursting of such enclosed GUVs. After the inner vesicle leaks its volume into the GUV (Fig. 4.7 B) and merges its bilayer with the lipid bilayer of the outside GUV via hemifusion (Fig. 4.7 C, D), a GUV is created with two lobes: in the first lobe the GUV bilayer membrane is supported by the bilayer of the inner vesicle, while in the second lobe the GUV bilayer remains unchanged (Fig. 4.4 B). How exactly this happens remains unclear, but we suspect that residual oil in the membrane may promote the formation of membrane defects and facilitate membrane fusion. This process should create an interface between the single and double bilayer membranes that is associated with a line tension, which is expected to drive the formation of a dumbbell shape (Fig. 4.4 B). Since two of the membrane leaflets of the bright lobe should be disconnected

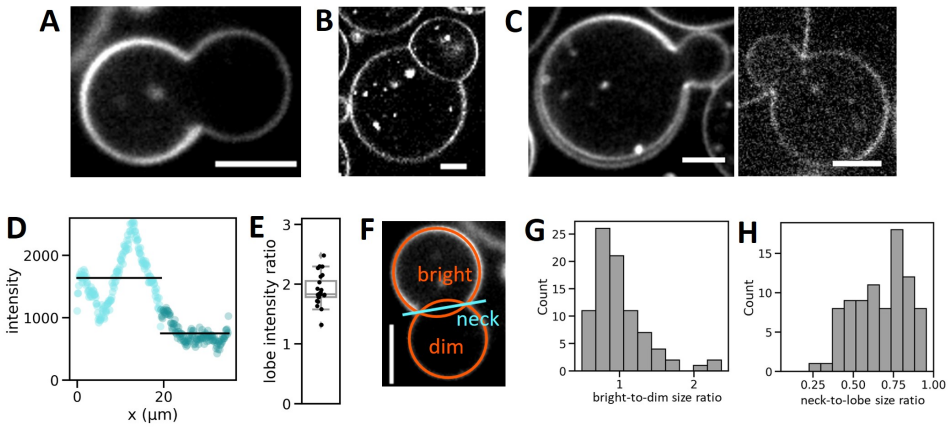

Figure 4.3: **Dumbbell-shaped GUVs formed by eDICE.** (A) Dumbbell-shaped GUV with a bright and a dim spherical cap connected by an open membrane neck. (B) GUV doublets clearly look different, exhibiting a membrane septum between the two lobes that each have equal membrane intensity. (C) Some dumbbells showed two clearly separate membranes in (parts of) the bright half of the dumbbell with a narrow (left) or wide (right) gap. (D) Membrane signal in a 5 pixel-wide line, starting at the neck and following clockwise along the GUV membrane shown in (A). Light cyan data points denote the bright half of the GUV, dark cyan data points show the dimmer half. The average signal is 1.8-fold higher (2.1-fold after background subtraction) in the bright than in the dim lobe (black lines). (E) Boxplot of membrane intensity ratios after background subtraction. The average ratio is 1.9 (N = 25 dumbbells from 5 independent experiments). (F) We measured morphological features of GUV dumbbells by fitting circles to their bright and dim lobes (orange circles) and measuring the neck diameter as the distance between the maxima in membrane fluorescence in a line profile drawn through the neck. (G) Histogram of the size ratio between bright and dim dumbbell lobes (N = 85). (H) Corresponding histogram of neck-to-lobe size ratios (N = 85). Scale bars: 5 µm.

from the two leaflets that envelop the whole dumbbell (Fig. 4.4 C), we were able to test this interpretation by fluorescence recovery after photobleaching (FRAP). Note that this double layer really comprises only one continuous leaflet, but is bent in on itself such that it appears as two layers (Fig. 4.4 C, detailed illustration in Supp. Fig. 4.23 C). The ratio between the average membrane intensities in the bright and the dim lobe should be 2 before bleaching, drop to 0 when we completely photobleach the bright lobe, and return to 1 over time, as the outer leaflets of the bright lobe are replenished by fluorescent lipids from the dim lobe, while the disconnected leaflets in the bright lobe remain bleached (Supp. Fig. 4.23). By contrast, if the leaflets in the two lobes were either fully connected or fully disconnected from one another, the final intensity ratio would be 2 or 0, respectively. Since lipids diffused rapidly in the membrane and recovered after photobleaching within less than 3 s (Supp. Fig. 4.24 A, B), we could not completely bleach the bright lobe to zero while retaining enough membrane intensity in the dim lobe for data analysis. We could, however, reduce the bright lobe fluorescence to around 30 % of its initial value. We found that the lobe intensity ratio recovered within a few seconds and indeed reached a final value that was just over half of its initial value, confirming that the lobes were hemifused (Fig. 4.4 D and additional data in Supp. Fig. 4.24 A).

To further test whether a model based on hemifusion of nested GUVs explains the formation of dumbbells, we asked whether the dumbbell geometries were also quantitatively

consistent with the geometries expected based on a simple membrane model. We assumed that a GUV of radius R_{tot} encapsulates another vesicle of radius R_v (Fig. 4.4 B). After the encapsulated vesicle bursts, we expect its membrane to stick to that of the outer vesicle. As the membrane area of the inner vesicle is smaller than that of the outer one, this process will inevitably create two regions, one with a single and another with a double membrane. The regions will therefore have different surface tensions, and experience a line tension at their boundary. We can account for these differences in a simple energy model (see Supplementary Information, section 4.5.1), from which we find that dumbbell shapes are indeed equilibrium solutions. Unsurprisingly, we found that the surface tensions are related to the osmotic pressure difference across the membrane according to Laplace's law (Eqn. 4.6 in Supplementary Information). Moreover, we found that the overall shape of the dumbbell GUVs is the result of the interplay between this osmotic pressure, which promotes spherical shapes, and the line tension, which tends to constrict the boundary between the two lobes (Eqn. 4.8 in Supplementary Material). Indeed, similar dumbbell shapes have been observed and theoretically predicted in case of GUVs made of phase-separating lipid mixtures, where line tension along the domain boundary also produces spherical cap shapes [377–380].

To verify the model, we used it to predict the distribution of dumbbell shapes, based on the observed distribution of (spherical) GUV sizes (Fig. 4.1 C). From the model, we could then calculate the ratio of the line tension to the osmotic pressure, as the physical parameter that sets the dumbbell shape. This value, which is difficult to measure directly, can thus be inferred from easily observable quantities like the lobe and neck radii. We could also compare it to values for multi-component membranes, which, due to phase separation, also develop multiple domains with line tensions at their boundaries [379].

In the model, the total membrane area (the surface area plus excess membrane area) of the bursting vesicle A_v equals the surface area of the double bilayer membrane lobe A_1, i.e. $A_v = A_1$. Moreover, the GUV's total membrane area A_{tot} minus the surface area of the bursting lobe A_1 equals the surface area of the single bilayer membrane lobe A_2, i.e., $A_{tot} - A_1 = A_2$ (Fig. 4.4 B (ii)). Therefore, we related the shape of the dumbbell GUV, given by R_1, R_2, θ_1 and θ_2, i.e. the radii and opening angles of the bright and dim lobe, to the GUV volume and the membrane area of the GUV and the bursting vesicle (for details see Supplementary section 4.5.2).

To determine the shapes of dumbbell GUVs, we sampled 10 000 radii R_{tot} and R_v and only recorded values of R_1 and R_2 that were in the experimental range (< 25 μm) and corresponded to a defined dumbbell shape ($\pi/2 < \theta_1, \theta_2 < \pi$) with smallest possible neck radius (i.e., minimal line tension energy). To reduce the number of free parameters in our model, we assumed that both the GUV and the enclosed vesicle have been created with the same reduced area, i.e., $v_{tot} = v_v = v$. To determine the reduced area v, we matched the simulated data to the experimental data. For $v = 1$, no vesicle shape transformations are possible. Hence, we started with $v = 1.01$ and increased v in steps of 0.01 until we reached $v = 1.1$. We found the best agreement for a reduced area of $v = 1.05$ between the slope and y–intercept of linear fits of the simulated data (Fig. 4.4 F and G) and the experimental data (Fig. 4.4 H and I).

We found good agreement between bright and dim lobe diameters for the model and the experimental data (Figs. 4.4 F, H). The same holds for the relation between the neck diameters and average lobe diameters (Figs. 4.4 G, I). The slopes of the linear fits to the

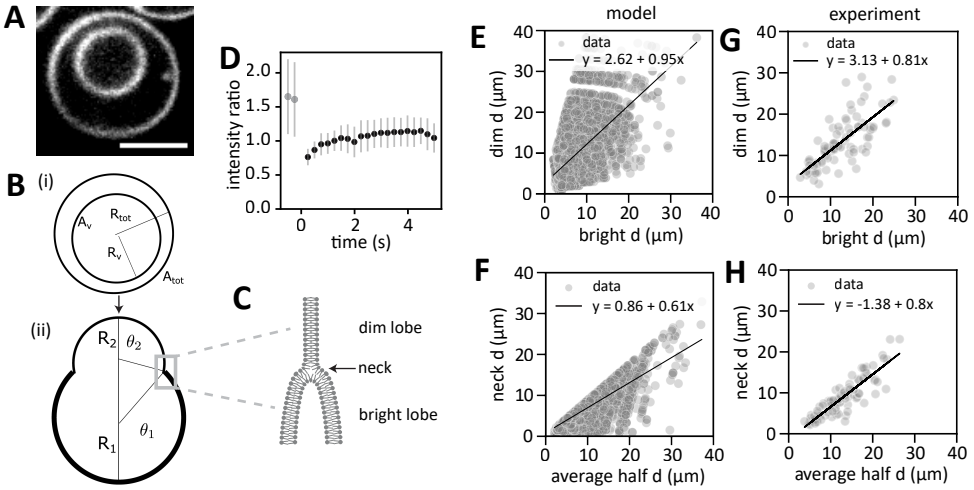

Figure 4.4: **Dumbbell shapes result from hemifusion and are determined by osmotic pressure and line tension.** (A) Confocal image of an eDICE GUV encapsulating another GUV (scale bar: 5 µm). Such nested GUVs were rare (~ 5-10 % of GUVs) but present at frequencies comparable with dumbbells. (B) Proposed mechanism for dumbbell formation. (i) One vesicle with radius R_{tot} encapsulates another vesicle with radius R_v. (ii) The inner GUV bursts and hemifuses with the membrane of the outer GUV. The shape of the resulting dumbbell is determined by membrane tension and line tension along the hemifusion line. (C) Proposed microscopic configuration of the dumbbell neck (grey rectangle in (B)), where one inner and one outer leaflet (dim lobe, top) join four concentric leaflets in the bright lobe (bottom). (D) FRAP measurement of the bright lobe of a dumbbell reveals a recovery of the normalized fluorescence intensity from ~ 2 (pre-bleach, $t < 0$) to ~ 1 (post-bleach, $t > 0$) within seconds. (E, F) The model predicted dumbbell shapes (relative lobe sizes, (E), and neck diameters relative to the dim lobe size, (F)) that quantitatively match the experimental data (G, H). Experimental and simulated data represent $N = 85$ and $N = 10^4$ dumbbell GUVs, respectively. Lines display linear fits (see legend for fit equations).

experimental and simulation data match nearly quantitatively, with slopes of 0.81 and 0.95 relating the dim and bright lobe diameters, and 0.8 and 0.61 relating the neck diameter and average lobe size. Moreover, the spread in the simulated data is similar to that of the experimental data.

The offset between the experimental and simulated data is likely an artifact of the way in which we select the size of the inner vesicle in the model: we choose a size from the same distribution as the outer GUV size. However, it is currently unclear how the inner vesicles actually form. It is therefore possible that the typical difference in total membrane area between inner and outer GUV is correlated in the experiments, thus resulting in an offset between the experimental and simulated data.

Based on the good agreement of the experimentally observed shapes with a model where line tension drives dumbbell formation, we concluded that membrane hemifusion is indeed sufficient to drive the formation of dumbbell GUVs. This conclusion was supported by the observation that the same geometrical correlations arose whether or not any actin was encapsulated in the GUVs (Supp. Fig. 4.25 A, B). The conclusion that membrane properties alone are sufficient to form dumbbell GUVs was further confirmed by the fact that they occur in eDICE GUVs irrespective of the composition of the inner aqueous solution, as well as by the fact that we occasionally found the similar dumbbells in GUV

samples produced by cDICE or gel-assisted swelling (Supp. Fig. 4.25 C, D).

Based on the strong agreement between the model predictions and experimental data, we now inverted the workflow and used the model to calculate the ratio between the line tension σ and osmotic pressure difference $P = P_{ex} - P_{in}$ between the outside and the inside of the vesicle, for the measured GUV dumbbell shapes. This ratio can be calculated directly from the neck radius R_n and opening angles θ_1, θ_2 (Eq. 4.8 in the Supplementary Information):

$$\frac{\sigma}{P} = \frac{1}{2} R_n^2 (\cot\theta_1 + \cot\theta_2). \tag{4.1}$$

We calculated this ratio for $N = 80$ dumbbell GUVs (Supp. Fig. 4.9), and found a mean value of 21 μm^2,which is around half of the measured value for a vesicle that undergoes budding due to phase separation of the membrane into different domains [379].

4.2.4 Arp2/3-nucleated actin networks recognize membrane curvature

Having established that dumbbell GUVs form by a mechanism that is independent of the presence of an actin cortex, we considered them a convenient template on which to study how membrane-nucleated actin cortices react to externally imposed variations in curvature. Due to the low number of dumbbell GUVs produced in one eDICE experiment, we could not directly compare dumbbells from a single experiment with good statistics. The following discussion will thus encompass GUVs from 7 different experiments and with several slightly different cortex compositions. We mainly used the human Arp2/3 isoform ArpC1B/C5L, but we obtain similar data for human ArpC1A/C5 and for porcine brain Arp2/3 (Supp. Fig. 4.26 A).

We found four different cortical actin distribution phenotypes in dumbbell shaped GUVs. First, actin could form a continuous and uniform cortex (Fig. 4.5 A). Second, we found GUVs where actin was enriched in a single patch at the GUV neck (Fig. 4.5 B). Third, actin formed a cortex throughout but was enriched in several distinct patches along the neck (Fig. 4.5 C). Fourth, the entire neck could be enriched in actin compared to the rest of the cortex (Fig. 4.5 D). These four phenotypes occurred at roughly the same frequency (around 25 % of N=27 dumbbells, Fig. 4.5 E). Importantly, we found that in cases where actin formed patches, there were always patches present at the neck. Rarely, we found a GUV which had bright actin patches both at the neck and elsewhere (Fig. 4.5 C). Preferential actin localization to the neck did not appear to be dependent on the presence of a continuous cortex: we found a few dumbbell GUVs where the cortical region was not significantly enriched in actin compared to the GUV lumen, but also for these, around 75 % exhibited actin enrichment at the neck (Fig. 4.5 F, N=27 in total). The likelihood that actin was enriched at a dumbbell neck depended on VCA concentration, with 88 % of dumbbells showing neck enrichment at 2 μM VCA, compared to 68 % in dumbbells at 6.5 μM VCA (Fig. 4.5 G, N=8 and 19 GUVs, respectively). This is consistent with our earlier observation that intermediate concentrations of VCA were most likely to produce deformed cortical actin patches (Fig. 4.2 I).

We quantified the degree of actin enrichment at the neck by comparing the maximum actin intensity in a line profile through the neck with that measured in a line profile through the dumbbell's axis of rotational symmetry (i.e., along the yellow lines in Fig. 4.5 H,

resulting line profiles in Fig. 4.5 I). The degree of actin enrichment in the neck was quite widely spread, ranging from no enrichment ($I_{max,\,neck}/I_{max,\,axis} \approx 1$) to an almost four-fold enrichment at the neck compared to the poles ($I_{max,\,neck}/I_{max,\,axis} \approx 4$), with a mean enrichment of $I_{max,\,neck}/I_{max,\,axis} = 2.2$ (Fig. 4.5 J, magenta points, N=27).

Importantly, in absence of actin, VCA itself did not preferentially accumulate at dumbbell necks (Supp. Fig. 4.26 B). Also, neck enrichment was only present in GUVs where actin was nucleated on the membrane with the help of Arp2/3 and VCA. In GUVs where actin spontaneously nucleated in the GUV lumen without these nucleating proteins, we observed no enrichment at the neck (Fig. 4.5 K and black points (N=21) in Fig. 4.5 J).

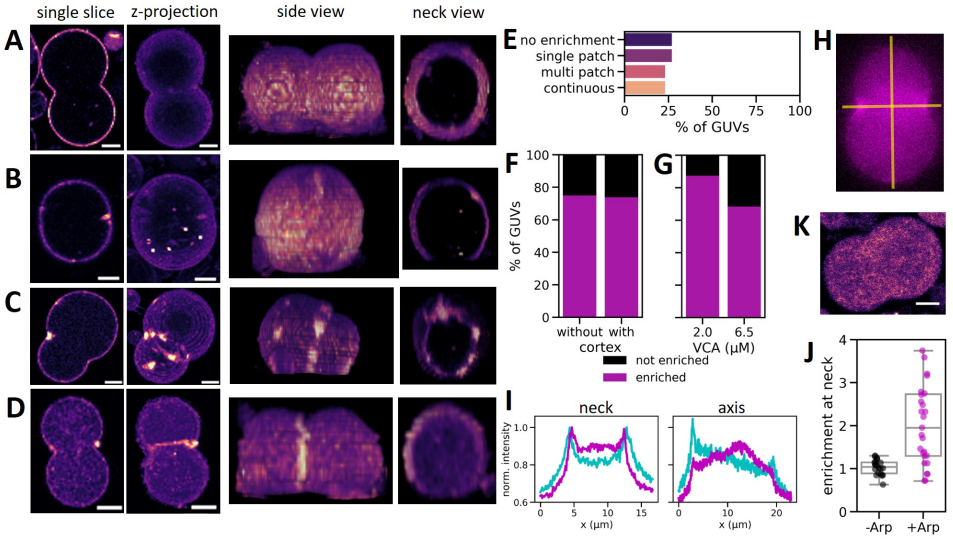

Figure 4.5: **Cortical actin networks preferentially localize to dumbbell necks, indicating curvature recognition.** (A-D) Dumbbell GUVs containing cortical actin showed four phenotypes: actin was evenly distributed (A), enriched in a single patch at the neck (B), enriched in several distinct patches around the neck (C) or enriched in the entire neck region (D). Columns show a single confocal slice, a maximum intensity projection, a sideview of the 3D-reconstructed z-stack, and a view through the neck section in the z-stack. Actin intensity is shown in false color (magma) for clarity. (E) Bar plot of actin enrichment patterns in dumbbell shaped GUVs, showing an even distribution over the four groups of (A-D) (N=27 dumbbell GUVs). (F) Bar plot shows that 75% of dumbbell shaped GUVs shows actin enrichment at the neck, both for GUVs with and without a continuous actin cortex (N = 23 and 4, respectively). (G) Bar plot shows that actin enrichment at the neck was slightly more common in GUVs with 2 μM VCA compared to 6.5 μM VCA (N = 8 and 19, respectively). (H) We quantified the amount of actin enrichment at the neck by comparing line intensity profiles across the neck versus the dumbbell's symmetry axis (yellow lines). (I) Line profiles of membrane (cyan) and actin (magenta) intensity along the neck and symmetry axis of the dumbbell GUV shown in (H), normalized to the maximum pixel value in the neck profiles. Peaks in actin and membrane intensity coincide at the neck, but not at the poles. (J) Box plot of the degree of actin enrichment at dumbbell necks in GUVs where actin nucleated spontaneously in the GUV lumen ('-Arp', black dots, N=21) or at the membrane with the help of Arp2/3 ('+Arp', magenta dots, N=27). (K) Confocal image of a dumbbell where actin polymerized spontaneously in the GUV lumen and does not localize to the neck region. Scale bars: 5 μm.

4.2.5 Analysis of membrane curvature associated with actin patches

Our data clearly demonstrates that Arp2/3-nucleated actin networks preferentially assemble at regions of negative membrane curvature, with the dumbbell-shaped GUVs providing a template for such curvature-sensitive actin enrichment. Conversely, it has previously been reported by Dürre et al. [141] that dendritic actin networks can generate concave actin-rich domains in GUVs, which in their case required the presence of capping protein. Interestingly, we also observed deformed actin-rich domains in GUVs containing 8 µM actin, but no capping protein (see example in Fig. 4.2 F). We note that the deformed actin-rich patches we observed in the absence of capping protein were broader than the tight patches reported by Dürre et al. [141], with actin distributed over a larger area both along the membrane and often extending into the GUV lumen (Supp. Fig. 4.27 C). In the presence of capping protein (Fig. 4.6 A, see white arrowheads), patches were small, strongly enriched in actin, and co-localized with regions of significant negative membrane curvature (Fig. 4.6 B, grey shaded regions), matching the observations of [141]. When we quantified the prevalence of such bent patches, we found at least one concave actin patch in 37 % of GUVs in the absence of capping protein, although the GUVs were more likely to have a

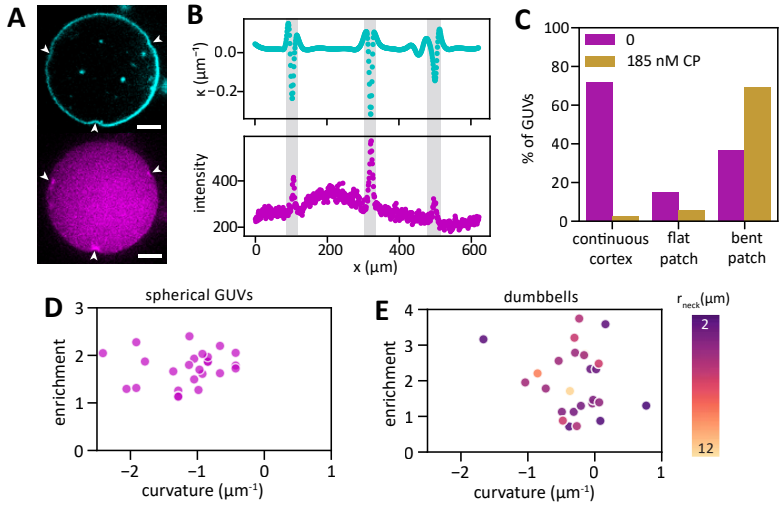

Figure 4.6: **Branched actin networks associate with curved membrane regions in both spherical and dumbbell GUVs.** (A) Confocal slice of a GUV co-encapsulating 8 µM actin, 50 nM Arp2/3, 2.6 µM VCA and 185 nM capping protein. Actin (magenta) is enriched in small, bright, concave patches (white arrowheads) colocalized with bent sections of the GUV membrane (cyan). Scale bars: 5 µm. (B) Line profiles of the local membrane curvature (top) and actin signal intensity (bottom) along the GUV membrane in (A) confirm that spikes in actin signal occur at locations of negative membrane curvature (grey shaded regions). (C) Bar plot of the fraction of spherical GUVs with a continuous cortex, flat cortical patches, or deformed cortical patches, for cortices without (magenta, N = 60 GUVs) or with (yellow, N = 36 GUVs) 185 nM capping protein. (D) Actin enrichment in bent patches as a function of patch curvature. (N = 37 patches in 20 separate GUVs containing 185 nM capping protein) (E) Actin enrichment at dumbbell necks as a function of curvature. The data is color coded to reflect the 3D structure of the neck: darker colors indicate tighter necks with smaller r_{neck} (see color bar on the right). N = 27 dumbbell necks.

continuous actin cortex (72 % of GUVs, see Fig. 4.6 C, N = 60 GUVs). When we added 185 nM capping protein, we observed a strong increase in the prevalence of concave patches, which is consistent with the study of Dürre et al. [141]: we now found concave patches in 69 % of N = 36 GUVs (Fig. 4.6 A and C) and continuous cortices or flat patches in only 3 or 5 % of GUVs, respectively (Fig. 4.6 C).

To study whether the actin-rich regions assembled preferentially at a specific curvature in the bent cortical actin patches observed in spherical GUVs and dumbbells, we quantified actin enrichment as a function of curvature. Concave patches in the presence of capping protein had peak curvatures around -1.1 μm^{-1} and showed consistent amounts of actin enrichment, with around 1.7-fold more actin intensity in the patch than in the surrounding cortex (Fig. 4.6 D). Dumbbell necks had similar negative curvatures across the neck, but the membrane curvature is positive along the neck, reducing the surface curvature to around -0.3 μm^{-1} (Fig. 4.6 E). Actin was enriched 1.2-fold on average, but enrichment varied widely, with no clear trends with respect to either the overall surface curvature, or the neck radius (color coded in Fig. 4.6 E). Note that the actin enrichments in Fig. 6 D and E are not quantitatively comparable, as the datasets were acquired on different microscopes. Furthermore, patches in spherical GUVs contained capping protein, whereas we studied actin enrichment at dumbbell necks in the absence of capping protein.

4.3 Discussion

To study the interplay of branched actin networks with lipid membranes, we developed a protocol that allows the reproducible and high-yield formation of GUVs with an actin cortex nucleated on the inner surface of the lipid membrane. Our method is facile, requires small sample volumes, and is fast enough to prevent premature actin polymerization during encapsulation. It is furthermore compatible with a range of widely used lipid compositions (Supp. Fig. 4.15) and actin-related proteins (Supp. Fig. 4.14), as well as different types and concentrations of density gradient media (Supp. Fig. 4.16 A). We note that commonly used density gradient media such as Optiprep and sucrose influence actin polymerization kinetics (Supp. Fig. 4.16 B-E), highlighting the need for careful experimental design and reporting when encapsulating cytoskeletal polymers.

The new method allowed us to systematically study the formation of actin cortices in GUVs as a function of the concentration of actin and the density of membrane-bound nucleators. We found that Arp2/3-nucleated cortices can grow in different regimes, depending on the amount of actin which is available in the GUV. This allows us to reconcile previous works, which reported that actin forms disconnected patches at low concentrations (3 μM [141]) but continuous actin shells at high concentrations (6.5 μM [119]). Our observations are also consistent with the known autocatalytic nucleation mechanism of actin by Arp2/3, which should produce isolated patches: New actin filaments will preferentially be assembled where Arp2/3 can be activated by nucleation promoting factors [381], i.e., at the membrane, and where an existing actin filament is available to act as a primer [344], i.e., in an existing patch. At low density or short filament length (promoted by capping protein), multiple primers generate independent networks. With increasing actin density and/or filament length, these independent networks can merge into a continuous cortex made of entangled filaments. Irrespective of the actin and VCA concentrations, we found variable phenotypes among GUVs, likely due to a significant variability in protein encapsulation

efficiency, which we demonstrated directly by quantitative microscopy and fluorescence correlation spectroscopy. We note that to form minimal actin cortices, the presence of additional regulatory proteins used in earlier works (profilin, gelsolin, ADF/cofilin and capping protein [119, 141]) was not required.

Under conditions where the actin cortex formed distinct patches, we found that the patches were often associated with flat or even negatively curved membrane sites. Thus, actin, membrane-bound VCA and Arp2/3 are sufficient to allow for curvature generation by actin on a network scale. We note that the exact formation process of such bent patches remains unclear. Colocalization of dense actin patches with concave sections of membrane could also arise as a consequence of preferential assembly of actin on curved membranes. If a concave section of membrane arises due to thermal membrane fluctuations, and triggers fast actin assembly at that site, actin may be able to trap the membrane in its concave shape. However, concave patches are, particularly in the presence of capping protein, very local membrane deformations that are not frequently observed in freely fluctuating GUVs in the absence of actin. The prevalence of such patches in the presence of actin and capping protein thus suggests that actin is actively contributing to the generation of negative membrane curvature.

Conversely, we found that the minimal dendritic actin networks also recognized membrane curvature: in GUV samples prepared by eDICE, we always observed some dumbbell-shaped GUVs where actin preferentially localized to the neck. These dumbbell GUVs form by a mechanism involving the hemifusion of two nested GUVs, whose combined shape is determined by an interplay of osmotic pressure across the membrane, and line tension in the hemifusion stalk. Again, we note that our data does not allow us to distinguish whether actin polymerizes on the membrane and subsequently accumulates at dumbbell necks by lateral diffusion, or whether net actin assembly is favoured where the membrane is bent. This distinction would shed light on the mechanism of curvature sensing and generation in branched actin networks, and should be followed up on in future works.

Our analysis of actin enrichment in spherical and dumbbell-shaped GUVs confirms that actin is found preferentially at curved surfaces, consistent with the concave actin patches reported in a previous reconstitution study [141]. Thus, actin, membrane-bound VCA and Arp2/3 are sufficient to allow for curvature sensing and potentially also generation of actin on a network scale, requiring none of the curvature generating or -sensing binding partners which are thought to mediate curvature sensitivity of actin networks in cells [46, 47, 159, 180, 350, 351].

Strikingly, actin enrichment happens on both patches and dumbbell necks, even though their 3D structures differ significantly, and we do not observe a specific preferred curvature: patches are symmetric, and the membrane curvature is negative in all directions, whereas surface curvature in dumbbells is negative across the neck, and positive along the neck. This complex 3D geometry, combined with the wide variation in protein encapsulation efficiencies, makes interpretation of the data difficult and may obscure weak preferences for actin assembly on specific membrane geometries. Furthermore, polydispersity in membrane tension will also impact the curvatures that actin networks can generate in spherical GUVs, as the GUV's membrane tension counteracts deformation of the membrane by actin.

In future studies, the curvature sensitivity of actin should be more systematically studied to gain insight into its mechanistic origins. In the cell-like environment of a GUV,

micropipette aspiration [382] or microfluidic deformation [160] may be used to impose curvature on GUVs with an existing cortex. However, variations in protein encapsulation efficiency will likely complicate the interpretation of such assays, making bulk approaches a useful tool for quantifying how exactly actin enrichment depends on surface curvature. 3D-structured supported lipid bilayers [383] may serve as substrates with tunable geometry, on which actin assembly could be observed live and on a variety of membrane geometries.

What exactly mediates the network-level curvature sensing remains elusive. It has been suggested that the competition of Arp2/3 and capping protein for actin monomers may be a driving factor behind the growth of curved actin networks [141], although it remains unclear how this mechanism would lead to membrane curvature generation. We found that capping protein was not strictly necessary for the formation of deformed actin patches in spherical GUVs, nor for curvature sensing happened robustly in dumbbell-shaped GUVs. On a molecular scale, the Arp2/3 complex itself has been shown to preferentially bind to actin filaments on their convex side, i.e., binding sites from which the mother filament bends away, are preferred [128]. This effect has been suggested to be amplified on the network level [128], which may help cells orient polymerization forces effectively in organelles like the lamellipodium. Curiously, if preferential assembly of actin on convex mother filaments occurs on an inwardly bent piece of membrane, we should expect curvature preference of Arp2/3 to drive nucleation of the densest networks at the sides of the bent membrane patch, rather than in its middle. If we imagine an initially flat membrane decorated with a branched cortex, where all the filament ends are anchored firmly on the membrane, local inward bending should splay apart the actin branches at the sides of this deformation (thus increasing nucleation there), while branches would be unaffected or slightly compressed at the tip of the deformation, hence lowering the nucleation rate there. By contrast, we observed that actin intensity peaked at the center of the concave membrane patches, which suggests that a different mechanism is behind the formation of such patches.

Membrane curvature sensing of actin networks in the absence of curvature-sensitive proteins to mediate actin-membrane interactions has so far, to the best of our knowledge, never been observed. We speculate that it may present a mechanism by which actin assembly can be robustly directed to actin-rich membrane structures with a micron-scale curvature, such as the early cytokinetic furrow [384], tunnel-like wounds [345], phagocytic cups [346], or when cell migration through physical constrictions imposes micron-scale inward curvatures on the plasma membrane. Actin enrichment at curved membrane sites has for instance been reported around the nucleus of immune cells squeezing through micrometric constrictions [348], osteoblasts in nanogrooves [385], and fibroblasts migrating on nanopatterned substrates with structure sizes of a few 100 nm in size [386]. While other proteins certainly contribute to this organization in live cells, our work raises the question whether an intrinsic curvature sensitivity of branched actin networks may help in making these associations more robust. Similarly, the curvature sensitivity of branched actin networks may potentially be used as a design strategy for building synthetic cells with an actin-based division machinery. Researchers in the growing field of bottom-up synthetic biology are pursuing different strategies to promote membrane constriction based on imposing membrane curvature by microfluidic trapping [148, 160] or addition of membrane-shaping proteins [184]. Our findings suggest that preferential assembly of actin cortices can be promoted in simpler systems, requiring fewer proteins and thus less careful

tuning of encapsulation stoichiometries or *in-vesiculo* transcription and translation.

4.4 Materials and Methods

4.4.1 Materials

Chemicals The following chemicals were purchased from Sigma-Aldrich: Tris(hydroxymethyl)aminomethane hydrochloride (Tris-HCl), potassium chloride (KCl), calcium chloride ($CaCl_2$), magnesium chloride ($MgCl_2$), Optiprep (Cat. # D1556-250ML), D-(+)-glucose, DL-dithiothreitol (DTT), Adenosine 5'-triphosphate magnesium salt (MgATP), Adenosine 5'-triphosphate disodium salt (Na_2ATP), proto-catechuic acid (PCA), proto-catechuate-3,4-dioxygenase (PCD), 3-(N-morpholino)propanesulfonic acid (MOPS), ethylene glycol-bis(β-aminoethyl ether)-tetraacetic acid (EGTA), ethylenediaminetetraacetic acid (EDTA), glycerol, β-casein, silicone oil (5 cSt), light mineral oil (BioReagent), and chloroform (Uvasol). n-decane (99% pure) was purchased from Arcos Organics. Chloroform, mineral oil and silicone oil were stored in a glove box with an ambient humidity below 1%.

Lipids All lipids were purchased from Avanti Polar Lipids: 1,2-dioleoyl-sn-glycero-3-phosphocholine (DOPC), 1,2-di- stearoyl-sn-glycero-3-phosphoethanolamine-N-[methoxy (poly- ethylene glycol)-2000] (DOPE-PEG2000), 1,2-dioleoyl-sn-glycero-3-[(N-(5-amino-1-carboxypentyl) iminodiacetic acid) succinyl] (DGS-NTA(Ni)), 1,2-dioleoyl-sn-glycero-3-phospho- ethanolamine-N-(Cyanine 5) (DOPE-Cy5). DOPC was purchased in powder form and dissolved in chloroform to 25 mg/mL, while the other lipids were purchased as a solution in chloroform and used as delivered. All lipids were stored in chloroform under argon at -20° C.

Proteins Rabbit skeletal muscle actin was purchased from Hypermol and labeled, stored and prepared for use as described in chapter 3. Purification and storage of SNAP-tagged murine capping protein was also described in chapter 3. The capping protein plasmid was a kind gift from David Kovar (University of Chicago).

The 10xHis-tagged VCA-domain of murine N-WASP (amino acids 400-501) was expressed in E. coli BL21 (DE3) cells and purified following ref. [115]. It was fluorescently labeled with AlexaFluor488 C5 maleimide (Molecular Probes) following the supplier's protocol. Excess dye was removed from the protein by buffer exchange on a PD MiniTrap gravity column with Sephadex G-25 resin. The plasmid was a kind gift from Kristina Ganzinger (AMOLF). Human Arp2/3 isoforms ArpC1B/C5L and ArpC1A/C5 purified from SF21 insect cells were kindly provided by Michael Way (Crick Institute). Details on their expression and purification are given in chapter 5. Arp2/3 was stored at a stock concentration of 1 μM in Arp2/3 storage buffer (20 mM MOPS pH 7.0, 100 mM KCl, 2 mM $MgCl_2$, 5 mM EGTA, 1 mM EDTA, 0.5 mM DTT, 0.2 mM ATP, 5% (v/v) glycerol). Arp2/3 protein complex from porcine brain was purchased from Hypermol EK (Cat. # 8413-01). The lyophilized protein was dissolved following the supplier's instructions and stored at 2.23 μM in Arp2/3 storage buffer. All proteins were snap-frozen and stored in small aliquots at -80° C.

4.4.2 GUV preparation

Buffers Buffer conditions were kept consistent between all experiments. Unless otherwise specified, the inner aqueous solution (IAS) inside the GUVs contained F-buffer (20 mM Tris-HCl pH 7.4, 50 mM KCl, 2 mM $MgCl_2$, 1 mM DTT, 0.5 mM MgATP) supplemented with 0.5 µM PCD and 10 mM PCA to minimize photobleaching [387], as well as 6.5 % V/V Optiprep to increase the mass density. We reduced the Optiprep concentration as compared to the cDICE method [138] as we found that it substantially impacts actin polymerization kinetics, while eDICE production of GUVs was effective over a range of Optiprep concentrations (Supp. Fig. 4.16). The IAS osmolarity was 168 mOsm/kg in all experiments and was unchanged by the addition of proteins, as measured using a freezing point osmometer (Osmomat 010, Gonotec, Germany).

The outer aqueous solution (OAS), in which the GUVs were first produced, contained 190 mM glucose (200 mOsm/kg). Immediately after GUV formation, we added a solution of 40 mM Tris-HCl pH 7.4 and 90 mM glucose (182 mOsm/kg), to stabilize the pH outside the GUVs and reach final buffer conditions of 10 mM Tris-HCl pH 7.4 and 170 mM glucose, with an osmolarity of 189 mOsm/kg to slightly deflate the GUVs and increase the available excess membrane area by an average of 7.6 % [388].

Lipid-in-oil solution Lipid stocks were prepared in chloroform solution. 94.985 % DOPC was mixed with 0.01 % DOPE-PEG2000 to increase GUV yield following [138], 5 % DGS-NTA(Ni) to recruit VCA, and 0.005 % DOPE-Cy5 for fluorescent visualization (molar percentages). Mixtures with a total lipid content of 1.7 µmol were dried under a gentle N_2 stream in a screw cap glass vial for each experiment and used within a day. This corresponds to a final lipid concentration of ~ 0.25 mmol/L in the oil phase. The vials with dried lipid films were then transferred into a glovebox under an inert environment containing <1 % environmental humidity, to promote a reproducible and high yield of GUVs [138]. In the glovebox, silicone oil and mineral oil were combined in a volumetric ratio of 5.3:1.2 and thoroughly mixed by vortexing. Dried lipid films were dissolved either in 415 µL chloroform, or they were dissolved in 50 µL chloroform and subsequently diluted with 400 µL n-decane. Under continuous gentle vortexing, 6.5 mL of the oil mix was slowly added to each lipid vial. The vials were sealed tightly with teflon tape and parafilm, removed from the glove box, and sonicated on ice in a bath sonicator for 15 minutes. The lipid-in-oil solutions were stored on ice and used for GUV formation within 30 minutes.

GUV formation and handling GUV preparation and imaging was performed at room temperature (24 ± 1° C). We used a home-built spinning chamber setup equipped with a spinning table and 3D-printed chamber described in [138] to prepare GUVs. We first set the spinning chamber to rotate at 2000 rpm (corresponding to a motor voltage of 14.5 V on our device), added 700 µL of OAS, and carefully layered on 5 mL of the oil solution. 1 mL of oil solution was set aside in a 2 mL Eppendorf tube. We then created droplets of IAS in the 1 mL oil solution by manual emulsification. 25 µL IAS were prepared on ice, adding G-actin last. The IAS was then pipetted into the 1 mL oil solution and emulsified by scratching the Eppendorf tube vigorously over an Eppendorf holder 14 times. This simple procedure allows us to form droplets within < 15 s. Note that a recent work has shown that droplets

can also be prepared by vigorous pipetting [139]. The emulsion was immediately pipetted into the spinning chamber and centrifuged for 3 minutes to form GUVs.

After GUV formation, the spinning chamber was stopped by slowly turning down the motor voltage, and excess oil was removed by careful pipetting. 233 µL of outer buffer were added to the remaining aqueous phase to stabilize the OAS pH, and the GUVs were concentrated by resting the spinning chamber at a 45° angle for 10 minutes. GUVs were retrieved using a cut-off 200 µL pipet tip to minimize shear forces during transfer. The samples were finally diluted threefold in imaging buffer (10 mM TrisHCl pH 7.4, 165 mM glucose).

4.4.3 Microscopy

Image acquisition GUVs were observed either in ibidi 18-well µ-slides (Cat. # 81817) or in chambers created by mounting silicone spacers (Sigma Aldrich, Cat # GBL665106) on # 1.5 coverslips (Superior Marienfeld, Cat. # 0107222). The wells were passivated by incubating with a 0.1 mg/mL β-casein solution in 10 mM Tris-HCl pH 7.4 for at least 15 min, rinsed with MilliQ water and dried under N_2 flow. After GUV addition, we closed the chambers to prevent solvent evaporation and keep the osmotic deflation of the GUVs constant. Ibidi wells were closed with the appropriate lid, which effectively prevents evaporation over several days. Chambers made from silicone spacers were sealed from the top with a glass coverslip, affixed to the spacer with vacuum grease (Dow Corning high vacuum silicone grease, Sigma-Aldrich Cat. # Z273554).

Confocal images were acquired either on an inverted Olympus IX81 confocal spinning disk microscope equipped with 491 and 640 nm CW lasers, a 100x oil immersion objective (UPlanSApo, WD 0.13 mm, NA 1.4) and an EM-CCD Andor iXon X3 DU897 camera, or on an inverted Leica Stellaris 8 laser scanning confocal microscope equipped with a white light laser, a 63x glycerol immersion objective (HC PL APO, WD 0.3 mm, NA 1.2) and HyDS and HyDX detector operated in photon counting mode. Z-stacks were acquired with a 1 µm step height unless otherwise specified. Further imaging settings are listed in Supplementary Table 4.2.

Quantitative confocal microscopy Quantitative confocal microscopy to determine the actin encapsulation efficiency in GUVs was performed on the Leica Stellaris 8 LSCM using the 63x glycerol immersion objective and the HyD S detector operated in counting mode. We performed all measurements in one day and in a single ibidi 18-well µ-slide to avoid artefacts from variations in coverslip thickness. To ensure that images were always taken at the same height above the coverslip surface, we first acquired a 256x256 pixel xz-image (Fig. S3 A). We subsequently acquired an image of 2048x2048 pixels 7 µm above the coverslip surface (Fig. S3 B). For each GUV sample, we acquired at least 10 fields of view, corresponding to > 1000 GUVs per condition. To convert fluorescence intensity to absolute actin concentrations, we obtained calibration data by imaging bulk F-actin solutions at a range of concentrations under identical imaging conditions (Fig. S3 H, I)

FRAP experiments FRAP experiments to determine membrane continuity for dumbbell-shaped GUVs were performed on the Leica Stellaris 8 LSCM with a 63x glycerol immersion objective. GUV membranes were labeled with 0.05 % mol/mol DOPE-Cy5. We imaged the

equatorial section of dumbbell GUVs at high zoom (typically 9x) and with a 512x512 pixel field of view. The white light laser was operated at 658 nm and at 8 % laser power with a pixel dwell time of 0.95 µs during acquisition of the pre- and post-bleach images. Bleaching was performed on a rectangular ROI, which encompassed the bright lobe of a dumbbell and was thus different in size and aspect ratio for each vesicle. The ROI was bleached using four laser lines (643, 648, 653 and 658 nm) operated at 100 % intensity each, to efficiently bleach the membrane within a single frame (= 249 ms). We acquired three images before bleaching the GUV at 4 fps. After bleaching, we acquired 50 frames at 4 fps, followed by another 50 frames at 2 fps, to capture membrane dynamics for 38 seconds.

Since dumbbell GUVs were in suspension and hence freely diffused during the course of imaging, we extracted line profiles for each frame individually, tracing the dumbbell membrane around first the bright and then the dim lobe, using the ImageJ 'plot profile' function [340]. Time-dependent intensity ratios $I_{\mathrm{bright}}/I_{\mathrm{dim}}$ were extracted from the profiles using a custom-written python script.

4.4.4 Image analysis

Quantitative analysis of actin encapsulation in GUVs Quantitative confocal microscopy images were analyzed in an automated procedure. First, we located GUVs in the membrane images using the Template Matching module in the open source DisGUVery toolbox [389] (See Fig. 4.20 C). The images were preprocessed by smoothing with a filter size of 15 and edge enhancement with a filter size of 45. A representative image of a GUV membrane was used as a template, and matches with a matching index of above 0.4 were detected with 40 size steps ranging from 0.3 to 2 times the template size. Since membrane labeling was deliberately kept low to avoid any spectral crosstalk artefacts, we could only detect 30-60 % of GUVs in any given image, but we observed no systematic bias in which GUVs were detected or missed. Next, we extracted the average actin fluorescence in the GUVs with a custom python script. We created a circular ROI of radius $R = d_{\mathrm{bb}}/2$, where d_{bb} is the size of the bounding box detected by the template matching GUV detection (Fig. 4.20 D,E). We then extracted the pixel intensities for the actin signal within the ROI and averaged these over the ROI for each GUV (Fig. 4.20 F). Resulting intensity distributions were converted to actin concentrations by means of a calibration curve determined for bulk actin networks (Fig. 4.20 H,I). For these bulk networks, we averaged the mean pixel intensity in at least 5 images of 2048x2048 px per condition. A proportional fit of measured actin signal vs nominal actin concentration in the form $I_{\mathrm{act}}(c_{\mathrm{act}}) = A \cdot c_{\mathrm{act}}$ was computed using *numpy* least squares fitting, and the resulting proportionality constant was used to convert actin intensity in GUVs into actin concentrations.

Classification of actin cortex phenotypes Cortex phenotypes for each GUV were categorized manually from confocal z-stacks in one of four categories: *'Inside patch':* GUV has one or more actin patches in the lumen. *'Concave patch':* GUV has one or more actin patches which visibly protrude into the GUV lumen and/or colocalize with a section of membrane that is locally bent inwards. *'Flat patch':* GUV has one or more actin patches on the membrane, which do not colocalize to a concave actin patch and do not encompass the entire GUV. *'Continuous cortex':* GUV has an enhanced actin signal on the membrane

compared to the lumen throughout the membrane. Dumbbell-shaped GUVs were excluded from the analysis of all GUVs and considered separately (below).

Dumbbell GUV shape analysis The size and shape of dumbbell GUVs were extracted manually from confocal z-stacks using ImageJ [340]. We fitted circular ROIs to each lobe in the equatorial slice of the dumbbell and measured the lobe diameters. We then drew a line profile across the neck of the dumbbell and extracted the distance between the two peaks in membrane signal on either side of the neck opening. Geometric features of the dumbbells (bright-to-dark size ratio, average lobe diameter, neck-to-lobe ratio) were computed from the lobe sizes and neck diameters in python.

Classification of actin localization on dumbbell GUVs Actin localization in dumbbell necks was classified manually in confocal z-stacks acquired on the Stellaris 8 LSCM. The dumbbell vesicles were first visually inspected to assess whether there was visible local actin enrichment anywhere on the membrane. It was further noted whether enrichment occured in the neck region. If so, a maximum intensity projection of the GUV was generated in ImageJ [340]. On the basis of visual inspection of the projection, we classified the GUV as possessing one or more than one actin patch at the neck (*single patch* or *multi patch*), or enrichment in the entire neck region (*continuous enrichment*).

Quantification of membrane curvatures Membrane curvatures in concave actin patches in spherical GUVs containing capping protein, or around dumbbell necks were assessed using the ImageJ plugin *Kappa - Curvature analysis* (version 2.0.0) [390]. For each patch, we drew a 5 px wide ROI around the curved membrane section (typically 5-10 µm long), and used Kappa to extract the membrane curvature in the $x-y$-plane in this region, based on a B-splines fit to the membrane contour. The full curves were exported to a custom python script, to compute the signed curvature along the κ_1 in the $x-y$-plane. The surface curvature was calculated as $\kappa = \kappa_1 + \kappa_2$, where κ_2 is the curvature in the orthogonal direction along the membrane. For actin patches on spherical GUVs, we assumed $\kappa_1 = \kappa_2$ to reflect a rotationally symmetric actin patch. For dumbbell necks, κ_2 was calculated from the dumbbell's neck diameter d_{neck} as $\kappa_2 = (d_{\text{neck}}/2)^{-1}$. Note that the two curvatures have the same sign in concave patches, but opposite signs in the necks of dumbbell vesicles. The curvatures measured here are limited by the resolution of confocal fluorescence microscopy, as well as by the segmentation. Local curvatures, particularly at the dumbbell neck, may be significantly higher than we can measure with optical methods.

Quantification of actin localization Actin localization at membrane necks was quantified using fluorescence line profiles extracted in ImageJ. We compared intensities in two line profiles, one through the region of interest (i.e., across the dumbbell neck) and one reference region (i.e., a line along the rotational symmetry axis of the dumbbell). Line profiles of 8 px width were extracted in ImageJ and exported to a custom python script to determine the degree of enrichment as the ratio between the maximum actin intensity in the neck region, divided by the maximum actin intensity in the reference region.

Code availability

The python scripts used for image and data analysis in this chapter, along with a script to generate the simulated dumbbell GUV shapes, is available on GitHub: https://github.com/BioSoftMatterGroup/actin-curvature-sensing

Acknowledgements

We are grateful to Jeffrey den Haan and Erik van Lagen for protein purification. Michael Way and Miroslav Mladenov are thanked for the kind gift of purified human Arp2/3, and we thank Guillaume Romet-Lemonne and David Kovar for the plasmids of profilin and mDia1 and capping protein, respectively. Stephan Grill and Lutz Vogeley are thanked for the kind gift of nonmuscle myosin-2. We thank Kristina Ganzinger for kindly providing the VCA plasmid, as well as inspiring discussions about GUV formation and actin cortex biochemistry. Thank you to Jérémie Capoulade and Michal Shemesh for useful discussions and instruction in quantitative confocal microscopy and FCS, and to Heike Glauner (Leica) for help with FCS data analysis. Bálász Antalizc is thanked for his help with the pyrene fluorescence measurements, which we were kindly allowed to do in Kristina Ganzinger's lab. We acknowledge financial support from The Netherlands Organization of Scientific Research (NWO/OCW) Gravitation program Building A Synthetic Cell (BaSyC) (024.003.019).

4.5 Supplementary Information

4.5.1 Theoretical model of equilibrium shapes of dumbbell vesicles

As described in the main text, we assume that a dumbbell GUV is created of two vesicles, a larger outer one containing a smaller inner one, of which the inner one has burst, resulting in a shape with two lobes: one with a single and the other with a double membrane bilayer. Here we study the shape of these dumbbells. Our approach is motivated by earlier theoretical work on domain-induced budding of vesicles composed of phase-separating lipid mixtures [377–380]. First we explain why the dumbbell shape can be described by two spherical caps, and second we explain how we infer the ratio between line tension and vesicle pressure from the shape of the GUV.

The shape energy of a GUV with negligible bending energy is given by [378]:

$$\mathcal{H} = \oint_{\partial 1} \sigma \, \mathrm{d}l + \Sigma^{(1)} A^{(1)} + \Sigma^{(2)} A^{(2)} + PV \, . \tag{4.2}$$

The first term in Eq. (4.2) describes the energy associated with the perimeter of the interface between the double bilayer surface and the single bilayer surface. Therefore, the integral runs along the edge of this interface, where σ is the line tension. The second and the third term correspond to the membrane tension, where A_i is the surface area and $\Sigma^{(i)}$ is the membrane tension of domain i, with $i = 1$ for the double membrane and $i = 2$ for the single membrane domain. The fourth term introduces a volume constraint, where P is the pressure difference $P = P_{\mathrm{ex}} - P_{\mathrm{in}}$ between the outside and the inside of the GUV and V is the volume of the GUV.

We consider the limiting case where the energy associated with the line tension and the volume constraint dominate the system, and thus the contribution of the bending energy

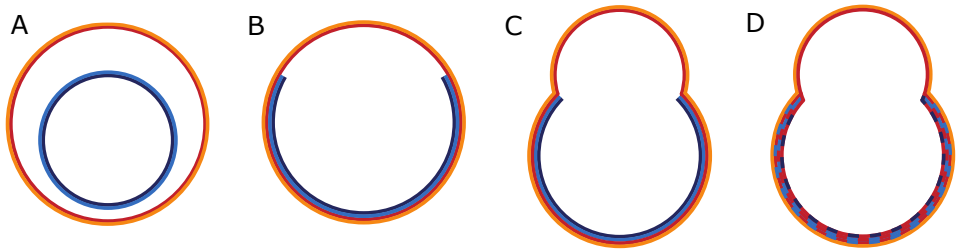

Figure 4.7: **Schematic of dumbbell vesicle formation from nested GUVs.** (A) During GUV formation, nested vesicles are created. The leaflets of the outer GUV are shown in orange (outer) and red (inner) and the leaflets of the inner GUV are shown in blue (outer) and black (inner). (B) After the inner vesicle bursts, it leaks its entire volume into the GUV. (C) The membrane of the inner vesicle merges along its edge with the outer GUV. (D) The membranes of the inner vesicle and the outer GUV undergo hemifusion. The lipids within the same leaflet mix. At the interface, where the double bilayer and single bilayer meet, a line tension emerges that leads to the formation of a dumbbell vesicle.

is negligible in Eq. (4.2). This assumption can be justified by estimating the various energy contributions based on typical parameter values. For simplicity, we consider a sphere with radius $10\,\mu$m, which is the limiting case of a dumbbell with equal cap sizes and maximum opening angles. We assume a pressure difference of P $0.02\,\mathrm{N m^{-2}}$ [379], a membrane tension of $\Sigma \sim 10^{-7}\,\mathrm{N m^{-1}}$ [379] (neglecting differences between the two halfspheres), a line tension of $\sigma \sim 1\,\mathrm{pN}$ [379] and a bending rigidity of $\kappa \sim 10^2\,\mathrm{pN nm}$ [379]. Using Eq. (4.2) and the bending energy of two half spheres, one with a double bilayer lobe and one with a single bilayer lobe ($8\pi\kappa + 4\pi\kappa$), we get: $E_{\mathrm{pressure}} \sim 80\,\mathrm{nN nm}$, $E_{\mathrm{tension}} \sim 100\,\mathrm{nN nm}$, $E_{\mathrm{line}} \sim 60\,\mathrm{nN nm}$ and $E_{\mathrm{bending}} \sim 4\,\mathrm{nN nm}$. Since the bending energy is over an order of magnitude smaller than the other contributions, we can neglect the energy contribution of membrane bending.

Since dumbbell shapes are axisymmetric, we can parameterize them by a (trivial) rotation angle ϕ about the symmetry axis, and a contour length s along their shape, see Fig. 4.8. The shape and local orientation of the contour can then be described by the radial position $r(s)$ and the tangent angle $\Psi(s)$. These parameters satisfy the geometric constraint $\dot{r} = \cos\Psi$, with a dot denoting the derivative with respect to the arc length s. To enforce this constraint, we add a term $\gamma(\dot{r} - \cos\Psi)$ to the shape energy, where γ is a Lagrange multiplier. We can then write the shape energy as the integral over an energy density

$$\begin{aligned}\mathcal{H} = \oint_{\partial 1} \sigma \,\mathrm{d}l + 2\pi \int_{s_0}^{s_1} \left[\Sigma^{(1)} r(s) + \frac{1}{2} P r^2 \sin\psi(s) + \gamma\,(\dot{r} - \cos\psi(s))\right] \mathrm{d}s \\ + 2\pi \int_{s_1}^{s_2} \left[\Sigma^{(2)} r(s) + \frac{1}{2} P r^2 \sin\psi(s) + \gamma\,(\dot{r} - \cos\psi(s))\right] \mathrm{d}s. \qquad (4.3)\end{aligned}$$

We can minimize the energy density within each domain, which gives us the following shape equations [378]:

$$\begin{aligned}0 &= \frac{1}{2} P r^2 \cos\psi + \gamma \sin\psi, \\ \dot{\gamma} &= \Sigma^{(i)} + P r \sin\psi, \\ \dot{r} &= \cos\psi. \qquad (4.4)\end{aligned}$$

Moveover, we get a matching condition at the boundary ($s = s_1$), where there is a jump in the tangent angle ψ:

$$\lim_{\varepsilon \downarrow 0} [\gamma(s_1 + \varepsilon) - \gamma(s_1 - \varepsilon)] = \sigma. \tag{4.5}$$

The spherical caps can be parametrized by $\psi(s) = s/R_i$ and $r(s) = R_i \sin(s/R_i)$. We solve the first line of Eq. (4.4) for γ, using the parametrization of the spherical caps, take the derivative with respect to s and equate the resulting equation with the second line of Eq. (4.4). As a result, we find an equation for the pressure difference P and the Lagrange multiplier γ.

$$p = -\frac{2\Sigma^{(i)}}{R_i}, \tag{4.6}$$

$$\gamma = -\frac{1}{2} p R_i^2 \sin\psi \cos\psi = \sigma^{(i)} R_i \sin\psi \cos\psi \tag{4.7}$$

Hence, if P and γ fulfill Eqs. (4.6)-(4.7), the dumbbell shape necessarily fulfills Eqs. (4.4)-(4.5). Therefore, the dumbbell shape is a minimal energy shape (with the boundary condition defined through Eq. (4.5)), as previously noted by Baumgart et al. [379] and Allain and Ben Amar [380].

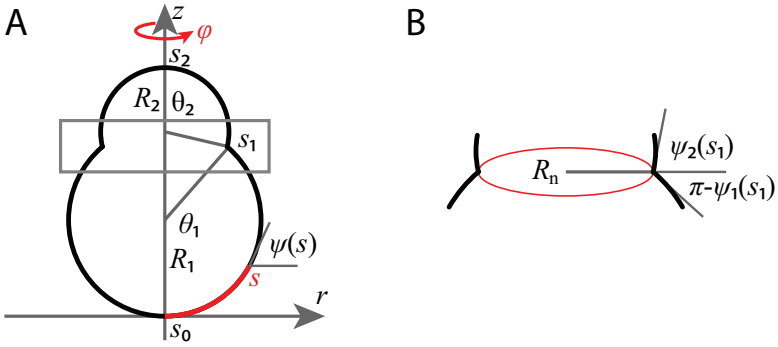

Figure 4.8: **Geometry of dumbbell GUVs.** (A) Parametrization of the dumbbell shape by the arc length s (red) along the (rotationally symmetric) membrane contour. We take $s_0 = 0$ at the south pole of the dumbbell. The local orientation of the membrane is given by the angle $\psi(s)$. The bright and dim lobes are spherical caps characterized by their radii R_1 and R_2 and their opening angles at the neck, θ_1 and θ_2. The neck is located at $s = s_1$, and the north pole at $s = s_2$. (B) Zoom-in to the dumbbell neck region (grey rectangle, panel A). The line tension of the hemifusion line (red) determines the neck radius R_n. Dumbbell lobes connect to the plane of the neck at angles $\pi - \psi_1$ and ψ_2, respectively.

Eq. (4.6) is the well-known Laplace pressure, relating the pressure difference across the membrane to the membrane's surface tension. Eq. (4.7) gives us the value of the Lagrange multiplier γ in each domain. The two domains meet at the neck, where $R_1 \sin\theta_1 = R_2 \sin\theta_2 = R_n$. Using the expressions for γ in the matching condition, Eq. (4.5), with $\psi_i = \theta_1$ and $\psi_2 = \pi - \theta_2$, allows us to calculate the ratio between the line tension σ and the pressure gradient P [379, 391]:

$$\frac{\sigma}{P} = \frac{1}{2} R_n^2 (\cot\psi_1 - \cot\psi_2) = \frac{1}{2} R_n^2 (\cot\theta_1 + \cot\theta_2) \tag{4.8}$$

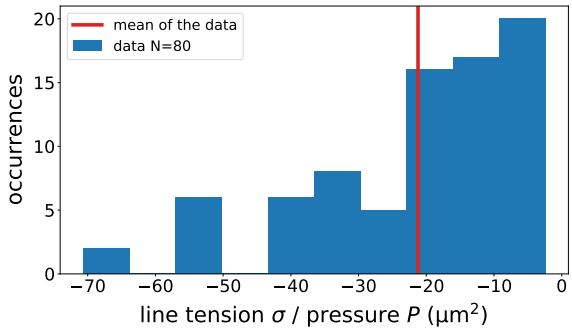

Figure 4.9: Histogram of the line tension σ divided by the GUV pressure difference P calculated from the measured GUV dumbbell shapes (main text Fig. 4 G,H), according to Eq. (4.8).

Fig. 4.9 shows the histogram of the ratio σ/P (blue) calculated from the measured GUV dumbbell shapes (main text Fig. 4.4 G,H), according to Eq. (4.8). Here, the opening angles of the bright and dark lobe of the dumbbell GUV, θ_1 and θ_2, are calculated from the diameters of the bright and dark lobe and the neck diameter of the GUV. The mean of the histogram (red) is at -21 μm^2, which is about half of the measured value for a vesicle that undergoes domain-induced budding (-49 μm^2) [379].

We note that the value of the ratio σ/P is negative because the (positive) pressure within the vesicle surmounts the pressure in the environment so that the pressure difference P is negative.

4.5.2 Modeling the formation of dumbbell shaped GUVs

In the model, the total membrane area (the surface area plus excess membrane area) of the bursting vesicle A_v equals the surface area of the double bilayer membrane lobe A_1, i.e. $A_v = A_1$. In addition, the GUV's total membrane area A_{tot} minus the surface area of the bursting lobe A_1 equals the surface area of the single bilayer membrane lobe A_2, i.e., $A_{tot} - A_1 = A_2$ (Fig. 4 B). We calculated the radius of the bright lobe, R_1, from the total membrane area of the bursting vesicle, A_v,

$$R_1(\theta_1, A_v) = \sqrt{\frac{A_v}{2\pi(1-\cos\theta_1)}}, \tag{4.9}$$

where θ_1 is the opening angle of the spherical cap. Similarly, we calculated the radius of the dim lobe, R_2,

$$R_2(\theta_2, A_v, A_{tot}) = \sqrt{\frac{A_{tot} - A_v}{2\pi(1-\cos\theta_2)}}, \tag{4.10}$$

where θ_2 is the opening angle of the spherical cap. The two caps are connected at a circular interface with neck radius

$$R_n = R_1 \sin\theta_1 = R_2 \sin\theta_2 \quad \longrightarrow \quad R_2 = R_1 \frac{\sin\theta_1}{\sin\theta_2}. \tag{4.11}$$

By equating Eq. (4.10) with Eq. (4.11) we obtain

$$\cos\theta_2(\theta_1, A_\mathrm{v}, A_\mathrm{tot}) = \frac{A_\mathrm{v}}{A_\mathrm{tot} - A_\mathrm{v}}(1+\cos\theta_1) - 1\,. \tag{4.12}$$

The total volume of the GUV is given by adding up the volumes of the spherical caps of the bright and dark lobe

$$\begin{aligned} V(R_1, R_2, \theta_1, \theta_2) = {} & \frac{\pi}{3} R_1^3 (2+\cos\theta_1)(1-\cos\theta_1)^2 \\ & + \frac{\pi}{3} R_2^3 (2+\cos\theta_2)(1-\cos\theta_2)^2\,. \end{aligned} \tag{4.13}$$

By substituting Eqs. (4.9), (4.10) and (4.12) in Eq. (4.13), we got an expression for the volume $V = V(\theta_1, A_\mathrm{tot}, A_\mathrm{v})$ of the GUV that only depends on θ_1, A_tot and A_v.

To connect the shape description derived above to the experiments, we calculated the geometrical correlations between the diameter of the bright and dim lobes from experimental data. First, we assumed that in the model, similar to the experiments, GUVs are created with excess membrane area that allows the GUV to change shape at constant volume. Therefore, the total membrane area A is larger than the surface area $A_\mathrm{s} = 4\pi R^2$, where R is the radius of the spherical GUV. In this case, the reduced area is given by $\nu = A/A_\mathrm{s}$, which varies across GUVs. Next, we sampled two radii $R_\mathrm{tot}, R_\mathrm{v}$ from the measured diameter distribution of GUVs (Fig. 1 C) that represent the sizes of the outer vesicle and the enclosed vesicle, respectively. From the radii $R_\mathrm{tot}, R_\mathrm{v}$ and the reduced areas $\nu_\mathrm{tot}, \nu_\mathrm{v}$ we calculated the GUV total membrane area,

$$A_\mathrm{tot} = 4\pi R_\mathrm{tot}^2 \nu_\mathrm{tot}\,, \tag{4.14}$$

and the total membrane area of the enclosed vesicle,

$$A_\mathrm{v} = 4\pi R_\mathrm{v}^2 \nu_\mathrm{v}\,. \tag{4.15}$$

We calculated the initial (spherical) GUV volume $V^* = 4\pi R_\mathrm{tot}^3/3$ and set V^* equal to the dumbbell volume obtained from Eq. (4.13),

$$V(\theta_1, A_\mathrm{tot}, A_\mathrm{v}) = V^*\,. \tag{4.16}$$

We solved Eq. (4.16) for θ_1 by using the values of A_tot and A_v from Eqs. (4.14) and (4.15). With the value of θ_1 and the values of A_tot and A_v we could calculate the remaining quantities, where we determine θ_2, R_1, R_2 and R_n from Eqs. (4.12), (4.9), (4.10) and (4.11), respectively. Together, θ_1, θ_2, R_1, and R_2 define the GUV dumbbell shape.

4.5.3 Optimization of the eDICE method

While robust encapsulation of actin in GUVs in G-buffer has been demonstrated using cDICE [138], we found that the yield in GUVs dropped dramatically when we tried to encapsulate actin in the more physiologically relevant F-buffer, irrespective of actin filament length (Fig. 4.10 A-C).

Rapid assembly of lipids on the droplet surface in the first stage of GUV formation (Fig. 4.1 A) has been found to be key for successful actin encapsulation [138, 370]. Indeed,

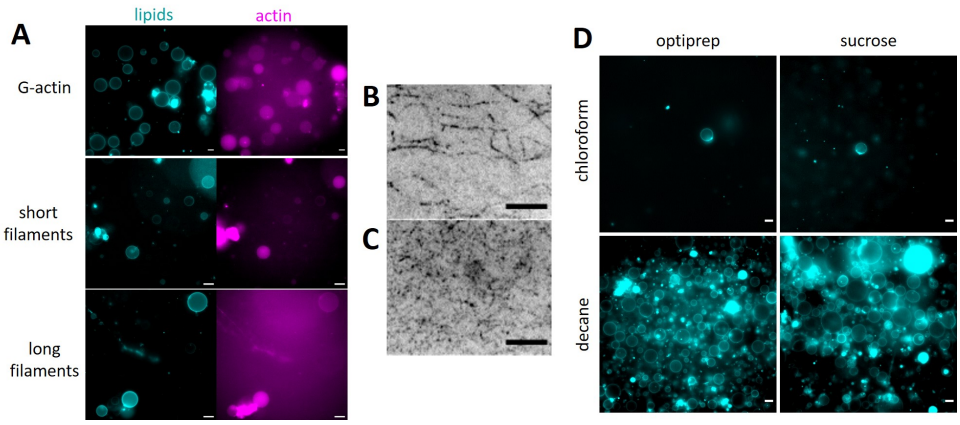

Figure 4.10: **Actin encapsulation in GUVs by cDICE and eDICE.** (A) Epifluorescence images of G-actin (top row), short actin filaments (middle row) and long actin filaments (bottom row) encapsulated in GUVs by cDICE. While encapsulation of 4.4 μM actin in buffers with physiologically high ionic strength was possible using cDICE, the yield of GUVs was severely reduced compared to encapsulation of actin in low ionic strength G-buffer. This was true independent of the length of encapsulated actin filaments. Actin is shown in magenta, membranes in cyan. (B, C) TIRF images of the actin filaments encapsulated in (A), shown in inverted gray scale for clarity. Long filaments (B) were formed by polymerizing actin at room temperature for 1 hr in the presence of phalloidin at a 1:1 molar ratio, and had a typical length of ~ 10 μm. Short filaments (C) were produced in the same way and subsequently broken by mechanical agitation, pipetting the sample 20 times (200 μL pipet tip), and were on average ~ 2 μm long. (D) Widefield images of GUVs encapsulating F-actin in F-buffer supplemented either with 18 % optiprep (left column) or 200 mM sucrose (right column). GUVs were prepared by eDICE on the same day and under identical conditions, using an oil phase where lipids were either resuspended in 415 μL chloroform (top row) or a mixture of 50 μL chloroform and 400 μL decane (bottom row). Images show the membrane fluorescence. Scale bars: 10 μm.

we found by pendant drop tensiometry that actin interacts with oil-water interfaces when lipids are present in the oil phase (Supp. Fig. 4.11). Surprisingly, the association of actin and lipids separately at the interface was slow[1], but association of both at the same time was much more rapid. This suggests that actin may rapidly coat the surface of emulsion droplets travelling through the oil phase, which would jeopardize zippering of the two monolayers to form a bilayer. This finding emphasizes the need to use lipid-in-oil suspensions which assemble quickly at the droplet surface.

It has previously been shown that lipids form aggregates by the 'ouzo effect', and such aggregates have been predicted to increase the rate of lipid adsorption at droplet interfaces [371]. The ouzo effect occurs when a solute (in this case lipids) is dissolved in a binary mixture of two solvents that are miscible among each other, but only one is a solvent for the solute [398]. Why this effect should be stronger in lipids prepared with decane compared to chloroform, however, remains unclear, since both are good solvents for lipids [371]. Nonetheless, Van de Cauter et al. showed that lipid monolayer assembly was significantly sped up when the oil phase was prepared by first dissolving the dried lipids in decane

[1]The fact that actin does adsorb to interfaces is not in itself surprising: many proteins are known to have an affinity for air-water and oil-water interfaces [392, 393] and may even form rigid films there [394, 395]. Both G- and especially F-actin have also been previously shown to adsorb at air-water inferfaces [396], and actin is known to interact with lipid mono- and bilayers in a buffer-dependent manner [224, 397].

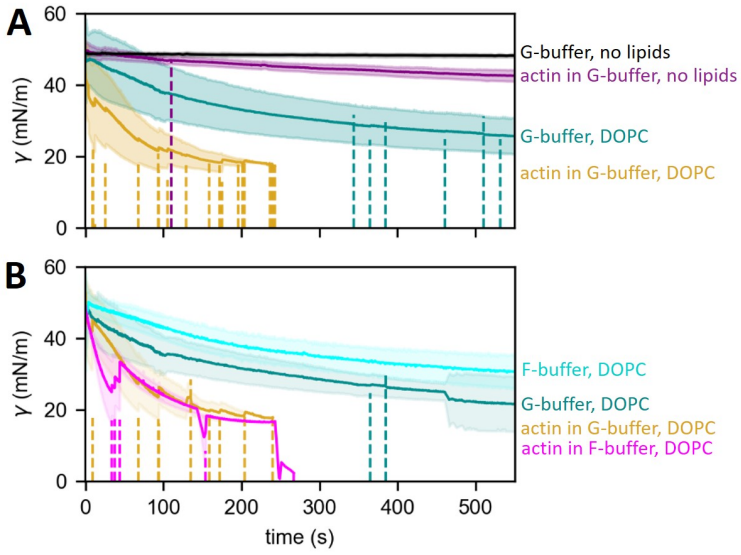

Figure 4.11: **Interfacial tension measurements of actin and lipids at oil-water-interfaces.** Interfacial tension of aqueous drops submerged in a lipid-in-oil solution prepared in the same way as eDICE oil phases, dissolving the lipids in chloroform only (thus without decane in the oil phase). (A) Interfacial tension between a lipid-free oil phase and G-buffer was almost constant (black, γ ~ 50 mN/m after 500 s). Adding actin in the G-buffer reduced the interfacial tension only slowly and to a small degree (purple, γ ~ 45 mN/m after 500 s). By contrast, interfacial tension dropped markedly when a DOPC-containing oil phase was brought into contact with G-buffer (teal, γ ~ 25 mN/m after 500 s), and the drop happened much faster when actin was additionally present in the aqueous phase (yellow, γ ~ 25 mN/m after 80 s). (B) The evolution of interfacial activity in the presence of both DOPC in the oil phase and actin in the aqueous drop is not markedly different between actin in G-buffer (yellow) or F-buffer (magenta). F-buffer alone (cyan) lead to a slightly weaker reduction in interfacial tension than G-buffer alone (teal). Bold lines and shaded regions indicate the means and standard deviations of at least 5 separate measurements from at least 2 different days for each condition, with the exception of G-buffer without lipids in panel (A). Sample sizes are listed below in table 4.1. Vertical dashed lines indicate times at which a drop fell from the tensiometer syringe and thus no longer contributes to the mean interfacial tension.

figure panel	buffer	lipids	actin (μM)	N
A	G-buffer	none	0	2
A	G-buffer	none	4	6
A	G-buffer	DOPC	0	21
A	G-buffer	DOPC	4	19
B	G-buffer	DOPC	0	11
B	F-buffer	DOPC	0	6
B	G-buffer	DOPC	4	9
B	F-buffer	DOPC	4	5

Table 4.1: Sample sizes for the tensiometry measurements shown in Fig. 4.11.

instead of chloroform, and then mixing them with silicone and mineral oils [138].

We adapted their lipid preparation procedure slightly, dissolving the lipids first in 50 µL chloroform and then diluting them with 400 µL decane. This helped us to quickly resuspend the lipids [371], while keeping close to the reportedly best oil phase composition for actin encapsulation [138]. Strikingly, this modification to the procedure improved our yield of actin-filled GUVs from dozens of GUVs per experiment to thousands (Fig. 4.10 D)[2]. Furthermore, due to the vastly improved yields we were now able to reduce the volumes of precious protein solutions needed per experiment.

To test whether emulsion based encapsulation could be used to encapsulate actin under low temperature conditions that have previously been used to inhibit actin polymerization during GUV formation [143], we performed a set of cDICE experiments in a climate controlled cold room at 4° C. This yielded a reasonable GUV yield, but all GUV membranes were decorated with small bright lipid structures that diffused along the GUV membrane (Supp. Fig. 4.12). This was likely due to the high ambient humidity, which has been shown to impact cDICE GUV quality [138]. Since encapsulation by eDICE is rapid and can be performed with ice-cold solutions within seconds, we concluded that the benefit of performing the encapsulation experiment at cold ambient temperatures was minimal and did not justify the reduction in overall GUV quality.

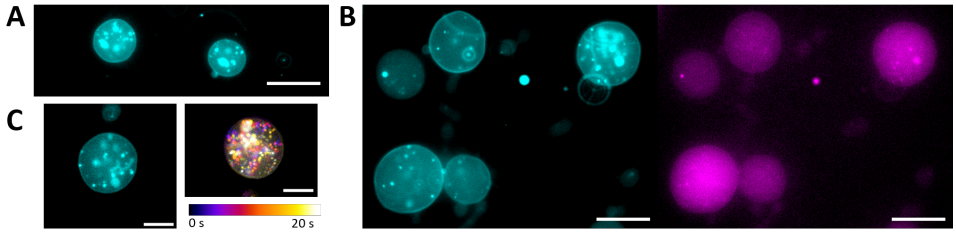

Figure 4.12: **GUV formation at 4° C.** Epifluorescence images of GUVs formed in a 4 ° C climate controlled room to prevent actin from polymerizing during GUV formation. Both empty GUVs (A) and GUVs encapsulating actin (B) were covered in small, bright lipid droplets or aggregates. (C) Lipid aggregates on the GUVs are mobile. The GUV membrane (left panel) was imaged for 20 s at 1 frame per second. The right panel shows a color-coded projection of the timelapse video, with lighter colors indicating later times. Membranes are shown in cyan, actin in magenta. Scale bars: 10 µm (A, B) and 5 µm (C).

GUV size distributions in eDICE samples were surprisingly consistent, despite the fact that eDICE relies on stochastic droplet breakup, and could thus reasonably be expected to yield highly variable GUV sizes depending on who performed the experiment, or how vigorously the emulsion was formed. We thus measured the size distribution of droplets produced in the first step of eDICE, where we emulsified IAS and oil phase by scratching an Eppendorf tube along a tube rack[3]. Strikingly, we found that droplet size distributions

[2] In GUV samples produced with only chloroform, we typically found ~ 30 GUVs per sample after scanning the entire sample chamber. By contrast, GUVs produced with decane and otherwise handled identically, always showed 50-100 GUVs in any given field of view, which spans much less than 1/20 of the chamber area, thus leading to our estimate of several thousand GUVs produced in any given run.

[3] Droplets were produced in an identical fashion to those produced in the intermediate GUV preparation step in eDICE, where we emulsified IAS into 1 mL of oil phase by mechanical agitation. To allow us to image the aqueous droplets in oil, we additionally dissolved 2 % V/V Span80 (nonionic surfactant, Sigma Aldrich, Cat. # 85548-250ML) in the oil phase to stabilize the interface [399]. We note that this addition of surfactant

were not only broader than the distributions of GUV sizes, but droplets were typically more than twice as large as GUVs (18.6 µm compared to 9 µm in diameter). This suggests that the classical image of droplets passing quasi-statically through the oil-OAS interface and turning into GUVs can not be accurate, and some size selective process must be occurring as droplets are transformed into GUVs.

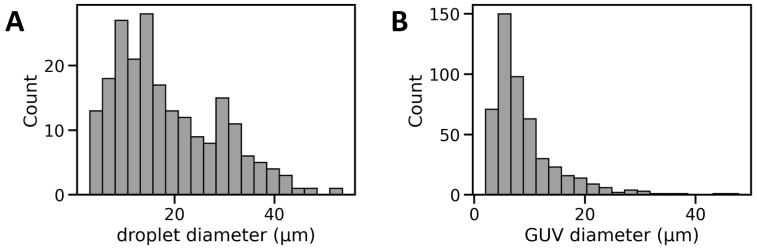

Figure 4.13: **Size distributions of droplets and GUVs differ significantly.** (A) Histogram of the sizes of droplets generated in the first step of eDICE (N = 213 droplets from 2 separate experiments). Droplets contained 4.4 µM actin in F-buffer with 6.5 % optiprep and were stabilized by surfactants in addition to lipids. (B) Histogram of GUV sizes generated by eDICE (N = 494 GUVs from 4 separate experiments)

4.5.4 eDICE is a versatile encapsulation technique

To demonstrate the broad applicability of eDICE for encapsulation of actin-related proteins, we formed a range of different types of GUVs by eDICE. We varied both the proteins and buffers in the inner aqueous solution (Supp. Fig. 4.14) and the membrane composition (Supp. Fig. 4.15). We also performed pilot experiments characterizing the formation of formin-nucleated actin cortices in GUVs, which yielded intriguing but inconsistent results (section 4.5.5). Finally, we demonstrated that GUV formation by eDICE works robustly with different density gradient media in the IAS: 18 % optiprep and 200 mM sucrose, which have been used in previous works [119, 138, 141, 370] both produced good GUV yields (Fig. 4.10 D), and we were even able to reduce concentration of density media to 4 % optiprep without significantly sacrificing GUV yield or quality (Supp. Fig. 4.16 A).

This is an important factor here, as density media can have a significant impact on actin dynamics, even at relatively low concentrations (Supp. Fig. 4.16 B-E). We note that buffer viscosity alone could not explain the differences in actin polymerization velocity between 0 and 6.5 % Optiprep: buffer viscosity increased by only ~2 % (Supp. Fig. 4.17 A, B), but the diffusion coefficient of actin as measured by fluorescence correlation spectroscopy was almost halved in the presence of 6.5% Optiprep (Supp. Fig. 4.17 C), consistent with a 30-50 % reduction in polymerization speeds (Supp. Fig. 4.16 D, E).

was necessary to keep the droplets from coalescing before or during the ~ 30 min necessary for imaging, but it changes the interfacial properties and may thus have an impact on the droplet size distribution we generate. However, the addition of extra surfactant has been shown to decrease the average size of emulsion droplets generated in turbulent flow [400], so our measurements likely underestimate the true size of droplets generated during the eDICE GUV formation process.

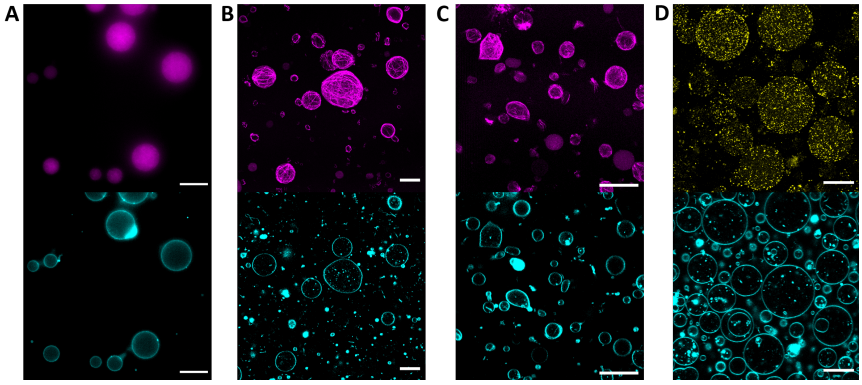

Figure 4.14: **A wide range of actin-related components can be encapsulated by eDICE** (A) 4.4 µM actin (magenta, doped with 5 % biotin-tagged monomers) co-encapsulated with 0.88 µM streptavidin and with 2.5 % biotin-DOPE in the membrane. (B) 8 µM actin co-encapsulated with 0.4 µM fascin. (C) 8 µM actin co-encapsulated with 0.4 µM fascin, 6.5 µM His-VCA, and 50 nM Arp2/3 from porcine brain. In the presence of fascin, actin self-assembles into bundles that show up as bright, linear or ring-like structures in GUVs. These bundles can deform the GUV membranes, producing prolate shapes (B, large central GUV, and C, center left), or, when combined with nucleation on the membrane, GUVs with sharp edges (C, top left) (D) 3.5 µg/mL non-muscle myosin-2 (yellow) in F-buffer. Lipid images (cyan, bottom row) always show a single slice for clarity. Actin (magenta) and myosin (yellow) images (top row) include a single slice acquired in epifluorescence on the Nikon fluorescence microscope (A), and maximum intensity projections of confocal z-stacks acquired at 1 µm step height on the Leica LSCM (B-D). Scale bars: 20 µm.

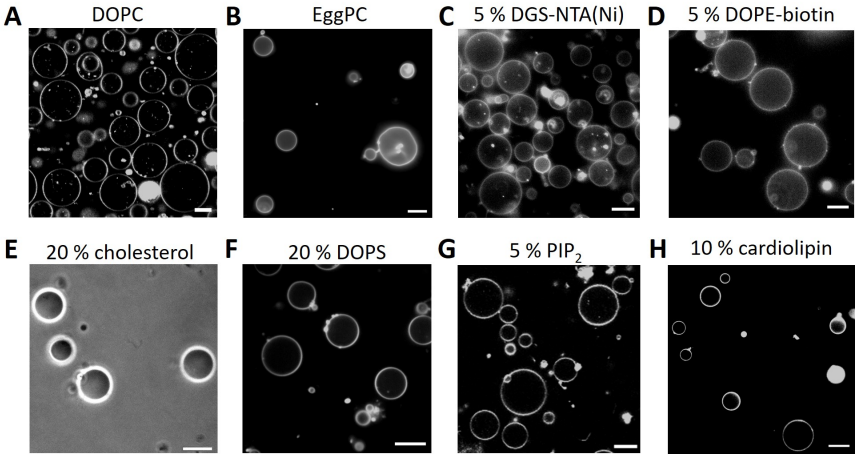

Figure 4.15: **eDICE successfully produces GUVs with different lipid compositions.** (A) DOPC, (B) EggPC, (C) 95 % DOPC and 5 % DGS-NTA(Ni), (D) 95 % DOPC and 5 % biotin-DOPE, (E) 80 % DOPC and 20 % cholesterol, (F) 80 % DOPC and 20 % DOPS, (G) 95 % DOPC and 5 % PIP2, (H) 90 % DOPC and 10 % cardiolipin. (A) and (H) are confocal images acquired on the Stellaris LSCM, (B-D) and (H) are epifluorescence images acquired on the Nikon epifluorescence microscope, (E) was acquired on the same Nikon microscope in phase contrast mode, and (F) is a confocal image taken on the Olympus spinning disk confocal microscope. All GUVs except those shown in (E) are labeled with either 0.005 or 0.05 % of Cy5-DOPE. Scale bars: 10 µm.

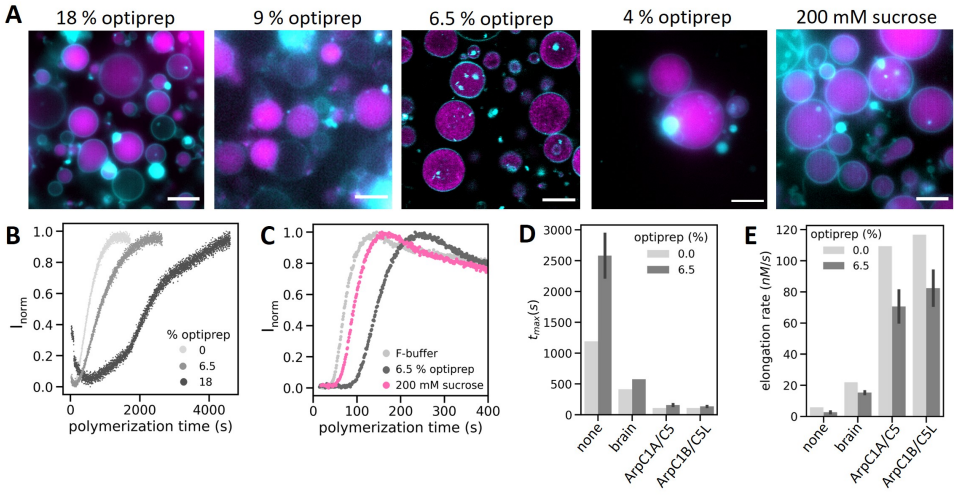

Figure 4.16: **Effect of density gradient media on actin encapsulation and polymerization.** (A) Fluorescence images of GUVs encapsulating F-actin using different concentrations of density gradient media (see legends) in the IAS. The GUVs containing 6.5 % optiprep are shown as a single confocal slice, the other images show widefield images. Lipids are shown in cyan, actin in magenta. Scale bars: 10 µm. (B) Actin polymerization curves measured by pyrene fluorescence assay at different concentrations of Optiprep showed that Optiprep interferes significantly with actin polymerization. (C) Pyrene actin polymerization curves indicate that sucrose used at a concentration compatible with eDICE also slowed actin polymerization dynamics, but to a lesser degree than Optiprep. (D) Bar plot of the time to reach steady state, t_{max} in the presence and absence of 6.5 % optiprep. (E) Bar plot of the actin elongation rate. Light grey bars in panels D, E represent one measurement in F-buffer, and dark grey bars represent the means of at least two separate measurements in F-buffer with optiprep, with error bars indicating the full spread of the data.

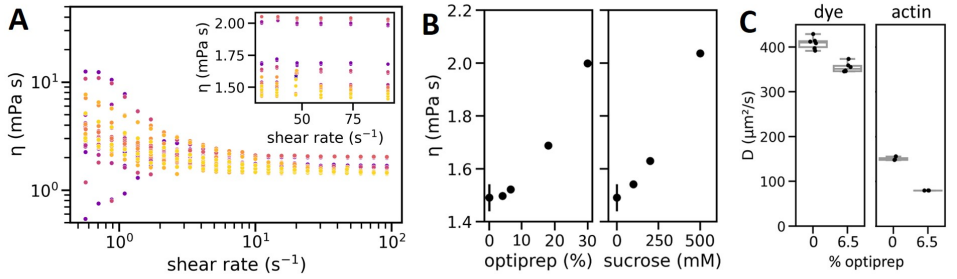

Figure 4.17: **Effect of density gradient media on buffer viscosity and actin diffusion.** (A) Buffer viscosities as a function of shear rate for reveal that F-buffer supplemented with either Optiprep or sucrose is a Newtonian fluid, i.e., the viscosity does not depend on shear rate. Note that the spread at low shear rates is caused by limitations of the rheometer due to very low torques. The curves are flat at shear rates where the measurement could be done reliably (inset). (B) Scatter plot of F-buffer viscosities (extracted from the plateau values in (A)) in the presence of different amounts of Optiprep and sucrose. Each datapoint represents the mean of 3 separate bulk rheology measurements of shear viscosity, and error bars indicate the full spread of the data. Error bars are smaller than the marker in all cases except for pure F-buffer. F-buffer viscosity increased by just 2 % upon addition of 6.5 % Optiprep. (C) Box plot of dye diffusion coefficients measured by FCS in the presence and absence of 6.5 % Optiprep.

4.5.5 Building formin-nucleated actin cortices in GUVs

We reconstituted actin cortices nucleated by membrane-bound formin mDia1 in GUV, analogous to those nucleated by Arp2/3, and found that mDia1 could indeed nucleate actin cortices in GUVs[4]. We always found a fraction of GUVs with no discernible localization of actin on the membrane (Supp. Fig. 4.18 A). While we did occasionally observe patchy cortices, the patches appeared only in conjunction with regions where bright lipid pockets were visible on the GUV membrane (B), likely indicating artefacts from unspecific interaction of formin with oil residues in the membranes. Homogeneous cortices were also observed, either with or without a significant cytoplasmic actin signal (C, D).

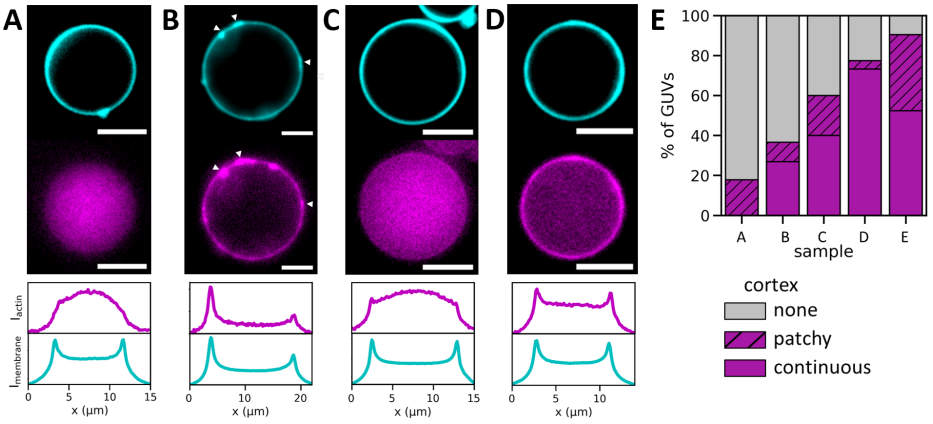

Figure 4.18: **Cortex nucleation by formin mDia1.** Epifluorescence images of GUVs containing 0.5 µM mDia1 and 4.4 µM actin (magenta). mDia1 was bound to the membrane by its 6xHis-tag that interacted with 5 % nickel-chelating lipids in the membrane. Some GUVs showed no actin localization to the membrane (cyan) (A). Actin sometimes appeared localized to the membrane and have significant intensity fluctuations around the membrane, but we observed this only in GUVs where the membrane intensity itself was also patchy (B, white arrowheads). Other GUVs had actin localized on the surface, with either a large (C) or small (D) amount of cytoplasmic actin remaining. Bottom panels in (A-D) show fluorescence intensity profiles along an 8 px wide diagonal line across each GUV, to illustrate the different localization phenotypes. (E) Cortex formation lacked reproducibility between experiments: Barplot of the fractions of GUVs showing either no actin localization (grey), a patchy actin cortex (magenta, hatched), or a continuous cortex (magenta, solid) in five separate experiments under identical conditions. Samples B and C as well as D and E were produced on the same days. N = 56, 82, 20, 284, 42 GUVs for samples A-E, respectively. Scale bars: 5 µm.

For reasons which we have been unable to identify, the formation of these cortices was extremely inconsistent, however: As shown in Fig. 4.18, identical experimental conditions yielded anywhere from 18 to 90 % of GUVs with some actin localization on the membrane, and the fraction of patchy cortices also fluctuated significantly. In all of these experiments, 4.4. µM actin was co-encapsulated with 0.5 µM formin and no profilin or other actin binding

[4] Method: Recombinant murine formin mDia1 (SNAP-mDia1-FH1-FH2-DAD-6xHis) was purified from *E. coli* following a published protocol [123]. In brief, the protein was expressed in Rosetta2 DE3 cells, and purified first by Nickel-affinity and subsequent size exclusion chromatography. The protein was flash-frozen in liquid N_2 and stored at -80° C. Membrane binding was facilitated by the C-terminal 6xHis-tag of the protein and 5 % mol/mol DGS-NTA(Ni) in the GUV membranes. The formin plasmid was a kind gift from Guillaume Romet-Lemonne (Institut Jacques Monod).

proteins. Notably, even sets of experiments conducted on the same day (samples B and C, as well as D and E in Fig. 4.18) clearly differed from each other. In the scope of this work, we could only briefly touch on the effect of profilin as well as formin concentrations, and observed no clear trends. However, our findings from Arp2/3 nucleated cortices suggest that co-encapsulating formin with high actin concentrations and also increasing the formin concentration may yield more reproducible results. It is furthermore an intriguing observation that formin was able to produce membrane-localized actin cortices even in the absence of profilin[5], even though profilin is required to increase the elongation speed of actin filaments produced by mDia1 [39]. We speculate that this effect may be due to the fact that spontaneous actin polymerization seems to be more severely impacted by the presence of optiprep than actin polymerization induced by nucleating proteins, which may make formin a comparatively more potent actin nucleator in Optiprep-containing buffers.

4.5.6 Supplementary experimental methods

Supplementary materials

Cholesterol (3β-Hydroxy-5-cholestene, 5-Cholesten-3β-ol, Cat. # C8667-1G) and sucrose (Cat. # S0389) were purchased from Sigma Aldrich. The following lipids were purchased from Avanti Polar Lipids: L-α-phosphatidylcholine (95 %) from chicken egg (EggPC), 1,2-dioleoyl-sn-glycero-3-phospho-L-serine (DOPS), 1,2-dioleoyl-sn-glycero-3-phospho-(1'-myo-inositol-4',5'-bisphosphate) (ammonium salt) (PIP_2), 1',3'-bis[1,2-dioleoyl-sn-glycero-3-phospho]-glycerol (sodium salt) (cardiolipin), and 1,2-dioleoyl-sn-glycero-3-phosphoethanolamine-N-(cap biotinyl) (biotin-PE). PIP_2 was stored in a mixture of chloroform, methanol and water at a 20:9:1 volumetric ratio, all other lipids were stored in chloroform and under argon at -20° C.

Supplementary microscopy methods

Widefield microscopy images were acquired on an inverted Leica Thunder Imager widefield microscope equipped with a 200 mW solid state LED5 light source, a 63x water immersion microscope (HC PL APO 63x / 1.20 W Corr CS2) and a monochrome sCMOS camera (Leica). Epifluorescence images were acquired on an inverted Nikon Ti Eclipse microscope equipped with a 60x water immersion objective (CFI Plan Apochromat VC), a digital CMOS camera (Orca Flash 4.0), and an LED light source (Lumencor Spectra Pad X). Phase contrast images were acquired on the same Nikon Ti microscope using its DIA illuminator at a voltage of 12 V and using the corresponding phase mask in the microscope's condenser.

GUV production by gel-assisted swelling

Gel-assisted swelling of GUVs was performed following ref. [403]. The detailed method is described in chapter 6.

[5] Method: Recombinant murine profilin1 was expressed in E. coli and purified following a published protocol [401]. In brief, the protein was expressed in BL21 DE3 Star cells and purified by polyproline-affinity purification. The polyproline resin was prepared in-house following the Mullins lab protocol (https://mullinslab.ucsf.edu/making-poly-l-proline-columns-for-profilin-purification) and [402]. Purified profilin was flash-frozen in liquid N_2 and stored at -80° C. The plasmid was a kind gift from Guillaume Romet-Lemonne (Institut Jacques Monod).

GUV production by cDICE

cDICE GUVs were prepared from the same solutions and in the same rotating chamber as eDICE GUVs. Droplets were formed by injecting IAS into the oil phase at a rate of 25 μL/min for 5 min using a syringe pump (KDS 100 CE, KD Scientific). The capillary setup was identical to that described in [138].

Actin polymerization assays

Actin polymerization was quantified by the classical pyrene actin assay [404], following an existing protocol [405], briefly summarized below. Actin polymerization was measured for 4 μM actin, 650 nM VCA and 50 nM Arp2/3.

Hardware Pyrene assays were performed on a Duetta fluorescence and absorbance spectrometer (Horiba Scientific), equipped with an 80 W S/N 1344-DL lamp and TC1 temperature controller (Quantum Northwest). The temperature varied between 25.0 and 25.4° C. Measurements were performed following a custom-defined procedure in the Horiba EzSpec software. For an excitation wavelength of 365 nm, the emission at 407 nm was recorded for a 1 s integration time per data point. The excitation window was set at 10 nm and the emission window at 5 nm. These parameters were chosen to maximise the relative difference in intensity between polymerized and unpolymerized pyrene-actin samples. All samples were measured in 3-window Quarz microvolume cuvettes from Hellma Analytics with an optical path length of 3 mm, holding 55 μL sample volumes. Cuvettes were cleaned by rinsing with 5 mL MilliQ water, 2 mL ethanol, and 2 mL MilliQ water between measurements, and dried under N_2 stream. Between different days of measurements, the cuvettes were further cleaned by sonicating in a 1 % Hellmanex solution for 5 min, sonicating for 5 min in MilliQ water to remove any excess detergent, and finally rinsing with 5 mL MilliQ water before drying under N_2 stream.

Procedure We performed all experiments in a final buffer with the same composition as the GUV IAS buffer, with at least two independent measurements per condition. Measurements with the different Arp2/3 isoforms but no Optiprep in the buffer were performed once per isoform. We first prepared an actin premix to ensure a consistent starting concentration and labeling ratio of monomeric actin. It contained 95 % unmodified actin and 5 % pyrene-labeled actin, at 23.8 μM total, corresponding to 5.95 x the final actin concentration for the pyrene assay, in G-buffer. In the cuvette, the actin premix was then diluted into Mg-G-buffer (5 mM TrisHCl pH 7.4, 0.2 mM $MgCl_2$, 1 mM DTT, and 0.2 mM MgATP) and allowed to incubate for 2 min. In this step, Ca^{2+} ions on actin monomers are exchanged for Mg^{2+} ions, ensuring that actin polymerization commences at a reproducible starting point. Salts, Arp2/3 and VCA were then added and mixed by pipetting 5 times. The cuvette was placed in the spectrophotometer and the measurement was started, noting down the delay between adding salt and the first recorded data point (usually 10-15 s). The measurement was left to run until the fluorescence intensity plateaued.

Data analysis While the Duetta spectrometer offers simultaneous buffer measurement and correction, we chose to perform a manual background correction to increase time resolution of our measurements. This allowed us to acquire one datapoint per 1.1 s. For

every measurement day, we first performed blank measurements on F-buffer and F-buffer including 6.5 % optiprep, where we repeated the same measurement 20 times. We then averaged these data points for every buffer individually, and subtracted the average from the sample data before further processing. To extract the time it takes to reach maximum pyrene fluorescence, as well as the actin elongation rate at the time where half of all G-actin is polymerized, we use a custom-written python script following the analysis laid out in [405]. We extract the time it takes each sample to reach maximum pyrene fluorescence and hence steady-state actin polymerization, as well as the actin elongation speed at the inflection point of the pyrene fluorescence curve. At this point, it is assumed half of all actin has polymerized and the increase in fluorescence intensity is only due to elongation, not nucleation [405].

Viscosity measurements

Buffer viscosities were measured on a Kinexus Malvern Pro rheometer using a stainless steel cone-plate geometry with 40 mm radius and a 1° angle. We performed a viscometry ramp, measuring viscosity as a function of shear rate from 0.5 s^{-1} to 100 s^{-1} in a logarithmic ramp with 10 samples per decade, with a total ramp time of ~2 min. This measurement was repeated at least three times for every sample condition. Since the buffers are very similar to water in their mechanical properties and barely resist deformation, the rheometer must control very low torques and thus generates noisy data at low shear rates (Supp. Fig. 4.17 A). As expected for a simple viscous liquid, we found constant viscosities for all samples at shear rates above 30 s^{-1}. The values measured above 30 s^{-1} were thus averaged to calculated the viscosity η of each buffer.

Tensiometry measurements

Pendant drop measurements were performed using a DSA 30S drop shape analyser (Kruss, Germany) and analysed with the Kruss Advanced software as described in [138]. For each measurement, a lipid-in-oil dispersion containing either no lipids or 100 % DOPC was prepared following the same procedure as when preparing oil phases for GUV formation. The mixture was divided over three glass 1.0 mm cuvettes (Hellma Analytics) immediately after sonication. In each cuvette, a 30 µL droplet containing buffer with 18.5 % V/V Optiprep was produced with a rate of 5 µL s^{-1} using an automated dosing system from a hanging glass syringe with needle diameter of 1.060 mm (Hamilton). As soon as the droplet reached its final volume, a timelapse video of the droplet was taken (100 frames at 5 fps and subsequently 500 frames at 1 fps). The droplet contour was automatically detected and fitted with the Young-Laplace equation to yield the interfacial tension. For measurements in dehumidified conditions, a dehumidifier was placed in the room and switched on at least 1 hour prior to the measurement. The lipid-in-oil dispersion was continuously mixed during each measurement using a magnetic stirrer. In several experiments, interfacial tension decreased very rapidly, causing the droplet to detach before the end of the measurement. These measurements were discarded for analysis.

TIRF microscopy

TIRF imaging of single actin filaments was performed on an inverted Nikon Ti-2 microscope equipped with an azimuthal TIRF/FRAP illumination module (Ilas^2, GATACA Systems), a 100x Apo TIRF 1.49 NA oil immersion objective and an EM-CCD Andor iXon Ultra 897

camera. Samples were illuminated at 488 nm with a 200 ms exposure time, gain of 80 and 15.3 % laser power. The TIRF angle was adjusted to yield a 188 nm TIRF penetration depth. Samples were mounted in flow channels as described in chapter 3, which were passivated by 20 min incubation with PLL-PEG-biotin (2 mg/mL in F-buffer) and flushed with 30 µL F-buffer before loading the samples and sealing them with vacuum grease to prevent drying.

Fluorescence Correlation Spectroscopy

FCS measurements of protein concentrations and diffusion coefficients in bulk and in GUVs were performed on a Leica Stellaris DMI8 micoscope equipped with a white light laser and a 63x water immersion objective (HC Plan APO 63x/1.20 W Corr CS2). The objective correction collar was adjusted to create the most well-matched light path possible on each day of experiments. The quality of the light path was assessed by how sharp the reflection line at the coverslip surface appeared in an xz-scan. The sample temperature was kept constant at 25° C using an Okolab environmental control box, and we used a single # 1.5 ibidi 18-well µ-slide per day of experiments, to avoid any artefacts introduced by variation in coverslip thickness. All measurements were performed 5.0 µm above the coverslip surface.

We performed quantitative FCS measurements only on AlexaFluor488 or AlexaFluor488-labeled actin. Measurements with AlexaFluor633 were performed but unsuccessful, as the dye's photophysical properties proved incompatible with FCS in optiprep-containing buffers (see Supp. Fig. 4.19 B). Laser powers for FCS measurements were optimized each day for optimal photon yield per molecule in F-buffer with 6.5 % Optiprep. For this, the laser power was first increased until the photons per molecule were maximal, and then brought back down to a level where the counts per molecule were around 1/3 of that maximum value. Maximum photon yields from AlexaFluor488 in this buffer were found to be around 25 kCPM (kilo counts per molecule). To get high photon yields while remaining well below saturation, we thus typically adjusted the laser intensity to 1.2 %, resulting in photon yields of 8-9 kCPM. The confocal volume V_0 and structure factor ω_0/ω_z, which characterizes the shape of the confocal spot, were determined by means of calibration curves obtained from 10 nM free dye diffusing in MilliQ water: We measured three independent intensity traces of 60 s length, fitted the resulting autocorrelation curves with a normal diffusion with triplet model at constant diffusion coefficient [406]. In this model, the autocorrelation function $G(\tau)$ is fitted as

$$G(\tau) = \left[1 - \tau + \tau e^{-\tau/\tau_T}\right] \cdot \frac{1}{N(1-\tau)} \cdot \frac{1}{1+\tau/\tau_D} \cdot \sqrt{\left[1 + (\tau/\tau_D) \cdot (\omega_0/\omega_z)^2\right]^{-1}} \tag{4.17}$$

where τ is the lag time, τ_T and τ_D are the characteristic times of the fluorophore's triplet state and the molecular diffusion respectively, and $N = cN_A V_0$ is the typical number of fluorescent particles in the confocal volume, V_0 [406]. We used literature values of the diffusion coefficient (414 $\mu m^2/s$ for AlexaFluor488, MW = 643 g/mol [407])

We then measured the free dye diffusion properties in the same buffer as the IAS (F-buffer supplemented with 6.5 % v/v Optiprep) to obtain the free dye diffusion time, as well as an upper limit for triplet state contributions in the measuring buffer. We found that fits for AlexaFluor488 never yielded triplet fractions above 23 %, and therefore imposed a

limit of no more than 25 % triplet contribution for all further fitting. We further limited possible triplet times to < 5 µs, in accordance with usual practice (Heike Glauner, personal communication).

In GUVs, we expect to find three species of fluorescent molecules: free dye left in the sample from the labeling process, dye bound to actin monomers, and dye bound to actin monomers which are incorporated in filaments. These three fluorescent species vary significantly in size, with molecular masses of ~ 0.7, ~ 42 and > 168 kDa (since an actin filament must consist of at least 4 monomers at 42 kDa each), and can hence be fitted as three separate diffusing species. To obtain more reliable fitting results, we first measured the diffusion coefficient (and hence diffusion time) of labeled G-actin in monomer buffer supplemented with 6.5 % optiprep. FCS measurements in GUVs were performed as follows: we first acquired an xz-image to identify the position of the coverslip surface, and the position and size of GUVs. We then defined a measurement point inside the GUV of interest, 5 µm above the coverslip surface and as central as possible inside a given GUV. We captured a 30 s intensity trace and calculated the autocorrelation curve. The autocorrelation curve was then fitted using a model assuming three freely diffusing fluorescent species with a triplet state. We imposed the diffusion times measured for free dye and monomer, and limited the triplet time and amplitude to 5 µs and 0.25, respectively. The third diffusion time as well as the diffusion amplitudes of all three species were fitted as free parameters. All analysis was perfomed using the commercial Leica LASX FLIM/FCS analysis software (Supp. Fig. 4.19).

4.5.7 Supplementary figures

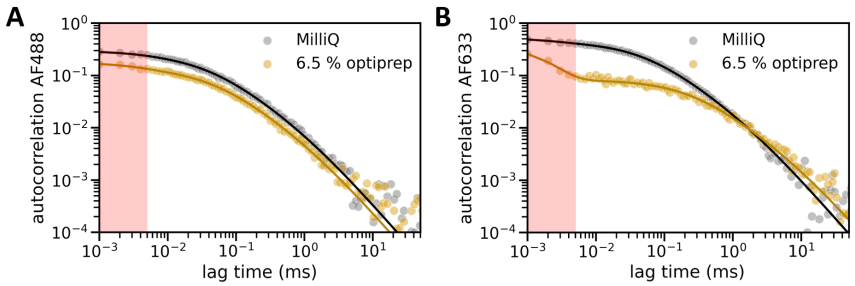

Figure 4.19: **FCS: Photophysical effects of optiprep.** Fluorescence correlation spectroscopy results for free AlexaFluor488 (A) and AlexaFluor633 (B) dyes. Fluorescence autocorrelation curves are plotted for both dyes in MilliQ water (grey datapoints and fits) and F-buffer with 6.5 % optiprep (yellow datapoints and fits). The autocorrelation curves are dominated by photophysical effects, namely fluorophores in their triplet state, for lag times up to 5 µs (red shaded areas). For AlexaFluor488, both autocorrelation curves are largely flat at short lag times, indicating that most dye molecules are in an emitting (singlet) state. By contrast, for AlexaFluor633 in optiprep-containing buffer, there is a marked decline in fluorescence autocorrelation within the first microseconds, indicating that a large fraction of fluorophores reside in a dark (triplet) state and thus cannot contribute to the diffusion-dominated part of the decorrelation curve (lag times τ >5 µs). In fact, we could not reduce the triplet fraction below 75 % for any samples with AlexaFluor633 in 6.5 % Optiprep. Triplet fractions above 25 % are generally considered too high to extract any meaningful diffusion data from FCS curves (H. Glauner, Leica, personal communication), rendering this fluorophore unusable for measurements where Optiprep is present in the buffer.

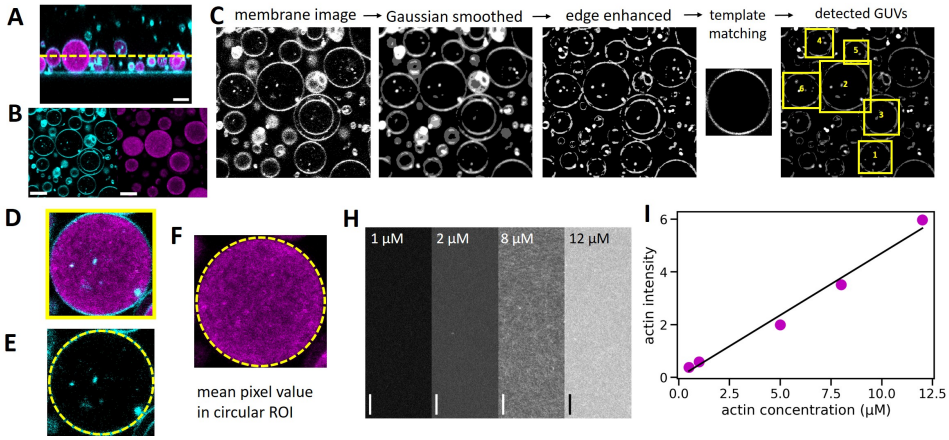

Figure 4.20: **Quantifying actin concentrations.** (A) For quantitative confocal imaging, we performed an xz-scan to locate the precise z-position of the coverslip visible from its reflection (horizontal cyan line). Actin is shown in magenta, lipids in cyan. The yellow dashed line indicates a 7 µm height above the coverslip, where we took subsequent images. (B) Next, we acquired a two-channel xy-confocal image (actin in magenta, lipids in cyan). (C) We used an automated pipeline to detect the vesicles by pre-processing the images and subsequently locating GUVs using the template matching module in the DisGUVery toolbox [389]. Yellow boxes indicate the detected GUVs. (D) To extract the actin intensity inside a given GUV, we used the original unprocessed two-color image. We loaded each GUV detected by the template matching algorithm (here: GUV 2 from panel C) and drew a circular ROI of the same size as the template matching box ((E), yellow dashed circle). The mean pixel value inside this circular ROI in the actin channel was then taken as the average actin intensity of the GUV. To convert actin intensities into concentrations, we acquired a series of reference images of bulk actin networks (H) and constructed a concentration-intensity-calibration curve (I). Magenta datapoints represent the average mean pixel values of at least four 2048x2048 px reference images per condition, with standard deviations smaller than the data points. We fit the datapoints with a proportional model ($I_{\mathrm{act}}(c_{\mathrm{act}}) = A \cdot c_{\mathrm{act}}$, black line), which yields a proportionality constant of 0.471. Scale bars: 5 µm.

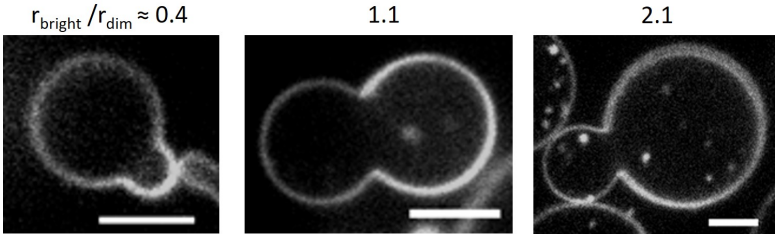

Figure 4.21: **Dumbbell GUVs exhibit a range of shapes.** Most dumbbells had nearly equal sized lobes (middle panel, $r_{\mathrm{bright}}/r_{\mathrm{dim}} \approx 1$), but both significantly lower and higher size ratios also occurred (left and right panel, $r_{\mathrm{bright}}/r_{\mathrm{dim}} \approx 0.4$ and 2.1, respectively).

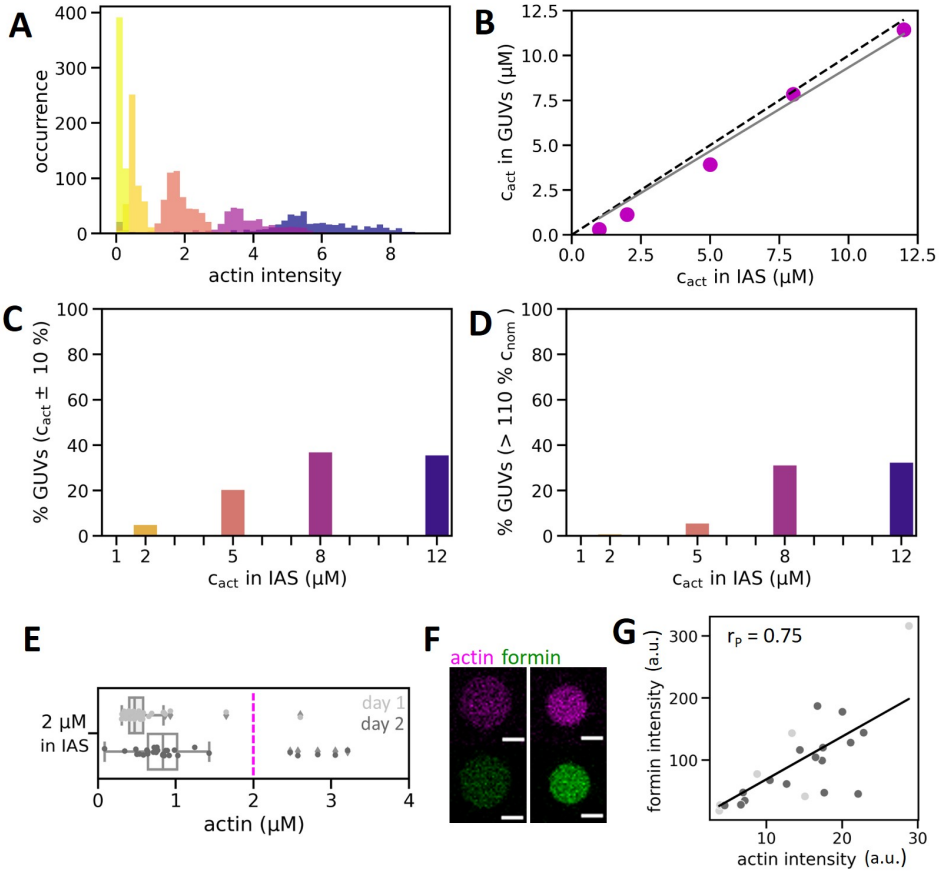

Figure 4.22: **Extended quantification of actin encapsulation efficiency by eDICE.** (A) Histogram of actin intensities measured in individual GUVs by quantitative confocal microscopy. Darker colours indicate higher nominal actin concentrations. N = 2334 GUVs, with individual sample sizes N_i = 515, 468, 536, 368 and 447 GUVs for i = 1, 2, 5, 8, and 12 μM actin, respectively. (B) Mean actin concentration in the GUVs as a function of the nominal actin concentration in the inner aqueous solution. Magenta datapoints represent the mean of all GUVs at one nominal concentration (same sample sizes as in (A)), and the solid grey line indicates the proportional fit $c_{GUV}(c_{IAS}) = \xi \cdot c_{IAS}$, with ξ = 93.3%. The dashed black line indicates perfect encapsulation, where the concentration in the GUVs equals the input concentration in the IAS. Error bars (95 % confidence interval on the mean) are not shown since they are smaller than the data points. (C) Bar plot showing the fraction of GUVs at different nominal actin concentrations containing actin at approximately the same concentration as the IAS (concentrations at $c_{nominal} \pm 10$ %). (D) Bar plot showing the fraction of GUVs that are significantly supersaturated in actin ($c_{GUV} > 1.1 \cdot c_{nominal}$). (E) Box plot of actin concentrations in GUVs, measured by fluorescence correlation spectroscopy (FCS) on two different days. The magenta dashed line indicates the nominally encapsulated concentration (2 μM). FCS confirmed that less actin was encapsulated in GUVs when its concentration in the IAS was low, and showed that there are significant day-to-day differences in actin encapsulation. (F) Confocal images of two typical GUVs co-encapsulating 4.4 μM actin (magenta) and 1 μM mDia1 (green). (G) Scatter plot of actin and formin signal measured in the same GUV. Different shades of grey indicate encapsulation on different days (N=27 GUVs in total) and the black line represents a linear fit to the data ($I_{formin} = 6.89 \cdot I_{actin}$). The signal intensities are strongly correlated (Pearson's correlation coefficient r_p = 0.75).

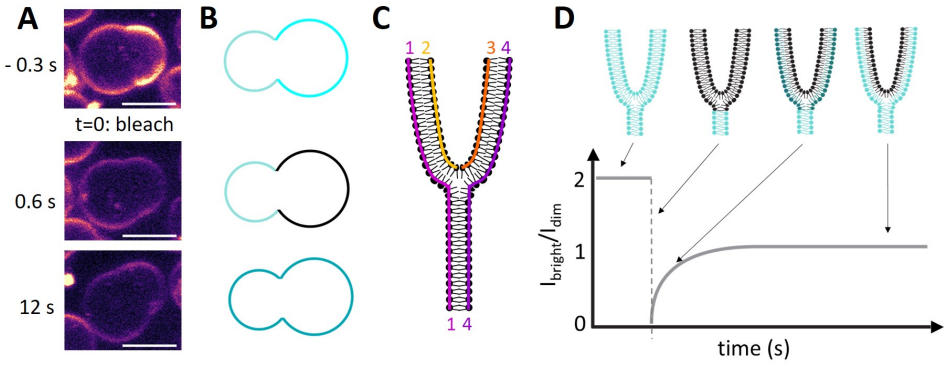

Figure 4.23: **FRAP analysis to test a mechanism for dumbbell formation based on hemifusion of nested GUVs.** (A) Confocal images taken at the equatorial plane of a dumbbell-shaped GUV before and after bleaching the bright lobe. Scale bars: 5 µm. Membrane fluorescence is shown in false color (magma) for clarity. (B) Schematic of the bleaching experiment. The GUV starts out with a dim and a bright lobe (top). Ideally, all of the bright lobe's fluorescence gets bleached (middle). The remaining fluorescence from the unbleached lobe then redistributes in all connected leaflets of both lobes. (C) Schematic of the different lipid leaflets at the neck, assuming that the dumbbell shape results from hemifusion: leaflets 1 and 4 connect the dim and bright lobe, while leaflets 2 and 3 are disconnected and only span the bright lobe. Note that 'leaflets' 2 and 3 are two halves of one continuous monolayer of lipids that is bent in on itself, making it macroscopically appear as two separate leaflets. (D) Expected ideal recovery curve (bottom) and illustration of the fluorescence distribution in the different leaflets (top). Leaflets 2 and 3 (C) do not exchange lipids with leaflets 1 and 4, and consequently remain dark after bleaching. The intensity ratio between the bright and dim dumbbell lobes thus recovers not to 2, but to 1.

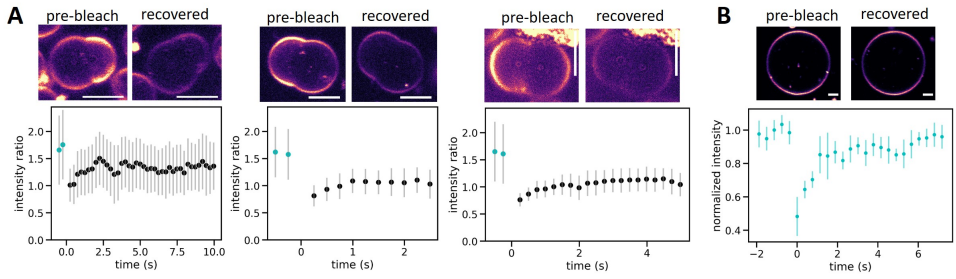

Figure 4.24: **Extended FRAP data for dumbbell-shaped GUVs.** (A) Example FRAP curves for three additional dumbbells not shown in the main text. The bright lobe was bleached to approximately 30 % of its initial fluorescence intensity at t=0. The intensity ratio between the bright and the dim lobe consistently started out at around 1.7 (cyan data points), and recovered to between 1.0 and 1.4 within 2 s (black data points). (B) FRAP curve of a non-dumbbell GUV. Here, a 2x5 µm rectangular ROI at the top of the GUV was photobleached and the fluorescence recovery was monitored relative to a reference region on the opposite side of the GUV. The effect of photobleaching appeared more pronounced here than in the dumbbell GUVs, as we could bleach the small region much faster and were thus able to capture more of the initial recovery period. The fluorescence recovery timescale matched that seen in dumbbell GUVs (< 3 s). Confocal images above each graph show the equatorial slice of the GUV before photobleaching and after at least 15 s of recovery. Scale bars: 3 μm. Membrane fluorescence is shown in false color (magma) for clarity.

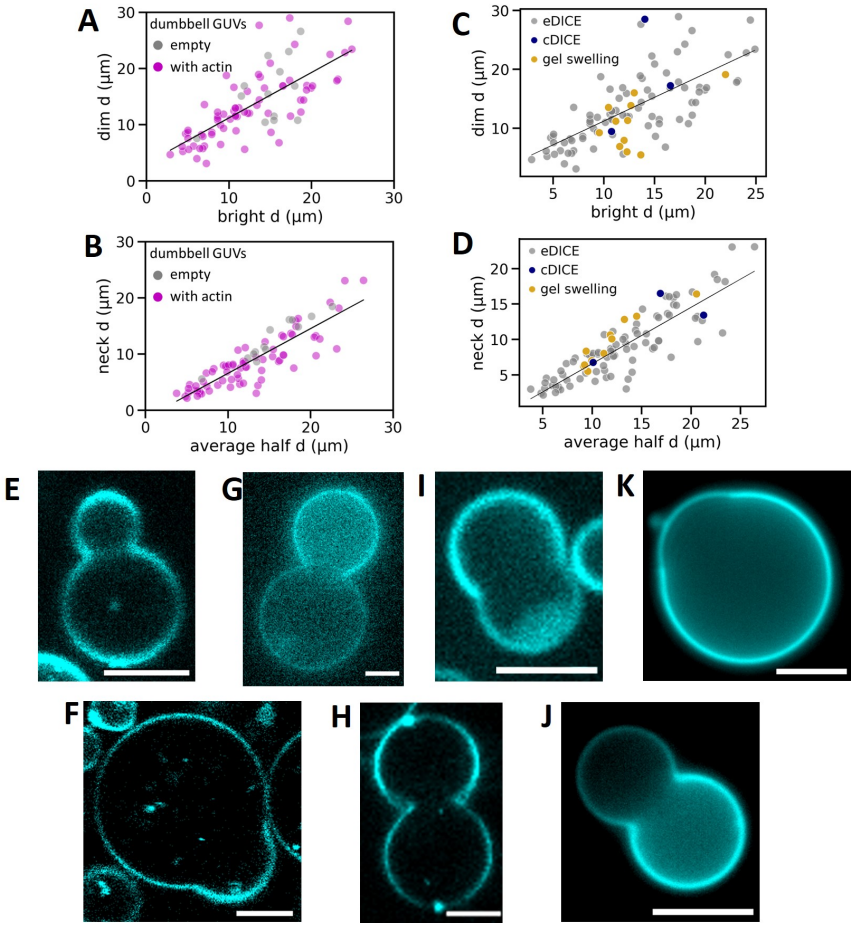

Figure 4.25: **Dumbbell GUVs form for a range of IAS compositions and GUV production methods.** (A, B) Data from Fig. 4 H and I are re-plotted to show which dumbbells contain actin (magenta datapoints, either 4.4 or 8 µM actin in F-buffer, N = 72 GUVs) or only F-buffer (grey datapoints, N = 13). Actin does not appear to alter the formation of dumbbell shaped GUVs. (C, D) The shapes of dumbbells produced by cDICE (blue datapoints, N=3) and gel swelling (yellow datapoints, N=11) follow the same trends in relative lobe dimensions (C) and neck dimensions (D) as those produced by eDICE (grey datapoints, N=72). (E-L) Fluorescence microscopy images of dumbbell shaped GUVs produced in different circumstances. Dumbbells form in GUVs encapsulating only buffer (E), actin which polymerizes in the lumen without nucleating proteins (F), different concentrations of actin nucleated on the membrane by Arp2/3 and VCA (G: 4 µM actin, H: 8 µM actin), and with cortices where Arp2/3 driven actin nucleation is modulated by capping protein (I). (J) Dumbbell vesicles are also occasionally observed in samples produced by cDICE, in this case encapsulating G-buffer. (K) We even find dumbbells (albeit only rarely, < 2 %) when GUVs are produced by gel-assisted swelling and encapsulate only a sucrose solution (L). E, F, and H were acquired on a laser scanning confocal microscope; G and I were acquired on a spinning disk confocal microscope, and J and K were acquired on a Nikon epifluorescence microscope. Scale bars: 5 µm.

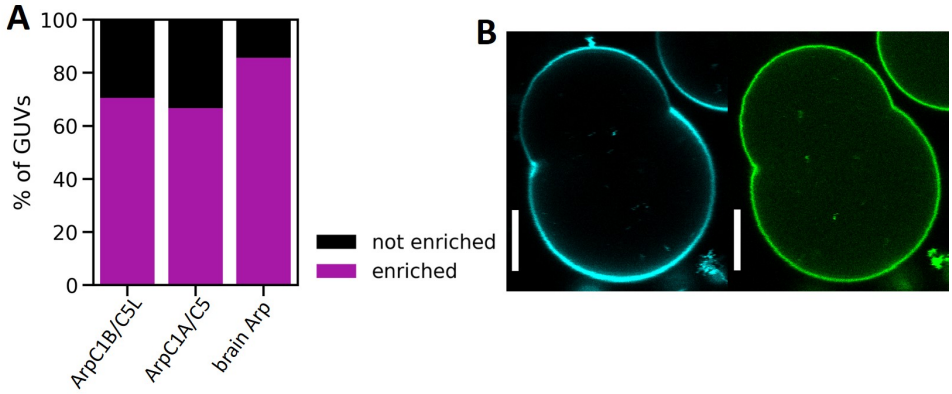

Figure 4.26: **Actin was consistently enriched at the necks of dumbbell GUVs for different Arp2/3 isoforms, while VCA alone did not show enrichment.** (A) Bar plot showing the fraction of dumbbell GUVs in which actin was enriched at the neck, depending on the isoform of Arp2/3 which nucleates actin at the cortex. Actin and Arp2/3 were always at 8 μM and 50 nM, respectively, and VCA was either at 2 or 6.5 μM. Capping protein was absent. N = 17, 3 and 7 for Arp2/3 isoforms Arp2/3C1BC5L, Arp2/3C1AC5, and mixed isoforms isolated from porcine brain, respectively. While statistics for Arp2/3C1AC5 and brain Arp2/3 are low, the data suggest that dendritic actin networks preferentially assemble at concave GUV neck regions for all these Arp2/3 isoforms. (B) Representative confocal image of a dumbbell GUV (membrane in cyan) encapsulating 6.5 μM fluorescent VCA (green). VCA covered the inner leaflet homogeneously, and we did not observe VCA enrichment at any of the 5 observed dumbbell necks.

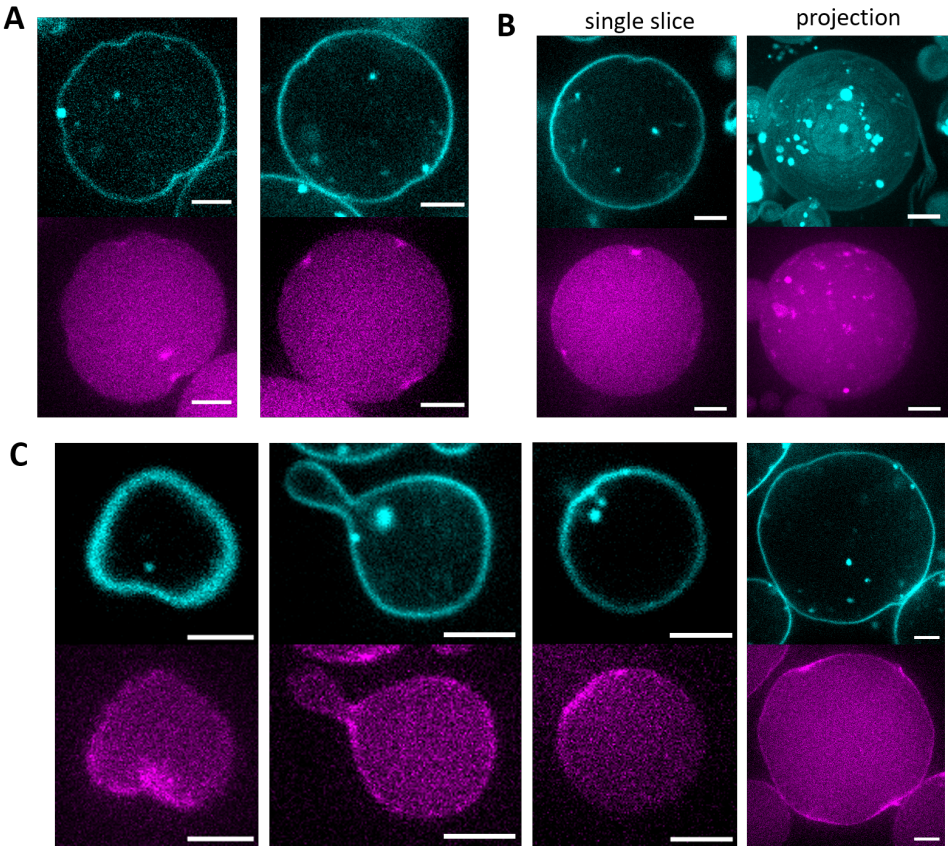

Figure 4.27: **Concave actin patches in the presence of capping protein.** Confocal microscopy slices of two representative GUVs containing 8 µM actin, 50 nM Arp2/3 and 2.6 µM VCA, combined with 185 nM capping protein. Under these conditions, we observed small regions in which actin (magenta) was enriched at an inwardly bent membrane region (cyan). Typically, GUVs had a few (2-5) patches like the two examples shown in (A), but they could also bear many more concave patches spaced all around the GUV (B). The left and right panels in (B) show a single confocal slice and a maximum intensity projection of the same GUV, and all bright spots visible in the projection represent concave patches. (C) Confocal slices of GUVs with bent actin patches in GUVs with 8 µM actin, but no capping protein. Scale bars: 5 μm.

Compound	Instrument	Excitation	Detection
actin-AF488	Olympus spinning disk	491 nm laser, 10.5 %, 200 ms	Andor iXon X3 EM-CCD, gain 250
membrane-Cy5	Olympus spinning disk	640 nm laser, 53 %, 200 ms	Andor iXon X3 EM-CCD, gain 250
actin-AF488	Leica Stellaris LSCM	WLL at 499 nm, 18 %, 3.16 µs dwell time	HyDS2 (504-590 nm), counting mode
membrane-Cy5	Leica Stellaris LSCM	WLL at 640 nm, 2 %, 3.16 µs dwell time	HyDX3 (658-809 nm), counting mode
VCA-AF488C5	Leica Stellaris LSCM	WLL at 499 nm, 2 %, 3.16 µs dwell time	HyDX1 (510-567 nm), Standard mode, gain 60
actin-AF488	Nikon widefield	470 nm LED, 25 %, 200 ms	Hamamatsu Orca Flash 4.0
membrane-Cy5	Nikon widefield	640 nm LED, 30 %, 50 ms	Hamamatsu Orca Flash 4.0
actin-AF488	Leica widefield	475 nm LED, 5 %, 200 ms	sCMOS camera, gain 2
membrane-Cy5	Leica widefield	635 nm LED, 5 %, 50 ms	sCMOS camera, gain 2

Table 4.2: **List of imaging settings**. The left column lists the compound and their label, which is Alexa Fluor 488 (AF488) or Cy5. The 'Excitation' column shows the excitation wavelength, laser attenuation, and exposure time (camera-based microscopes) or pixel dwell time (confocal scanning microscope).

5

Biomimetic actin cortices shape synthetic cells

Abstract

Animal cell membranes are shaped by the actin cortex, a thin layer of cytoskeletal filaments. This cortex serves two seemingly opposing functions: on the one hand, it provides mechanical stability by stiffening the cell surface and opposing external deformations, but on the other hand it is highly dynamic, turning over constantly and exerting pushing forces that can deform the membrane. How these two factors play out to shape the cell surface remains poorly understood. Here we use bottom-up reconstitution to build dynamic actin cortices in vitro that turn over within around 60 s, comparable to the actin dynamics in living cell cortices. We show that thin branched actin cortices are stiff enough to trap the shapes of giant unilamellar vesicles (GUVs) far from equilibrium, and impart a shape memory on the vesicles that exceeds the actin turnover time by two orders of magnitude. Using both photoablation and treatment with an actin depolymerizing drug, we demonstrate the reversibility of these deformations. We show that the same cortices can produce finger-like protrusions in GUVs without requiring actin bundling proteins. Combining theoretical modeling and experiments to explore under what conditions such protrusions form, we find that the concentration of nucleators is crucial, as locally concentrated actin polymerization forces can drive a positive feedback loop between recruitment of actin and its nucleators, and membrane deformation. Finally, we combine our findings to propose a working model for how actin polymerization forces shape synthetic cell membranes.

This chapter is based on a manuscript entitled 'Biomimetic actin cortices shape cell-sized lipid vesicles' by Lucia Baldauf, Felix Frey, Marcos Arribas Perez, Miroslav Mladenov, Michael Way, Timon Idema and Gijsje Koenderink, which is currently in preparation for publication. Felix Frey and Timon Idema (TU Delft) developed the model for spike initiation, and Miroslav Mladenov and Michael Way (Francis Crick Institute, London) expressed and purified the human Arp2/3 isoforms used in this work. Marcos Arribas Perez performed the experiments involving fluorescent VCA and additional FRAP measurements, and Lucia Baldauf performed all other reconstitution experiments, analyzed the data, and advised in the development of the model.

5.1 Introduction

The actin cortex is a thin, dynamic and tightly regulated cytoskeletal structure that supports the plasma membrane [6]. It combines two seemingly opposing functions, acting as a rigid scaffold that confers mechanical stability to the cell surface, while also actively generating forces and allowing the cell to change shape, form protrusions, and migrate. At the center of this functional dichotomy is a network of interpenetrating actin filaments that generate a mesh in which subsets of filaments have different structural and dynamic properties. Linear and relatively long (~ 1 μm) filaments are nucleated mostly by formins [26, 40] but also by Spire [130] and Arp2/3 activated by Spin90 [408]. Branched meshworks of shorter filaments (~ 100 nm [40]), by contrast, are nucleated by the Arp2/3 complex upon activation by nucleation promoting factors such as N-WASP or WAVE [32, 35]. In animal cells, the cortical actin layer is around 150 – 400 nm thick [56, 192, 409] and turns over within tens of seconds [116], while at the same time determining cell surface mechanics in an architecture-dependent manner (reviewed in [59]). Conceptually, we could expect this machinery to rigidify the cell surface, preventing shape changes, but also to exert membrane-directed polymerization forces that promote membrane deformations. How these opposing effects play out in cells remains elusive.

In cells, the complexity of the actin cortex and associated proteins makes it difficult to identify the biophysical principles that govern actin-mediated membrane shaping. In light of this, efforts have been made to reconstitute simpler, *in vitro* cell-free systems in which the interplay between the actin cortex and lipid membranes can be studied. Using these systems it has been demonstrated that, while single actin filaments are semiflexible and cannot withstand large compressive loads [410], stiffer filament bundles can effectively deform membranes [136, 139] when their bending rigidity surpasses the bending stiffness of the membrane. Inside cell-sized lipid vesicles, actin bundles can therefore form membrane protrusions that are reminiscent of filopodia or stereocilia, which contain parallel bundled actin filaments [411, 412]. In cells, however, correlative light and electron microscopy has shown that actin filament bundling proteins are recruited to protrusions only after precursors of the protrusion have already been established [413], suggesting that polymerization forces alone may be sufficient to initiate cellular protrusions.

The convergent elongation model of filopodia formation [413] indeed suggests that so-called Λ-precursors form when actin filaments nucleated by Arp2/3 in the lamellipodium are re-organized into bundles of increasing thickness while they grow, pushing on the membrane in the process. Greater molecular complexity only comes into play later, when the protrusions elongate with the help of additional proteins such as VASP [413], formins [414] and myosin X [415]. *In vitro* reconstitution has confirmed that dendritic actin networks can be re-organized into bundles by fascin in membrane-free systems [416], and can induce membrane deformations when co-encapsulated in lipid vesicles with fascin and myosin-2 [139]. Even actin polymerization forces alone can deform simple lipid membranes [352, 417], although this has so far only been shown in systems where thick actin networks were grown on the outer surface of lipid vesicles. It remains an open question whether polymerization forces generated by a cortex with more physiological geometry and thickness are also capable of driving the formation of membrane protrusions.

Furthermore, it is so far unclear how the rigidity of actin structures impacts membrane shapes. It is well established that the architecture and turnover dynamics of the actin cortex

both strongly modulate cortical mechanics and thus the shape of living cells [40, 418]. For instance, continuous membrane-directed actin polymerization in the lamellipodium allows cells to deform and migrate [419, 420]. *In vitro* reconstitution has, by contrast, focused mostly on systems without significant actin turnover [136, 137, 143, 144], or with little excess membrane area [119, 141], making membrane re-shaping difficult to observe.

Here we reconstitute biomimetic actin cortices in giant unilamellar vesicles (GUVs) to better understand how rigid yet dynamic actin cortices shape biological membranes. We show that simple dendritic actin cortices can stabilize nonequilibrium GUV shapes over timescales way beyond the actin turnover time, but at the same time drive the formation of finger-like protrusions. We use theoretical modeling to understand how protrusions form, and find that the density of actin nucleators, more so than their activity, is crucial to protrusion formation. This is confirmed by *in vitro* experiments, in which we also surprisingly find that protrusions can form in large bouquets, likely as a result of actin accumulation and membrane pinning by a high density of VCA-mediated actin-membrane links.

5.2 Results

5.2.1 Membrane-nucleated actin networks mimic cellular actin cortices

To study how actin polymerization forces shape lipid membranes, we reconstituted a simplified biomimetic actin cortex on the inner surface of giant unilamellar vesicles (GUVs). We used a modified emulsion transfer method based on continuous droplet interface crossing encapsulation (cDICE) [138, 370] to form the vesicles, which contained the cortex constituents in a physiological buffer (see chapter 4) [421]. The method is optimized for use with small volumes (~ 20 µL) and for speed (~ 1 min to form GUVs). Droplets were formed within $\lesssim$ 15 s starting from ice-cold solutions, ensuring that actin polymerization, even in the presence of nucleating proteins, occured only after the actin was already encapsulated in the GUVs. GUV diameters covered a broad distribution with a typical GUV size of around 9 µm, but ranging up to 40 µm (see chapter 4) thus covering typical sizes of mammalian cells [423] and making the vesicles appropriate model systems for reconstituting simplified cellular cortices. We encapsulated actin along with its regulatory proteins, the Arp2/3 complex [129] and the VCA-domain of murine N-WASP [115] (Fig. 5.1 A). To selectively restrict actin nucleation to the membrane surface as in cells [422], we used a 10xHis-tagged VCA construct that can bind to DGS-NTA(Ni) lipids. Membrane-bound VCA activated the Arp2/3 complex, which in turn allowed Arp2/3 to nucleate branched actin cortices.

In most GUVs, actin was strongly localized to the membrane, although $\lesssim$ 10 % of GUVs also had a significant cytosolic actin signal. Furthermore we found in every sample GUVs which had no actin signal (Fig. 5.1 C, white arrow), consistent with the broadly distributed encapsulation efficiencies we quantified in chapter 4. In the following, all analysis refers to GUVs in which we observed membrane-localized actin signal.

To assess whether the thickness of the reconstituted cortices matched the 150-400 nm reported for the actin cortex of living cells [56, 192, 409], we computed the radially averaged intensity profile from confocal images of the equatorial plane of GUVs. Intensity profiles revealed that most actin signal was indeed concentrated in the periphery of the GUV

(Fig. 5.1 C). A lower, homogeneous actin signal was also observed in the GUV lumen. This likely originated from a small cytosolic pool of actin along with contamination by free dye molecules which were incompletely removed after fluorescent labeling of the actin monomers. The presence of such free dye was confirmed by fluorescence correlation spectroscopy (FCS, Supp. Fig. 5.15).

The peak in actin intensity was equally narrow as the peak in membrane intensity, indicating that the actin cortical thickness is smaller than the optical resolution of the confocal microscope (< 300 nm)[1]. This is in line with the estimated maximum actin filament lengths we expect in our system ($\lesssim$ 300 nm), assuming for simplicity that each Arp2/3 complex nucleates one actin filament, and all proteins in the IAS get encapsulated stoichiometrically in the GUVs [2].

A key characteristic of the cellular actin cortex is the turnover of actin filaments [116]. Reconstitution of Arp2/3-nucleated actin cortices has been reported in previous studies, but turnover was either not characterized [140–142] or only assessed qualitatively [119]. We therefore measured the dynamics of our cortices by fluorescence recovery after photobleaching (FRAP), similar to approaches used to evaluate turnover in cell cortices [116] or lamellipodial fragments [420]. We bleached a small rectangular region of the cortex (Fig. 5.1 D, white rectangle). The bleached region recovered its fluorescence over time, getting shallower but not changing significantly in width (Fig. 5.1 D). Note that in the raw data, one may get the visual impression that the bleached region becomes narrower over time, but correcting for photobleaching confirms that it does not (Supp. Fig. 5.7). This observation suggests that fluorescence recovery is dominated by exchange of actin monomers with the GUV lumen via turnover, rather than by lateral diffusion of actin along the membrane. To analyze the turnover timescale, we monitored how the average fluorescence intensity in the bleached region recovered over time. Full details on the image and data processing are given in the Supplementary Information (Supp. Fig. 5.7). After correcting for photobleaching during image acquisition, we found that an exponential recovery with characteristic time τ in the form of $I(t) = I_{\text{inf}} - A \cdot \exp\left(-\frac{t}{\tau}\right)$ described the data well (Fig. 5.1 E). $I(t)$, I_{inf} and A are the fluorescence intensity at time t and long after bleaching, and a recovery prefactor, respectively. Note that with a 6 µm sized FRAP region and an actin monomer diffusion coefficient of $D = 97\ \mu\text{m}^2/\text{s}$ (measured by FCS, Supp. Fig. 5.10), recovery by actin diffusion in the vesicle lumen had a characteristic time of $\tau \sim 40$ ms and was thus complete within the time it took to record the first frame. We found an average recovery timescale of $\tau = 59 \pm 32$ s ($N = 9$ GUVs from 2 independent samples, Fig. 5.1 F). This timescale is consistent with typical time scales of ~ 20 s measured in living cells [116]. The factor 2-3 discrepancy is likely due to our much simpler system, which lacked for instance any proteins specifically inducing actin filament severing and disassembly (reviewed in [35, 424]). We also confirmed that GUV membrane fluidity was not affected by the presence of an actin cortex, with membrane fluorescence recovering with $\tau \sim 1.6$ s (Supp. Fig. 5.8).

[1] Resolution was limited here by pixel sampling density; depending on the exact zoom we measured full peak widths at half maximum ranging between 300 and 800 nm. The peaks were generally slightly wider in the membrane channel (i.e. for the fluorophore with the longer wavelength), confirming that the peak widths were indeed diffraction limited.

[2] Note that this calculation is intended as a rough estimate of the expected upper limit of filament lengths. We therefore ignore the Arp2/3 complex' autocatalytic properties [344].

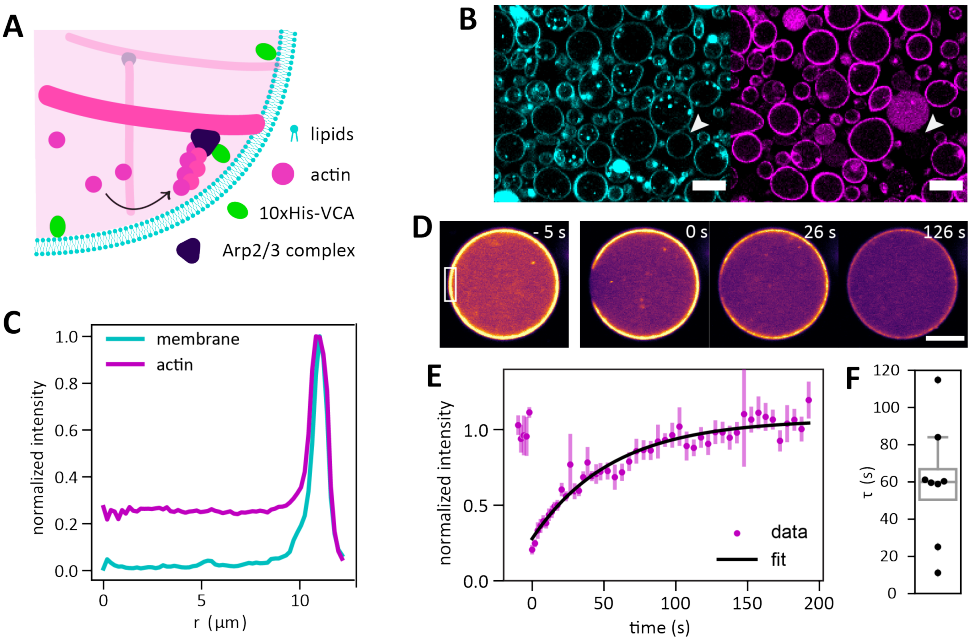

Figure 5.1: **Formation of biomimetic actin cortices in Giant Unilamellar Vesicles (GUVs).** (A) Branched actin cortices are nucleated at the inner leaflet of the GUV membrane by recruiting 10xHis-tagged VCA to the membrane, where it activates the Arp2/3 complex. Arp2/3 can in turn bind actin filaments and nucleate daughter filaments. (B) Confocal images of a typical sample of GUVs. Actin (magenta) localizes strongly to the membrane (cyan) of almost all vesicles. We also always find some GUVs with no encapsulated actin (white arrowhead) as well as some bright lipid aggregates. (C) Radially averaged actin and membrane intensity profiles in the equatorial plane of a typical GUV. Actin is largely localized to the periphery of the GUV, closer to the membrane than the optical resolution limit (~ 300 nm). (D) Confocal images during different time points in a typical FRAP measurement of the turnover time of the actin cortex. Actin is shown in false color (magma) for clarity, with brighter colors indicating higher actin signal. The white rectangle marks the region that was photobleached at $t = -2$ s. Note that the entire vesicle becomes darker over time due to photobleaching during imaging. (E) FRAP curve of the same GUV, showing the fluorescence intensity in the FRAP region after correcting for photobleaching during acquisition. Error bars denote the standard deviation, the solid black line shows an exponential fit with a time constant $\tau = 60$ s. (F) Characteristic recovery timescales in 9 GUVs from 2 separate experiments, with a mean of $\tau = 59 \pm 32$ s. Scale bars: 10 µm.

5.2.2 Branched actin cortices stabilize GUV deformations

Prompted by prior in-vitro reconstitution studies of actin in GUVs showing that actin can only shape lipid membranes at low tension [136, 142, 352], we produced osmotically deflated GUVs. We adjusted the osmotic mismatch between IAS and OAS to generate GUVs with on average 7.5 % excess membrane area, i.e. 7.5 % more membrane than is necessary to cover a sphere of the same volume [388]. Strikingly, many of the cortex-bearing GUVs were frozen in highly irregular shapes, well outside the range of equilibrium shapes for deflated vesicles with a fluid surface, where we should expect spherical shapes that become prolate or oblate, but always largely symmetric, upon deflation [425]. Here, by contrast, we found many GUVs with sharp corners (pink arrows in Fig. 5.2 A), bleb-like protrusions (yellow arrows), sharp elongated protrusions (cyan arrows), or highly anisotropic indented

or banana-like shapes (yellow asterisk). Globally deformed GUVs were present as soon as we could image them (~ 20 min after GUV formation) and there were no clear changes in the fraction of deformed vesicles over the course of 2.5 hours. Individual GUV shapes could remain unchanged over many minutes (Supp. Fig. 5.17), and globally deformed GUVs were observable for at least 16 hours after formation. The highly deformed GUVs invariably had a bright actin cortex.

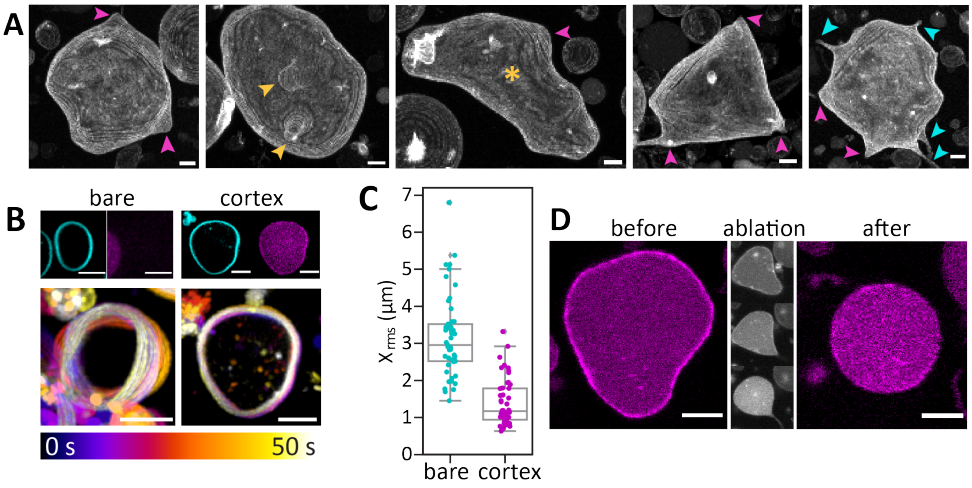

Figure 5.2: **Actin cortices stabilize GUV shape deformations.** (A) Gallery showcasing the diverse GUV shapes in the presence of an actin cortex. Images show maximum intensity projections of confocal z-stacks at 1 µm step height. GUVs exhibited sharp corners (pink arrows), rounded bleb-like protrusions (yellow arrows), sharp elongated protrusions (cyan arrows) or global deformations into irregular elongated shapes (yellow asterisk). (B) Actin cortices suppressed membrane fluctuations. The bottom images show a color-coded representation of 50 s long time-lapse videos of two GUVs, with brighter colors indicating later times. The left GUV membrane was bare, while the right one was supported by an actin cortex (confocal images in top row, membrane in cyan and actin in magenta). (C) Quantification of the membrane displacements shown in (B). Individual data points show the root mean square displacement of the membrane between consecutive frames with a 1 s interval. Median X_{rms} in one second was 3 µm for the bare membrane and 1.2 µm for the cortex-supported GUV (D) Ablating the actin cortex by laser light returned vesicles to the spherical shapes expected for bare membranes. First and last image: equatorial plane of a GUV before and after ablation of its entire actin cortex for 8 s with a 1.6 W UV laser. Middle colum: the same GUV after 1, 4 and 8 s of UV illumination. Scale bars: 5 µm.

Next, we followed GUVs with and without an actin cortex over shorter time scales. We found that GUVs without an actin cortex fluctuated freely, deforming significantly on the time scale of seconds, whereas actin-supported GUVs showed practically no shape fluctuations over the same time scales (Fig. 5.2 B). Cortex-supported GUVs were around 3 times less deformable over 50 s than GUVs lacking a cortex (Fig. 5.2 C). This behavior was consistent, as all deflated cortex-supported GUVs were similarly rigid, and their thermal membrane motion was inhibited.

We therefore surmised that the submembranous actin cortex generates or stabilizes global GUV deformations. If that is the case, we should be able to recapture 'normal' GUV shapes by completely removing the actin cortex in a deformed vesicle. To test this hypothesis, we used intense UV laser light to photoablate the cortex of a deformed vesicle as

shown in Fig. 5.2 D. Photoablation has previously been used to disrupt cellular actin stress fibres [426] and the actin cortex [427, 428], as well as to destabilize the shapes of GUVs deformed by stiff actin bundles [137]. Here we used it to fragment the actin cortex. During illumination with an intense UV laser, the GUV rounded up and produced a thin membrane tube from the excess membrane area (Fig. 5.2 D, center bottom). After photoablation, the GUV was spherical, but retained the thin, actin-filled membrane tube (Fig. 5.2 D, right panel). Upon ablation, the actin signal in the GUV lumen increased, indicating that the cortex was disrupted. This return to a 'normal' GUV shape upon removal of the cortex confirmed that stiff dendritic actin cortices can stabilize GUV shapes far from equilibrium lipid vesicle shapes. Likewise, actin depolymerization with cytochalasin D [429] also returned deformed GUVs to spherical shapes (Supp. Fig. 5.11).

5.2.3 Active actin cortices drive cell-like membrane protrusions

In addition to globally deformed GUVs, we found that active actin cortices could also give rise to long and thin membrane protrusions reminiscent in shape of filopodia and other actin-driven cellular protrusions. We observed two types of membrane protrusions: tubes, which pointed outwards and were so narrow that we could not optically resolve the width of their base (Fig. 5.3 A), and spikes, whose base was open far enough for us to resolve a finite base width ($\gtrsim$ 500 nm) (Fig. 5.3 B). Both tubes and spikes could be very long (> 30 µm), often longer than the GUV diameter, but were almost always limited to base widths below 3 µm regardless of GUV size (Supp. Fig. 5.20 A-C).

Membrane tubes can form spontaneously in GUVs with excess membrane area when there are asymmetries in pH, buffer, or lipid composition between the two membrane leaflets [430]. Although buffer composition differed between the inside and outside of the GUVs studied here, we only observed two outward-pointing lipid tubes and no spikes whatsoever across 60 GUVs made in the absence of actin (Fig. 5.4 D, Supp. Fig. 5.18 A). Moreover, GUVs also did not display protrusions when actin polymerized in the GUV lumen (Supp. Fig. 5.18 B). By contrast, protrusions were common in GUVs where actin polymerized on the membrane, occurring in up to 50 % of vesicles when actin was nucleated on the membrane. We therefore concluded that actin polymerization on the inner leaflet of the membrane was driving protrusion formation.

Since an actin cortex appeared to be required to initiate spike formation, we tested whether its removal led to retraction of the spike. We photoablated a small rectangular region at the base of a spike (Fig. 5.3 C, yellow arrowheads, and Supp. Fig. 5.20 D) by irradiating it with a UV laser. Photoablation indeed led to spike collapse, either leaving behind a thin membrane tube (Fig. 5.3 C, left) or retracting completely (Fig. 5.3 C, right). The remaining tube could be thin or retain volume in the outlying regions, but the site of photoablation always collapsed down to below optical resolution. Interestingly, ablating the actin cortex locally at the base of membrane spikes also often led to shape changes further away. Magenta arrows in Fig. 5.3 C denote places where the previously stable GUV shape changed during photoablation, indicating that photoablation of spike bases removed shape constraints on the entire GUV cortex, leading to stress relaxation elsewhere on the GUV surface.

To better understand how actin drives the formation of membrane protrusions, we

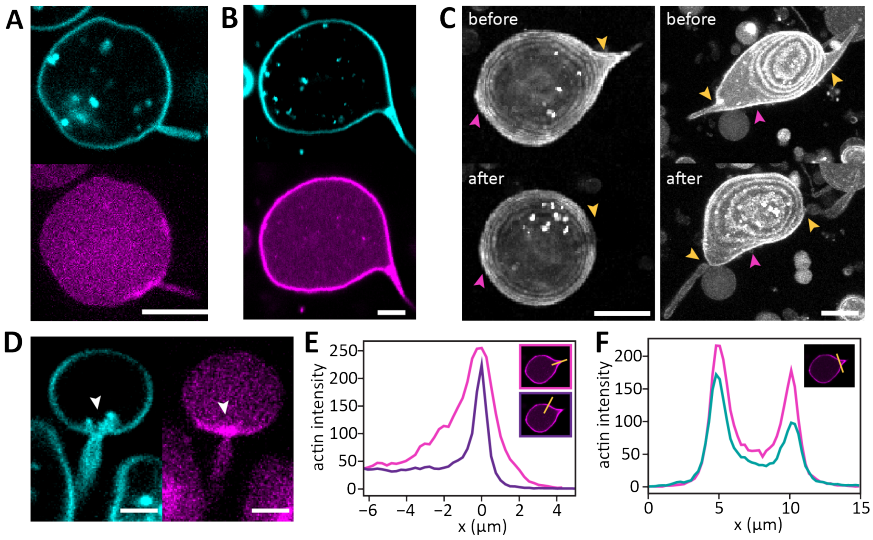

Figure 5.3: **Cortex-supported GUVs have cell-like membrane protrusions.** Confocal images of GUVs with tube-like (A) and spike-like (B) membrane protrusions. (C) Maximum intensity projections of two GUVs before (top) and after (bottom) ablation of spike bases (yellow arrows). Ablation of the actin network at the spike base either led to complete retraction of the spike (left), or left the outer regions of the spike intact while the base collapsed to a diameter below the diffraction limit (right). Ablation of the spikes often caused deformations elsewhere in the GUV (magenta arrows), indicating mechanical coherence of the cortex. (D) For the majority (78 %, of $N = 154$ protrusion-bearing GUVs) of the protrusions, actin is visibly enriched at the base and is often accompanied by a region of fuzzy inwards membrane signal surrounding the protrusion base (white arrows). (E) Line profiles comparing actin fluorescence intensities perpendicular to the membrane inside a spike (magenta, top inset) and next to one (dark purple, bottom inset). The GUV lumen is located at $x < 0$ and the membrane at $x = 0$. The actin signal is slightly increased in the spike, and extends further into the GUV lumen than in the rest of the cortex. Insets indicate where the line profiles were acquired (yellow lines, 3 px linewidth). (F) Comparing actin (magenta) and membrane (cyan) intensity profiles across the spike base shows that the peaks in cortical actin fluorescence are only slightly wider than those in the membrane fluorescence. Therefore, even in the spike, the thickness of the actin network is around the diffraction limit. Scale bars: 5 µm.

characterized its distribution in spike-like protrusions. Actin was visibly enriched in a patch at the base of the protrusion (Fig. 5.3 D) in 78 % of the 154 GUVs. Accompanying actin patches, we often observed an associated inward-pointing membrane signal (white arrow in Fig.5.3 D), whose structure we could not resolve optically. Such a diffuse membrane signal may originate from thin tubes pulled from the GUV membrane by the polymerizing actin network, similar to membrane tubes pulled into an actin network that polymerized on the outer surface of floppy GUVs [352].

Intensity profiles of actin through the spike apex compared to the membrane next to spikes revealed that actin was slightly brighter in spikes and was enriched in a wider region compared to the rest of the cortex (Fig. 5.3 E). Integrating the actin signal in the peak region ($-6.2 < x < 4.0$ µm, where $x = 0$ denotes the position of highest membrane signal), we found that there was about twice as much actin in the spike profile compared to the rest of the cortex. In an intensity profile through the spike base, and roughly perpendicular to the spike walls, we found that the width of the main actin peak nearly matched that of the

membrane peak, indicating that the cortical network was still largely concentrated within a region thinner than optical resolution, rather than extending throughout the spike cross section (Fig. 5.3 F).

5.2.4 Actin polymerization determines the conditions for protrusion initiation

We turned to mathematical modelling to understand how spikes may be initiated, depending on the nucleation activity of actin in the cortex that drives the membrane deformation. Our model describes the early stages of the 3D shape evolution of an initially planar membrane under the influence of actin polymerization, and was inspired by previous work of Gov and Gopinathan [431, 432]. We considered the locally flat membrane patch of a GUV to which the actin polymerization activator VCA was bound, and treated the local VCA density as a proxy for local actin polymerization, which may drive membrane deformations. We assume that the evolution of the VCA surface density $n(x, y)$ over time is determined by diffusion and autocatalytic actin growth [433]:

$$\partial_t n = D\nabla^2 n + \alpha\, n(1-n)K^2\,. \tag{5.1}$$

The first term on the right-hand side of Eq. (5.1) describes the lateral diffusion of VCA on the membrane with the diffusion constant D. The second term on the right-hand side of Eq. (5.1) describes the membrane accumulation of VCA. FRAP experiments confirmed that VCA diffused freely on the membrane in the absence of actin (Supp. Fig. 5.9). We assumed that VCA is more likely to reside on the membrane where actin, and therefore VCA, are already present. In addition, we chose the term to be proportional to $n(1-n)$ so that the VCA number density n is normalized and bounded between 0 and 1, reflecting the constraint that VCA can only bind the membrane up to a maximum density. Since the VCA density is normalized, the phenomenological 'enrichment constant' α carries the same units as a diffusion constant. Experimentally, we found no membrane deformations with high membrane curvature unless actin was present and polymerizing on the membrane. Thus, wherever the membrane is curved, the probability is high that actin is present at that site. For our model, we thus posited that the actin (and thus VCA) density is correlated to the (total) membrane curvature K, but independent of whether the membrane is curved inward or outward. The simplest way to accommodate this symmetry is to assume that VCA enrichment is proportional to K^2. Note that we did not make any explicit assumptions about curvature generation by actin nucleating proteins, which is often postulated in theoretical works [431, 432, 434] but so far lacks clear experimental evidence. We described the shape of the membrane patch by a 'height field' $h(x, y)$, which described the distance between the membrane position and some flat reference plane. We assumed that the time evolution of the membrane height h is determined by the polymerization of actin filaments and the tendency of the membrane to mechanically relax to a flat state,

$$\partial_t h = v f(n) - w\, h(x, y, t)\,. \tag{5.2}$$

The first term on the right-hand side of Eq. (5.2) describes how the membrane is pushed outward in the normal direction by polymerizing actin filaments. Here, v represents the polymerization velocity of actin. The VCA response function $f(n)$ describes how the VCA

density affects actin polymerization. We chose it to reflect the reasonable assumption that we need some minimal concentration of VCA for actin to start polymerizing, and that actin polymerization saturates at high VCA density. Details on the response function are given in the Supplementary Information (section 5.5.4). The second term on the right-hand side of Eq. (5.2) describes how membrane deformations mechanically relax towards a flat state with rate w, which is determined by membrane tension and bending rigidity [431].

We solved the model numerically in polar coordinates, assuming rotational symmetry for low, intermediate and high density of VCA on the membrane. VCA was initially homogeneously distributed on a membrane patch with a small, local Gaussian shaped deformation at the origin, such as may be caused by thermal fluctuations of the GUV membrane [352]. Details are given in the Supplementary Information along with the parameter values used (Table 5.1). We then followed how the VCA distribution evolved over time, and how the height of the membrane at the origin of the membrane patch (i.e., in the center of the deformation) changed compared to the flat outer boundary of our simulation box (Fig. 5.4 A).

For the low initial VCA density (Fig. 5.4 B, blue line), we found that the membrane remained flat. For a high initial VCA density (Fig. 5.4 B, dashed black line), the membrane was pushed outward with the same velocity everywhere. Therefore, the membrane again remained flat. By contrast, the localized membrane deformation grew rapidly for intermediate initial VCA density (Fig. 5.4 B, dark blue line). Similarly, the difference in VCA density at the center of the spike and the outer boundary vanished at all times for both low and high VCA densities, but grew and plateaued after a few seconds for intermediate VCA density (Fig. 5.4 C). The model thus suggests that the prevalence of thin membrane protrusions should depend on the density of nucleation promoting factors on the membrane. Indeed, this was confirmed when we compared GUVs in which we varied the concentration of encapsulated VCA while keeping all other membrane and cortical components the same (Fig. 5.4 E). At low VCA concentrations ($\lesssim$ 1.3 μM in the IAS, corresponding to an estimated surface coverage of ~ 4.5 %), we observed no spikes and only very few tube-like protrusions. Both tubes and spikes became more prevalent at intermediate VCA concentrations, with 14 % of GUVs exhibiting spikes and almost half of GUVs exhibiting some thin protrusions. At high VCA concentrations (6.5 μM, corresponding to almost 25 % surface coverage), we observed a slight reduction in tubes and a significant reduction in GUVs with spikes, consistent with the predictions of the model. Here, 8 % of GUVs had spikes and 44 % had some sort of protrusion.

We also experimentally tested what the impact of the nucleation ability of Arp2/3 was on protrusion formation, by comparing three different types of Arp2/3 complex: the human Arp2/3 isoforms containing ArpC1B/C5L and ArpC1A/C5 [129] (green and dark grey, Fig. 5.4 F) as well as the Arp2/3 complex from porcine brain (light grey), which comprises a mix of isoforms and is widely used in reconstitution studies [115, 119, 141, 352]. Pyrene assays showed that actin elongation rates of actin in the presence of the VCA and two human Arp2/3 isoforms were comparable, with ArpC1B/C5L leading to slightly faster polymerization (82 and 71 nM/s for ArpC1B/C5L and ArpC1A/C5, respectively), but were reduced by a factor of 5 for brain Arp2/3 (15 nM/s) (Supp. Fig. 5.19, elongation rates calculated from the slopes of the polymerization curves). The abundance of protrusions was virtually identical in GUVs with the two human Arp2/3 isoforms but was reduced

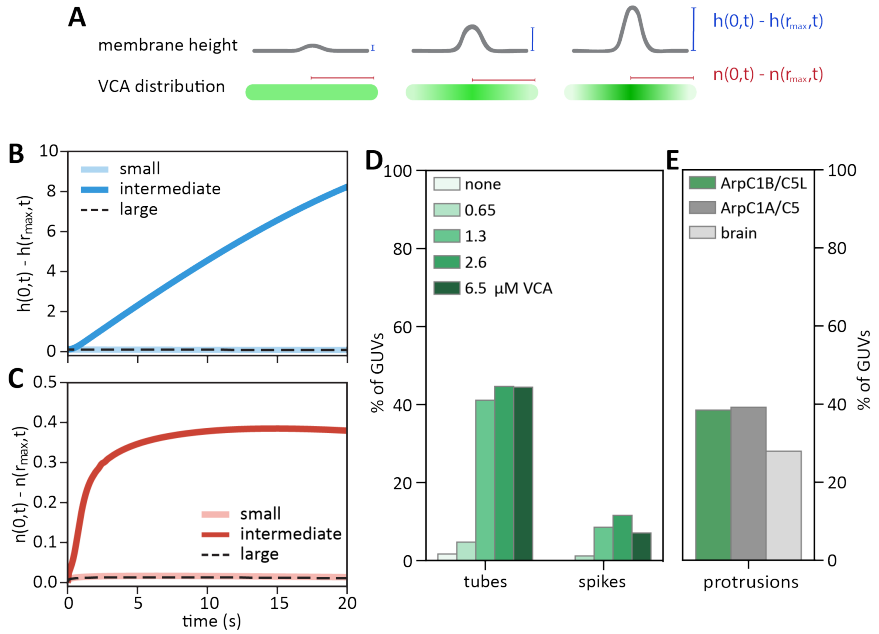

Figure 5.4: **Prevalence of protrusions is predicted by polymerization activity in the actin cortex.** (A) Illustration of the model, where an initial deformation (height h) grows over time and changes the initially uniform VCA distribution n. (B) Evolution of the height difference between the center of the protrusion ($r = 0$) and the boundary of the simulation box ($r = r_{\max}$) for small ($n_s = 0.1$, light blue line), intermediate ($n_i = 0.5$, dark blue line) and large ($n_l = 0.9$, dashed black line) density of VCA on the membrane. (C) Evolution of the VCA concentration difference between the center of the protrusion and the edge of the bounding box for small (light red), intermediate (dark red) and large (black dashed line) densities of VCA on the membrane. (D) Bar plot of the fractions of GUVs with tubes or spikes, as a function of the concentration of VCA in the IAS. $N = 60, 85, 129, 121, 99$ for empty GUVs and GUVs with 0.65, 1.3, 2.6 and 6.5 µM VCA, respectively. (E) Bar plot of the fractions of GUVs with protrusions as a function of Arp2/3 isoform, for a fixed VCA concentration of 2 µM. In all other experiments, we use the human Arp2/3 isoforms ArpC1B/C5L shown here in green. Grey bars denote protrusions formed by cortices with the human Arp2/3 isoform ArpC1A/C5 and commercial Arp2/3, which is a mix of isoforms isolated from porcine brain. $N = 78, 97$ and 111 GUVs for ArpC1B/C5L, ArpC1A/BC5 and brain Arp2/3, respectively.

significantly for brain Arp2/3 (Fig. 5.4 E). While this was a clear drop, the 30 % difference in protrusion formation was much less significant than the 5-fold difference in pyrene actin polymerization speeds (Supp. Fig. 5.19), indicating that the rate of actin elongation was not the most limiting factor in protrusion initiation. This observation is consistent with the results from our model, where we can vary the parameter v, which describes the growth velocity of the actin network, by 3 orders of magnitude without qualitatively changing the outcome (Supp. Fig. 5.21).

5.2.5 Protrusions can form in bouquets

In around 10 % of actin-containing GUVs, we found regions of the GUV where multiple protrusions emanated from the same spot to resemble 'bouquets' (Fig. 5.5 A, B). The bouquet bases were often associated with fuzzy membrane signal like individual protrusions

(Fig. 5.5 C) and were almost always (88 % of 58 bouquets) strongly enriched in actin (Fig. 5.5 D). Bouquets arose across the entire size range of our GUVs, and we also observed multiple bouquets on the same GUV (Fig. 5.5 E). We found bouquets with as many as 11 individual protrusions, and the prevalence of bouquets decreased roughly linearly with increasing number of protrusions (Supp. Fig. 5.20 E). The angle between protrusions in one bouquet tendend to be large (~ 60 – 110° , Supp. Fig. 5.20 E).

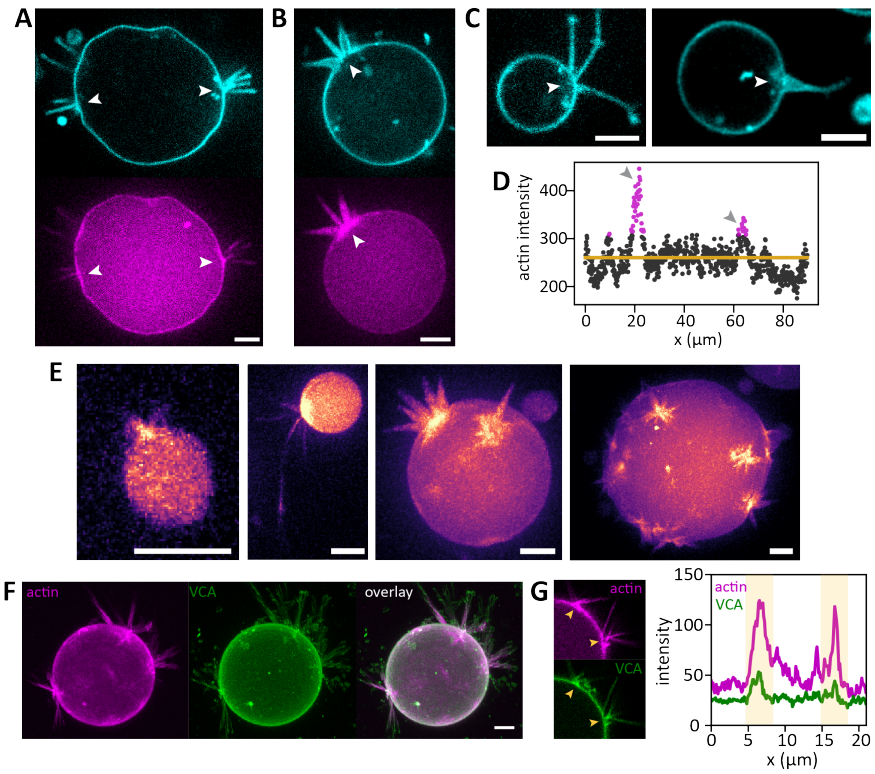

Figure 5.5: **Protrusions occur in bouquets** (A, B) GUVs with bouquets of tubes (A) or spikes (B). Membranes are shown in cyan, actin in magenta, and bouquet bases are indicated with white arrows. The images show the maximum intensity projection of three consecutive 1 µm confocal slices to depict the bouquets more fully. (C) Confocal images often also reveal fuzzy membrane signal (white arrows) at the base of bouquets. (D) Actin intensity profile along the membrane of the GUV shown in (A), clockwise from the top. Grey arrows indicate the positions of the bouquets indicated in (A). Points are highlighted in magenta where the intensity exceeds the mean actin signal (yellow line) by more than 2.5 standard deviations. (E) Gallery of different GUVs with bouquets. We found bouquets on GUVs of all sizes (first image: diameter of 5 µm, last image: diameter of 35 µm), and with widely varying protrusion lengths. One GUV could also have multiple bouquets. Images show maximum intensity projections of z-stacks, convoluted with a 0.5 px Gaussian filter and with actin shown in false color (magma) to better visualize the faint protrusions. (F) Maximum intensity projection of a GUV with protrusion bouquets. Actin is shown in magenta, VCA in green. (G) Single slice of the same GUV, showing two bouquet bases (yellow arrows). Line intensity profiles along the membrane (clockwise from the top) reveal that VCA was also enriched in the actin-rich bouquet bases (yellow shaded regions).

The strong actin enrichment at practically all bouquet bases led us to speculate that

bouquets form when actin accumulates at the base of one tube or spike, increasing the local polymerization force density and initiating the formation of a new protrusion. We surmised that such bouquet-configurations were stable due to strong membrane pinning in the dense actin networks, consistent with the enhanced fuzzy membrane signal which was common at bouquet bases (Fig. 5.5 C). If this is true, then VCA should also be enriched in bouquet bases, as it mediates the interaction between the membrane and the actin cortex by both binding Arp2/3 and capping actin barbed ends [435, 436]. Indeed, confocal microscopy of GUVs where actin was nucleated by Arp2/3 and fluorescently labeled VCA confirmed that VCA was also enriched at the base of bouquets (Fig. 5.5 F, G).

This leads us to a working model for the interactions that shape the GUV surface. First, actin begins to polymerize at the GUV membrane, where it is nucleated by VCA and Arp2/3 (Fig. 5.6, top). If actin polymerization proceeds at similar speeds on an essentially flat membrane, then the actin cortex grows to homogeneously cover the GUV surface, stiffening it (Fig. 5.6, left). If however a small thermally induced membrane deformation happens to coincide with locally enhanced actin polymerization, a positive feedback loop takes hold that recruits more VCA to the deformation, ultimately producing a long and thin membrane protrusion (Fig. 5.6, right). Since large amounts of growing actin filaments accumulate at these protrusion sites, the likelihood increases that they initiate another protrusion in the same area, creating a bouquet (Fig. 5.6, right bottom).

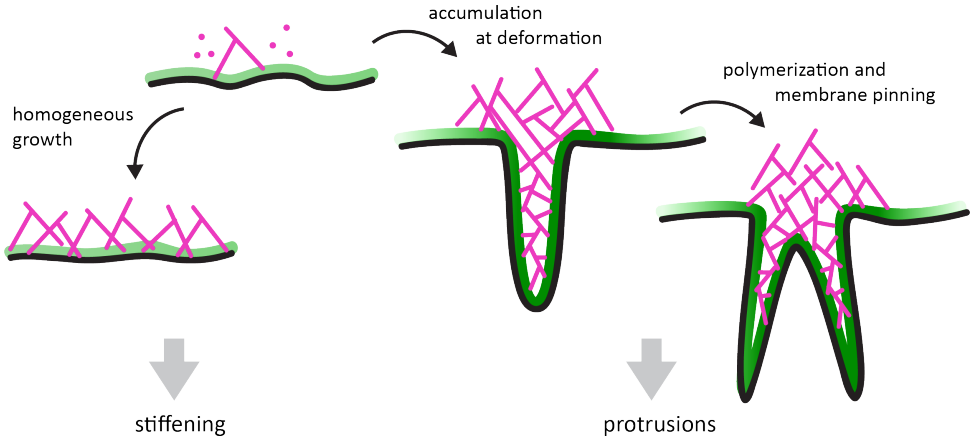

Figure 5.6: **Proposed mechanism of membrane shaping by dynamic actin cortices.** Branched actin networks (magenta) grow on the GUV membrane (black) mediated by VCA (green). Where a sufficient number of growing actin filaments, and thus polymerization forces, accumulate concurrently with a thermally induced membrane deformation, finger-like protrusions can be initiated. The resulting accumulation of yet more actin, and also VCA that mediates actin-membrane-binding, can lead to the formation of more protrusions from the same place, producing a bouquet. Otherwise, the membrane is homogeneously coated with a branched actin cortex that stiffens the vesicle surface.

5.3 Discussion

The actin cortex is a fascinating system from both a biophysical and cell biological standpoint since it confers rigidity to cell surfaces while also being highly dynamic, and actively exerting polymerization forces on the membrane. Here, we probed the interplay of such

dynamic actin cortices with simplified cell membranes by reconstituting them in cell-sized GUVs. We found that our reconstituted actin cortices were thin and dynamic, forming cortical layers with thickness below optical resolution and with turnover times consistent with those reported in living cells. In fact, we are surprised to find such rapid actin turnover in our GUVs, as depolymerization in vitro is usually very slow (~hours [437]). We attribute this rapid turnover to the potency of N-WASP VCA and Arp2/3 as an actin nucleator: when VCA is bound to the membrane, it generates a gradient in the critical concentration for barbed end elongation from the membrane to the GUV lumen [438]. In the presence of the potent nucleator on the membrane, G-actin is rapidly incorporated into the cortical network, depleting the GUV lumen of actin monomers and bringing the concentration there below the critical concentration for barbed end elongation. Consequently, any uncapped actin filaments in the GUV lumen will rapidly depolymerize, feeding their constituent monomers back into the cortical layer. This nonetheless leaves the question how such uncapped actin filaments end up in the lumen. In dendritic actin networks, debranching is thought to be the rate limiting step for disassembly [439] which in vitro happens on the timescale of several minutes in unloaded conditions [135]. However, we see clear evidence of elastic stress throughout the cortical networks in our GUVs, indicating that the branches are under some load. This may explain the rapid turnover in our system, as Arp2/3 dissociation from the mother filament is highly force sensitive, with Piconewton forces on the filaments accelerating debranching to well under one minute [135]. To hone in on the precise mechanisms governing actin disassembly in our system, it would be interesting to compare turnover rates in the presence and absence of cortactin, which (depending on its other binding partners [440]) can protect dendritic actin networks from debranching [129, 441]. While phalloidin is known to also stabilize branches by inhibiting phosphate release from actin [343], it will also interfere with depolymerization of the mother and daughter filament and is thus a less attractive candidate.

The Arp2/3-nucleated actin cortices stiffened GUV membranes and suppressed thermal fluctuations of the membrane. Strikingly, they also generated and stabilized highly anisotropic vesicle shapes over many minutes, more than two orders of magnitude longer than the timescales of actin turnover. This finding is intriguing as it suggests that collective interactions within the dendritic actin networks, and between the network and the membrane, can induce an elastic-like behaviour of GUVs on the whole-cell scale, while the network is locally highly dynamic.

While we could not directly observe how the out-of-equilibrium GUV shapes are formed, we speculate that they arise from buckling of continuous actin cortices with local inhomogeneities in thickness or mechanical properties. We saw evidence of such inhomogeneities in our cortices, whose cortical actin intensity was not constant throughout the cortex (Supp. Fig. 5.7). Time-resolved imaging of GUVs during cortex formation could give new insights into this phenomenon. Our encapsulation technique is robust, but not straightforwardly compatible with using cold temperatures to arrest actin dynamics until imaging, as previous studies have done for actin encapsulation experiments [143]. Instead, it would be necessary to trigger actin polymerization *in situ*, either by permeabilizing the GUV with membrane pores to allow for content exchange with the OAS [119, 442], or by delivering content by targeted membrane fusion [443]. The latter would be a particularly attractive option, as it could also provide excess membrane area on demand. Optogenetics

could be another excellent tool to trigger actin polymerization in a well-defined manner, and a number of such tools have already been developed to control various aspects of the cytoskeleton [444].

Beside stiffening GUV surfaces, we found that dynamic actin cortices also drove protrusion formation in a manner dependent on VCA density on the membrane. Protrusions were generally slim, with base widths ranging from below optical resolution (tubes) up to ~ 3 μm for spikes. Their maximum lengths (~ 30 μm) far exceeded typical lengths of filopodia, which are usually limited to a few microns in length due to G-actin diffusion and buckling of filopodial actin bundles [410, 445]. Importantly, since we did not include any additional actin crosslinking proteins, we do not expect actin in the protrusions to be bundled. Confinement in membrane tubes has been shown to give rise to spontaneous actin bundling [446, 447], which may well happen in the tips of the protrusions we observe. However, this was clearly not the case at the base of the wide, spike-like protrusions, where we observed a clear membrane-localized cortex which did not extend throughout the spike and was thus unlikely to fundamentally differ in architecture from the cortex found outside of the spikes. Instead, we suspect that it had the same branched architecture as in the rest of the cortex, which allowed it to keep spike bases wide open by exerting outward polymerization pressure normal to the membrane, as our spike ablation experiments indicate. Due to the overall low membrane tension and the absence of additional molecular motor activity in the reconstituted actin cortices, protrusions in our GUVs did not retract back into the cortex in the same way as filopodia in living cells [445, 448, 449].

We built a mathematical model which allowed us to probe the mechanism by which spikes are initiated. We expanded previous models by explicitly accounting for the autocatalytic mechanism by which Arp2/3 nucleates actin networks, and studying how protein distribution and membrane deformation evolve over time. With our model, we could predict that protrusion initiation should be favoured at intermediate concentrations of the nucleation promoting factor VCA on the membrane, but suppressed at both low and high VCA concentrations. At low VCA concentration, only single filaments can push on the membrane, which are too weak to initiate a protrusion. At intermediate VCA concentrations, multiple actin filaments can polymerize in close proximity, and due to increased recruitment of VCA to where actin is already present, small membrane deformations are stabilized and develop into larger protrusions. At high VCA concentrations, spatial fluctuations in VCA density become small and growth of a continuous networks is favoured over the formation of local protrusions. Actin barbed-end capping by VCA likely also helps to inhibit protrusion formation at high VCA concentrations [435, 436, 450], although we did not account for this in our model. We experimentally confirmed our model's prediction, and observed that especially large (spike-like) protrusions were suppressed at high VCA concentrations.

By varying the isoform of the Arp2/3 complex which nucleates our cortices, we probed the relative importance of polymerization speed and likelihood of polymerization in regulating protrusion formation. We found that the actin nucleation ability of Arp2/3 did influence its propensity to form membrane protrusions, but much less so than the concentration of VCA. This observation was supported by our mathematical model, which confirmed that actin polymerization speeds can be varied over three orders of magnitude without qualitatively changing the outcome. We therefore conclude that, while fast actin

elongation is beneficial for protrusion formation, the limiting factor in our system is really local VCA availability, suggesting that localized force, not polymerization velocity, is key for generating actin-driven protrusions. This is consistent with the molecular view that Arp2/3-mediated actin nucleation requires the cooperation of two VCA domains to efficiently produce new actin filaments [451]. Note that in our system, VCA mediated not only actin polymerization by activating the Arp2/3 complex, but also actin-membrane adhesion by binding to filament barbed ends. To hone in on the relative contributions of both functions, it would be interesting to test experimentally how varying not the concentration of VCA, but its nucleation efficiency, impacts protrusion initiation. In this chapter we have used the VCA-domain of N-WASP, which is a powerful nucleation promoting factor including two actin-binding WH2-domains. VCA domains from other proteins such as WAVE or WASH possess only one WH2 domain and have been shown to differ in their efficiency in driving actin polymerization through activation of Arp2/3 and in concert with SPIN90 [408, 452], making them interesting candidates to probe the relative importance of actin nucleation and membrane binding.

We note that our simplified experimental model system did not include any cell-substrate-interactions, which are intimately involved in protrusion formation and maintenance in cells, and regulate actin-driven pattern formation [453]. Our work opens up new questions, such as how temporally controlled recruitment of actin binding proteins influences the reorientation of polymerization forces, and what the role of surface adhesion in protrusion formation is. Further, it will be interesting for follow-up work to probe the influence of longer, linear formin- or Arp2/3 and SPIN90-nucleated actin filaments [408], which interpenetrate with branched networks in the cortices of living cells [26, 40], on both surface rigidification and protrusion formation.

Our work demonstrates that actin polymerization alone, without any assistance from actin bundling or membrane curving proteins, is sufficient to produce cell-like protrusions from biomimetic actin cortices. It also highlights the intriguing phenomenon that branched actin cortices can stabilize shapes over timescales much longer than the turnover timescales of actin in the cortex, which may hint at so far underappreciated dependencies of actin turnover on stress or curvature, which should be explored in future research.

5.4 Materials and Methods

5.4.1 Chemicals

The following chemicals were purchased from Sigma-Aldrich: Tris(hydroxy-methyl)aminomethane hydrochloride (Tris-HCl), potassium chloride (KCl), calcium chloride ($CaCl_2$), magnesium chloride ($MgCl_2$), Optiprep (Cat. # D1556-250ML), D-(+)-glucose, DL-dithiothreitol (DTT), Adenosine 5'-triphosphate magnesium salt (MgATP), Adenosine 5'-triphosphate disodium salt (Na_2ATP), proto-catechuic acid (PCA), proto-catechuate-3,4-dioxygenase (PCD), 3-(N-morpholino)propanesulfonic acid (MOPS), ethylene glycol-bis(β-aminoethyl ether)-tetraacetic acid (EGTA), ethylenediaminetetraacetic acid (EDTA), glycerol, β-casein, silicone oil (5 cSt), mineral oil (BioReagent), and chloroform (Uvasol). n-decane (99% pure) was purchased from Arcos Organics. Chloroform, mineral oil and silicone oil were stored in a glove box with an ambient humidity below 1%.

5.4.2 Lipids

All lipids were purchased from Avanti Polar Lipids: 1,2-dioleoyl-sn-glycero-3-phosphocholine (DOPC), 1,2-distearoyl-sn-glycero-3-phosphoethanolamine-N-[methoxy (polyethylene glycol)-2000] (DOPE-PEG2000), 1,2-dioleoyl-sn-glycero-3-[(N-(5-amino-1-carboxypentyl) iminodiacetic acid)succinyl] (DGS-NTA(Ni)) and 1,2-dioleoyl-sn-glycero-3-phosphoethanolamine-N-(Cyanine 5) (DOPE-Cy5). Lipids were stored in chloroform under argon at -20° C.

5.4.3 Expression and purification of human Arp2/3 isoforms

Cloning and construction of baculoviruses

The open reading frames (ORFs) for all Arp2/3 complex subunits were synthesised with codon-optimisation for expression in insect cells by Twist Bioscience. The ArpC3 ORF was synthesised with an additional in frame TEV clevage site followed by a Twin-Strep-tag at its C-terminus. The seven required Arp2/3 complex subunit ORFs were amplified from the Twist Bioscience templates with 15 bp overhangs compatible with the appropriate termini of the linearised pGB vectors [454], which were also amplified at the same time using compatible primers with Q5 polymerase (New England Biolabs). The PCR products and linearised, amplified pGB vectors (ThermoFisher Scientific) were treated with Dpn I (ThermoFisher Scientific) for 1 hour at 37° C prior to gel purification (QIAquick Gel Extraction Kit, Qiagen). Individual purified Arp2/3 subunit ORFs were mixed with the corresponding pGB vector (2:1 insert:vector) in a 10 µL In-Fusion reaction (Takara Biosciences) and incubated for 1 h at 50° C. Chemically competent NEB 5-alpha Competent cells (New England Biolabs) were transformed with 5 µL of the In-fusion reaction and plated on gentamicin-containing LB agar plates. The DNA sequence of the inserted genes and flanking BsaI sites from single clones were verified by Sanger sequencing. In the second step, the Arp2/3 complex subunit ORFs were released from the pGB vectors by cleavage with the BsaI and simultaneously ligated into the final destination vector pGBDest, based on the inter-compatible overhangs flanking the ORFs in a Golden Gate reaction following the method of [454]. In addition, the final position in the co-expression construct was closed off by a "dummy" pGB-dummy-08-16 [454] (BCCM/GeneCorner), that was inserted between the end of the 7th ORF and the pGBDest vector. The ligation mixture was transformed into chemically competent NEB 5-alpha Competent cells (New England Biolabs) and clones were selected on kanamycin-containing LB agar plates. The final expression vector containing the seven Arp2/3 subunit ORFs was verified by Sanger sequencing before being transformed into MAX Efficiency DH10Bac Competent E. coli (Invitrogen) on to antibiotic plates with blue/white X-Gal/IPTG screening. White colonies were used to inoculate 3 ml cultures for overnight growth, followed by purification of bacmid DNA using QIAprep Spin Miniprep kit (Qiagen).

Baculovirus and protein production

To generate baculoviruses, bacmid DNA (2 µg) was mixed with 100 µL SF900-III medium (Life Technologies) and 3 µL FuGene HD transfection reagent, and incubated for 15 min before being added dropwise to 1 x 10^6 adherent Sf21 insect cells in a 6-well plate with 2 mL of SF900-III medium at 27° C. After 3 days, the supernatant (P1 virus) was added to a 50 mL culture of Sf21 cells (1–2x10^6 cells/mL) in SF900-III medium with constant shaking at 110 rpm at 27° C. After 3 days, 50 µL of supernatant (P2 virus) was used to

infect a second 50 mL Sf21 culture and incubated for 3 days. The resulting supernatant (P3 virus) was stored at 4° C and 500 µL were used to infect 0.5 L of Sf21 insect cells at 1–2×10^6 cells/mL for protein production. Three days after infection, cell pellets were harvested by centrifugation, washed with PBS, flash frozen in liquid nitrogen, and stored at -80° C. Frozen cell pellets were resuspended to a final volume of 50 mL in purification buffer (50 mM Tris pH 8, 150 mM NaCl, 2 mM $MgCl_2$, 2.5 % v/v glycerol, 1 mM DTT, 0.2 mM Mg-ATP) supplemented with cOmplete EDTA-free Protease Inhibitor Cocktail (Roche) and BaseMuncher Endonuclease (5 µL per 50 mL) (Abcam, Cat. # ab270049). Resuspended cells were lysed by sonication for 120 seconds (5 s on followed by 10 s off) at 4° C using a Branson Digital Sonifer at 40 % power. After 1 hour incubation, EDTA and EGTA were added to a final concentration of 1 mM and 5 mM respectively. The lysate was then clarified by ultracentrifugation in a Type 45 Ti rotor (Beckman) at 41,000 rpm for 45 min, followed by passage through a 0.45 µm syringe filter. The resulting filtrate was loaded onto a 1 mL StrepTrap XT column (Cytiva) attached to an ÄKTApure system (GE Healthcare) at a rate of 1 mL/min. After washing with 30 column volumes of purification buffer, the bound Arp2/3 complex was eluted with 15 column volumes of Buffer BXT (IBA) supplemented with ATP, DTT, EGTA, $MgCl_2$ and glycerol. Fractions containing Arp2/3 were pooled and loaded on a Superdex 200 Increase 10/300 GL column that was pre-equilibrated with purification buffer containing 5 % v/v glycerol. Column Fractions (0.4 mL) were analysed by SDS-PAGE (4 – 12% Bolt Bis-Tris Plus gels (Invitrogen) stained with Quick Coomassie Stain (Neo Biotech)). Fractions with Arp2/3 complexes were analysed by mass photometry (Refeyn) to confirm that all seven subunits were stoichiometric prior to being pooled and concentrated to ~4-5 mg/mL before aliquotes were flash-frozen in liquid N_2 and stored at -80° C. An SDS PAGE gel of Arp2/3C1A/C5 and Arp2/3C1B/C5L is shown in Supp. Fig. 5.22.

5.4.4 Other proteins

Rabbit skeletal muscle actin, 10xHis-VCA from murine N-WASP, and Arp2/3 from porcine brain were obtained, labeled, prepared and stored as described in chapter 3 and 4.

5.4.5 GUV preparation

Buffers

Buffer conditions were kept consistent between all experiments. G-actin was stored in G-buffer (5 mM Tris-HCl pH 7.8, 0.2 mM $CaCl_2$, 0.2 mM Na_2ATP, 1 mM DTT) and mixed in a 1:10 molar ratio of fluorescent and unlabeled monomers for imaging. The inner aqueous solution (IAS) inside the GUVs contained F-buffer (20 mM Tris-HCl pH 7.4, 50 mM KCl, 2 mM $MgCl_2$, 1 mM DTT, 0.5 mM MgATP, supplemented with 6.5 % V/V optiprep to increase IAS density for GUV formation), as well as 0.5 µM PCD and 10 mM PCA to minimize photobleaching [387], 8 µM actin, and other proteins as appropriate for each experiment. In order to match the osmotic pressure across the GUV membranes, we prepared inner and outer buffers at controlled osmolarity, measured using a freezing point osmometer (Osmomat 010, Gonotec, Germany). The IAS osmolarity was 168 mOsm/kg in all experiments, and was not measurably changed by the addition of proteins. The outer aqueous solution (OAS), in which the GUVs were first produced, contained 190 mM glucose (200 mOsm/kg). Immediately after GUV formation, we added a solution of 40 mM Tris-HCl pH 7.4 and 90 mM glucose (182 mOsm/kg), to stabilize the pH outside the GUVs and reach

final buffer conditions of 10 mM Tris-HCl pH 7.4 and 170 mM glucose, with an osmolarity of 189 mOsm/kg to slightly deflate the GUVs and increase the available excess membrane area.

Oil phase

Lipid stocks were prepared in chloroform solution. 94.985 % DOPC was mixed with 0.01 % DOPE-PEG2000 to increase GUV yield [138], 5 % DGS-NTA(Ni) to recruit VCA, and 0.005 % DOPE-Cy5 for fluorescent visualization. The oil solutions were prepared as described in chapter 4.

GUV formation and handling

GUVs were formed following the eDICE method we developed in chapter 4, using 25 µL of IAS for each experiment. The osmotic pressure difference between the inside and outside of a GUV, and hence its membrane tension, can be regulated by adjusting the osmotic mismatch between IAS and OAS. We deflated the GUVs by placing them in a hypertonic OAS of +21 mOsm/kg higher osmolarity than the IAS. This yields an average excess membrane area of 7.6 % due to osmotic deflation [388].

5.4.6 Microscopy

Image acquisition

GUVs were observed either in ibidi 18-well µ-slides (Cat. # 81817) or in chambers created by mounting silicone spacers (Sigma Aldrich, Cat # GBL665106) on # 1.5 coverslips (Superior Marienfeld, Cat. # 0107222). The wells were passivated by incubating with a 0.1 mg/mL β-casein solution in 10 mM Tris-HCl pH 7.4 for at least 15 min, rinsed with MilliQ water and dried under N_2 flow before GUV addition. Upon GUV addition, we closed the chambers to prevent solvent evaporation and keep the osmotic deflation of the GUVs constant. Ibidi wells were closed with the appropriate lid, which prevented evaporation over several days. Chambers made from silicone spacers were sealed from the top with a glass coverslip, affixed to the spacer with vacuum grease (Dow Corning high vacuum silicone grease, Sigma-Aldrich Cat. # Z273554). Images were acquired either on an inverted Olympus IX81 confocal spinning disk microscope equipped with 491 and 640 nm CW lasers, a 100x oil immersion objective (UPlanSApo, WD 0.13 mm, NA 1.4) and an EM-CCD Andor iXon X3 DU897 camera, or on an inverted Leica Stellaris 8 point scanning confocal microscope equipped with a white light laser, a 63x glycerol immersion objective (HC PL APO, WD 0.3 mm, NA 1.2) and HyD S detector operated in photon counting mode. Imaging settings were identical to those described in chapter 4, except for FRAP experiments on fluorescent VCA (see below).

FRAP experiments

All FRAP experiment were performed on a Leica Stellaris 8 microscope.

Probing actin turnover First, a z-stack of the GUV was acquired with a step height of 1 µm, to verify that the actin cortex was homogeneous around the GUV. We imaged both membrane and actin with a pixel dwell time of 3.16 µs and 2 and 13.7 % laser power, respectively. The FRAP experiment was then performed on the GUV midplane: After 5

frames capturing the initial actin distribution (488 nm laser at 13.7 % laser power, pixel dwell time 6.34 µs), a 3 x 6.4 µm rectangular ROI was bleached three times sequentially, using 483, 488, and 492 nm laser lines in parallel at 100 % intensity each and with a pixel dwell time of 6.34 µs. This was effective in reducing cortex fluorescence by at least 80 % in the FRAP region. The ROI size was chosen such that it was large enough that analysis was robust against small thermal fluctuations in GUV position and orientation, while most of the actin cortex remained unaffected in GUVs with typical diameters around 10 µm. The recovery period was then recorded in three stages, first acquiring 10 images with a frame rate of 0.51 fps, then 10 images at 0.33 fps, and finally 30 images at 0.2 fps, and otherwise using the same settings as for the pre-bleach images. FRAP data analysis was performed using a combination of the ImageJ [340] 'plot profile' function and a custom-written python script. First, we used ImageJ to extract data along a circular ROI at the GUV membrane, at a line width of 3 pixels. The correct positioning of the ROI was confirmed by eye for each frame, and if necessecary adjusted to avoid artefacts from small movements of the GUVs. The resulting intensity profiles were then smoothed and fluorescence intensity in the bleached region was extracted over time. Full details on data processing and analysis are given in the Supplementary Information, Fig. 5.7. Fluorescence recovery was fitted by a single exponential function with the form $I(t) = I_{\text{inf}} - A \cdot \exp\left(-\frac{t}{\tau}\right)$, where τ is the characteristic recovery time. We measured 13 GUVs from 2 samples and excluded results where the fit was poorer than $R^2 = 0.8$.

Probing membrane fluidity and VCA mobililty For FRAP experiments on VCA and the membrane, the procedure was essentially the same as for probing actin turnover. However, diffusion of VCA and lipids was much more faster than actin turnover, so we could capture the full recovery period by imaging at a single framerate (650 ms per frame for VCA, 249 ms for lipids) for 50 frames. For FRAP experiments, fluorecent VCA was bleached using three lines of the white light laser (499, 491 and 483 nm) at 100 % laser power each, and imaging was performed using the 499 nm line at 0.5 % power. The pixel dwell times was 6.34 µs in all cases. FRAP on the membrane was performed with identical settings as dumbbell FRAP described in chapter 4, except that the FRAP region was always chosen as a 3 x 5 µm rectangle at one side of the GUV.

Photoablation

GUV cortices were ablated, either in their entirety or at the base of spikes, by illumination with a 1.6 W UV laser diode at 405 nm on the Leica Stellaris 8 microscope. Imaging settings for both actin and membrane imaging were identical to those described for FRAP experiments. We first recorded a z-stack of the GUV before ablation. Before ablation, one image of the actin distribution in the midplane of the spike was then acquired. A rectangular ROI was placed on the base of the spike, with the exact dimensions adjusted to fit each spike individually. Typically, the ablated region was 3-3.5 µm wide and around 1.5 µm high. This region was then illuminated with the 405 laser at 100% laser power and a pixel dwell time of 6.24 µs. Three consecutive ablation rounds, typically taking around 4 s in total, were sufficient to collapse the base of membrane spikes. For ablation of the entire GUV cortex, we followed the same overall procedure but defined the ablation ROI to span the entire GUV, instead of just the spike base. We generally ablated the entire cortex using

8 consecutive illuminations with the UV laser, but rounding of the GUV surface and the start of thermal undulations was already visible after 3 ablation rounds. We checked by visual inspection of the actin and membrane signals that no membrane damage occurred.

Tracking membrane displacements

Time-lapse videos of the equatorial slice of two GUVs (acquired at 1 fps and covering a total of 50 s) were visualized in a color-coded projection using the ImageJ plugin Temporal Color Code [455]. The same videos were then analyzed using a custom-written python script to measure the average membrane displacements over time. The membrane tracking code was kindly provided by Lennard van Buren. The images were first smoothed by convolving with a Gaussian filter of 3 px kernel size. Radial line intensities were then extracted in 1° angular intervals, and were smoothed by a Gaussian filter with 3 px kernel size. The membrane position was then set as the location of maximum intensity in the line profile. Displacements of each angular membrane segment between consecutive frames were measured, and the root mean square displacement X_{rms} of the ensemble of membrane segments was computed.

Analysis of GUV sizes and protrusions

GUV sizes and membrane protrusions were manually analyzed in Fiji [340]. GUV sizes were measured by fitting the GUV with the largest circle which did not encompass thin protrusions. To measure the width of a protrusion, we extracted the membrane intensity profile along a straight line across the base of the protrusion, and extracting the distance between the membrane intensity peaks on either side. If the protrusion base was so thin that no separate peaks could be resolved, we set the width to zero and classified the protrusion as a tube, otherwise we classified it as a spike. Protrusion lengths were measured from the base to the outermost visible tip of the protrusion. The number of protrusions per bouquet was counted manually, and the widest angle between any two protrusions in the same bouquet was measured using the Fiji 'Angle' tool. Bouquets were always dense and well-separated from each other, so protrusions could be unambiguously counted towards only one bouquet. Actin intensity profiles were extracted by manually tracing the GUV membrane with an 8 px-wide segmented line ROI. To classify GUVs in the most unbiased way possible, we first inspected only the membrane channel in a z-stack of each GUV, and noted whether any membrane structures (tubes, spikes, bouquets, inward-pointing fuzz) were visible. Afterwards, we inspected the actin channel and recorded whether there was any visible actin enrichment at any of the membrane structures. To avoid any artefacts from day-to-day variability in encapsulation efficiency, we only quantitatively compare samples produced on the same day. Independent repetitions of the same experiments differed in the exact numbers, but consistently showed the same trends.

5.4.7 Actin polymerization assay

Pyrene actin polymerization assays were performed in the same way as in chapter 4. All measurements reported here were repeated at least twice.

Code availability

Python-based data analysis scripts used in this chapter are available on GitHub: github.com/BioSoftMatterGroup/GUV-deformations

Acknowledgements

The authors thank Kristina Ganzinger (AMOLF) for the kind gift of the VCA plasmid, and for hosting us to perform pyrene assays in her lab. The GoldenBac vectors and guidance were kindly provided by Thomas Puehringer in the Alessandro Costa lab at the Francis Crick Institute. Jeffrey den Haan and Erik van Lagen are thanked for protein purification, and James Conboy for assistance with the cytochalasin D experiments. We thank Dyche Mullins (UCSF), Stephan Grill (MPI-CBG Dresden), Dan Fletcher (UC Berkeley) and Guillaume Charras (UCL) for helpful and inspiring discussions. Jérémie Capoulade and Michal Shemesh are thanked for useful discussions and instruction in quantitative confocal microscopy and FCS, and Heike Glauner (Leica) for help with FCS analysis. We acknowledge financial support from The Netherlands Organization of Scientific Research (NWO/OCW) Gravitation program Building A Synthetic Cell (BaSyC) (024.003.019).

5.5 Supplementary Information

5.5.1 FRAP Analysis

We analyzed FRAP data by first extracting an intensity profile along the GUV cortex and smoothing it (Fig. 5.7 A, B) for each frame. To correct for photobleaching during acquisition, we then defined a reference ROI along with the bleached FRAP ROI (Fig. 5.7 C, D). As a reference region, we chose a section of at least 10 µm long and no closer than 10 µm to the bleached region, to avoid any artefacts from broadening of the bleached region. The reference region was chosen individually for each GUV to ensure that it did not show large intensity fluctuations over time which might impact the analysis. Such fluctuations sometimes happened when a bright actin spot in the GUV lumen came close to the cortex. We then normalized the entire profile to the reference intensity (Fig. 5.7 E) and computed an average intensity in the FRAP region for every frame. To avoid artefacts from spatial inhomogeneities in cortical actin fluorescence, we normalized the data again such that the average intensity in the FRAP region before bleaching ($t < 0$) was 1. We computed the asymptotic recovered intensity I_{inf} by calculating the average intensity in the last three time points, and fitted the data to a single exponential decay with characteristic time τ, recovering to that asymptotic value ($I(t) = I_{\text{inf}} - A \cdot \exp\left(-\frac{t}{\tau}\right)$). We considered fits valid if they were better than $R^2 = 0.8$.

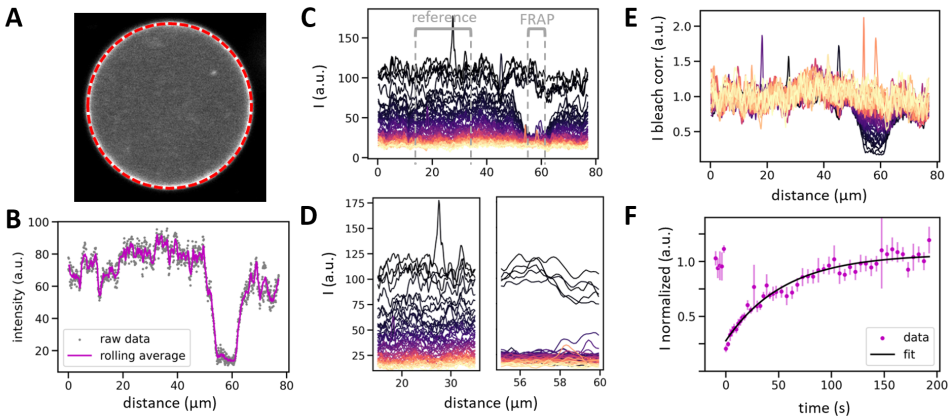

Figure 5.7: **FRAP analysis procedure.** Here we show a FRAP experiment assessing actin turnover in the cortex, but the data analysis procedure was identical for FRAP of the membrane or VCA. (A) In each frame, we extract the intensity profile along the cortex (red dashed line) using the 'plot profile' function of ImageJ along a segmented line with a linewidth of 3 px. (B) The intensity profile (grey points) is smoothed by pre-processing with a rolling average over 3 data points (purple line). Here we show the intensity profile immediately after bleaching (dip around 60 µm). (C) Intensity profiles over time before correcting for bleaching. Each line represents one frame, with brighter colours indicating later times. Bleached region and reference region are indicated in grey. (D) Zoom-in on the reference (left) and FRAP ROI (right). We use the average intensity in the reference ROI to correct the whole intensity profile for bleaching in each frame. (E) Intensity profiles over time after correcting for photobleaching during image acquisition. Brighter colours indicate later times. (F) Fitting procedure. Data points show the average intensity in the FRAP region and error bars indicate the standard error of the mean intensity in the bleached region. We normalized the bleach-corrected data again such that the mean intensity before bleaching ($t < 0$) was 1. The black line shows a single exponential fit recovering to an asymptotic intensity I_{inf}.

To assess fluorescence recovery in the membrane, we performed the same procedure on vesicles in which we increased the membrane dye concentration 10-fold compared to our other experiments, where we kept membrane labeling as low as possible to avoid any artefacts from fluorescence crosstalk into the actin channel. The acquisition and analysis were identical to the actin cortex experiments, but we acquired images with a lower resolution (128x128 pixels as opposed to 256x256) and with shorter pixel dwell times, in order to be able to capture the rapid fluorescence recovery in the membrane.

Measuring VCA mobility on the membrane again followed the same procedure, but we were able to keep the field of view at 256x256 pixels, since fluorescence recovery in VCA was less rapid than in the membrane, and thus did not require such fast acquisition.

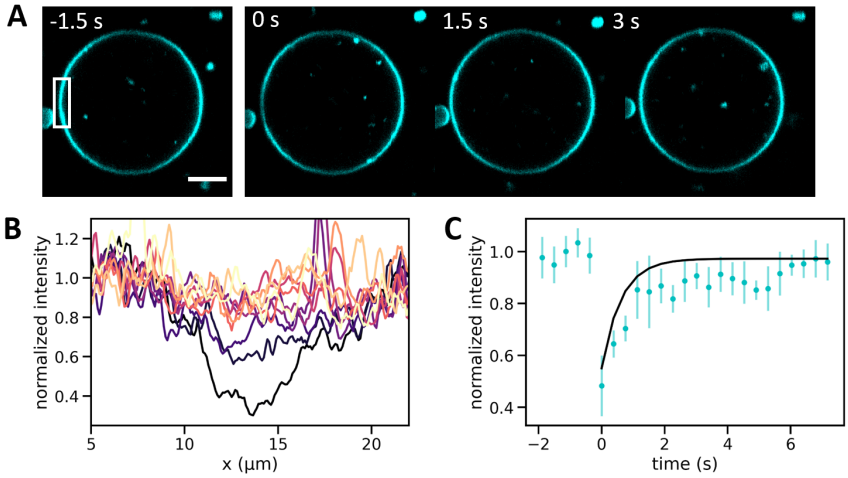

Figure 5.8: **FRAP measurements of lipid mobility.** (A) Snapshots of a GUV membrane before and after bleaching of the rectangular region marked in white. (B) Line profiles in the FRAP region, starting at $t = 0$ immediately after bleaching (darkest line) and up to 3.5 s post-bleach (brightest line). (C) GUV membranes show exponential fluorescence recovery with a characteristic timescale of $\tau = 1.6$ s (solid line). Scale bar: 5 µm.

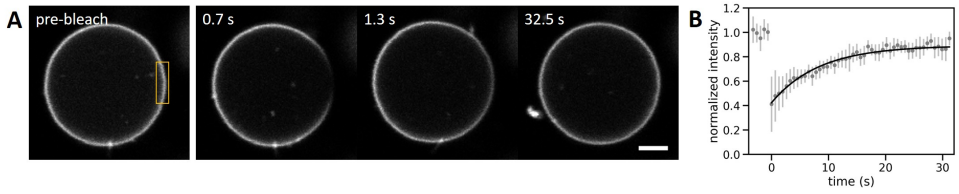

Figure 5.9: **VCA diffuses freely on GUV membranes.** (A) Snapshots of a GUV containing 6.5 µM VCA labeled with AlexaFluor488 C5-maleimide, before bleaching and at t=0.7, 1.3, and 32.5 s after bleaching the region indicated by the yellow rectangle. Scale bar: 5 µm. (B) Normalized VCA fluorescence intensity in the FRAP region over time, with data points and error bars denoting mean fluorescence intensity and standard deviation in the FRAP region. The curve was well described with a single exponential recovery with characteristic time $\tau = 8.4$ s (black solid black line).

5.5.2 Fluorescence correlation spectroscopy

We used fluorescence correlation spectroscopy (FCS) to determine the diffusion coefficient of fluorescently labeled actin monomers in our GUVs. All measurements were performed on a Leica Stellaris DMI8 micoscope equipped with a white light laser and a 63x water immersion objective (HC Plan APO 63x/1.20 W Corr CS2), at a sample temperature of 25 °C (controlled by an Okolab environmental control box). We measured on # 1.5 ibidi 18-well µ-slides, 5.0 µm above the coverslip surface. Optimization of photon yields, calibration of the FCS focal volume, measurements and fitting procedures were identical to those described in chapter 4.

Measurements were done on AlexaFluor488-labeled bulk solutions of actin at a nominal concentration of 10 nM fluorescent monomers. Note that we measured actin in G-buffer supplemented with 6.5 % Optiprep here, as this allowed us to achieve better fits and therefore more reliable measurements of the concentrations of actin monomers and free dye molecules, as well as the actin monomer diffusion coefficient.

Monomer diffusion coefficients averaged 96.7 ± 8.4 µm^2/s (Supp. Fig. 5.10).

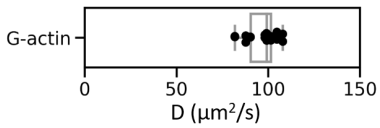

Figure 5.10: **Diffusion coefficient of G-actin in the IAS buffer as measured by FCS.** We found a mean diffusion coefficient of 96.7 ± 8.4 µm^2/s, $N = 9$ measurements from 3 separate samples.

5.5.3 Actin depolymerization by cytochalasin D

Exposure of biological membranes to high laser light intensities has been reported to produce membrane shape transformations and can lead to oxidative damage of the sample [456]. We therefore performed an experiment to independently confirm our conclusion that removing the actin cortex from GUVs returns their shapes to those predicted for fluid vesicle membranes. To this end, we used the membrane-permeable drug cytochalasin D, which is thought to act specifically on dynamic actin [457, 458], to depolymerize the actin cortices. We prepared GUVs with cortices composed of 8 µM actin, 6.5 µM VCA, and 50 nM ArpC1B/C5L, and acquired confocal z-stacks of the sample (Fig. 5.11 A). As expected, we observed many globally deformed GUVs with bright actin cortices. We then added cytochalasin D to a final concentration of 10 µM based on typical application of the drug in cells [116] and incubated the GUVs with the drug for 90 minutes. Finally, we acquired another set of confocal z-stacks (Fig. 5.11 B), which revealed that the distinctive actin cortices had disappeared, and most vesicles instead showed a homogeneous, bright luminal actin signal. Importantly, we no longer observed any vesicles with stable, large-scale deformations.

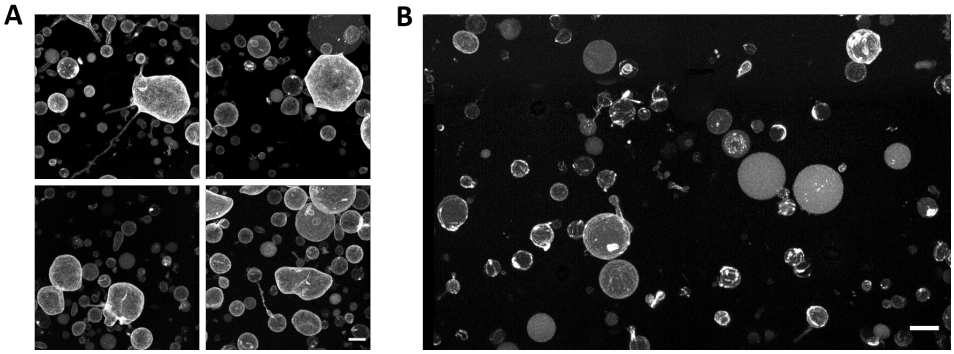

Figure 5.11: **Cytochalasin D-induced actin depolymerization removes actin cortices and returns deformed GUVs to a spherical shape.** (A) Typical GUV morphologies before treatment with cytochalasin D. We observe many globally deformed GUVs, where actin is localized strongly to the membrane. (B) Typical GUV morphologies after incubating the same sample with 10 µM cytochalasin D for 90 minutes. We no longer observe globally deformed GUVs and now find actin almost exclusively in the GUV lumen. All images show maximum intensity projections of confocal stacks at 1 µm step height. Scale bars: 10 µm.

5

5.5.4 Modelling the formation of protrusions

To model membrane deformation as a function of the density of the Arp2/3 activator VCA on the membrane, we assumed a VCA response function $f(n)$ that describes how the VCA density n affects actin polymerization. Multiplying $f(n)$ by the (maximum) actin polymerization velocity v gives the effective actin polymerization velocity, which determines how fast the membrane is pushed outward. We chose a sigmoidal shape for $f(n)$ to reflect the reasonable assumptions that we need a minimal concentration of VCA for actin to start polymerizing, that actin polymerization saturates at high VCA density, and that in between we expect actin polymerization to increase linearly with VCA density

$$f(n) = \frac{1}{2}\left[\tanh(a(n-b)) + 1\right]. \tag{5.3}$$

We set $b = 0.5$, i.e., the inflection point of the response function is at half the membrane coverage of VCA. We arbitrarily set $a = 10$ to interpolate smoothly between the regime of low and high VCA density. We note, however, that our qualitative results did not depend on the exact choice of a and b (Supp. Fig. 5.13). The resulting function is plotted in Fig. 5.12.

We considered the VCA density n on a 2D membrane, which we described by the membrane height function h. We assumed rotational symmetry, i.e., $n = n(r,t)$ and $h = h(r,t)$, and rewrote Eqs. (5.1) and (5.2) in polar coordinates as a function of the distance r to the z-axis

$$\begin{aligned}\frac{\partial n(r,t)}{\partial t} &= D\left(\frac{1}{r}\frac{\partial}{\partial r} + \frac{\partial^2}{\partial r^2}\right) n(r,t) \\ &\quad + \alpha n(r,t)(1-n(r,t))\left[\left(\frac{1}{r}\frac{\partial}{\partial r} + \frac{\partial^2}{\partial r^2}\right) h(r,t)\right]^2 \end{aligned} \tag{5.4}$$

$$\partial_t h(r,t) = v f(n(r,t)) - w h(r,t), \tag{5.5}$$

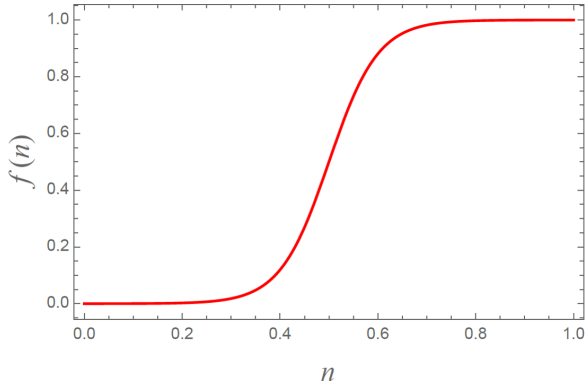

Figure 5.12: **VCA response function** The VCA response function $f(n)$ for $a = 10$ and $b = 0.5$ (see Eq. (5.3)) reflects that some minimum local density of VCA on the surface is necessary to initiate actin polymerization, and that actin polymerization saturates above a certain VCA density.

with the Laplacian in polar coordinates, $\nabla^2 = \left(\frac{1}{r}\frac{\partial}{\partial r} + \frac{\partial^2}{\partial r^2}\right)$.

To solve Eqs. (5.4) and (5.5) we had to set up suitable initial conditions. To represent the cases of a low, intermediate and high homogeneous initial density of VCA, we assumed that the membrane coverage was *sparse*, i.e. , $n_{\mathrm{l}}(r,0) = 0.1$, *intermediate*, i.e. , $n_{\mathrm{i}}(r,0) = 0.5$ or *dense*, i.e. , $n_{\mathrm{h}}(r,0) = 0.9$. To represent a localized membrane deformation, we chose the membrane height function to initially have a Gaussian shape, $h(r,0) = A\,\mathrm{e}^{-r^2/\sigma^2}$, with amplitude A and width σ. As we wanted to investigate the effect of a small initial membrane perturbation, we chose for the amplitude $A = 0.1$ µm and for the width $\sigma = 0.2$ µm, similar to [352].

In order to complete the model, we also had to specify the boundary conditions. To shorten our notation, in the following we use primes to denote radial derivatives. We considered a membrane within a spherical domain. To avoid numerical instability we chose a cutoff of $r_{\mathrm{min}} = 10^{-6}$ µm at the inner domain boundary. In addition, we set the outer domain boundary to $r_{\mathrm{max}} = 10$ µm. We assumed a no-flux boundary condition of VCA at both boundaries, i.e. $n'(r_{\mathrm{min}}, t) = 0$ and $n'(r_{\mathrm{max}}, t) = 0$, respectively. Moreover, we assumed that typically membrane spikes are pushed outward by more than one actin filament sharing the membrane load, as shown in simulations [447]. Therefore, we assumed that the membrane remains flat at the spike center, $h'(r_{\mathrm{min}}, t) = 0$. Finally, we assumed that the membrane remains flat far from the initial deformation, $h'(r_{\mathrm{max}}, t) = 0$.

We solved Eqs. (5.4) and (5.5) with the numerical Method of Lines from *Mathematica*. For the spatial discretization we used the 'TensorProductGrid' method. In order to provide sufficient numerical accuracy, we manually set the minimum number of points for each dimension of the grid to 1000, by using the 'MinPoints' method. To represent the initial time domain of membrane spike initiation, we chose the time range between 0 and 20 s. The parameter values that were used for the calculations are summarized in Table 5.1.

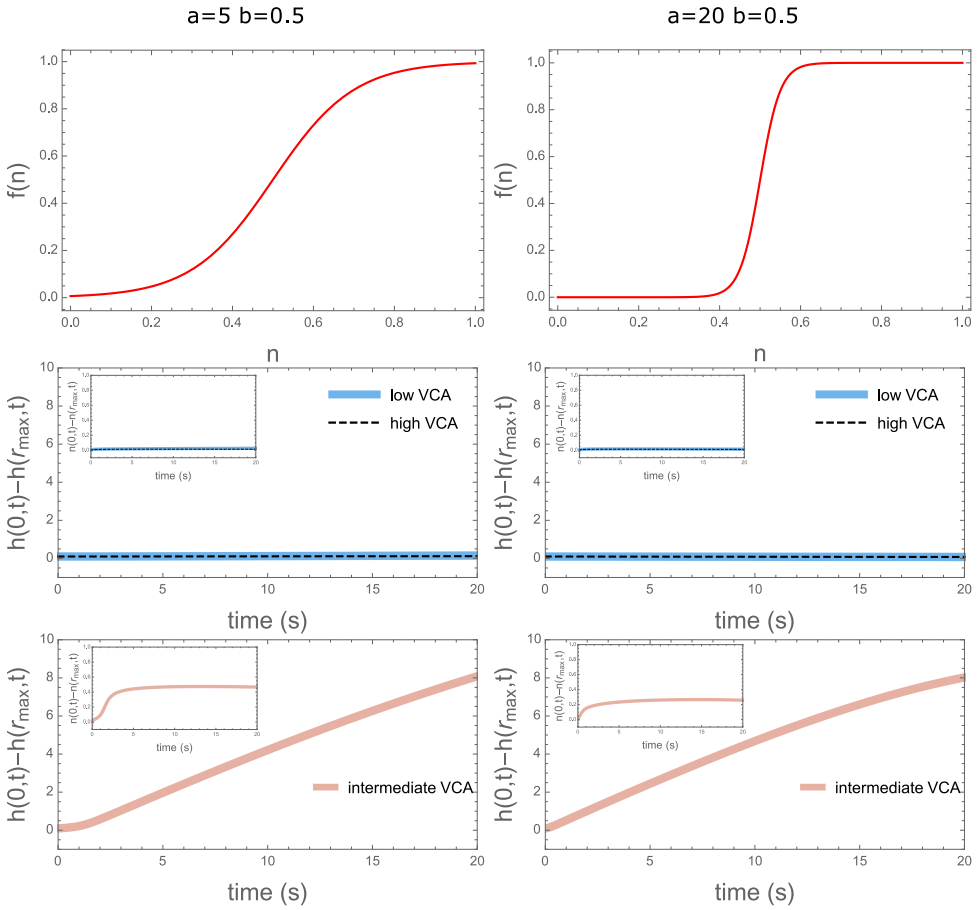

Figure 5.13: **VCA response function: influence of parameters a and b.** Response functions with two different sets of parameters a and b (top panels) result in comparable predicions for the membrane height evolution (middle and bottom panels) and VCA distribution (insets in middle and bottom panels).

Table 5.1: Summary of the model parameters.

Parameter	Used value	Reference
VCA diffusion constant D	$1\,\mu\text{ms}^{-2}$	[432]
Actin (maximum) polymerization velocity v	$1\,\mu\text{ms}^{-1}$	[432]
Rate of membrane deformation relaxation w	$0.013\,\text{s}^{-1}$	[431]
VCA enrichment constant on the membrane α	$0.1\,\mu\text{ms}^{-2}$	–
VCA response function parameter a in Eq. (5.3)	10	–
VCA response function parameter b in Eq. (5.3)	0.5	–

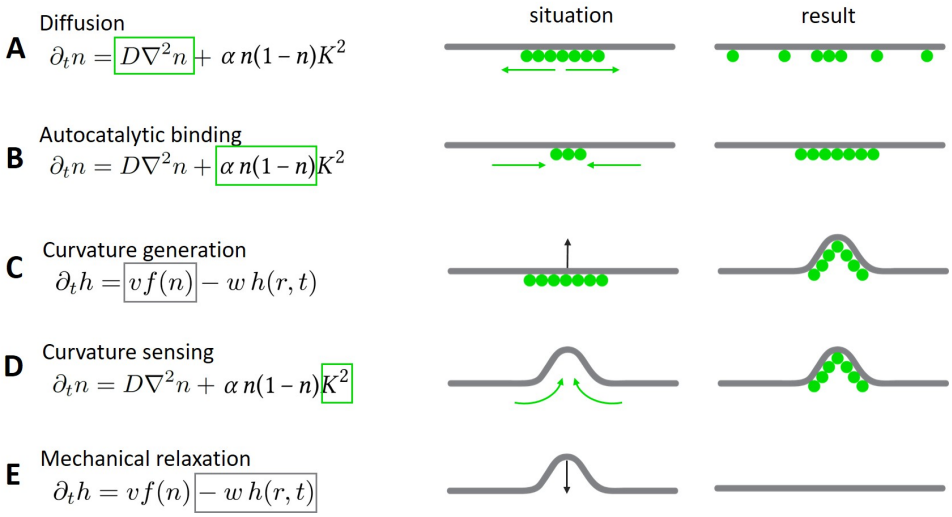

Figure 5.14: **Interplay between membrane deformation and VCA density in the model of protrusion formation** Schematic representations of the interaction terms in the model, illustrating how the different terms drive the evolution of the membrane position (grey) and VCA surface density (green). (A) **Diffusion** smears out concentrated regions of VCA along the membrane. (B) **Autocatalytic binding**, modeled after the autocatalytic growth of Arp2/3 nucleated actin networks, means that new VCA accumulates preferentially where VCA is already bound. (C) **Curvature generation** depends on VCA density: Where there is a lot of VCA (and thus actin polymerization), membranes are displaced and thus bent. (D) **Curvature sensing** emerges because a membrane deformation implies the presence of actin and thus mother filaments, with which VCA can interact to generate new daughter filaments. Via actin, VCA is thus recruited to locations where the membrane is curved. (E) **Mechanical relaxation** occurrs since a deformed membrane experiences a restoring force driving it back to a flat conformation.

5.5.5 Supplementary figures

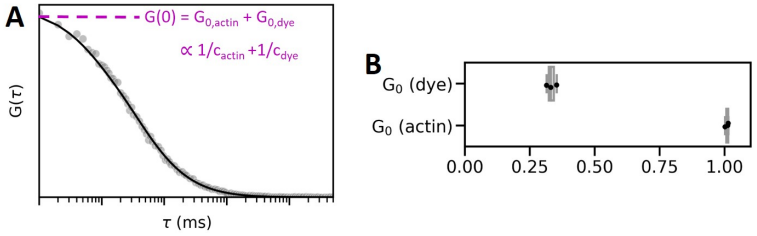

Figure 5.15: **Actin contains contamination from unbound dye.** (A) Example of a fluorescence autocorrelation function $G(\tau)$ as a function of lag time τ, measured by fluorescence correlation spectroscopy (FCS). In this plot, the total diffusion amplitude G(0) is the sum of the diffusion amplitudes of all fluorescent compounds that contribute to the fluorescence decorrelation measurement. Each diffusion amplitude is inversely proportional to the concentration of the fluorescent compound. (B) Box plot of diffusion amplitudes for free AlexaFluor488 and actin-bound AlexaFluor488 measured by FCS, in a sample of AlexaFluor488-labeled actin in G-buffer. No extra free dye was added, yet the diffusion amplitude of the dye was smaller than that of the labeled protein, indicating that the sample contains a significant amount of free dye.

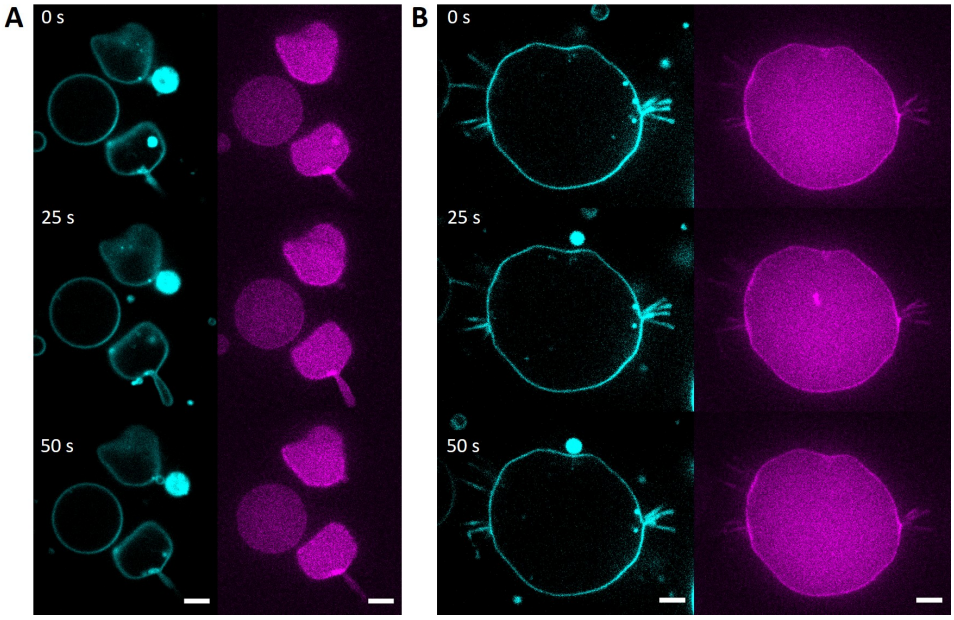

Figure 5.16: **The surfaces of deflated, cortex-supported GUVs are rigid.** Confocal images of (A) small and (B) large deflated GUVs (membrane in cyan) with an actin cortex (magenta). GUV shapes remain unchanged over the course of 50 s. Scale bars: 5 µm.

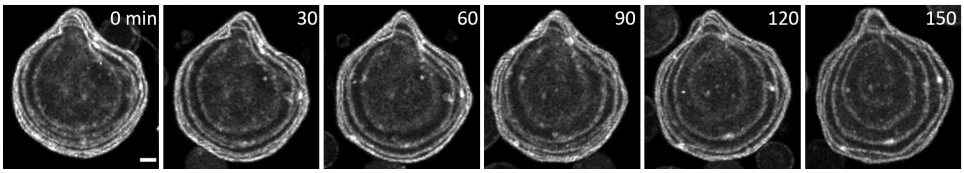

Figure 5.17: **GUVs can retain their shape for up to several hours.** Maximum intensity projections of a GUV whose shape is stabilized by an actin cortex. Timelapse imaging with a framerate of two frames per hour reveals that GUV shapes can remain stable over the course of many minutes, up to several hours. To minimize photodamage to the actin cortex, the confocal z-stacks were acquired with a step height of 3 µm. Scale bar: 5 µm.

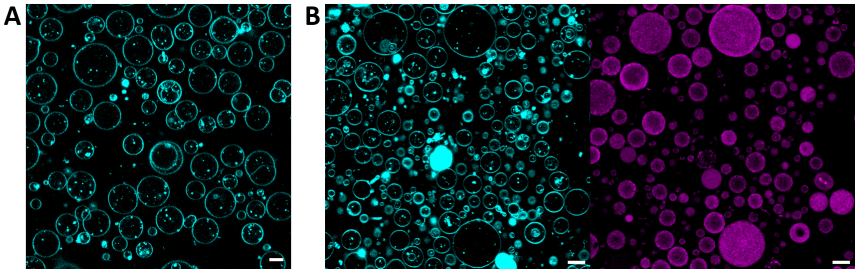

Figure 5.18: **Protrusions do not form in the absence of actin, or when actin polymerizes in the GUV lumen.** Typical confocal image of GUVs (cyan) with (A) or without (B) actin (magenta) spontaneously polymerizing in the cytoplasm. The GUVs are produced in the same way as all others in this chapter, but VCA and Arp2/3 are omitted from the IAS. Scale bars: 10 µm.

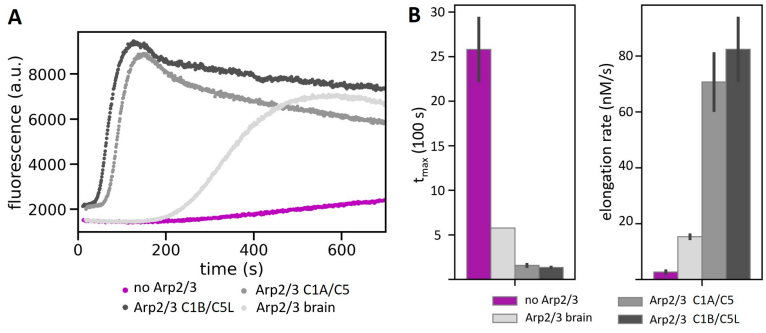

Figure 5.19: **Pyrene fluorescence-based quantification of actin polymerization by different Arp2/3 isoforms.** (A) Typical examples of pyrene polymerization curves of actin without nucleating proteins (magenta) or with different isoforms of Arp2/3 (shades of grey). (B) Time after which the maximum pyrene fluorescence was reached, and elongation rate at the time when half of all actin was polymerized. Bars and error bars denote the average of 2 measurements and their SEM. Quantitative analysis of the polymerization curves reveals that while all Arp2/3 isoforms speed up actin polymerization significantly compared to spontaneous actin polymerization, commercially available Arp2/3 isolated from porcine brain was around a factor of 5 less effective at promoting actin polymerization than the pure human isoforms ArpC1A/C5 and ArpC1B/C5L.

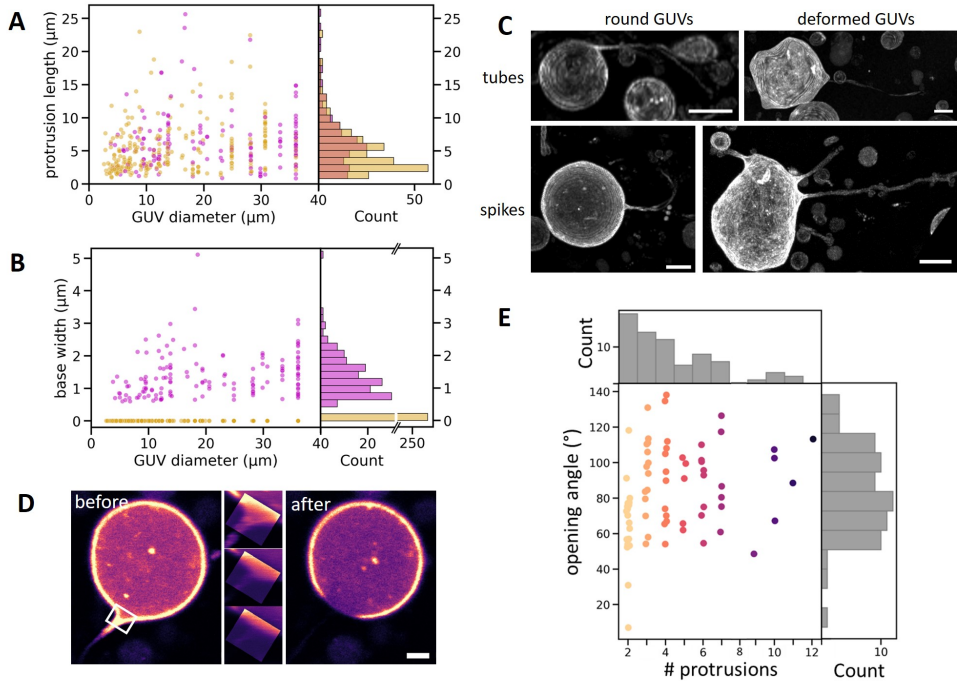

Figure 5.20: **Extended characterization of GUV protrusions.** (A, B) Scatter plot of the length (A) and base width (B) of protrusions as a function of GUV size (left panels), together with corresponding histograms (right panels). N = 261 tubes and 157 spikes. Widths that were optically not resolvable ($\lesssim$ 500 nm) were set to zero. (C) Examples of GUVs with very long tubes and spikes. We found both rounded (left) and globally deformed GUVs (right) that bore protrusions longer than the GUV diameter. This was true both for tubes (top) and spikes (bottom), and we even found GUVs with multiple long protrusions (bottom right). All images show maximum intensity projections of z-stacks in the actin channel. For the top left images, we projected only the bottom half of the GUV as the long tube was otherwise obscured underneath a different GUV. All GUVs contained 8 µM actin, 6.5 µM VCA, and 50 nM ArpC1B/C5L. Scale bars: 10 µm. (D) Illustration of photoablation of a spike base. False-colour (magma) confocal images of actin show a spike-bearing GUV, before and after photo-ablation at the base of the spike (area highlighted with white rectangle, 5.9 × 5.2 µm). Destruction of the actin cortex led to retraction of the spike (middle and right panel). Scale bar: 5 µm. (E) Opening angles and number of protrusions per bouquet (N = 70 bouquets on 42 GUVs).

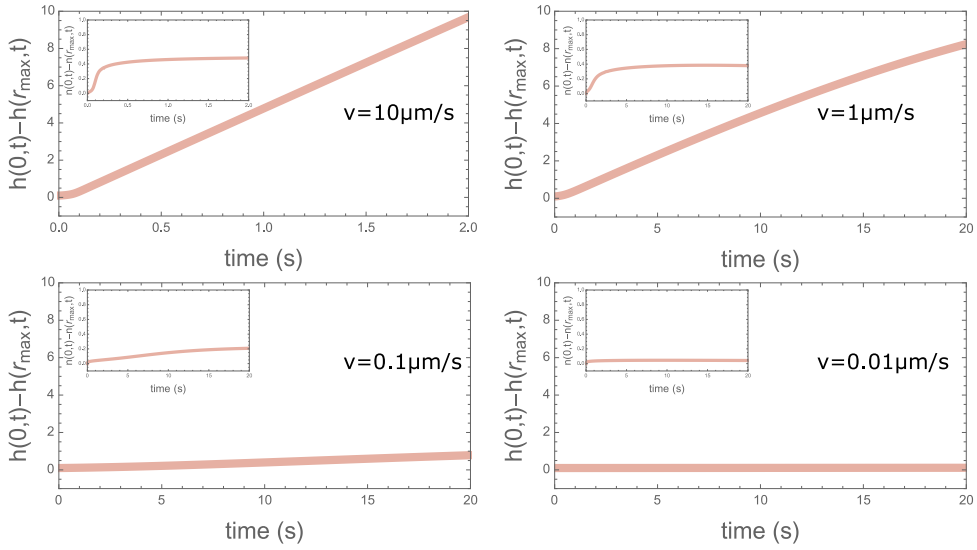

Figure 5.21: **Protrusions form consistently over a wide range of actin polymerization velocities.** Main plots: Relative membrane height at the origin when intermediate concentrations of VCA induce actin polymerization for different actin polymerization velocities ranging from 0.01 to 10 μm/s (see legends). Spikes grow more rapidly when actin polymerization is fast, but spikes are initiated for polymerization velocities as low as 0.1 μm/s.

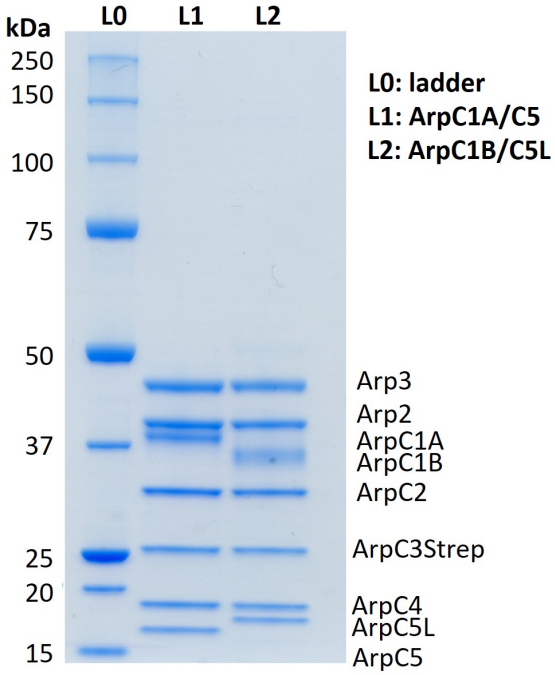

Figure 5.22: **SDS PAGE gel of human Arp2/3 isoforms.** SDS PAGE demonstrates that the two human Arp2/3 isoforms are pure and express all the expected subunits.

6

Vesicle fusion for synthetic cell growth

Abstract

To achieve sustained growth and division, synthetic cells must expand their membrane area. At present, *in vesiculo* production of lipids is not sufficient to fill this need, and introducing extra membrane area from the outside is a necessity to supply lipids and other vital membrane components such as proteins. In this chapter, we present a membrane fusion protocol inspired by SNARE proteins, which mediate membrane fusion in mammalian cells. We use complementary DNA strands with a cholesterol end-tag to induce binding and fusion between giant unilamellar vesicles (GUVs) and large unilamellar vesicles (LUVs), which we supply to the outside of the GUVs. Fluorescence imaging and quantitative image analysis allow us to characterize DNA insertion in GUV membranes, binding of LUVs to GUVs, and vesicle fusion. Strikingly, we find that a widely used content mixing assay actually shows GUV membrane permeabilization rather than fusion in our assay. Using this content mixing assay, we find that many GUVs (~ 30%) are permeabilized when LUVs are bound on their surface, while we observe much lower rates of permeabilization when only individual DNA strands are inserted in the membrane. Finally, we present evidence that GUV-LUV fusion, while so far not detectable via content mixing, is nonetheless evident from significant GUV growth. Our findings point a way towards delivering membrane and luminal components to synthetic cells, but also raise important questions concerning the effects of cholesterol-tagged DNA and tension on GUV membrane permeability.

This study was designed in close collaboration between Lucia Baldauf and Lennard van Buren. Experiments were performed by Lennard van Buren and Tom Aarts under the joint supervision of Lucia Baldauf and Lennard van Buren. Data analysis was performed primarily by Lennard van Buren with additional in-depth data evaluation by Lucia Baldauf and Tom Aarts.

6.1 Introduction

Building a synthetic cell that can autonomously grow, divide and fuel itself, poses great engineering challenges. Not only do we need to reconstitute a lipid-membrane container (see chapter 4), we must also introduce ways in which the container composition and surface area can be changed. For instance, a sustained cell cycle requires a doubling of the membrane surface area once per cycle. Even on the less ambitious end, facilitating just one round of cytokinesis at constant cellular volume means that the surface area must increase by almost 30 % [100]. Throughout the process, control over membrane composition and incorporation of other functional modules, such as transmembrane proteins to drive cellular metabolism [459], is highly desirable so that different cellular functions can be regulated, e.g. by providing receptor lipids or delivering ATP at specific points in the cell cycle. To achieve such control, we thus need a technique to increase membrane area and deliver membrane and cytosolic components on demand and on timescales that are compatible with other reconstituted cellular processes, such as constriction of cytoskeletal networks.

In living cells undergoing cytokinesis, membrane area is supplied specifically to the cytokinetic furrow by endosomal trafficking [235] after lipids are produced in the Golgi apparatus and endoplasmatic reticulum [460]. Reconstituting this entire process *in vitro*, including the necessary metabolic and regulatory pathways, is currently out of reach. Nonetheless, simplified versions have been established, with *in vitro* production of lipids driven by purified enzymes [242] or even enzymes produced *in situ* by cell-free transcription and translation [243, 461, 462]. These techniques are promising for the ambitious long-term goal of generating synthetic cells which can function autonomously, but are not readily usable to supply membrane area for dividing cells in their current state of development. *De novo* synthesis of lipid-producing enzymes and subsequent lipid synthesis is slow, requiring between 3 and 20 hours to produce membrane area growth of, at maximum, around 10 % [243, 462]. It furthermore remains poorly understood what limits protein and phospholipid production in this system. Phospholipid production from purified enzymes and fatty acids was shown to be more efficient and limited only by substrate availability, yielding membrane area increases of up to 30 % [242]. However, the system is also slow (18 hours) and has only been established in small (30-100 nm) vesicles [242], making it likely to be less efficient in GUVs due to their much smaller surface-to-volume ratio.

From an engineering standpoint, it is thus attractive to simplify the system further and, instead of producing lipids *in situ*, feed them to the GUVs from the outside. This makes the system less autonomous, but allows more precise control over the time at which new membrane is added, and also opens the possibility for targeted changes in membrane composition as it is needed. Such targeted changes in membrane composition may be necessary to modulate, for instance, binding between cytoskeletal components and the membrane, to facilitate membrane deformations driven by an underlying actin cortex (see chapter 2). A conceptually simple way to do this is to feed a cell-sized giant unilamellar vesicle (GUV) with smaller vesicles of sub-micron size, called large unilamellar vesicles (LUVs). Since volume increases with the vesicle radius as r^3 but area as r^2, fusing an LUV to a GUV delivers relatively more membrane area than cytosolic volume, thus increasing the surface-to-volume ratio as required in cytokinesis [100].

This feeding mechanism requires membrane fusion, such as it happens in membrane trafficking and signalling in cells (reviewed in [463, 464]). How membrane fusion works

in detail remains debated, and may depend on the exact biological context [465–467]. However, the process can generally be split in two stages: first, the two lipid bilayers are brought into close contact, and second the lipids must rearrange to merge the two bilayers into one [466, 468]. The first step requires pushing through the hydration layers of both surfaces (separation $\lesssim 1$ nm), and overcoming the repulsive interactions between the lipid headgroups [466, 467]. The second step is less straightforward but always requires destabilization of the lipid bilayers. Such destabilization can happen spontaneously [468] or be induced by proteins [469] or nanoparticles [443, 470], opening a fusion pore which expands until the two bilayers are fully fused. Intermediate states such as hemifusion pores or stalks may form and the process can even be stalled in a state where the two proximal leaflets have fused, while the distal ones remain separate [466, 471].

The second step of the fusion process is intimately linked to the molecular composition and structure of the fusing bilayers, but the first step can be achieved by a variety of different physical and chemical means. Most simply, macromolecular crowding [472] or electrostatic binding via divalent cations in solution [473] can be used to bring two membranes into close contact. Using vesicles with opposite electrostatic charges on the fusing membranes can achieve the same effect [474]. However, these mechanisms are poorly controllable from the outside, are severely limited in the accessible range of membrane compositions, or require unphysiological buffer conditions which may interfere with other bottom-up reconstitution efforts.

To overcome these problems, we can take inspiration from biology to design a more flexible and specific binding mechanism. In eukaryotic cells, membrane fusion in exocytosis and vesicular trafficking is mediated by Soluble N-ethyl maleimide sensitive-factor Attachment protein REceptor, or SNARE proteins [475]. Proteins of this family form heterodimers, with each monomer bound to a lipid membrane by insertion of a transmembrane domain. As they dimerize, SNARE proteins form a zipper-like link between the two opposite membranes, progressively bringing them closer together and ultimately facilitating membrane fusion. The precise mechanisms governing this process are still unclear, but the conceptual idea has nevertheless been adapted for rational design of fusion mechanisms in synthetic biology applications. In essence, the goal there is to produce a heterodimeric molecule whose constituent parts are each anchored in separate membranes, and which bind in a zipper-like fashion from the membrane-distal towards the membrane-proximal end. Such molecules have been designed in the form of short peptides [237] and membrane-anchored ssDNA oligonucleotides [240, 476]. Since DNA oligonucleotides are commercially available and can be purchased with a wide array of chemical modifications, they present a membrane fusion system that is easy to implement, and simple to adapt to specific needs such as different membrane binding domains suited for different lipid phases [240]. Furthermore, DNA-mediated fusion has been well characterized, focusing primarily on fusion between small unilamellar vesicles (SUVs, < 100 nm) or LUVs with supported lipid bilayers. Interesting recent studies have furthermore demonstrated DNA-mediated fusion between GUVs, giving rise to vesicles that can divide as a consequence of phase separation [240] or undergo ‘synthetic cell differentiation’ as a response to external stimuli [477]. The influences of the membrane anchor [476, 478], DNA linker sequence and length [131, 476], and membrane composition [479] on fusion have been explored. However, membrane fusion is known to additionally depend on biophysical parameters such as membrane geometry and tension

(reviewed in [238]), making it difficult to directly apply the findings from these studies to fusion between LUVs and GUVs.

In this chapter, we use DNA-mediated binding between LUVs and GUVs with the aim of driving vesicle fusion in a specific and programmable way. We use fluorescence imaging and high-throughput automated image analysis to study how all three steps of the fusion process - DNA insertion, GUV-LUV binding, and membrane fusion - depend on process parameters like DNA concentration and buffer conditions. We find indications that our fusion protocol facilitates the growth of GUV membrane area by 75 %, making it an effective tool for delivering membrane and cytosolic components to synthetic cells. However, our findings also show that DNA-mediated binding between GUVs and LUVs leads to significant membrane permeabilization, pointing out a so far underappreciated challenge on the road to building synthetic cells.

6.2 Results

6.2.1 Experimental system

Inspired by the biological example of SNARE proteins [475], and by their minimal DNA-based counterparts [240, 478], we set up an vesicle system to promote and study membrane fusion. Since we ultimately want to use the system for delivery of membrane- and cytosolic components to synthetic cells, we used GUVs of comparable sizes to animal cells (~ 5 - 20 µm) as a substrate, and much smaller LUVs (100 - 200 nm) as the fusion partner (Fig. 6.1 A). The vesicles were brought into contact by two complementary strands of DNA, henceforth called DNA1 and DNA1' (Fig. 6.1 B, orange and yellow, respectively). Both strands were modified with a trietyhleneglycol (TEG) cholesterol moiety at one end, such that both cholesterol tags sat on the same end of the double stranded DNA when the two ssDNA strands hybridized (Fig. 6.1 B, bottom panel).

To undergo full fusion, three separate processes (illustrated in Fig. 6.1 C) must occur in the system: First, the complementary DNA strands must insert into the GUV and LUV membranes by means of their cholesterol tag. The membrane-bound DNA strands can subsequently hybridize, binding the LUV to the GUV membrane. Once the membranes are in close proximity, they can undergo fusion, which allows the mixing of membrane components (cyan from the LUVs with red from the GUVs) and cytosolic cargo (pink).

In the following, we will experimentally characterize all three steps. To this end, we performed high-throughput analysis of epifluorescence images of the GUV membranes and lumen. The details of the analysis procedure are laid out in the Supplementary Information (Supp. Fig. 6.10). This data will allow us to draw population-level conclusions about the efficiencies of each step in the vesicle fusion process, and hence to develop a protocol for optimal membrane fusion in the context of synthetic cell membrane growth.

6.2.2 DNA insertion

The first step towards vesicle fusion is the insertion of the DNA linkers in the respective membranes. Insertion of cholesterol-tagged DNA in lipid membranes is well established [480, 481], and we confirmed that it also worked in our assay. We probed binding of ssDNA to GUVs at concentrations below the critical micelle concentration of comparable oligonucleotides with a single cholesterol tag ($\lesssim$ 10 µM [481]), ranging from 0.25 to 5 µM.

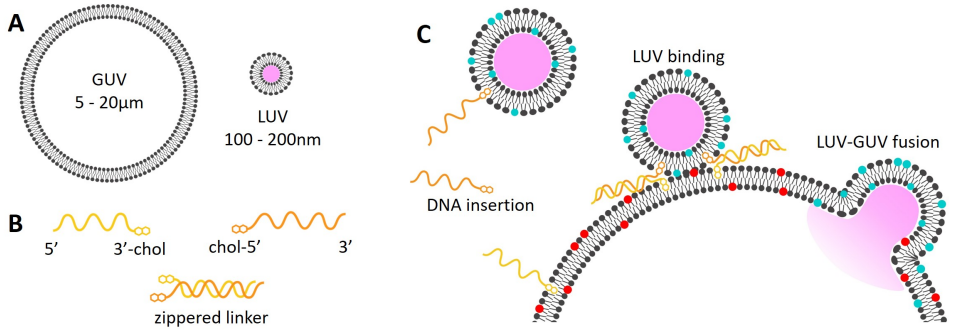

Figure 6.1: **Experimental setup: GUV-LUV fusion.** (A) We used LUVs to deliver membrane and cytosolic components to cell-sized GUVs by in vitro membrane fusion. (B) Two complementary ssDNA strands were used to bind LUVs and GUVs together and facilitate fusion. Both ssDNA strands were functionalized with a TEG-cholesterol group on one end to facilitate insertion into the membrane. We used 5'-modified ssDNA (orange) to bind to LUVs and 3'-modified ssDNA (yellow) to bind to GUVs. When the complementary strands hybridized, they formed a zippered linker which bears both cholesterol-modifications on the same end, thus bringing the GUV and LUV membranes close together. (C) Schematic of the three stages of DNA-mediated membrane fusion. First, DNA must insert into the outer leaflets of both LUVs (cyan) and GUVs (red). When the bound ssDNA strands hybridize, they bind the LUVs to the GUVs. Finally, the vesicles fuse, leading to mixing of both the membrane- and cytosolic components (pink). Schematics were not drawn to scale.

Since the ssDNA strands with which we perform the fusion assays were not inherently fluorescent, we could not directly ascertain their membrane insertion. We instead used a two-step binding assay which allowed us to probe both insertion of the chol-ssDNA strands and their hybridization at the same time (Fig. 6.2 A). To this end, we first bound one ssDNA strand (DNA1'-chol, no fluorescent label, yellow in Fig. 6.2 A) to the GUVs and added the complementary ssDNA strand (DNA1-fluo, fluorescently labeled, orange in Fig. 6.2 A) to the external solution. DNA1-fluo was identical to DNA1-chol apart from the functional group, which made it highly suitable for confirming that the chol-tagged version of the same ssDNA strand would also effectively bind to GUV-bound DNA1'-chol. We used GUVs as the model membrane on which we probed DNA insertion, as we could visualize them using fluorescence imaging, and analyzed how much DNA bound to any given GUV. This is not possible for the LUVs, since their size is below the optical diffraction limit.

First, we incubated GUVs with different concentrations of DNA1'-chol for 60 min. We then added DNA1-fluo at equimolar concentrations and used epifluorescence imaging to measure the DNA fluorescence on the GUVs after 90 minutes. For all DNA concentrations studied here, this resulted in significant enrichment of DNA fluorescence at the GUV membranes when there was a DNA1'-chol present on the GUVs (Fig. 6.2 B). Furthermore, the GUV lumens showed up as dark spots against a bright background, which indicated the presence of soluble fluorescent molecules in the outside buffer. Strikingly, this background fluorescence was comparatively brighter in the 5 µM DNA sample than in the samples with lower DNA concentration. Quantitative analysis revealed that for any given DNA concentration, we got a distribution of intensities which did not depend on the GUV radius (Fig. 6.2 C). We could therefore conclude that DNA inserted in different GUVs at a consistent surface density, and that the contribution of out-of-focus fluorescence did not

systematically skew our analysis. However, it was apparent that the distribution of DNA intensities on the GUVs broadened as the soluble DNA concentration increased (Fig. 6.2 C and D). This likely stemmed from an increased contribution of the background signal in the analysis, which decreased the signal-to-background ratio from 1.26 at 0.25 µM DNA to just 1.07 at 5 µM DNA. Furthermore, the peak in the intensity distribution not only widened with increasing DNA concentration, but an additional smaller peak appeared at high intensities, which will be examined in more detail in Fig. 6.3. This further increased the spread in the intensity distribution.

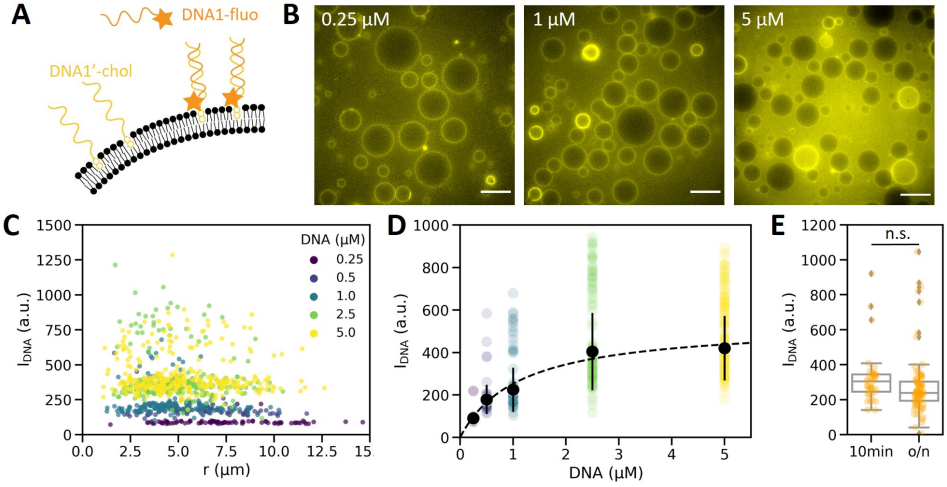

Figure 6.2: **DNA insertion in GUV membranes.** (A) Insertion of DNA1'-chol (yellow) into the GUV membrane was assessed by a fluorescently tagged, complementary reporter strand (DNA1-fluo, orange) which was added to the GUVs after the DNA insertion step. (B) Epifluorescence images of GUVs after binding of the fluorescent DNA at DNA concentrations of 0.25, 1 and 5 µM. Scale bars: 20 µm. (C) Scatterplot of DNA intensity over GUV radius. Each data point represents the DNA fluorescence intensity (corrected for the local background signal) of a single GUV. Data is color coded for DNA concentrations, with brighter colors indicating higher concentrations. N = 83, 91, 171, 236, and 328 for 0.25, 0.5, 1, 2.5, and 5 µM DNA, respectively. (D) The mean DNA signals followed a Langmuir-type absorption isotherm. Black datapoints and error bars indicate the means and standard deviations of the underlying distributions (sample sizes identical to C), and the black dashed line indicates a Langmuir adsorption isotherm with equilibrium constant $K = 0.89\ \mu M^{-1}$. (E) Boxplot of DNA intensities on GUVs, comparing incubation with 1 µM DNA for 10 min with overnight incubation. Individual datapoints represent the DNA intensity of one GUV. N = 37 and 91, respectively. The distributions are not significantly different ($p > 0.5$ by Welch's t-test)

Next, we tested the functional dependence of DNA incorporation in the membrane on the soluble DNA concentration (Fig. 6.2 D). The mean GUV-bound DNA fluorescence increased monotonously with soluble DNA concentration, but plateaued for concentrations of 2.5 µM and higher. This behaviour was described well with a Langmuir adsorption isotherm (Fig. 6.2 D, dashed line) of the form

$$I_{\mathrm{DNA}}(c_{\mathrm{DNA}}) = \frac{I_{\mathrm{DNA,\,max}} K c_{\mathrm{DNA}}}{1 + K c_{\mathrm{DNA}}}, \tag{6.1}$$

where I_{DNA} is the DNA intensity (which we took as a proxy for the DNA surface density

on the GUV membrane), $I_{\mathrm{DNA,\,max}}$ is the DNA intensity at complete monolayer coverage, c_{DNA} is the DNA concentration in solution, and K is the binding constant. The fit yielded a binding constant of $K = 0.89\ \mu\mathrm{M}^{-1}$, or a concentration of $c_{\mathrm{DNA}} = 1/K = 1.1\ \mu\mathrm{M}$ at which the DNA occupied half of all possible binding sites on the GUV membrane. The qualitative dependence of DNA intensity on soluble DNA concentration matched that which has previously been observed by quartz crystal microbalance measurements with dissipation monitoring (QCM-D) for cholesterol-tagged DNA inserting in supported lipid bilayers (SLBs) [481, 482]. Univalent cholesterol tags have been shown to insert reversibly in phospholipid bilayers, and to follow a Langmuir adsorption isotherm, behaving like an ideal gas adsorbing to a surface which can at most support one monolayer of adsorbates. However, we found significantly weaker DNA binding than that observed in the QCM-D studies ($1/K$ ~ 17 and 80 nM in ref. [482] and [481], respectively). This order of magnitude difference is striking given that the DNA oligonucleotides used in both studies were similar in length and modification to ours (20 compared to 24 base pairs in our study), and that the lipids differed only in their tail groups (POPC compared to DOPC here). It may, however, be partially explained by the fact that QCM-D by its nature requires interaction of the lipid film with a solid substrate, which is known to alter membrane properties like compositional leaflet asymmetry and bilayer fluidity [483–485]. In our study, by contrast, we worked with freestanding GUV membranes. A further difference between the systems was the local availability of new DNA: QCM-D measurements are performed in a chamber where there is a constant flow of DNA solution across the lipid bilayer, which is thus constantly supplied with fresh solutes through convection [486]. In our study, by contrast, both the GUVs and the outer solution were stationary in the imaging chamber, so that DNA adsorption could only happen when DNA diffused into the vicinity of the membrane, which in turn led to local DNA depletion from the solution. This may artificially increase the soluble DNA concentration needed to saturate binding sites on the GUV membrane. For most of our further experiments, we worked at 1 μM DNA, to ensure a high surface coverage of DNA while keeping the DNA concentration in solution low.

In Fig. 6.2 C and D we observed that the DNA intensity distributions broadened with increasing DNA in solution. Upon closer inspection, we noted that this was in part due to a fraction of GUVs which showed a roughly double membrane intensity compared to that of most GUVs. In epifluorescence images, these appeared strikingly bright (Fig. 6.3 A, yellow asterisk). Analyzing the intensity distribution of GUVs at 5 μM DNA, we found that the distribution was in fact bimodal, with ~ 20 % of all GUVs in the high-intensity population as determined by Otsu thresholding (Fig. 6.3 B, yellow part of the distribution beyond the dashed line). Since the high intensity population was centered around 700 a.u., about double the average of 350 a.u. for the dimmer subpopulation, we surmise that the bright GUVs may have DNA bound to both the outer and inner leaflet of the GUV. Both ssDNA strands are much too large to be spontaneously membrane-permeable. Thus, for DNA to be bound inside the GUV, the membrane must have been permeabilized at some point, for instance as a transient membrane pore opened and allowed DNA to diffuse through. Note that the DNA linkers are large macromolecules, so any such fusion pore would have to be of a substantial size to let them pass the membrane. This leakiness is also consistent with the observation that the GUVs with bright membranes tended to have a brighter lumen compared to the other GUVs in the sample, indicating the presence of soluble DNA inside

the GUV. We assessed what fraction of GUVs had this bright membrane signal in each sample, and found that higher DNA concentrations in solution correlated with a greater fraction of bright GUVs. The fraction increased from 2.5 % at 0.25 µM to around 20 % at 5 µM, indicating that more DNA in solution may lead to a greater likelihood of membrane permeabilization.

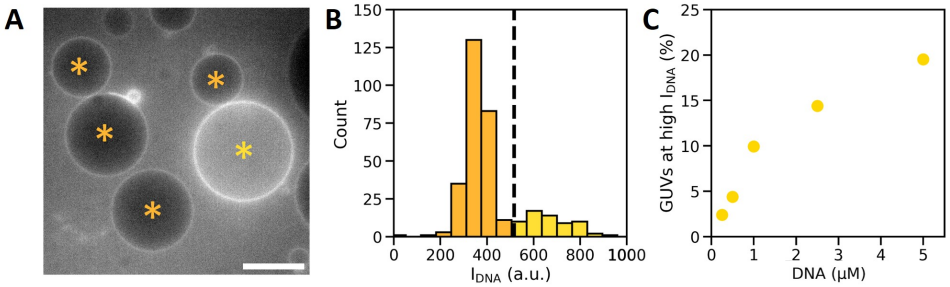

Figure 6.3: **Bimodal intensity distribution of DNA on GUVs.** (A) Epifluorescence image of GUVs incubated with 5 µM fluorescent DNA. Some GUVs showed a much higher signal on the membrane (yellow asterisk) than the majority (orange asterisks). Scale bar: 10 µm. (B) Histogram of DNA intensities on GUVs incubated with 5 µM fluorescent DNA, N=328. The dashed black line at I_{DNA} = 561.5 a.u. indicates the border between the low- and high-intensity GUV populations as determined by Otsu thresholding. (C) Fraction of GUVs in the high-intensity part of the distribution as a function of the concentration of DNA in solution.

6.2.3 LUVs bind GUV membranes most densely at intermediate linker concentrations.

The second step in the membrane fusion process is the binding of LUVs to GUVs, which brings their membranes into close proximity and thus ultimately facilitates membrane fusion. We assessed this in a similar way to the DNA binding assay: First, both LUVs and GUVs were incubated separately with the ssDNA strands DNA1-chol and DNA1'-chol, respectively. We varied the concentration of DNA, but ensured that the same concentration was present for both types of vesicles. After 10 min, GUVs and LUVs were mixed and left to bind for 60 min at room temperature by hybridization of the complementary DNA strands (Fig. 6.4 A). We did not test the DNA hybridization separately (e.g. by calorimetry) since the DNA binding assay in the previous section already confirmed that DNA1 and DNA1' did indeed bind to each other as expected. We then acquired epifluorescence images of both the GUV and LUV membranes, which we used to perform population-level analysis of the GUVs. In each GUV, we measured the median LUV fluorescence on the membrane and corrected it by subtracting the local LUV background intensity (see Supp. Fig. 6.10). Note that we could not resolve individual LUVs, which were smaller than the diffraction limit (~ 200 nm) and showed up as a homogeneous fluorescent background (Fig. 6.4 B). In some fields of view, we found a more grainy pattern in the LUV channel. Intensity line profiles in the background revealed that the bright specks were around 1 µm in size, and thus larger than the individual LUVs (Supp. Fig. 6.11). Since we did not observe such large structures when measuring LUV size distributions in the absence of DNA (Fig. 6.13 A), these background speckles may hint at some DNA-mediated aggregation of LUVs.

When no DNA was added to the vesicles, GUVs appeared as dark regions from which LUVs were excluded, and we detected no enrichment of LUVs on their surface (Fig. 6.4 B, panel '-DNA'). We could thus conclude that any binding of LUVs was indeed specific and mediated by the DNA linkers. By contrast, when we added any concentration of DNA (0.25 - 5 μM), we observed LUV binding on all GUV surfaces, although the localized LUV intensities varied even within the same field of view (Fig. 6.4 B, panel '0.25 μM'). The contrast between localized LUV signal and LUV signal in the background was most pronounced at a DNA concentration of 1 μM. A population level analysis confirmed the visual impression: Irrespective of GUV size, the vesicles which bore the highest LUV signal on their membrane were among the 1 μM DNA population (Fig. 6.4 C). Indeed, the average LUV intensity on the membrane increased sharply for DNA concentrations between 0.25 and 1 μM, sextupling from 514 to 3204 a.u.. At higher concentrations, the average LUV intensity dropped again to just 1285 a.u. at 5 μM DNA. We note that these measurements were performed using the same batches of LUVs and GUVs for all DNA concentrations, so we do not expect significant variations in relative vesicle densities, which might otherwise skew the results.

What could cause the apparent drop in LUV binding efficiency? Our DNA-binding results showed that, while DNA insertion was most efficient at 1 μM DNA, the surface density of oligonucleotides still increased from there. We would thus have expected LUV binding to also increase, but it did not. One possible explanation may be binding of free DNA (whose concentration will increase at concentrations above 1 μM) from the LUV buffer to the DNA on the GUV membrane, where it would saturate those binding sites before they can be occupied by LUV-bound DNA. This likely does play a role here (as we also see signs of such an effect in the speckly LUV background, Supp. Fig. 6.11) but most probably was not the only factor at play: Others have found that a similar decrease in DNA-mediated binding at high DNA concentrations could also occur in SLBs, where unbound DNA was washed away before LUV addition (L. Laan, personal communication, 2021). A decrease in binding activity at high linker densities has also been reported for antibody binding to solid substrates [487], where it was attributed to oligomerization of antibodies in solution at high concentration, which we do not expect in our system. We do consider that ssDNA strands bound on the GUV are in close contact and may thus experience some self-dimerization, even though this is not particularly energetically favourable (see Methods section). This effect would reduce the effective number of LUV binding sites at high linker DNA concentration.

Finally, we assessed the effect of GUV-LUV incubation time on LUV localization. DNA hybridization was fast (Fig. 6.2 E) and LUVs were dispersed quickly in solution as we pipetted them in. Consequently, we expected GUV-LUV incubation time to have only a minimal effect on LUV binding after several minutes. Indeed, we found no consistent increase in the average LUV intensities on the membrane over the course of 120 minutes (Fig. 6.4 E). Since this experiment was performed at 1 μM DNA in solution, which we identified as the DNA concentration at which LUV binding was maximal, we surmised that we were close to saturating the GUV surface with LUVs here, which was confirmed by a back-of-the-envelope calculation[1].

[1] In a typical experiment, we had on the order of 1000 GUVs in an observation chamber. If an average GUV has a radius of 10 μm, this corresponds to a total GUV surface area of around 10^6 μm^2. To fully cover all of this GUV

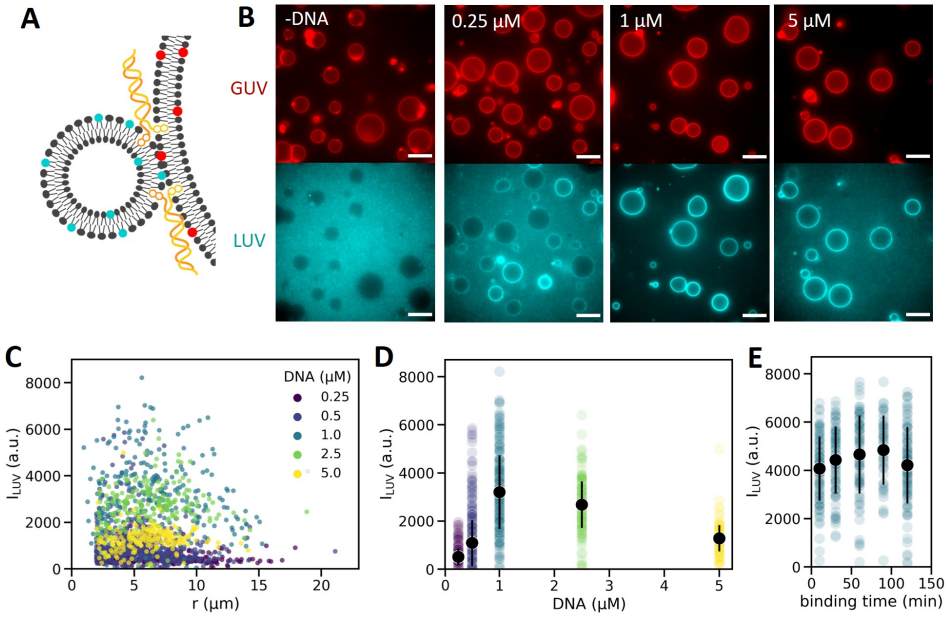

Figure 6.4: **DNA-mediated LUV-GUV-binding.** (A) Schematic of an LUV (cyan) bound to a GUV (red). Note that, since the LUV size was below the resolution limit of conventional fluorescence microscopy, we could not distinguish whether or not fusion has occurred. (B) Epifluorescence images of GUVs (red, labeled with DOPE-Atto488) and LUVs (cyan, labeled with DOPE-Atto655), incubated with either no linking DNA ('-DNA') or with 0.25, 1, and 5 µM ssDNA on both the GUVs and LUVs. In the absence of DNA, we saw the GUVs as dark spots from which LUVs were excluded, with no significant LUV signal localized on the membrane. In the presence of DNA, we found LUV signal enriched on all GUV membranes, but also present in the background. The contrast between membrane-localized and background LUV signal was greatest at 1 µM DNA. Scale bars: 20 µm. (C) Distribution of LUV intensity on GUV membranes as a function of GUV radius, color coded for the concentration of DNA in solution. We found no strong correlations beween GUV size and DNA signal, but the average intensities varied strongly with DNA concentration. Individual data points indicate the average LUV intensity on the membrane of one GUV. N = 300, 517, 262, 199 and 195 GUVs for 0.25, 0.5, 1, 2.5 and 5 µM DNA, respectively. (D) Mean LUV intensities on GUV membranes as a function of DNA concentration. Black data points and error bars denote the mean and standard deviation. LUV intensities increased steeply between 0.25 and 1 µM, above which the LUV signal dropped again. (E) LUV intensity on the surface of GUVs incubated with 1 µM DNA over time. Black data points and error bars indicate the mean and standard deviation. N = 104, 115, 91, 93 and 57 GUVs for 10, 30, 60, 90 and 120 min binding time, respectively.

surface area with LUVs, we must estimate the combined cross-sectional area of all LUVs in the sample. In our assay, we added 10 µL of an LUV suspension prepared at 0.5 mg/mL ≈ 6.8 mM lipids to a total reaction volume of 100 µL. If we set the footprint of each lipid molecule to 33 Å^2 (using 66 Å^2 as the area per lipid [488], and dividing by 2 to account for the two leaflets of an LUV), and assume that all lipids were incorporated in spherical LUVs with a 100 nm radius, this gives us a total cross-sectional area of all LUVs on the order of 10^8 µm^2. We can thus assume that there are enough LUVs in the sample to cover the combined surface area of all GUVs 100 times over, indicating that surface saturation was very likely.

6.2.4 Content mixing is most prevalent at intermediate linker densities.

Since full fusion of LUV and GUV membranes was our ultimate goal, we developed an assay with which to detect such fusion events. Content-mixing assays, as they are commonly used for detecting LUV-LUV or SUV-SUV fusion, are not straightforwardly transferrable to our system, in which the fusing vesicles are of drastically different sizes. When LUVs fuse with other LUVs, the contents of both become diluted by roughly a factor of 2, which may be enough to trigger or inhibit self-quenching of a concentration-sensitive dye, or quenching by a dye which is brought into contact with another compound by content mixing. Here, however, the LUVs and GUVs differed in size by a factor of 50-100, which meant an up to 10^6-fold difference in volumes. Any dye which was encapsulated in LUVs initially, would thus be diluted very significantly upon content mixing with a GUV. By contrast, the concentration of any solute encapsulated in the GUVs would be barely diluted at all, even if many LUVs fused with the GUV.

We thus based our content mixing assay on the combination of the dye 8-Hydroxypyrene(1,3,6)-trisulfonic acid (HPTS) and its quencher p-Xylene-bis-pyridinium bromide (DPX). HPTS was encapsulated at high concentration (10 mM) in LUVs (Fig. 6.5 A). If the LUVs bind to a GUV but do not fuse, the dye remains trapped in the LUVs on the GUV surface, and the interior of the GUV will not become fluorescent (Fig. 6.5 A, left GUV). By contrast, when sufficiently many LUVs fuse with the GUV and release their contents into the GUV, its lumen lights up and becomes fluorescent. In order to suppress HPTS signal from the buffer (where it will invariably be present due to its presence in the LUV buffer), we added the quencher DPX to the outside solution for imaging. We first demonstrated that HPTS and DPX show the expected fluorescence behaviour in a bulk fluorescence measurement (Fig. 6.5 B). This revealed that HPTS fluorescence was effectively quenched by DPX as long as DPX was in excess. We thus perform all our experiments at a concentration of 2.5 mM DPX in the imaging chamber, to quench the 2.5 mM HPTS contributed by the LUV buffer to the final concentration. Pure HPTS fluorescence exceeded that of HPTS+DPX at concentrations above 0.01 mM (Fig. 6.5 B), so we expect that the lumen of a GUV should be brighter than the background HPTS fluorescence if it contains more than 0.01 mM of HPTS. When a typical GUV (5 µm radius) fuses with a single 200 nm LUV, the dye from the LUV is diluted by a factor of $V_{\mathrm{GUV}}/V_{\mathrm{LUV}} = 125{,}000$. Fusion should thus become detectable in a typical GUV when it has fused with at least 125 LUVs, assuming that all LUVs encapsulate HTPS at 10 mM.

Indeed, we found that some GUVs in our samples acquired bright HPTS signal in the lumen. Within the same sample, we found both GUVs whose lumen was darker than the surrounding solution (Fig. 6.5 C, GUV 1) and GUVs which had a strongly increased HPTS signal in the lumen (Fig. 6.5 C, GUV 2). In the GUV intensity profiles, the non-fused GUVs were thus characterized by a dip in HPTS fluorescence towards the center of the GUV, whereas HPTS fluorescence peaked in the center of 'fused' GUVs (Fig. 6.5 D). We therefore used the ratio of HPTS fluorescence intensities in the center of the GUV compared to just outside the GUV membrane, $\rho_{HPTS} = I^{in}_{HPTS}/I^{out}_{HPTS}$, to assess whether a GUV had undergone content mixing or not. To avoid false positives in our detection of bright GUVs introduced by leaking of quenched HPTS into GUVs during imaging, we used 1.05 as a cutoff value in ρ_{HPTS}, above which we counted GUVs as having undergone content mixing

(Fig. 6.5 E). We note that by this metric, we will underestimate the fraction of bright GUVs, as we do not count GUVs as fused if their internal HPTS fluorescence is higher than it was pre-fusion, but still below the background HPTS signal. Our reported fusion efficiencies should thus be interpreted as lower bounds for true 'fusion' efficiencies.

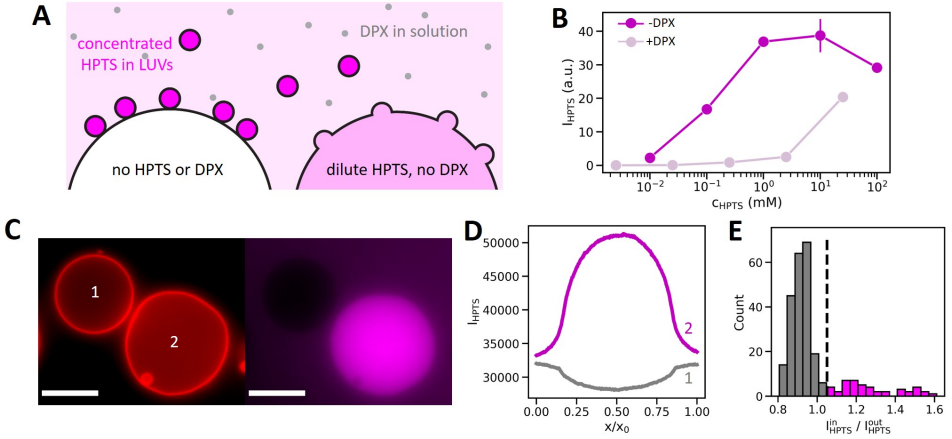

Figure 6.5: **Content mixing assay.** (A) Schematic representation of the assay. We produced LUVs encapsulating HPTS (magenta). Since the LUV buffer contained free HPTS, adding the LUVs also introduced some HPTS into the final sample, where we suppressed its fluorescence by adding the quencher DPX (grey). When LUVs bind to GUVs but do not fuse, their encapsulated dye is kept outside of the GUV, and the GUV interior appears nonfluorescent (left GUV, white). When fusion and content exchange do happen between the LUVs and GUV (right GUV, pink), the HPTS dye delivered by the LUV becomes diluted in the GUV lumen, where it ceases to self-quench and produces a HPTS signal higher than that of the outer solution. (B) Fluorescence of HPTS solutions with (grey) and without (magenta) the quencher DPX. HPTS on its own increased in fluorescence intensity as the concentration increased, but self-quenched above ~ 10 mM. In the presence of 7.5 mM DPX, HPTS fluorescence was suppressed almost completely up to HPTS concentrations above 1 mM, where HPTS fluorescence begins to overpower the quenching ability of DPX. Each datapoint shows the average of 6 measurements, and the standard deviation of the measurements was smaller than the data point in almost all cases. (C) Epifluorescence image of two typical GUVs in a sample containing GUVs, LUVs, and 1 µM of linker DNA on each membrane. GUV membranes are shown in red, and HPTS is shown in magenta. GUV 2 has undergone content mixing as apparent from a bright HPTS signal in the lumen, whereas GUV 1 appears dark in the HPTS channel. Scale bars: 10 µm. (D) Intensity line profiles drawn through the two GUVs shown in panel C. The dark, non-fused GUV (1, grey) had a lower internal fluorescence than the background, whereas the 'fused' GUV (2, magenta) showed much higher intensity in the lumen than outside the GUV. (E) Histogram of ratios of HPTS signal in the center compared to the outside of the GUV, for GUVs which have undergone content mixing in the presence of 1 µM linker DNA on both GUVs and LUVs. The distribution showed a large peak at HPTS ratios just below 1 (grey bars), corresponding to GUVs which have not undergone content mixing. We considered GUVs with an HPTS ratio above a cutoff of 1.05 (black dashed line), i.e. more than 5 % above the background, to be 'fused' (magenta bars). N = 262 GUVs.

Just like for DNA- and LUV binding, we assessed the influence of DNA density on the efficiency of the fusion process. In the absence of DNA linking the vesicles, we again found barely any LUV localization on the GUV membrane, nor any high numbers of GUVs with a bright HPTS intensity in their lumen (Fig. 6.6 A, panel '-DNA'). By contrast, both localization of LUVs on the GUV membrane and the presence of GUVs with a bright HPTS interior increased for samples containing linker DNA, peaking at 1 µM DNA (Fig. 6.6). Plotting ρ_{HPTS} against the LUV intensity on the membrane revealed that for all DNA

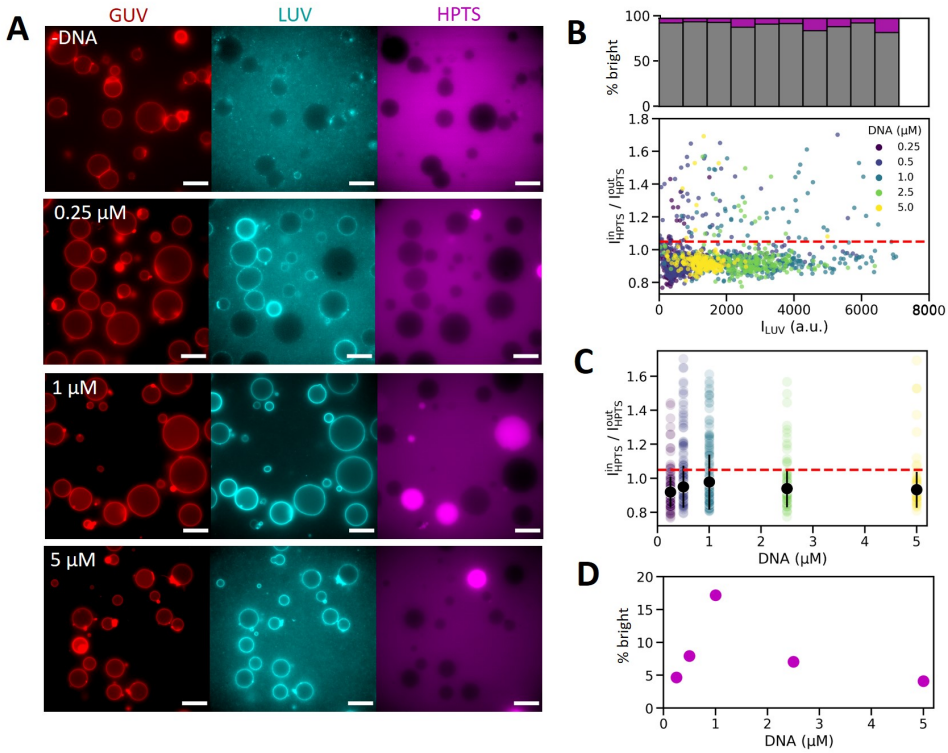

Figure 6.6: **Apparent fusion rate depends on DNA-concentration.** (A) Epifluorescence images after a 75 min incubation of GUVs with LUVs in the presence of different concentrations of linker DNA. Images show GUV membranes labeled with DOPE-Atto488 (red), LUV membranes with DOPE-Atto655 (cyan), and HPTS (magenta). In the control without DNA ('-DNA'), we observed minimal interaction between the LUVs and GUVs, and practically no GUVs with a bright HPTS signal in their lumen. By contrast, LUVs were localized to the membranes of all GUVs in the presence of 0.25-5 µM DNA, with the strongest localization observed at 1 µM DNA. In the presence of DNA, we always observed some GUVs with a bright internal HPTS signal. The percentage of such bright GUVs was again highest for 1 µM DNA. Scale bars: 10 µm. (B) Scatterplot of HPTS ratios as a function of the LUV intensity on the GUV membrane (bottom panel). DNA concentrations are color coded, with brighter colors denoting higher DNA concentrations. N = 300, 517, 262, 199 and 195 GUVs for 0.25, 0.5, 1, 2.5 and 5 µM DNA. We counted GUVs with an HPTS ratio above 1.05 (red dashed line) as 'bright'. The bar plot shows the same data, aggregated for all DNA concentrations and binned by LUV intensity. Bars are split into bright (magenta) and dark (grey) fractions. The fraction of bright GUVs increased from 5.4 % in the lowest LUV intensity bin, to 16.2 % in the highest LUV intensity bin. Note that the corresponding average LUV intensity increased 33-fold. (C) HPTS ratio as a function of linker DNA concentration. Black data points and error bars denote the mean and standard deviation. The red dashed line denotes an HPTS ratio of 1.05. (D) Fractions of bright GUVs as a function of DNA concentration, showing a nonmonotonic dependence on the DNA concentration that peaks at 1 µM DNA (17 % bright GUVs).

concentrations, a small fraction of vesicles had a bright internal HPTS signal in the entire range of LUV intensities (Fig. 6.6 B). Intuitively, one might expect that more LUVs bound to the membrane of a given GUV should increase its chances of fusing with a sufficient number of LUVs in order to be classified as 'fused'. Indeed, when we binned all data into different intensity-brackets, we found that the fraction of fused GUVs tripled from 5.4 % in

the GUVs with the lowest LUV intensity, to 16.2 % in the GUVs with the highest LUV signal on their membrane. While this increase is substantial, it required a 33-fold increase in LUV intensity between the two outermost LUV intensity brackets. 'Fusion' efficiency thus appeared surprisingly weakly linked to LUV density on the GUV membrane. Furthermore, we did not observe any GUVs which had a bright rim of HPTS signal colocalizing with the membrane-bound LUV signal, as one should expect if brightly fluorescent LUVs bind to, but do not fuse with, a GUV.

Finally, we assessed how content mixing efficiency depends on DNA concentration. The HPTS ratio ρ_{HPTS} was on average below the 1.05 cutoff in all conditions between 0.25 and 5 μM DNA (Fig. 6.6 C). However, there was a fraction of GUVs with a bright HPTS signal in the lumen in all cases (datapoints above dashed line). This fraction depended on DNA concentration in the same way as LUV binding: at 0.25 μM DNA, only around 5 % of GUVs had undergone content mixing, rising to 17 % at 1 μM. At higher DNA concentrations, the bright fraction dropped again to 5% at 5 μM (Fig. 6.6 D).

6.2.5 A refined assay reveals that membrane porosity dominates content mixing results

In the previous sections, we pointed to several surprising results that made us question whether our content mixing assay was in fact sensitive enough to report true LUV-GUV fusion rates. Firstly, we could not observe localization of HPTS signal on the membrane of GUVs with bound LUVs, indicating that background fluorescence from free HPTS overwhelmed subtle changes in HPTS localization. It was therefore especially surprising that we saw such clear signatures of content mixing: we already know that large numbers of fusion events are necessary to elevate the levels of HPTS fluorescence above those from the background (section 6.2.4). Contributions from out of focus fluorescence in widefield imaging mean that significant amounts of HPTS fluorescence inside the GUV are necessary for detection, suggesting that the brightly fluorescent GUVs must contain remarkably high concentrations of HPTS. Furthermore, we observed structures indicating excess membrane reservoirs even in GUVs in hypotonic conditions, where they should in theory be very taut (Supp. Fig. 6.12), suggesting that there may be exchange between the cytoplasm and outside buffer.

Prompted by these suspicions, we thus refined our assay to test whether what we detect was in fact fusion: Firstly, we moved from widefield microscopy to confocal imaging on a point scanning microscope, where out of focus HPTS fluorescence from outside the GUVs was filtered out and thus no longer influenced our analysis. Secondly, we repeated the fusion assay in a cleaner system that was better suited to distinguish between GUV-LUV fusion and GUV leaking (Fig. 6.7 A). Instead of adding the LUVs to the GUVs in their original formation buffer, which still contained free HPTS, we first washed the LUVs on a desalting column to remove any free dye (Fig. 6.7 B). We then repeated the assay described in Fig. 6.6 at 1 μM DNA, where we had previously observed the highest fusion efficiencies, using the washed LUVs. This revealed that LUVs did indeed bind to the GUVs, and now we could detect the bright ring of HPTS fluorescence we expected as a result of bound but unfused LUVs (Fig. 6.7 C). However, out of more than 2000 analyzed GUVs, not a single one showed significant internal HPTS fluorescence, indicating that we were not in fact detecting any fusion by our content mixing assay (Fig. 6.7 C).

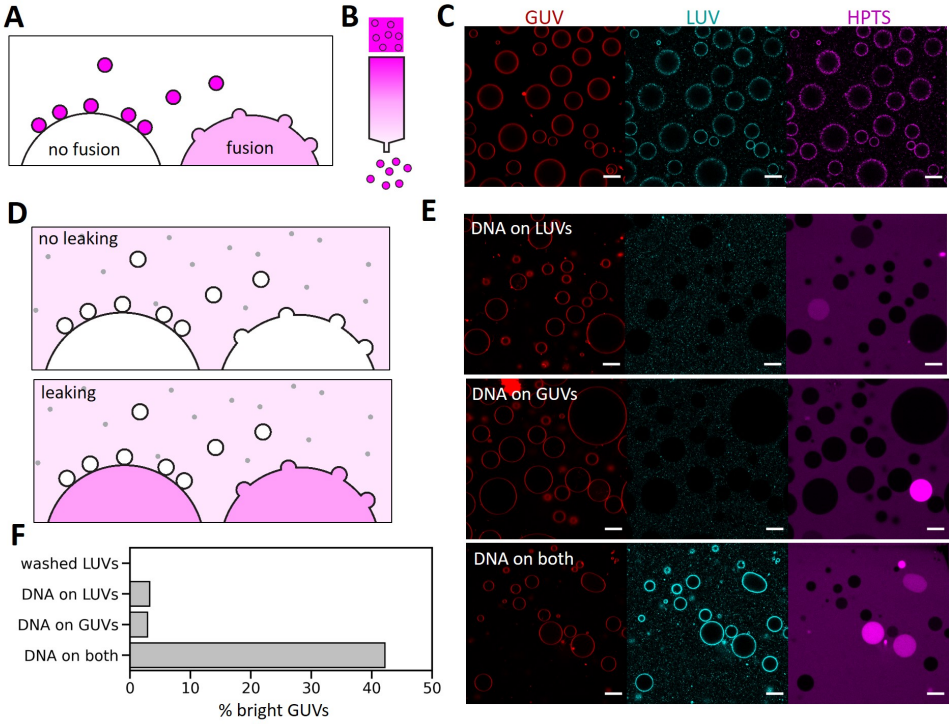

Figure 6.7: **Controls reveal that apparent fusion detected in our content mixing assay is dominated by DNA-dependent membrane permeabilization.** (A) Control experiment designed to distinguish membrane leakage, fusion, and binding without fusion. We added purified LUVs encapsulating HPTS (magenta) but with no residual dye outside the LUVs. Bound and fused LUVs should then be easily distinguishable by where HPTS signal is observed. (B) Dye was removed from the outside solution by passing LUVs through a desalting column, where LUVs passed through while the dye stayed behind in the column. (C) Confocal images of GUVs (red) upon incubation with pre-washed LUVs (cyan) that contained HPTS (magenta). Both GUVs and LUVs had bound DNA to facilitate GUV-LUV binding. Both LUV- and HPTS signal clearly localized to the periphery of the GUVs, but no GUVs had any detectable HPTS signal in their lumen, indicating that we did not observe any fusion. (D) A further control established when GUV membranes were permeabilized: We formed empty LUVs in the absence of any dye. We then added HPTS to the environment in which LUVs and GUVs were incubated together for fusion, and finally added DPX for observation. If GUVs were devoid of HPTS signal, their membrane had remained impermeable throughout the fusion step (top panel). If GUVs acquired bright HPTS signal, this signal must have come from the outside solution, indicating membrane permeabilization (bottom panel). (E) Confocal images of GUVs after fusion with 'empty' LUVs in the presence of HPTS in the outside solution. When only the GUVs or only the LUVs were incubated with their respective DNA strands (top, middle) a small fraction of GUVs showed enriched HPTS signal in the lumen, and none of the GUVs had significantly enriched LUV signal on the membrane. When both GUVs and LUVs were incubated with DNA, the LUVs localized to the GUV membranes as expected, and a significant number of GUVs carried bright HPTS signal. (F) Quantification of apparent fusion efficiency. 0 % of GUVs appeared bright in the absence of HPTS in the outside solution, even though both LUVs and GUVs were incubated with DNA. 3.3 and 2.9 % of GUVs appeared bright when only either GUVs or LUVs carried DNA, and HPTS was present in the outside solution. When both GUVs and LUVs had bound DNA and HPTs was present in solution, 42.2 % of GUVs appeared bright. N = 2094, 800, 2148 and 882 GUVs. Scale bars: 20 µm.

We thus asked where the apparent fusion originated from in our previous experiments, hypothesizing that instead of fusion, we were really observing HPTS that leaked into a fraction of the GUVs. To confirm this, we set up another control assay (Fig. 6.7 D): Instead of using washed LUVs with HPTS inside, we now formed LUVs in a buffer devoid of any dye. We then performed the fusion protocol as described in previous sections, adding HPTS to the solution at the same time as we incubated GUVs and LUVs together in the fusion step. For observation, we finally added DPX to the outside solution to quench ambient HPTS fluorescence. Since there was no HPTS inside the LUVs, HPTS fluorescence inside the GUV lumen could only originate from the surrounding solution, irrespective of any fusion events. GUVs with a bright HPTS signal must thus have been permeabilized during the fusion step, allowing dye to leak into the GUV (Fig. 6.7 D). Using confocal microscopy, we assessed what the requirements were for such membrane permeabilization (Fig. 6.7 E) [1]. When either only GUVs or only LUVs were incubated with the respective DNA strands, we did not observe any LUV localization to the GUV membrane, and most GUVs appeared as dark circles in the HPTS background. However, a small fraction of the GUVs did have a bright interior, indicating some membrane leakiness (Fig. 6.7 E, top and middle). By contrast, GUVs with bright HPTS signal in the lumen were much more common when DNA was present on both the GUVs and LUVs (Fig. 6.7 E, bottom). In fact, the fraction of GUVs with bright luminal HPTS signal was over 42 % for DNA-decorated GUVs and LUVs, compared to around 3 % for the samples where only one of the two vesicle types was decorated with DNA, and 0 % in the sample with no free dye outside the vesicles (Fig. 6.7 F). We thus concluded that rather than probing membrane fusion, our content mixing assay predominantly measured the effects of membrane porosity induced by DNA insertion and GUV-LUV-binding. Note that this does not necessarily mean that no fusion is happening in our assays; we may just be unable to detect it with our content mixing assay. This will be discussed in more detail in section 6.2.7.

6.2.6 DNA-mediated vesicle binding permeabilizes GUVs with different membrane compositions

In the context of constructing synthetic cells, a membrane- and volume delivery system should ideally be compatible with a range of membrane compositions and GUV formation methods. In ref. [240], it was shown that DNA-mediated fusion can work with phase-separated GUVs. Here we expanded this to different membrane compositions and demonstrated that successful LUV binding can be achieved with emulsion transfer produced GUVs as well, even though our content mixing assay was not sufficient to conclude whether membrane fusion occurred. In addition to DOPC vesicles, like those we have studied so far, we applied our protocol to GUVs containing 70 % DOPC and 30 % POPE, GUVs containing 60 % DOPC, 20 % DOPS, and 20 % cholesterol, as well as GUVs with

[1] Note that this set of experiments was performed with slightly different DNA strands (DNA2, DNA2') than the other results reported in this chapter, as we corrected a sequence error that had previously meant that DNA1 and DNA1' were not fully complementary (see Methods section for details). We do not expect this change in sequences to alter DNA insertion at all, as the TEG-cholesterol modification and DNA length was identical between the two sets of ssDNA strands. As a result of the longer stretch of complementary base pairs in DNA2/DNA2', the Gibbs binding energy of these strands used here was ~ 36 % higher than that of DNA1 and DNA1', but both far exceeded thermal energy ($\Delta G \approx 40 - 50\ k_BT$), so GUV-LUV binding should be very strong in both cases.

a DOPC membrane but produced by eDICE as described in chapter 4 (Fig. 6.8 A). In all cases, we worked with 200 nm LUVs that contained only DOPC and were bound to the GUVs by 1 µM DNA. Across all conditions, we found that LUVs bound successfully to the GUV membranes, and a fraction of GUVs always showed a bright cytosolic HPTS signal (Fig. 6.8 A). Analyzing the LUV intensity on all GUV membranes revealed that binding happened to a comparable degree across all samples (Fig. 6.8 B).

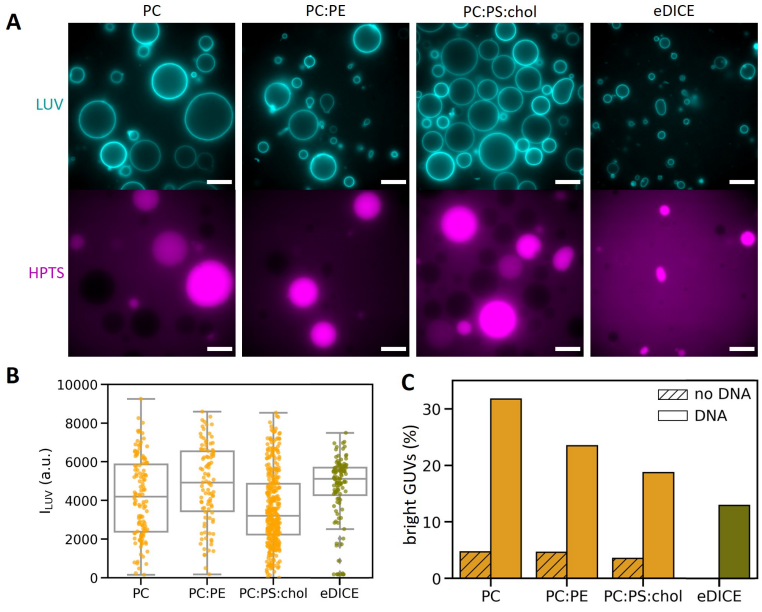

Figure 6.8: **DNA-mediated GUV-LUV binding induces membrane porosity in a range of different GUVs.** (A) Epifluorescence images of GUVs after incubation with 200 nm LUVs for 70 min in the presence of 1 µM DNA. LUVs are shown in cyan, HPTS in magenta. Scale bars: 20 µm. The GUV membranes all contain 0.05 % DOPE-Atto655, combined with either 99.95 % DOPC ('PC'), or 69.96 % DOPC and 30 % POPE ('PC:PE'), or 59.95 % DOPC, 20 % DOPS and 20 % cholesterol ('PC:PS:chol'). Vesicles marked 'eDICE' contain 99.95 % DOPC but were produced by eDICE (chapter 4). (B) Box plots of the LUV intensities at GUV membranes in the different samples revealed that all GUVs could bind LUVs via the linker DNA. GUVs represented in orange were formed by gel-assisted swelling, and GUVs represented in green were formed by eDICE. (C) Bar plot of the apparent fusion efficiencies in the different samples. Solid bars denote samples incubated with 1 µM DNA, and hatched bars represent controls where no DNA was added. The control sample for eDICE GUVs contained less than 20 vesicles and was thus not quantified. N = 277, 252 and 748 for gel swollen vesicles with the membrane compositions PC, PC:PE, and PC:PS:chol, respectively, and N = 118 GUVs for eDICE vesicles.

Assessing the internal HPTS intensities revealed that DOPC GUVs produced by gel-assisted swelling were most prone to membrane permeabilization (~ 32 %, Fig. 6.8 C), but fractions of leaky GUVs remained high (23 and 20 %, respectively) for both PC:PE and PC:PS:chol GUVs. In all cases, around 5 % of GUVs showed a bright internal HPTS signal in the absence of DNA, consistent with our findings from Fig. 6.15 D and 6.7 F. The increased propensity to form GUV membrane pores in pure DOPC membranes compared to more biomimetic membranes (PC:PS:cholesterol) is consistent with the notion that cholesterol-containing membranes are more tightly packed and generally less permeable. [489, 490]

It is however interesting that this trend seems to hold even when DNA-mediated LUV binding increases membrane permeabilization. Note also that this experiment should be repeated to confirm that the conclusion holds when we account for day-to-day variability in permeabilization rates. DOPC vesicles produced by eDICE had a lower fraction of HPTS-filled GUVs, with only ~ 13 % of GUVs showing detectable luminal HPTS signal (green bar in Fig. 6.8 C). This reduced propensity for membrane permeabilization may again be due to altered lipid packing, as previous works have suggested that emulsion transfer-based methods can leave traces of oil trapped between the GUV leaflets, altering the resulting membrane properties [491].

We note that the size of the LUVs bound to the GUVs did not change the degree of membrane permeabilization significantly, with 20-25 % of GUVs showing bright internal HPTS fluorescence both when incubated with 120 and 170 nm sized LUVs (see Supp. Fig. 6.13).

6.2.7 Indications of surface area growth by LUV fusion

We now know that the content mixing assay primarily showed the results of membrane permeabilization, but the fact that we could not detect membrane fusion with it does not necessarily mean that no membrane fusion was happening. Therefore, we compared the size distributions of GUVs that did or did not have the chance to undergo DNA-mediated fusion with LUVs. Population-level GUV growth has been used in a previous study as a reporter for GUV-LUV fusion [239], and may be useful to show membrane fusion even in the absence of detectable content mixing.

We first plotted the data for all experiments where GUVs were formed under identical conditions, and incubated with DNA in the absence of any LUVs. The GUV size distributions from these experiments are shown in the left part of Fig. 6.9 A. Similarly, we collected all the data from experiments where GUVs were incubated with LUVs, and where both vesicle types were decorated with DNA at 1 μM (Fig. 6.9 A, right of the dashed red line). The size distributions of GUVs that were incubated with LUVs (and thus in principle had the opportunity to undergo membrane fusion) tended to be shifted towards larger sizes. Indeed, when we joined the distributions from Fig. 6.9 A in one SuperPlot, we found that GUVs incubated with DNA and LUVs were on average larger (Fig. 6.9 B). In the SuperPlot, datapoints from each sample are shown in a different hue, and each sample is summarized with a circle whose position denotes the mean of the distribution, and whose size encodes the underlying sample size, giving an overview of the reproducibility of data across different experiments [492]. The graph was generated using the online tool SuperPlotsOfData [493]. We found that GUVs that had the chance to undergo fusion were on average significantly larger than those which did not, with average GUV radii almost a third bigger (7.4 ± 3.6 μm versus 5.6 ± 2.3 μm, $p < 10^{-5}$ by Welch's t-test). Furthermore, the combined size distribution gained a small additional peak at GUV radii above 10 μm, whereas we saw no such peak in the GUVs which have not undergone any fusion.

We thus conclude that this observation indicates strongly that GUVs were in fact fusing with LUVs, increasing their membrane area and volume in the process. We were not able to corroborate this via the content mixing assay as we report it above, since its results were dominated by membrane permeabilization rather than fusion. However, the refined content mixing assay we show in Fig. 6.7 A-C may be capable of reporting true membrane fusion:

with the artefacts from membrane permeability eliminated, it may yet be possible to detect the small amounts of fluorescence coming from dilute HPTS that is delivered to the GUV lumen by LUVs. Setting up this assay will be challenging from an imaging perspective: it requires good confocality (to avoid artefacts from out-of-focus light originating from non-fused LUVs bound to the GUV membrane) as well as high detector sensitivity and dynamic range, so that both the concentrated HPTS inside the membrane-bound LUVs, and the much more dilute dye in the GUV lumen, can be observed simultaneously.

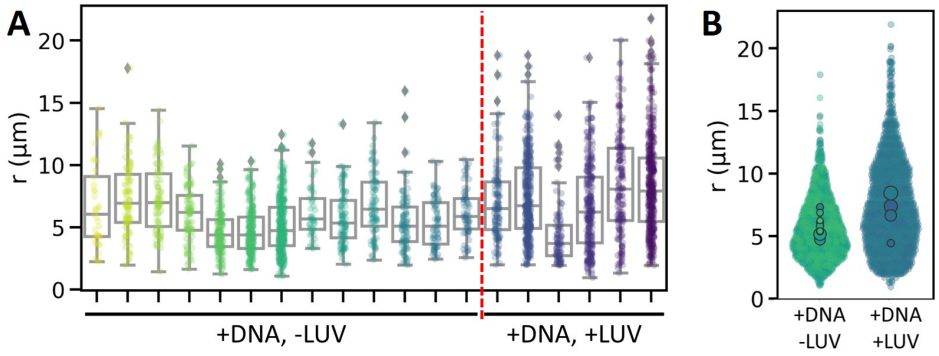

Figure 6.9: **Population-scale size analysis suggests that GUVs and LUVs are fusing.** (A) Boxplots and underlying data showing the GUV size distributions measured across different assays (see Supplemental Table 6.7 for details). In the experiments denoted as '+DNA, -LUV', we measured GUV sizes in the absence of any LUVs, so the size distribution could not have been influenced by membrane fusion. The samples denoted as '+DNA, +LUV' show the GUV sizes in samples where DNA-decorated GUVs were incubated with DNA-decorated LUVs at 1 µM DNA. Colors of datapoints denote different samples, and the dashed red line separates samples where fusion can and cannot have taken place. (B) SuperPlot summarizing the data from A. Datapoints from different samples are shown in different hues, and the mean of each individual distribution is shown as a circle in the center of the distribution. Circle sizes denote the number of datapoints in that sub-distribution, with sample sizes ranging from 37 to 416. The average size of all GUVs incubated with LUVs was significantly larger than that of the GUVs in the absence of LUVs, at 7.4 ± 3.6 µm compared to 5.6 ± 2.3 µm ($p < 10^{-5}$ by Welch's t-test). Sample descriptions, population sizes and mean radii shown in this figure are summarized in Supp. Table 6.7.

6.3 Discussion

Establishing a GUV-LUV fusion protocol

Here we have implemented a protocol for binding LUVs to GUVs via biomimetic ssDNA constructs, and found evidence for GUV growth by membrane fusion. We furthermore found that our content mixing assay, which we adapted from a previously established protocol [472], was dominated by GUV leakiness rather than actual membrane fusion.

We used an automated quantitative analysis pipeline to study the different steps involved in the fusion process on a population-level, analyzing large numbers of GUVs in each condition. Systematically studying the three steps involved in DNA-mediated LUV-GUV fusion, we first found that cholesterol-modified ssDNA rapidly inserts in GUV membranes in a manner consistent with a Langmuir adsorption model, where ssDNA binding to GUV membranes increases monotonously with ssDNA concentration in solution, but plateaus

as it approaches monolayer saturation. The Langmuir-like behaviour is consistent with previous reports, where cholesterol-tagged DNA adsorption was measured on supported lipid bilayers [480, 481]. However, the equilibrium constant was significantly higher in our system, with ~ 1 μM^{-1} compared to the range of tens of nM^{-1} reported for SLBs. It is not entirely clear whether the small curvature of the GUV membranes may change the adsorption behaviour of DNA on GUVs compared to SLBs. We speculate that it is more likely that interactions with the solid substrate and flow effects in the previously reported studies biased those systems towards more efficient adsorption [483–485].

The next step in the fusion process, binding of LUVs to GUV membranes via hybridization of ssDNA inserted into both membranes, revealed more surprising trends. We observed binding across all DNA concentrations probed, and no significant binding of LUVs in the absence of linker DNA. However, the LUV binding efficiency declined at DNA concentrations above 1 μM. This may stem from different factors whose exact contributions we cannot assess with our assay. Firstly, increasing concentration of DNA on the GUV membrane may lead to steric hindrance and thus reduce the chances that an LUV-bound DNA strand can bind to any given GUV-bound DNA strand. However, if this effect dominates, we would expect a reduction in apparent DNA binding as well, which we do not observe in the range of DNA concentrations we probed. A second possible origin of the drop in LUV binding may stem from the increasing amounts of free DNA in solution. With lower insertion efficiencies at higher DNA concentrations, we expect that there should be more free DNA which can diffuse quickly in solution and thus occupy binding sites on GUVs before they can be bound by LUV-bound DNA. Higher DNA concentrations in solution may thus effectively reduce the number of binding sites on the GUVs, lowering the possible maximum LUV density on the GUV membrane.

Finally, we adapted a content mixing assay based on HPTS, a quenchable fluorescent dye which we encapsulate in the LUVs, to assess whether they release their contents into the GUV lumen, indicating fusion. We indeed found that the apparent fusion rates measured by this assay followed the same trend as LUV binding: the fraction of apparently fused GUVs increased up to DNA concentrations of 1 μM and dropped off above that. However, we discovered that the results of this assay were in fact dominated not by fusion, but instead is a signature of GUV membrane permeabilization during the fusion step. Control experiments showed that a large fraction of GUVs (30-40 %) took up dye from the environment when LUVs bind to their outer leaflets via the DNA linkers. This introduced HPTS into the GUV lumen at much larger concentrations than LUV fusion would, obscuring any contribution from membrane fusion.

Membrane disruption by DNA-anchored LUVs

We confirmed that GUV membranes became leaky upon addition of cholesterol-anchored DNA: in the presence of fluorescent DNA outside the GUVs we identified a small population of GUVs where the DNA had entered the lumen during DNA-binding (section 6.2.2). We also always observed a fraction of GUVs that had a luminal HPTS signal in content exchange assays, whether or not LUVs or DNA were present in the sample (section 6.2.5). This is consistent with a previous study that found disruption and thus permeabilization of membranes by insertion of membrane-binding peptides [494]. Strikingly, we found that GUVs were permeabilized at much higher rates when LUVs were bound, compared to

samples where the cholesterol-tagged DNA was inserted in the GUV membrane but free on the other end. This suggests that either membrane tension or steric constraints on the orientation of the DNA linker disrupt the membrane, encouraging the opening of fusion pores.

Indeed, content exchange of LUVs with their environment has been reported in a study where synthetic peptides were used to drive LUV-LUV fusion. The authors reported there that the insertion geometry of the peptide made a significant difference in LUV leakiness, suggesting that membranes were permeabilized much more when a peptide was partially inserted into the membrane, disrupting lipid packing [494]. This idea is consistent with our observation that DNA insertion alone lead to several times less GUV content exchange than DNA insertion combined with LUV binding: when the hybridized ssDNA's cholesterol anchor is tethered to a LUV via a rigid, very strongly bound DNA zip, this is likely to sterically confine the orientations the cholesterol anchor can assume in the membrane. As a consequence, packing of the surrounding lipid membrane may be disrupted, destabilizing the membrane and leading to an increased propensity to open fusion pores. This may explain why lipid membranes that were either formed by a an emulsion-based method, or that contained a significant fraction of lipids which alter lipid packing, were less prone to permeabilization (Fig. 6.8).

If membrane destabilization is induced by DNA- and LUV-binding by a mechanism that changes membrane organization, then we may expect the same effect when we increase membrane tension, which is also known to destabilize GUV membranes [14]. Indeed we find a remarkable increase in the fraction of GUVs that show the signature of membrane permeabilization (from ~ 5 to ~ 30 %) when we combine DNA-mediated vesicle binding with osmotic shock during the fusion step, thus increasing membrane tension (Supp. Fig. 6.15). In fact, it appears that membrane disruption by DNA-induced packing defects and by increased membrane tension act synergistically: the fraction of GUVs which showed internal HPTS signal when both osmotic shock and DNA-mediated LUV binding were present was 30 – 40 %, significantly higher than the sum of the GUV fractions with HPTS in the lumen when only osmotic shock or DNA were applied (~ 5 % each, Supp. Fig. 6.15).

Given this synergistic action of membrane tension and DNA insertion, it is surprising that the fraction of permeabilized GUVs does not depend sensitively on the number of LUVs bound to a GUV. While we did observe a slight increase in permeabilization with LUV signal on the membrane, we found that a 33-fold increase in LUV intensity is required to produce a 3-fold increase in the permeabilized GUV fraction (Fig. 6.6 B). This suggests that the likelihood of membrane permeabilization is not directly proportional to the number of LUV binding events. Interestingly, we observed that those GUVs that had a bright HPTS signal in their lumen were consistently larger than those GUVs without luminal HPTS in the same sample (Supp. Fig. 6.16), implying that larger GUVs had a higher likelihood of being permeabilized by LUV-bound DNA. Note that our GUVs were already in isotonic conditions before the fusion step, and were thus largely spherical with very little visible excess membrane area. Membrane permeabilization should therefore not lead to any significant GUV inflation in these samples, which means that permeabilized GUVs must have been larger prior to permeabilization, rather than becoming bigger as a result of it. The simplest explanation of this effect is to assume that the probability of membrane disruption is constant per unit area: those GUVs that are larger and thus possess a larger

membrane surface, run a proportionally higher risk of being permeabilized, consistent with previous reports suggesting that vesicles become more mechanically fragile with increasing size [495]. This relationship of GUV size and leakiness is potentially important to note for synthetic cell applications: there, it is usually not desirable to allow spontaneous opening of membrane pores, to avoid uncontrolled uptake or loss of material. Consequently, membrane fragility may impose a limit on how large synthetic cells can be designed with simple membranes.

Indications of DNA-mediated vesicle fusion

Finally, we assessed whether we could observe any membrane fusion despite the fact that our content mixing assay was dominated by membrane permeability. Inspired by previous works that relied on population-level growth of GUVs as a reporter for tension-driven membrane fusion [239], we compared population-wide GUV size measurements to assess whether there are any indications of GUV-LUV fusion in our sample. Indeed, we found that GUVs were consistently larger in samples that had been incubated with DNA-decorated LUVs, compared to samples where the GUV membrane was only incubated with DNA (Supp. Fig. 6.16). This indicates that significant membrane fusion was indeed taking place in our assay. In fact, we measured a cumulative shift in GUV radii from 5.6 μm to 7.4 μm, indicating an area gain of 294 μm^2, or almost 75 % of the original membrane area, in an average GUV. Assuming that such a size increase originated from fusion of 200 nm LUVs with a GUV, this would mean that over 2000 fusion events were in fact happening per GUV in our assay. This is significantly more than we calculated as a lower bound of 125 fusion events for detecting fusion in section 6.2.4. Nonetheless, it is not surprising that we were unable to detect fusion with our fluorescence based assay, even when we refined it to remove free HPTS and used confocal instead of widefield imaging. The limit of 125 fusion events was calculated on the basis of bulk fluorescence measurements taken on a spectrophotometer, whereas we observe our GUVs individually in the microscopy-based assay to assess whether they have undergone fusion. Detector sensitivities may vary widely between the two systems, and the volume of solution over which the signal is integrated was much lower for single GUVs than in the spectrophotometric assay, where we measured signal from several 100 μL of solution. Furthermore, we must consider not just the sensitivity, but also the dynamic range of the detector: even when 2000 LUVs fuse with an average sized GUV, the dye inside the GUV will be over 200 times more dilute than that in each of the LUVs which are bound to the GUV surface but not (yet) fused. Careful tuning of imaging conditions will be required to visualize both the LUVs with concentrated HPTS, and the dilute HPTS inside the GUVs.

Future directions

Our work shows encouraging indications that DNA-mediated GUV-LUV fusion can be used to generate significant membrane area growth. These should be carefully interrogated using the refined experimental setup we propose in section 6.2.5, but may also be corroborated by other techniques. Firstly, if typical GUV membranes indeed expand by 75 % due to GUV-LUV fusion, it should be possible to adapt FRET-based lipid mixing assays that have previously only been used in fusion of similarly-sized vesicles [474, 496] to demonstrate lipid mixing in our assay.

Furthermore, such a large increase in membrane area also implies that it should be possible to significantly change the membrane composition of a GUV by fusing it with LUVs with different membrane components. This opens the door to a new type of membrane fusion assay based on binding of components encapsulated inside the GUV: if the LUVs contain a significant fraction of a receptor lipid (e.g. 10 % lipids with a biotin-modified headgroup), lipid mixing between GUV and LUV membranes upon vesicle fusion could be assessed by the binding of some encapsulated reporter (e.g. fluorescent streptavidin) to the GUV membrane post-fusion. This should make it possible to not only make a binary assessment of whether or not vesicles have undergone fusion, but even give insight into the resulting change in membrane composition.

As we serendipitously found, DNA-mediated binding between GUVs and LUVs can induce pore formation in a significant fraction of GUVs. While this complicated the interpretation of content mixing results, it also draws attention to an important issue: if membrane fusion necessarily involves destabilization of the vesicle membrane, how do we prevent this destabilization from also leading to the uncontrolled release of the GUV's cytosol? Our preliminary data suggests that tuning of the GUV membrane composition and formation method may help limit the fraction of GUVs that is permeabilized by DNA-mediated LUV binding. Note, however, that the true fusion efficiency in these samples remains a question for further study.

Finally, we consider the wider implications of our observations for building synthetic cells. Our population-wide measurements suggest that GUVs which undergo fusion with LUVs may indeed be experiencing significant surface area growth. This is extremely encouraging not only in the context of synthetic cell division - where at least a factor of 1.28 in membrane area must be reached to divide a cell while keeping its volume constant, with more growth necessary for sustained growth and division cycles. The significant amounts of membrane area growth also suggest that our fusion protocol may be a viable tool for incorporating membrane components in GUVs. Most obviously, such components can be lipids, giving the researcher control over membrane composition in a time-resolved manner [240]. Perhaps even more crucially, however, DNA-mediated fusion may also serve as a tool for integrating transmembrane proteins in GUVs. So far, in vitro reconstitution of transmembrane proteins has largely focused on LUVs, where the large surface-to-volume ratio makes it easy for transmembrane enzymes and transporters to detectably alter properties of the vesicle interior (such as increasing the cytosolic concentration of nucleotides and other reagents, or creating pH gradients across the membrane [459, 497, 498]). However, such systems will eventually need to be integrated with other modules on the way to building synthetic cells, and must therefore be transferred into GUV membranes. Since transmembrane proteins are usually unstable outside of lipid membranes [499], they must be kept in a hydrated environment free of organic solvents such as chloroform or other oils. Consequently, transmembrane proteins cannot generally be reconstituted directly in GUV membranes. Instead, they are first reconstituted in small liposomes [500], detergent micelles [501] or peptide-stabilized lipid nanodisks [502], and transferred into GUV membranes in a separate second step. Typically, membranes are partially destabilized with detergent during this step to facilitate transfer of integral proteins into the GUV membrane [498, 501, 503]. This require careful tuning of detergent concentrations, to ensure that GUVs remain intact, and necessitates a lengthy detergent removal step afterwards [498].

DNA-driven vesicle fusion may simplify this delivery of membrane components. Using DNA as a mediator of vesicle fusion is attractive, as it provides a route towards fusion that is controllable in time (by adding LUVs at the desired time) and somewhat controlled in space (by locally injecting DNA into the environment using micromanipulation tools). It can also be applied in cycles, due to the reversible nature of the cholesterol anchor's membrane insertion. For even more controlled delivery of membrane and cytosolic components to synthetic cells, DNA mediated fusion may be complemented by other membrane fusion techniques, such as light-controlled fusion mediated by gold nanoparticles [443].

6.4 Materials and Methods

6.4.1 Materials

Potassium chloride (KCl), D-(+)-glucose, sucrose, Tris(hydroxy-methyl)aminomethane hydrochloride (Tris-HCl), 8-hydroxypyrene-1,3,6-trisulfonic acid trisodium salt (HPTS), p-xylene-bis-pyridinium bromide (DPX), cholesterol and β-casein were obtained from Sigma Aldrich. All non-fluorescent lipids 1,2-dioleoyl-sn-glycero-3-phosphocholine (DOPC), 1-palmitoyl-2-oleoyl-sn-glycero-3-phosphoethanolamine (POPE) and 1,2-dioleoyl-sn-glycero-3-phospho-L-serine (DOPS) were obtained from Avanti Polar Lipids. The fluorescent lipids Atto488-DOPE and Atto655-DOPE were purchased from Atto-TEC.

6.4.2 GUV preparation

GUVs were prepared by gel-assisted swelling [76], a facile and quick formation technique which successfully yields vesicles for a range of membrane lipid compositions and swelling solutions. In short, cover glasses (22 x 22 mm, No. 1.5H, Paul Marienfield GmbH & Co. KG) were first rinsed with ethanol and MilliQ water and dried under a stream of nitrogen. They were then plasma cleaned for 30 seconds (PlasmaPrep III, SPI supplies), after which 100 µL of a 5 % (w/v) polyvinyl alcohol (PVA, 145 kDA, 98 % hydrolysed, VWR) solution in 200 mM sucrose in MilliQ water at room temperature was spread over each coverslip. The gel was solidified by baking it in an oven for 30 minutes at 50° C. Then, 10 µL of a lipid solution at a total lipid concentration of 1 mg/mL in chloroform, typically consisting of DOPC:Atto488-DOPE in a molar ratio of 99.5:0.5, was spread over the gel. The gel was placed in a vacuum desiccator for 30 minutes to ensure complete evaporation of the organic solvent. The cover glasses were then placed in a compartmentalized petri dish (4 compartments, VWR), and to each gel we gently added 300 µL of GUV swelling buffer containing 100 mOsm sucrose, 10 mM KCl and 10 mM Tris-HCl at pH 7.4. After swelling for one hour at room temperature, GUVs were collected by taking the swelling solution up with a pipette (1 mL tip), flushing the solution again over the cover slip once to dislodge the GUVs, and pipetting it up again. To compare the effect of GUV formation technique on fusion, we also produced GUVs with eDICE (see chapters 4 and 5). eDICE vesicles were prepared with a membrane composition of DOPC:Atto488-DOPE in a molar ratio of 99.5:0.5, and contained 100 mM KCl, 10 mM Tris pH 7.4, 6.5 % (vol/vol) Optiprep, and 52 mM sucrose in the IAS. They were spun into an outer aqueous solution of 310 mM glucose in MilliQ, and were diluted into a buffered solution (10 mM TrisHCl pH 7.4) immediately after formation. After this dilution step, the outer buffer components matched those of the gel swollen GUVs. All GUVs, formed by gel-swelling or eDICE, were stored in the fridge and

used within two days of formation.

6.4.3 LUV preparation and characterization

LUVs were prepared by extrusion. To this end, 5 ml glass tubes (Pyrex) were first cleaned with tap water and soap, and then rinsed with demineralized water. The tubes were subsequently rinsed with ethanol, acetone and MilliQ water, and finally dried with nitrogen air. Once cleaned, the bottom of the glass tubes was filled with 200 µL chloroform to create volume for mixing. In the cleaned tubes, lipids with a total mass of 0.75 mg were mixed in ~ 200 µL of chloroform at a typical volumetric ratio of 29 µL DOPC (25 mg/mL) and 6.5 – 62 µL of fluorescently labelled lipids (0.1 mg/mL), depending on the desired fraction of lipid dye in the vesicles. Lipids were mixed and then dried under a gentle stream of nitrogen, and any remaining solvent was removed by placing them in a vacuum desiccator for two hours. The lipid films were rehydrated in 1.5 mL LUV swelling buffer (100 mM KCl, 10 mM Tris-HCl pH 7.4), supplemented with 10 mM HTPS, to obtain a lipid dispersion at a final concentration of 0.5 mg/mL. After 2 min incubation time, the solution was vortexed for 30 s and sonicated in a bath sonicator for 30 s (Branson 2510 Ultrasonic Cleaner, Marshall Scientific), to redissolve the lipid films and form small liposomes. To decrease the size polydispersity and promote unilamellarity, we extruded the produced liposomes 21 times through a polycarbonate filter (Nuclepore, Whatman) of a pore size 200 nm using the Avanti Mini Extruder (Avanti Polar Lipids, Inc.). To produce LUVs with a target size of 100 nm, the liposomes were instead extruded 21 times through a 100 nm polycarbonate filter. The resulting LUV dispersion was stored at 4° C and used within one week of formation.

For the control experiments shown in Fig. 6.7 C, LUVs were formed as described above, encapsulating 10 mM HTPS. Subsequently, excess HPTS outside the vesicles was removed by loading the solution onto a PD 25 desalting column (MiniTrap column with Sephadex G-25 resin, Sigma Aldrich) and eluting them with 1.5 mL LUV formation buffer without HTPS.

LUV size distributions were measured by dynamic light scattering (DLS) using a Zetasizer Nano ZS (Malvern Panalytical). For each measurement, 70 µL of LUV sample was placed in a disposable cuvette (ZEN0040, Malvern Panalytical). Each sample was measured twice in a backscatter measurement at 25° C, with each measurement consisting of a minimum of 12 runs. The time-dependent raw scattering intensity was converted to the intensity autocorrelation function and finally the particle size distribution using the commercial instrument software.

6.4.4 DNA incorporation

The sequences of single-stranded DNAs for fusion assays were adopted from [240] and are shown in Table 6.3. For all experiments except those reported in Fig. 6.7, we used chol-3'-DNA1-5' and its complementary strand chol-5'-DNA1'-3', called chol-DNA1 and chol-DNA1' henceforth. We used chol-DNA1 to functionalize LUV membranes and chol-DNA1' to functionalise GUV membranes. DNA1-Atto488 was used to visualized DNA insertion into GUV membranes. The strands chol-DNA1 and chol-DNA1' have their cholesterol membrane anchors on opposite ends to allow antiparallel hybridization, which has previously been shown to promote membrane fusion [61, 476]. All DNA strands arrived as powder and were dissolved and diluted to 100 mM DNA in MilliQ-water containing

10 mM Tris-HCl at pH 7.4. Dissolved DNA was stored at 4° C and could be used for months.

Note that due to a reporting error in one of the ssDNAs in ref. [240], chol-DNA1 and chol-DNA1' have a different number of base pairs and are therefore not fully overlapping (K. Jahnke, personal communication). We discovered this only late in the project, which is why most results reported here were obtained with DNA strands that were not fully complementary. The corrected sequences are reported in Table 6.3, we call them chol-DNA2, chol-DNA2' and DNA2-Atto488 in analogy to the original DNA strands. These were fully complementary. We analyzed different DNA dimerisation modes using an open-source online analysis program (Integrated DNA Technologies, eu.idtdna.com/calc/analyzer), assessing (1) dimerisation between complementary strands, (2) self-dimerisation of the individual strands, and (3) the formation of hairpin structures due to self-binding. Due to the sequence error in DNA1', DNA1 and DNA1' could hybridize either with 13 base pairs in a membrane-distal configuration or with 11 base pairs on the membrane-proximal side. The Gibbs energies of these configurations were comparable with each other, but more than 30 % reduced compared to the hybridization energy of the corrected, fully complementary strands. All hybridization energies are listed in Table 6.1 and range from 37 to 52 k_BT. These binding energies are very high compared to the thermal energy, making unbinding unlikely. Thus, once a strand hybridizes in one of the two modes, we can assume that it is trapped in that configuration. As the membrane-distal sides of the strands have more freedom of movement, we expect binding to mainly happen at the far end. This effectively creates a sub-optimal zippering mechanism, leaving a spacer of 10 bp between the membrane and the hybridized strand, which is not present in the fully complementary strands. Analysis of self-dimerisation showed a maximum hybridisation length of 2 base pairs for both chol-DNA1 and chol-DNA1', with a corresponding Gibbs energy about 10 times lower than the hetero-dimerisation energy. Self-dimerized DNA strands can thus easily thermally unbind and are only transiently linked. The formation of hairpin structures due to self-binding was energetically unfavourable. In summary, we cannot exclude transient self-dimerization in our fusion experiments, but we do not expect it to interfere significantly with hetero-dimerisation.

To fluorescently visualize DNA incorporation, GUVs were incubated overnight in swelling buffer with chol-DNA1' and DNA1-Alexa488, both at 1 µM unless specified otherwise. To test the effect of DNA concentration on incorporation, both ssDNA strands were added to unlabelled GUVs at concentrations ranging from 0 to 5 µM at a 1:1 ratio between the two DNA strands, keeping the osmotic conditions constant throughout. To investigate the effect of osmotic conditions on DNA incorporation, 10 µL GUVs in swelling buffer were mixed with 29.2 µL observation buffer of varying glucose concentration. Osmolarities were using a freezing point osmometer (Osmomat 3000, Gonotec GmbH). To test the effect of DNA incubation time, GUVs were incubated with both DNA strands either for 10 minutes or overnight before imaging. GUVs were left at 4° C for overnight incubation. The effects of both osmolarity and time were tested with GUVs labelled with 0.01 % Atto 655 DOPE.

6.4.5 LUV binding

Binding of LUVs to GUVs was done by first incubating LUVs and GUVs with the respective chol-DNA strand. LUVs were incubated with 1 µM chol-DNA1, while GUVs were incubated separately with 1 µM chol-DNA1'. We used DOPC LUVs doped with 0.05 mol% Atto655-

Pairing	ΔG (kcal/mol)	ΔG (k_BT)
DNA1 + DNA1', membrane-proximal hybridization	-22	37
DNA1 + DNA1', membrane-distal hybridization	-23	39
DNA2 + DNA2', full hybridization	-32	52

Table 6.1: Sequences of ssDNA used for DNA and LUV binding and fusion assays.

Measurement	GUV dye	LUV dye	DNA (μM)	DNA incubation	vesicle incubation
DNA conc.	0.5 % Atto488	0.05 % Atto655	0-5	overnight	60 min
binding time	0.5 % Atto488	0.05 % Atto655	1	25 min	10 min - 2 hr
osmolarity	0.1 % Atto488	0.05 % Atto655	1	overnight	2 hr

Table 6.2: Experimental conditions used in GUV-LUV binding assays.

DOPE for all binding experiments. To induce GUV-LUV binding, 10 μL GUVs with DNA and 10 μL LUVs with DNA were added to 20 μL quenching observation buffer (100 mM KCl, 100 mM glucose, 10 mM Tris-HCl at pH 7.4 and 5 mM DPX). Note that the LUV buffer is of lower osmolarity than the GUV swelling and observation buffers, resulting in an osmotic shock of ~ 30 mOsm for the GUVs during the binding/fusion step. Experimental conditions in binding experiments are listed in Table 6.2.

6.4.6 Content mixing

To visualize which GUVs had fused with LUVs, we performed content mixing experiments. We encapsulated the fluorescent dye HPTS at high concentration (10 mM) in LUVs by adding it to the LUV swelling buffer. Both GUVs and LUVs were first incubated with 1 μM DNA as described above. After incubation, GUVs and LUVs were mixed 1:1 (vol/vol) in quenching observation buffer to a final concentration of dye and quencher of 2.5 mM HPTS and 2.5 mM DPX, respectively. Note that fusion occurs in the same step in the experimental protocol as binding. Like in the binding experiments, GUVs were subjected to a small osmotic shock during this step. The effect of the osmotic shock is discussed in Supp. Fig. 6.15. The specific experimental conditions in each fusion experiment are listed in Table 6.4. We used the same membrane dyes throughout, as the choice of lipid dye has been shown to impact fusion outcomes, since certain dyes can promote lipid exchange between vesicles [504].

6.4.7 Imaging

GUVs were visualized in 200 μL imaging chambers. To create the chambers, glass coverslips (# 1.5H, 24x50 mm, Paul Marienfeld GmbH & Co. KG) were first cut to fit a custom-made holder and subsequently rinsed with ethanol and MilliQ water. Coverslips were dried under a vigorous nitrogen stream and used immediately. Chambers were created by cutting the lid and bottom off 0.2 mL PCR tubes (Fisher Scientific) and adhering them upside-down onto the coverslip with two-component epoxy glue. Once the glue was dry, the chambers were incubated for at least 15 min with a 1 mg/mL β-casein solution in 10 mM Tris-HCl at

	Name	Sequence	Application
original	chol-DNA1	5'-TGG ACA TCA GAA AGG CAC GAC GA-3'-Cholesterol-TEG	LUVs
original	chol-DNA1'	Cholesterol-TEG-5'- TCC GTC GTG CCT TAT TTC TGA TGT CCA-3'	GUVs
original	DNA1-Atto488	5'-TGG ACA TCA GAA AGG CAC GAC GA-3'-Atto488	imaging
corrected	chol-DNA2	5'-TGG ACA TCA GAA AGG CAC GAC GA-3'-Cholesterol-TEG	LUVs
corrected	chol-DNA2'	Cholesterol-TEG -5'- TCG TCG TGC CCT TCT GAT GTC CA-3'	GUVs
corrected	DNA2-Atto488	5'-TGC ACA TCA GAA AGG CAC GAC GA-3'-Atto488	imaging

Table 6.3: Sequences of ssDNA strands used in this study.

Experiment	GUV dye	LUV dye	DNA (µM)	DNA incubation time	vesicle incubation time
osmotic shock	0.5 % Atto488	0.05 % Atto655	1	15 min	70 min
DNA concentration	0.5 % Atto488	0.05 % Atto655	0-5	overnight	60 min
LUV size	none	0.05 % rhodamine-PE	1	90 min	70 min
GUV membrane composition	0.5 % Atto488	0.05 % Atto655	1	15 min	70 min
GUV formation method	0.5 % Atto488	0.05 % Atto655	1	15 min	79 min

Table 6.4: Experimental conditions in content mixing assays.

	Microscope	Excitation	Detection
GUV-Atto488	Nikon Widefield	508 nm, 20 % LED power	100 ms exposure time
LUV-Atto655	Nikon Widefield	640 nm, 40 % LED power	100 ms exposure time
HPTS	Nikon Widefield	440 nm, 1 % LED power	10 ms exposure time
GUV-Atto488	Leica LSCM	WLL at 501 nm, 1 % laser intensity	HyDS (506-577 nm), counting mode
LUV-Atto655	Leica LSCM	WLL at 663 nm, 10 % laser intensity	HyDX (673-729 nm), standard mode, gain 100
HPTS	Leica LSCM	405 nm solid state laser, 0.4 % laser intensity	HyDS (445-524 nm) counting mode

Table 6.5: Imaging conditions used in this chapter.

pH 7.4, and finally washed twice with observation buffer.

Epifluorescence images were aqcquired on an inverted Nikon Eclipse Ti microscope equipped with a digital camera (Orca-Flash 4.0, Hamamatsu), an LED light source for monochromatic illumination (Spectra X, Lumencor), and a 100x magnification oil immersion objective (CFI Plan Apochromat VC 100x oil, NA 1.4, Nikon). Confocal images were acquired on the Leica Stellaris 8 microscope (see chapter 4 for technical details) using a HC PLAN APO 63x glycerol immersion objective with a pinhole of 103 μm and a pixel dwell time of 3 μs in all channels. Detailed imaging settings are listed in Table 6.2; identical settings were used in all experiment on each setup, to allow for comparability between samples. Absence of spectral crosstalk between different colour channels was ascertained by imaging unlabelled control samples, and confirmed by the fact that we observed no correlation between intensities from different dyes in population analysis

Microscopy fluorescence images were analysed with a custom-written python-based software named DisGUVery [389], and the analysis procedure is illustrated in Supp. Fig. 6.10. In brief, epifluorescence images showing several GUVs were pre-processed by a smoothing and edge enhancement step, and GUVs were detected using the circular Hough transform (CHT) module of the DisGUVery toolbox [389]. This allowed us to analyze at least ~ 100 separate GUVs for every condition probed, and thus draw statistically valid conclusions about the population-level properties of the GUVs. The locations and radii of GUVs detected by CHT were saved and used to automatically analyze the images further. For DNA- and LUV-binding assays, we analyzed the average intensity of the respective label on the GUV membrane. Angular averages of pixel intensities were computed to extract a radial intensity profile for each GUV, and find the average local background signal just outside the GUV. Further, we detected the maximum pixel intensity along lines perpendicular to the membrane in a toroidal ROI encompassing the membrane. The median of these maximum intensities on a single GUV was used as the average intensity on the membrane, and further corrected by subtracting the local background intensity just outside the GUV. To analyze fusion assays, we performed the same type of GUV detection and extracted the angular average of HPTS intensities at each radial distance from the GUV center. The HPTS intensity ratio, which was our measure for apparent fusion, was then computed as the ratio of HPTS signal in the GUV center divided by HPTS signal just outside the GUV membrane.

Control samples reported in Fig. 6.7 were imaged on an inverted Leica Stellaris 8 laser scanning confocal microscope equipped with a white light laser (WLL) as well as a 405 nm solid state laser, and 63x glycerol immersion objective (HC PL APO CS2 63X/1.30). HPTS was excited using the solid-state laser operated at 0.4 % power, and fluorescence was detected with a HyDS detector operated in photon counting mode. GUV membranes tagged with Atto488 were illuminated at 501 nm with 1 % laser power on the WLL and fluorescence was detected on a HyDS detector operated in counting mode. LUV membranes (Atto655) were illuminated at 663 nm with 10 % laser power (WLL) and fluorescence was detected using a HyDX detector operated in analog mode with a gain of 100. All fluorophores were imaged with a pixel dwell time of 3 μs and at a pinhole of 1 Airy unit.

To analyze apparent fusion efficiencies from these control experiments, we manually classified GUVs as brighter or darker than the surrounding HPTS signal using the ImageJ plugin CellCounter (plugin authored by Kurt de Vos in Fiji [340]).

Statistical tests (Welch's t-test and ANOVA) on the analysis results were performed using the Python package 'scipy.stats'.

Acknowledgements

We thank Yannick Dreher, Kevin Jahnke and Kerstin Göpfrich for useful instructions for the experiments, Liedewij Laan, Christine Linne, Kate Adamala and Ali Azadbakht for useful discussions about DNA-mediated interactions, and Marcos Arribas Perez and Ludo Schoenmakers for useful discussions on membrane fusion more broadly. Christophe Danelon is thanked especially for his helpful suggestions on the refined fusion assay. We acknowledge financial support from The Netherlands Organization of Scientific Research (NWO/OCW) Gravitation program Building A Synthetic Cell (BaSyC) (024.003.019)

6.5 Supplementary Information

6.5.1 Supplementary figures

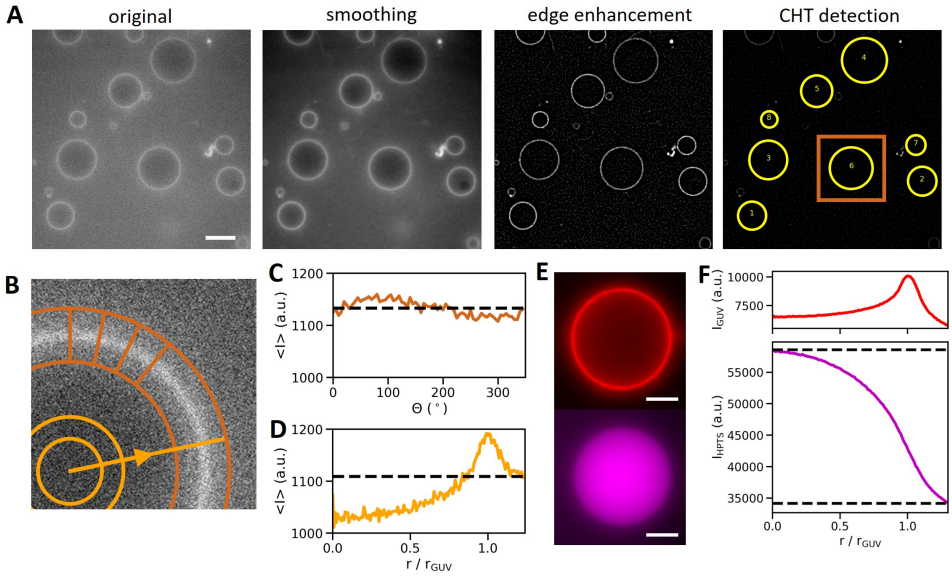

Figure 6.10: **Image analysis pipeline** (A) GUV detection using the DisGUVery toolbox [389]. Fluorescence images are first smoothed by convolution with a Gaussian filter. After an edge enhancement step, GUVs are detected using the circular Hough transform (CHT) detection module. Yellow circles indicate detected GUVs. Scale bar: 5 µm. (B) Zoom-in on the GUV marked in orange in the last panel of (A). A radial slice 50 pixels in width was used to compute the signal on the membrane. In the radial slice between the orange circles, radial line intensity profiles were computed at 5° intervals. The maximum intensity in each of those profiles is set as the intensity (DNA or LUV, depending on the experiment) at that angle (see panel C). Separately, line intensity profiles were extracted on concentric circles at radial intervals of 5 pixels (yellow). For each radial slice, this data was averaged to yield the average radial intensity (see panel D). (C) Maximum intensity on the membrane as a function of the radial coordinate Θ. The dashed line indicates the median intensity in the angular profile. (D) Radially averaged intensity as a function of the distance from the GUV center r/r_{GUV}. The dashed line represents the intensity at the outermost pixel of the analyzed ROI, which we use for local background subtraction. (E) Epifluorescence image of a GUV (membrane in red) containing HPTS (magenta). Scale bars: 5 µm. (F) For fusion assays, GUVs were detected using their membrane fluorescence by the same procedure outlined in (A). The radially averaged HPTS signal (bottom panel, magenta) was extracted as outlined in (B) and (D), and used to compute the HPTS intensity ratio between the center of the GUV ($I_{HPTS}(0)$, top dashed line) and the outermost radial slice ($I_{HPTS}(r_{GUV} + 25px)$, bottom dashed line). The radially averaged GUV membrane signal (top panel, red) is shown for reference.

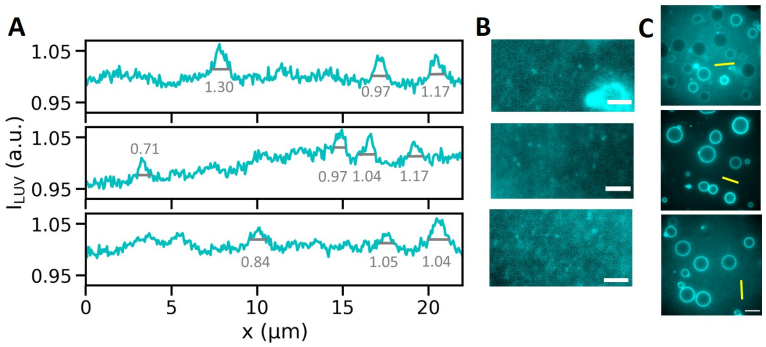

Figure 6.11: **The LUV background sometimes has a grainy structure** (A) Intensity profiles of the LUV signal along a 5 px wide line drawn through the background of the images shown in Fig. 6.4 B. At all DNA concentrations (top: 0.25 μM, middle: 1 μM, bottom: 5 μM), the background shows small bright structures around 1 μm across (grey lines, distances in μm). (B) The features are visible as small speckles in the region where we drew the line profiles. Scale bars: 5 μm. (C) Yellow lines indicate where the line profiles were extracted in the epifluorescence images. Panels shown in (B) are zoom-ins on a section around these lines. Scale bar: 20 μm.

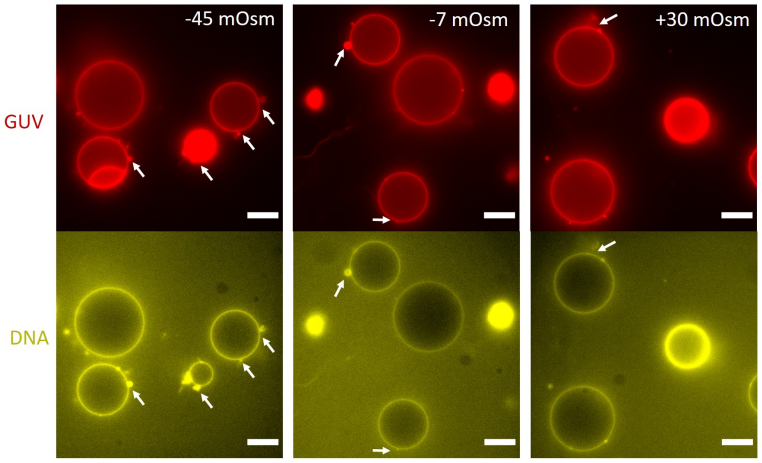

Figure 6.12: **Regulating excess area by osmotic shock .** Epifluorescence images of DNA (yellow) bound to GUVs (red) at different osmotic mismatches between inner and outer solution. At both hyper- and hypotonic conditions, most GUVs are spherical and some bear outward-pointing membrane structures (buds and tubes, white arrows). These structures are more prevalent in GUVs where the inner osmolarity is lower (-45 and -7 mOsm) than the outer osmolarity, consistent with excess membrane area being stored in such structures upon GUV deflation. Surprisingly, even GUVs in hypotonic conditions (+30 mOsm) show some such structures, indicating that the GUVs did not deflate as expected, or may have released pressure by opening transient membrane pores.

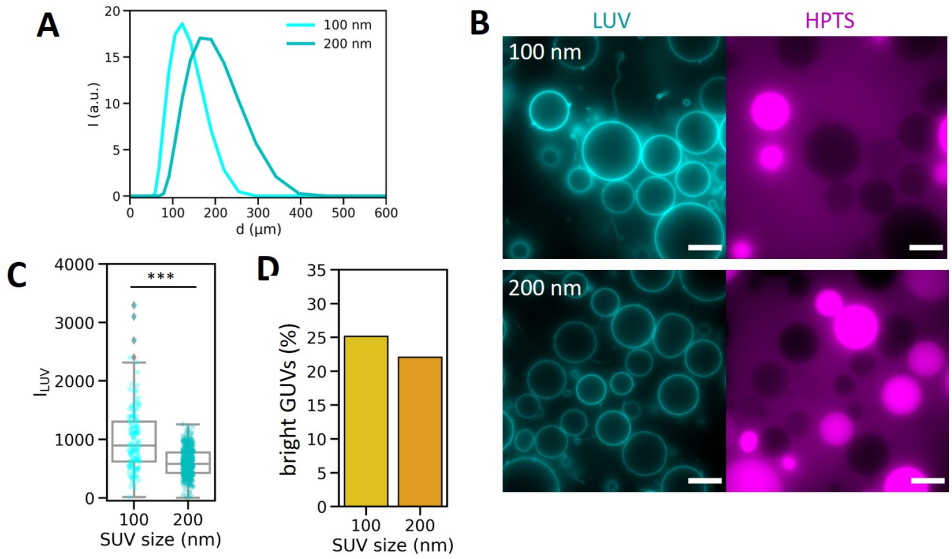

Figure 6.13: **Membrane permeabilization does not depend strongly on the size of the bound LUVs.** (A) Diameter distributions of SUVs measured by DLS with peaks at 120 and 170 nm for 100 and 200 nm LUVs, respectively. (B) Epifluorescence images of GUVs after 70 min incubation with 100 and 200 nm sized LUVs in the presence of 1 μM DNA. LUV signal is shown in cyan, HPTS in magenta. In both samples, the LUV signal is represented with an identical lookup table, so the absolute LUV intensities on the GUV membrane are significantly higher for 100 nm LUVs than for 200 nm SUVs[2]. Scale bars: 20 μm. (C) Box plots of the LUV intensity on the membranes for 100 and 200 nm sized LUVs. Individual datapoints represent single GUVs; N = 159 and 408 GUVs for 100 and 200 nm SUVs, respectively. The underlying distributions are significantly different ($p<10^{-5}$ by Welch's t-test). We note that this is unexpected and may point to higher fusion rates in the case of 100 nm SUVs[3]. (D) The fraction of GUVs with internal HPTS signal is similar for 100 and 200 nm SUVs (25 compared to 22 %), indicating that membrane disruption does not depend strongly on the size of the bound vesicles.

[2]It is surprising to see a difference in GUV-bound membrane signal between the samples incubated with different sizes of SUVs, as geometrical arguments would suggest that the same overall LUV signal should be the same irrespective of LUV size: If LUVs bind to the GUV surface (assumed here to be flat) at their maximum packing density (~ 0.9 for hexagonal dense packing of monodisperse circles on a plane), then the number of LUVs binding to a unit area is inversely proportional to the cross-sectional area of one LUV, and thus $N_{LUV,A} \propto r_{LUV}^{-2}$. At the same time, the number of fluorophores in one LUV membrane is proportional to its surface area, thus $N_{fluo,LUV} \propto r_{LUV}^{2}$. Since the LUVs are smaller than the optical diffraction limit, we measure the total fluorescence intensity of one LUV in one diffraction limited spot as $I_{fluo,LUV} \propto N_{fluo,\,LUV}$, and the overall fluorescence on a piece of membrane as $I_{fluo,A} = I_{fluo,LUV} \cdot N_{LUV,A} \propto r_{LUV}^{0} \propto 1$. We should thus expect to find the same LUV fluorescence intensity on the GUV membrane irrespective of LUV size, if LUVs bind at the same density. This suggests that some other non-trivial factor must be at play in our assay. LUV binding may curvature sensitive, or depend on the density of DNA on the LUV surface (which is likely to be lower for 100 nm LUVs, as there is more LUV surface area in the sample for the same amount of DNA to bind).

[3]Alternatively, the increased LUV signal on the GUV membranes may be an indication of membrane fusion: if LUVs fuse to the GUV membrane, then their fluorophores will still contribute to local fluorescence intensity, but they will no longer occupy space on the GUV membrane and thus preclude more LUVs from binding.

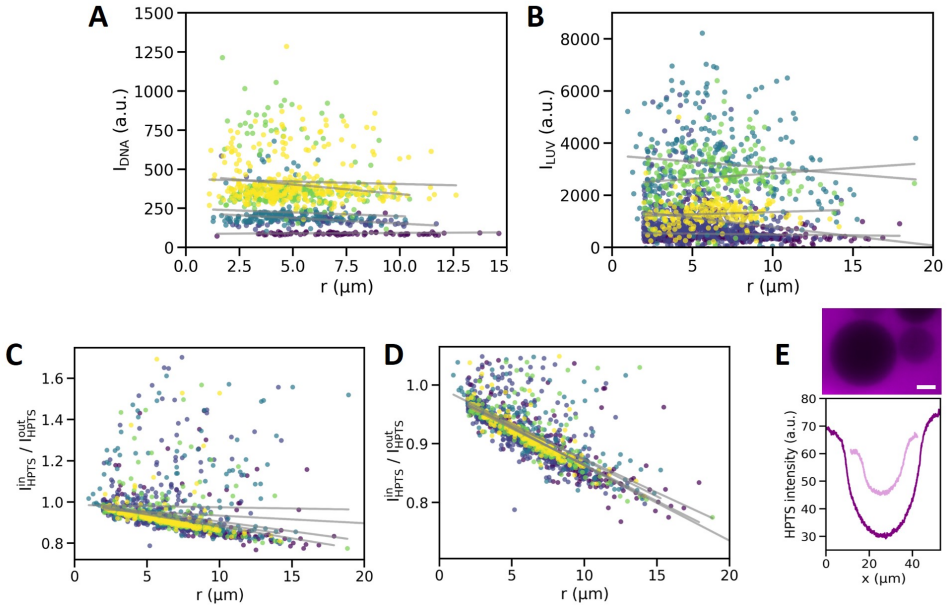

Figure 6.14: **Membrane-bound and luminal signal is affected differently by epifluorescence imaging.** (A) DNA signal on the membrane as shown in Fig. 6.2 C, along with linear fits for each DNA concentration. DNA signal on the membrane is largely independent of GUV size. Only 0.5 μM DNA shows a slight negative correlation with GUV size (Pearson's correlation coefficient $r_P = -0.24$) (B) Similarly, LUV signal shows no consistent correlation with GUV size (data is identical to that shown in Fig. 6.4 C). The strongest correlations are found for 0.5 μM DNA ($r_P = -0.20$) and 2.5 μM ($r_P = 0.08$), but they are all extremely weak and inconsistent between different DNA concentrations, consistent with an imaging artefact. (C) Correlations between GUV radius and HPTS ratio is stronger and consistently negative (ranging from $r_P = -0.01$ at 1 μM DNA to $r_P = -0.25$ at 2.5 μM). Data shown here correspond to that in Fig. 6.6 C, but plotted against GUV radius rather than LUV intensity on the membrane. (D) The effect becomes much clearer when we filter out the GUVs with significant HPTS signal inside. Here, the HPTS intensity ratio is strongly negatively correlated with the GUV radius (r_P is between -0.67 and -0.82 for all conditions). (E) The effect seen in (D) is a direct consequence of the fact that the non-fluorescent interior of a GUV displaces the fluorescent surrounding solution and thus leaves a shadow in the fluorescent image, showing up as dark spots in the image. The larger the GUV, the larger the non-fluorescent region, and thus the more negative the HPTS intensity ratio will be. Graphs show line intensity profiles drawn through the two GUVs depicted in the top panel, with the lighter curve showing the smaller GUV. Scale bar: 5 μm.

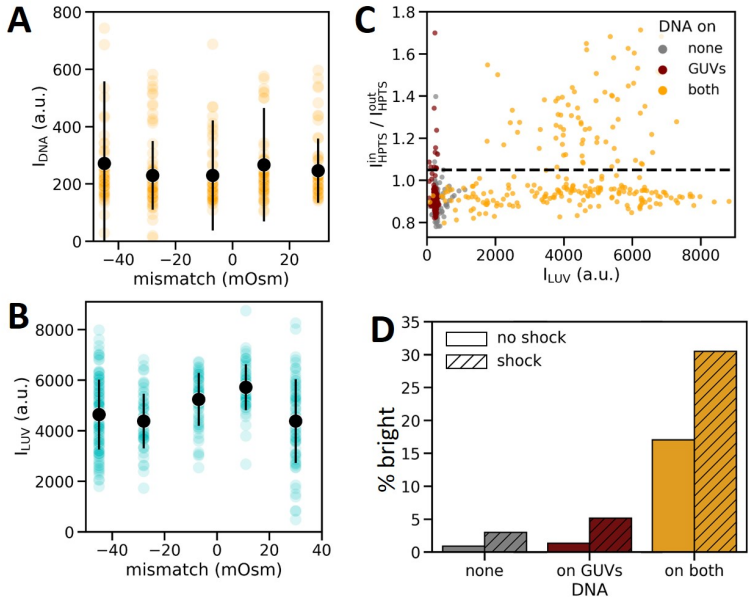

Figure 6.15: **Membrane permeabilization and content mixing is enhanced by osmotic shock.** (A) DNA fluorescence on GUV membranes at different osmotic mismatches between outside and inside solution, with 1 µM linker DNA in solution. DNA binding to GUVs happens at all tested osmotic conditions, and yields consistent DNA densities on the surface. Black datapoints and error bars indicate the mean and standard deviation (orange datapoints, N = 72, 91, 89, 81, 66 GUVs for -45, -28, -7, 11 and 30 mOsm mismatch, respectively). (B) LUV fluorescence on GUV membranes in the presence of 1 µM linker DNA at different osmotic mismatches between outside and inside solution. LUV binding is highest at an osmotic mismatch of +11 mOsm. Black datapoints and error bars indicate the mean and standard deviation (cyan datapoints, N = 132, 62, 61, 70, 78 GUVs for -45, -28, -7, 11 and 30 mOsm mismatch, respectively). (C) HPTS ratio as a function of LUV signal on the GUV membrane. We incubate either none of the vesicles (grey), or just the GUVs (red) or both (orange) with 1 µM DNA for 10 min separately, before bringing GUVs and LUVs together to allow them to interact. The black dashed line indicates the 1.05 cutoff HPTS ratio, above we consider classify the GUV as 'bright'. N = 166, 233 and 246 GUVs for no DNA, DNA on the GUVs only, and DNA on both vesicle types, respectively. All vesicles undergo a -25 mOsm osmotic shock during the fusion step. (D) Bar plot showing the fraction of GUVs which have undergone content mixing in samples with no DNA, DNA on just the GUVs, and DNA on GUVs and LUVs, after a 70 min fusion step at either isotonic conditions (solid bars) or with a -25 mOsm osmotic shock (hatched bars).

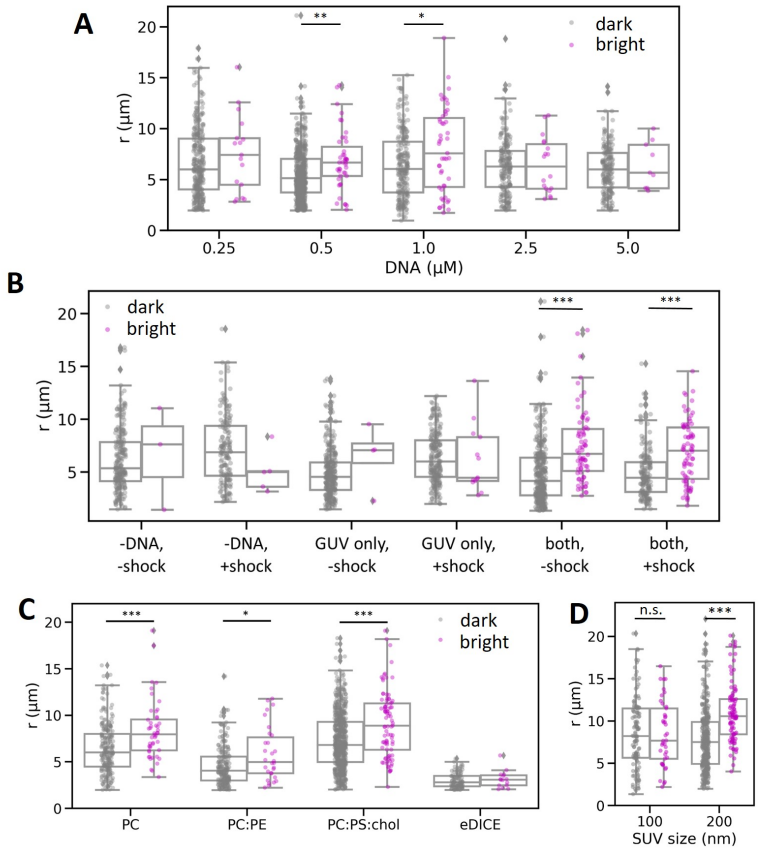

Figure 6.16: **Population-scale size analysis suggests that GUV size correlates with porosity.** Box plots comparing the GUV size distributions from different fusion experiments. For each condition, we compare vesicles with HPTS ratios above 1.05 ('bright' GUVs, magenta datapoints) with those with lower HPTS ratios ('dark', grey datapoints). Boxes and lines denote the median and quartiles of the data distribution shown underneath. All p-values listed below are computed by Welch's t-test. Sample sizes are listed in Supplementary Table 6.6. (A) Content mixing as a function of DNA concentration (same data as in Fig. 6.6). Only at 0.5 and 1 μM DNA do we observe more than 20 bright GUVs, so we compare only those two populations. In both cases, bright GUVs are on average larger than their dark counterparts in the same sample (r = 6.89 compared to 5.50 μm for 0.5 μM DNA, p = 0.004, and r = 7.95 compared to 6.45 μm for 1 μM DNA, p = 0.024). (B) Comparing membrane permeability in the presence and absence of an osmotic shock during the LUV binding and fusion step (same data as in Fig. 6.15), we found more than 20 bright GUVs only when DNA was added to mediate GUV-LUV binding. Again, bright GUVs were significantly larger than dark ones, with radii of 7.44 compared to 4.90 μm (no osmotic shock, $p < 10^{-7}$) and 6.89 compared to 4.89 μm (with osmotic shock, $p < 10^{-6}$). (C) Bright GUVs were significantly larger than dark GUVs in the gel swelling DOPC sample (p=0.0002), the gel swelling PC:PE sample (p=0.024), and the gel swelling PC:PS:chol sample ($p<10^{-5}$). Only 15 GUVs were fused in the eDICE sample, so we could not statistically compare the distributions. The data is the same as in Fig. 6.8. (D) Bright GUVs incubated with 200 nm LUVs had a larger average size than the dark ones (r = 7.80 and 10.98 μm, $p < 10^{-11}$). However, GUVs incubated with 100 nm LUVs showed no significant difference in average radius between bright and dark GUV populations. (r = 8.59 compared to 8.52 μm, p = 0.92). This analysis is based on the same data as Fig. 6.13.

6.5.2 Supplementary tables

Panel	Condition	Population	N	r (µm)
A	0.25 µM DNA	dark	290	6.69
A	0.25 µM DNA	bright	17	7.56
A	0.5 µM DNA	dark	491	5.50
A	0.5 µM DNA	bright	43	6.89
A	1 µM DNA	dark	224	6.46
A	1 µM DNA	bright	47	7.95
A	2.5 µM DNA	dark	192	6.32
A	2.5 µM DNA	bright	18	6.44
A	5 µM DNA	dark	188	6.02
A	5 µM DNA	bright	9	6.46
B	-DNA, -shock	dark	222	6.16
B	-DNA, -shock	bright	3	6.70
B	-DNA, +shock	dark	164	7.15
B	-DNA, +shock	bright	5	5.04
B	GUV only, -shock	dark	291	4.87
B	GUV only, -shock	bright	4	6.49
B	GUV only, +shock	dark	222	6.36
B	GUV only, +shock	bright	13	6.21
B	both, -shock	dark	339	4.90
B	both, -shock	bright	72	7.44
B	both, +shock	dark	174	4.89
B	both, +shock	bright	76	6.89
C	PC	dark	229	6.43
C	PC	bright	48	8.37
C	PC:PE	dark	222	4.56
C	PC:PE	bright	30	5.86
C	PC:PS:chol	dark	659	7.24
C	PC:PS:chol	bright	89	9.08
C	eDICE	dark	103	3.00
C	eDICE	bright	15	3.13
D	100 nm SUVs	dark	122	8.60
D	100 nm SUVs	bright	41	8.53
D	200 nm SUVs	dark	322	7.80
D	200 nm SUVs	bright	94	10.98

Table 6.6: Sample sizes and average GUV radii in fusion experiments shown in Fig. 6.16.

Experiment	Type	N	r (μm)
DNA incorporation, 10 min binding time	+DNA, -LUV	37	(6.73 ± 3.33) μm
DNA incorporation, overnight binding	+DNA, -LUV	91	(7.21 ± 2.81) μm
DNA incorporation, 0.25 μM DNA	+DNA, -LUV		(7.29 ± 2.67) μm
DNA incorporation, 0.5 μM DNA	+DNA, -LUV	91	(6.08 ± 2.19) μm
DNA incorporation, 1 μM DNA	+DNA, -LUV	171	(4.63 ± 1.72) μm
DNA incorporation, 2.5 μM DNA	+DNA, -LUV	236	(4.71 ± 1.84) μm
DNA incorporation, 5 μM DNA	+DNA, -LUV	328	(5.13 ± 2.24) μm
DNA incorporation, osmolarity control	+DNA, -LUV	42	(6.19 ± 2.08) μm
DNA incorporation, hypertonic	+DNA, -LUV	91	(5.79 ± 2.16) μm
DNA incorporation, hypotonic	+DNA, -LUV	81	(6.84 ± 2.52) μm
DNA incorporation, isotonic	+DNA, -LUV	90	(5.35 ± 2.37) μm
DNA incorporation, superhypertonic	+DNA, -LUV	72	(5.39 ± 1.94) μm
DNA incorporation, superhypotonic	+DNA, -LUV	66	(6.21 ± 1.98) μm
fusion, PC	+DNA, +LUV	128	(7.03 ± 3.07) μm
fusion, physiological	+DNA, +LUV	369	(7.35 ± 3.22) μm
fusion, PE	+DNA, +LUV	100	(4.42 ± 2.42) μm
fusion, DNA dependence, 1 μM	+DNA, +LUV	271	(6.61 ± 3.39) μm
fusion, 100 nm SUVs	+DNA, +LUV	163	(8.45 ± 4.05) μm
fusion, 200 nm SUVs	+DNA, +LUV	416	(8.39 ± 3.78) μm

Table 6.7: Sample sizes and average GUV radii in fusion experiments shown in Fig. 6.9, in the same order as in the figure.

7

Outlook

Abstract

All chapters in this thesis have presented steps towards building a synthetic cell: we produced cell-like containers with a cytoskeleton, characterized them and their constituent parts, and fed them with building blocks from the outside world. However, these steps are far from a comprehensive list of things we need to consider in order to build a synthetic cell, or even just a molecular machine that can take care of a single complex function such as cytokinesis. In the final chapter, we position this thesis in the context of rebuilding animal cell cytokinesis, and building life-like systems more broadly. We present preliminary work advancing on the road towards synthetic cell division as laid out in chapter 2, showing how both external guidance by light, and internal cues from curvature-generating proteins, may be used to template cytokinetic furrows. We furthermore show a minimalist approach to building membrane-bound actin cortices, by demonstrating with molecular dynamics modeling and *in vitro* experiments how electrostatic interactions can be used to tune actin-membrane adhesion. Finally, we lay out next steps towards integrating our work with other functional modules necessary to bring synthetic cells to life.

This chapter includes parts of the paper *Charge-dependent interactions of monomeric and filamentous actin with lipid bilayers*, PNAS 117 (11), 2020, by Carsten Schroer, Lucia Baldauf, Tjerk Wassenaar, Manuel Melo, Gijsje Koenderink and Siewert Jan Marrink, in which Lucia Baldauf led the experimental effort and Carsten Schroer led the computational work. Optimization of blebbistatin-based photoactivation of actomyosin contractility was performed by Kabir Razack under the joint supervision of Lucia Baldauf and Irene Istúriz Petitjean. The truncated IQGAP construct used for furrow templating was generated by the lab of Darius Köster and kindly provided to us in purified form.

7.1 Introduction

Throughout this thesis, we have made use of of bottom-up reconstitution as a simplified model for processes that are observed in living cells. However, bottom-up reconstitution may also shed light on, and make use of, subtle molecular interactions that are drowned out in the context of a natural living cell, where more robust but complex systems dominate. Two examples of such 'hidden' functions are highlighted in chapters 4 and 5 of this thesis, where we found that actin networks can self-assemble in a curvature-sensitive manner and generate protrusive forces even in the absence of the dedicated proteins that are thought to drive the same processes in living animal cells. What relative contribution these intrinsic capabilities of actin networks make to directing actin cortex assembly to specific places in the cell, remains an open question to be carefully explored in living cells.

Reconstitution can elucidate not just actual biological functions of a protein or system, but also potential other functions that are not exploited in nature [505]. This may open the path to new rational design principles for synthetic lifelike systems: principles which have not emerged through evolutionary pathways. In Chapter 6, we have demonstrated how biological functions (in this case membrane binding and ultimately fusion driven in cells by dedicated proteins) may be recapitulated by simpler DNA-based technological biomimicry. In this chapter we will take this concept one step further and present two examples of technological shortcuts which may help in constructing synthetic cells using simple, but not necessarily physiological, design principles. We show how computational approaches can help design truly minimal actin-membrane adhesions. Following our roadmap from Chapter 2, we also explore approaches to templating and positioning a cytokinetic furrow in synthetic cells. First, we use light to manipulate actomyosin contractility, opening a potential route towards positioning a cytokinetic furrow in space and time. Second, we show how a cytokinetic ring may be built and positioned using membrane-associated proteins which have recently been shown to generate curvature in actin filaments [46–48]. Finally, we address the key challenges ahead in the field of bottom-up cellular reconstitution. We argue for a more holistic view, and propose relatively simple steps on the way to building an increasingly autonomous synthetic cell.

7.2 Synthetic actin cortices: a minimalist approach

In chapters 4 and 5, we demonstrated how actin cortices can be reconstituted in GUVs. The design of these cortices was inspired by what we know about the actin cortex in mammalian cells, as we aimed to understand how the interplay of passive actin mechanics and active actin turnover may shape the plasma membrane. However, such dynamic actin cortices require several regulatory proteins, introducing molecular complexity which is generally undesirable in synthetic cells. We thus asked whether a simpler design could be found to facilitate actin-membrane interactions, thus allowing actin to act as a mechanical support for the membrane without the need for extra proteins.

Since actin filaments carry a net negative charge in physiological buffers [506], we expect that electrostatic interactions can be leveraged to bind actin to lipid membranes. Indeed, previous studies have shown that actin can interact with charged membranes [507–509], and its polymerization may even be induced by proximity to a membrane [510, 511]. However, charge distributions around macromolecules are complex and highly sensitive to

ions and small molecules in the buffer [512, 513], and reports even show that actin can, surprisingly, bind to negatively charged membranes [514, 515]. We therefore collaborated with the Marrink group at the University of Groningen to use computational modeling to get a better mechanistic understanding of actin-membrane interactions [224]. Martini modeling, a coarse-grained molecular dynamics (MD) simulation framework developed by our collaborators, which has been widely used to study biological membranes [516, 517], is ideally suited for this. In Martini models, biomolecules are coarse-grained by considering the aggregated properties of four heavy atoms and their associated hydrogen atoms as one bead, which interacts with the other beads in the same macromolecule, other macromolecules, and the solvent. This means that the technique resolves enough detail to effectively describe molecular properties of actin and lipids, such as their complex charge distributions, but is computationally efficient enough that interactions can be simulated over length- and timescales relevant to actin-membrane-interactions (tens of nanometers and several microseconds). The Marrink group simulated single actin monomers and filaments in proximity to a lipid membrane, surrounded by an explicit solvent and with periodic boundary conditions. In parallel experiments, we varied the ionic properties of the solvent, changing the concentrations of mono- and divalent ions, and watched how actin and the lipid membrane interact with one another, depending on the lipid compositions of the membrane [1].

Unsurprisingly, we found that actin interacted most strongly with membranes that contained the positively charged lipid 1-palmitoyl-2-oleoyl-3-trimethylammonium-propane (POTAP) when surrounded by a solvent containing only monovalent ions. We assessed this by measuring the mean equilibrium distance of actin filaments from the membrane ($\Delta z = 6.70 \pm 0.13$ nm for 20 % POTAP, compared to 7.36 ± 0.18 nm and 8.37 ± 0.47 nm for POPC and 20 % POPS, respectively), and by observing how closely the contour of the membrane followed that of the actin filament's helical twist (Fig. 7.1 A). Only POTAP membranes followed the shape of the actin filament closely, indicating an attractive interaction between filament and membrane. However, this behaviour was reversed when the monovalent ions in the buffer were replaced by divalent ions carrying the same cumulative charge. Here, POTAP containing lipid bilayers did not follow the shape of the actin filament, but those containing negatively charged POPS did (Fig. 7.1 B).

[1] Methods: Supported lipid bilayers (SLBs) containing DOPC and either 20 mole% DOPS, 20 mole% DOTAP, or no charged lipids, were formed as follows: Lipids were mixed in chloroform and dried under gentle N_2 flow, and fully dried in a vacuum dessicator overnight. Lipid films were resuspended to a final concentration of 1.25 mg/mL by brief hydration in F-buffer and subsequent vigorous vortexing. Resuspended lipids were sonicated using a Bandelin Sonoplus HD2070.2 equipped with a BR30 resonator cup for 2 h to produce small unilamellar vesicles (SUVs). SLBs were formed on the walls of fresh base piranha treated flow chambers (see chapter 3) by incubating them with SUV suspension for 10 min to allow for SUV spreading, and subsequently removing any excess SUVs by extensive flushing. The SLBs were flushed with 7 chamber volumes of the target assay buffer before adding actin filaments. Actin was pre-polymerized at 30 μM for 1 h in the presence of phalloidin, then diluted to 2 μM in the target buffer, and incubated with the SLB in flow chambers sealed with vacuum grease for 4 h before imaging. To allow for fluorescence imaging, 10 % of actin monomers were labeled with AlexaFluor647 and 1 % of DOPC lipids were replaced by Lissamine rhodamine PE lipids. Images were acquired on an inverted Nikon Eclipse Ti-E microscope equipped with a Roper TIRF module and QuantEM:512SC EM-CCD camera. The surface coverage with actin was determined by quantitative image analysis using a custom-written python script in which we classified pixels as 'actin' or 'background' using Otsu thresholding. Both monomeric and polymeric actin was simulated using a polarizable Martini field (version Martini 2.1P). Detailed simulation methods are beyond the scope of this thesis but are described extensively in ref. [224].

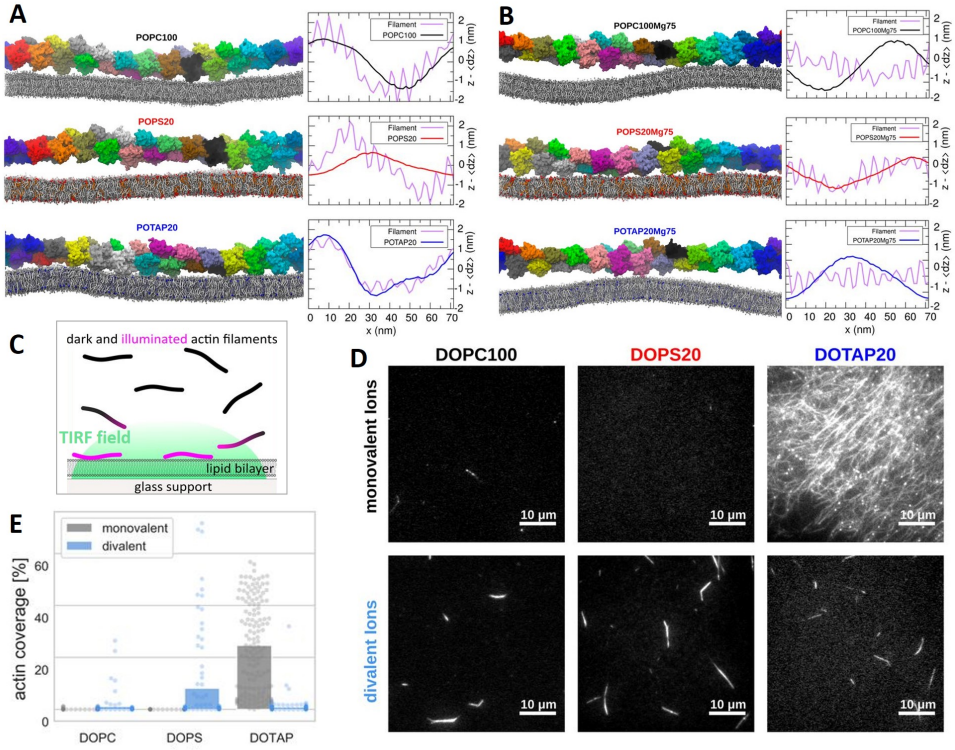

Figure 7.1: **Charge-based actin-membrane adhesion is reversed by divalent ions.** (A, B) Representative snapshots of simulated actin filaments close to lipid membranes composed of POPC with or without an additional 20 mole% POPS or POTAP (left panels). Colors in the actin filaments distinguish different monomers. Red and blue lipids in the membranes indicate 20 % negatively charged PS and positively charged POTAP, respectively. Graphs in the right panels show the average equilibrium distance between the centers of mass of the actin filament and the membrane $z- < dz >$ as a function of the position x along the actin filament, where x covers a complete helical turn of the actin filament's double helix. Results are shown for a solvent containing 150 mM KCl (A) or 75 mM $MgCl_2$ (B). (C) Experimental setup for validating the simulation results: Actin filaments were allowed to interact with a lipid bilayer supported on a glass coverslip. In TIRF microscopy, only actin filaments close to the coverslip (< 100nm) and thus illuminated by the evanescent TIRF field (green shading), appeared bright on the TIRF micrographs. (D) Representative TIRF images of actin on supported lipid bilayers containing only DOPC (left), or DOPC with 20 % DOPS (center) or 20 % DOTAP (right), in a buffer containing either 50 mM KCl (top row) or 25 mM $MgCl_2$ (bottom row). Scale bars: 10 µm. (E) Quantification of actin surface coverage as measured by TIRF microscopy for the different lipid compositions at either 100 mM KCl ('monovalent', grey) or 50 mM $MgCl_2$ ('divalent', blue). Data represent n≥ 80 images from N ≥ 3 independent experiments for each condition.

Positively charged lipids are not found in any significant concentration in plasma membranes of extant cells [11] and are therefore likely to interfere with the activity of integral membrane proteins and other cellular systems that have evolved in the absence of such lipids [518, 519]. It is therefore encouraging that simulations predict that actin can also bind negatively charged lipid membranes, which are more physiologically relevant [11]. We set up a series of *in vitro* experiments to test this prediction: in a flow chamber setup, we produced lipid bilayers supported by a glass coverslip, and allowed pre-polymerized actin

filaments to interact with the bilayer (Fig. 7.1 C). We varied the lipid bilayer composition between 100 % DOPC and 80 % DOPS or DOTAP, and performed the incubation in different buffer conditions. TIRF microscopy conveniently distinguishes those actin filaments that are close to the coverslip (and thus the supported lipid bilayer) from those in bulk solution. Only actin filaments within a short distance ($\lesssim$ 100 nm) of the coverslip are illuminated by the evanescent field of the TIRF laser and light up. We could thus use the density of visible actin filaments on the surface as a proxy for the binding between actin and the supported lipid bilayer. Our experimental observations confirmed the predictions from the simulation (Fig. 7.1 D): in a buffer dominated by monovalent ions, neither DOPC nor DOPS membranes bound any significant densities of actin filaments, whereas DOTAP membranes were covered with dense actin meshes. Conversely, surface-bound filament densities were strongly reduced on DOTAP membranes in buffers containing divalent ions, where more filaments adsorbed to DOPC and especially DOPS membranes. This trend reversal was further confirmed by quantitative image analysis (Fig. 7.1 E).

Our results showed that direct charge-mediated actin adhesion to the plasma membrane is unlikely to occur to a significant degree in cells, as it requires either positively charged lipids or unphysiologically high concentrations of divalent cations. However, the mode of interaction we show here may resemble the cellular situation more closely than is immediately obvious: instead of the unphysiologically strong linking proteins that are commonly used in actin reconstitution studies [143, 323], charge-mediated adhesion links actin filament meshes to membranes by the collective action of individually weak bonds, reminiscent of our current understanding of actin-membrane interactions in the cortex of animal cells [197–199], as we mentioned in chapter 2. Charge-based interactions could thus be a minimal design strategy for actin cortices in synthetic cells, especially if the main function for actin would be acting as a mechanical support for the plasma membrane.

7.3 Towards controlled cytokinesis: patterning the cytokinetic furrow

7.3.1 Spatiotemporal control of myosin-driven contractility

To reconstitute cytokinesis, we clearly need more than a layer of actin bound to a lipid membrane. As we highlighted in chapter 2, sustained constriction of a cytokinetic furrow requires out-of-equilibrium activity in a membrane-bound actin cortex, and this activity must be differentially regulated between the furrow region and the cell poles. Animal cells use complex regulatory networks to induce this symmetry breaking and coordinate it with other cellular processes such as spindle construction and chromosome segregation, but these are far out of reach of what can currently be reconstituted *in vitro*. A technological shortcut is therefore required: ideally, we wish to both spatially control contractility, enhancing it in the cellular midplane compared to the poles, and control in time when the furrow contracts.

Light-based manipulation offers a way to achieve such spatiotemporal control: targeted illumination with blue light can be used to trigger binding, unbinding or activation of molecules where and when the researcher decides. Recent works in living cells have made strides in developing optogenetic tools that can control the activity and recruitment of cytoskeletal components [147, 520]. Myosin in particular is an attractive target for light-

based manipulation in synthetic cell division, as regulation of its activity or recruitment to an actin network would offer a direct handle on network contractility. Indeed, myosin's processivity has been a target for protein engineering by artificial oligomerization [521] and an optogenetic tool has been developed to control oligomerization by light in living cells and organisms [522]. However, optogenetically controlled myosin is so far not available in purified form, so a more indirect approach to controlling its activity is needed.

Previous reports have shown that blebbistatin, a drug used widely for myosin inhibition, is light sensitive: it is active in the dark but becomes inactivated upon illumination by blue light [145]. This property has previously been exploited to locally manipulate contractility of reconstituted actomyosin networks [120, 146]. We have implemented this protocol in our lab and fine-tuned it to establish the appropriate blebbistatin concentrations to inhibit myosin, and light intensities necessary to inactivate blebbistatin and recover network contractility [2]We found that the contraction of millimeter-sized bulk actomyosin networks formed in flow channels was slowed down 8-fold by adding 3 μM blebbistatin (Fig. 7.2 A, top and middle panel). Normal contraction could be recovered by continuously illuminating the network with a 488 nm LED (Fig. 7.2 A, bottom panel) [3]. We note that we did not optimize this protocol for photoactivation of specific micron-sized regions of interest, as we would need to do to generate equatorial-polar asymmetry in cortical contraction of synthetic cells. However, it has already been shown that photoactivation can be used for spatial regulation of active actin networks [120, 146]. We are therefore confident that this protocol will need only minor adjustments for application in smaller systems such as synthetic cells, where it may be used to trigger enhanced actomyosin contractility in the cytokinetic furrow, while maintaining lower levels of contractility at the poles.

Blebbistatin acts by inhibiting myosin ATPase activity and trapping myosin-2 mostly in its unbound state [523], so actin gels with blebbistatin-inhibited myosin-2 are not strongly crosslinked by the motor. However, bundling of actin induced by binding of rigor-state myosin may actually be desirable when constructing an isolated cytokinetic ring to drive synthetic cytokinesis (see chapter 2). We therefore also tested an alternative method for local activation of myosin-driven contractility: instead of trapping myosin in the unbound state using blebbistatin, and locally enhancing its ability to bind and remodel actin networks by blebbistatin inactivation, we first trapped myosin in its actin-bound rigor state. This was achieved by depriving myosin of usable ATP, which is required for myosin to unbind from actin at the end of its power stroke. We used ATP caged with a P^3-(1-(2-nitrophenyl)-ethyl)-ester group (NPE), which can be cleaved by illumination with ultraviolet light, releasing ATP that can then be metabolized by myosin [524]. To gauge whether NPE-caged

[2] Methods: Actin gels were assembled in Pll-PEG-passivated flow channels (see chapter 3). Contractile networks contained 15 μM actin doped with 5 % AlexaFluor647-labeled monomers, 0.75 μM murine fascin, and 0.15 μM rabbit skeletal muscle myosin-2 (see chapter 3). We included either 10 % vol/vol DMSO (control) or 3 μM blebbistatin dissolved in DMSO to modulate network contraction. Networks always contained 10 mM creatine phosphate and 0.1 mg/mL creatine kinase to ensure a constant supply of ATP (see Chapter 3). For photoactivation, the 475 nm solid-state LED (nominally 200 mV) was left continuously 'on' for the duration of the experiment. Experiments with blebbistatin were performed on a Leica Thunder widefield microscope using a 10x PlanApo air objective.

[3] Network contraction was measured as the time evolution of the total area occupied by the network, normalized by its initial area. Here we defined contraction time as the time the network took to decrease to 75 % of its initial area, which was between 140 and 160 s for networks containing no blebbistatin or light-inactivated bebbistatin, and ~ 1200 s for networks with active blebbistatin.

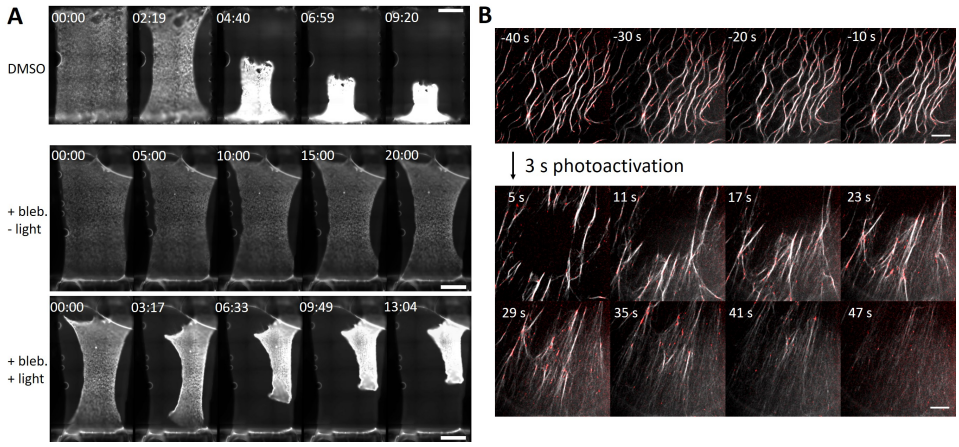

Figure 7.2: **Activating muscle myosin-2 motor activity by light.** (A) Global contraction of large bulk actomyosin gels in flow channels happens spontaneously within 10 min in control samples where only 10 % DMSO (solvent for blebbistatin) is added (top). Adding 3 μM blebbistatin slows contraction down around 8-fold (middle). Rapid contraction in the same network was recovered by illuminating the gel with intense blue light (bottom). Time stamps are in minutes, actin is shown in greyscale and scale bars are 500 μm. (B) In the presence of NPE-caged ATP, myosin (red) binds and bundles actin filaments (grey) in a quasi-2D cortex formed by molecular crowding, but does not contract the network (top). Photoactivation of the unstable NPE caging group by 405 nm ultraviolet laser leads to local bleaching of the actin (dark circle) and triggers contraction of the network (bottom). Note that the network remains uncontracted at distances of more than ~ 100 μm from the site of photoactivation. Scale bars: 10 μm.

ATP could be used to trigger myosin activity, we formed quasi-2D actomyosin cortices in flow channels [4]. In these 2D cortices, we saw that myosin bound and bundled actin filaments in the presence of caged ATP, but did not induce any appreciable remodeling of the actin network over the course of 50 s (Fig. 7.2 B, top panel). Upon a single burst of photoactivation with a 405 nm laser, the density of myosin on the actin bundles decreased slightly, indicating weakening of myosin binding, and the network rapidly began to remodel, a sign of motor activation. A large part of the actomyosin network was contracted away from the field of view within tens of seconds. Other parts of the same flowchamber, however, some no more than 100 μm away from the site of photoactivation, appeared unchanged minutes later. Experimental finetuning is still needed before caged ATP can be used to precisely steer actomyosin contractility in space and time. However, our findings indicate that there may be two orthogonal ways to gain spatiotemporal control over activity of contractile actomyosin networks even without requiring complicated protein engineering, thus patterning a cytokinetic furrow in synthetic cells.

[4] Methods: Actin cortices were assembled in Pll-PEG-passivated flow channels (see chapter 3) and crowded to the coverslip walls by 0.2 % methylcellulose. The cortex was composed of 2.4 μM actin, 48 nM rabbit skeletal muscle myosin-2 and 48 nM α-actinin-1 [525]. The α-actinin-1 plasmid was a kind gift from Christophe Le Clainche (I2BC, Paris). NPE-ATP was added to a final concentration of 1 mM, and uncaged by a 405 nm laser pulse at 50 % laser power (5 mW nominal) for 3 s. Experiments with caged ATP were performed on an inverted Olympus IX81 confocal spinning disk microscope equipped with a 100x PlanApo oil immersion objective. A 405 nm solid state laser and Andor FRAPPA unit were used for photoactivation.

7.3.2 Controlling curvature: templating curly rings

Controlling activity in an actin cortex by light is one possible strategy for templating a cytokinetic furrow. This strategy requires that the synthetic cells have a continuous cortex, like those we build in chapters 4 and 5. However, in chapter 2 we discussed a conceptually different method of building synthetic cytokinetic rings: building rings of bundled actin and adding some mechanism by which these rings contract. Contractility can be achieved by motor activity [158], but passive crosslinkers [48] and proteins which generate curvature in actin filaments or bundles [46–48] have also been recently shown to drive ring contraction, and may offer an alternative way to constrict synthetic cells, either alone or in synergy with motor proteins.

One class of these curvature generating proteins is the family of IQGAP proteins, which are found in the cytokinetic ring of yeast cells [526]. Purified 'curly' fragments of IQGAP proteins were recently shown to bend actin filaments into rings with micron-scale curvature when bound to a lipid membrane, and the rings could be even further constricted by muscle myosin-2 [47]. However, curly has so far only been tested on lipid bilayers atop a solid support, which do not allow for deformation of the membrane. It therefore remains an open question whether curly curves only actin, or whether the curly-actin rings may also be able to directly shape the plasma membrane. We performed preliminary tests of actin and curly co-encapsulated in GUVs, where curly was anchored to the membrane by its His-tag, and actin was allowed to polymerize spontaneously in the GUV lumen[5].

Since curly can act as an actin crosslinking protein, we expect it to induce actin bundle formation at high concentrations (1 μM curly and 8 μM actin). Indeed, we find that actin forms thick, curved bundles which are bound to the GUV membrane (Fig. 7.3 A). In GUVs that had visible excess membrane area, the bundles were associated with areas where the GUV membrane was bent inwards, resulting in large-scale deformation of the GUV (Fig. 7.3 B). This could result in a single large bundle that constricted part of the GUV (top panel), or several bundles associated with more complex GUV shapes (bottom panel). These preliminary results indicate that combining actin with curvature generating proteins can indeed be harnessed to build constrictive rings even in the absence of myosin.

We suggested in chapter 2 that curvature-generating proteins could be particularly interesting for templating cytokinetic furrows in concert with external shaping of GUVs, for instance through microfluidic trapping [148, 160] or mechanical micromanipulation [80, 382]. In chapter 4, we found that our GUV formation method produced some vesicles that were intrinsically shaped like dumbbells, and could thus be used as curved membrane templates. When encapsulating actin in GUVs with curly, we indeed also found a dumbbell vesicle, and observed that the bright actin structure localized to the dumbbell neck, with a small part of the bundle protruding into the larger (and thus less curved) part of the dumbbell, and most of the actin structure being confined to the neck and nearby parts of the highly curved small lobe of the dumbbell (Fig. 7.3 C). This is an encouraging finding, confirming that external GUV shaping may work synergistically with curvature-generating proteins to position contractile actin structures.

[5] Methods: GUVs were prepared using eDICE as described in chapter 5, including the same buffer and membrane compositions. 8 μM actin was co-encapsulated with 1 μM curly (fragment Rng2(1-250)-6xHis) without any additional actin-binding or -nucleating proteins. Curly was kindly provided by Darius Köster, whose lab produced the truncated construct and purified the protein as described in ref. [47].

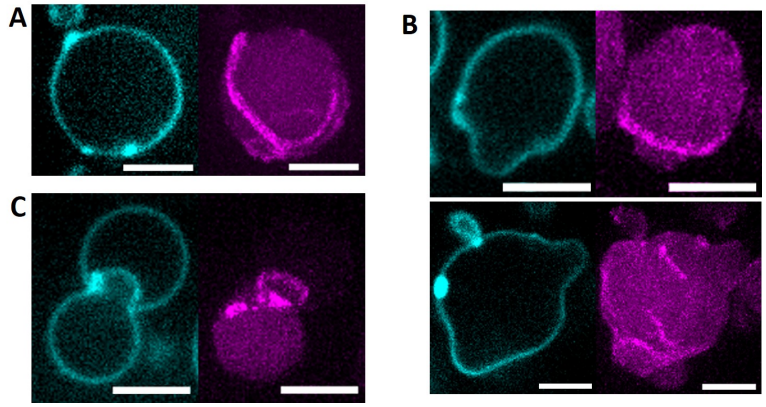

Figure 7.3: **Formation of curved bundles and rings in GUVs by curly.** Confocal images of GUVs containing 8 µM actin and 1 µM curly. Buffer and membrane compositions were identical to those used in Chapter 5, and curly was bound to the membrane by 5 mole% DGS-NTA(Ni). (A) Actin forms curved, membrane-associated bundles in GUVs when co-encapsulated with membrane-bound curly. (B) In GUVs with visible excess membrane area, inward deformations of the GUV membrane are associated with one or more bright actin rings. (C) Curly induces actin localization to the neck of dumbbell shaped vesicles. Lipids (cyan) are shown as single z-slices through the GUV equator for clarity. Actin (magenta) is shown in maximum intensity projections of z-stacks encompassing the entire GUV, to visualize the bundles. Note that bundles were always localized to the membrane and did not protrude into the GUV lumen. Images were acquired on an inverted Olympus IX81 confocal spinning disk microscope using a 100x PlanApo oil immersion objective. Scale bars: 5 µm.

7.4 Into the future: Module integration in synthetic cells

In this thesis, we presented advances in reconstitution and characterization of cytoskeletal components that can serve as a mechanical support for synthetic cell membranes, and potentially form the basis of a synthetic cell division machinery. This means that we focused on one particular functional module of a cell. However, such modular reconstitution efforts face a tough challenge: While we by necessity assume that processes like cytokinesis and DNA processing are modular, and can be fully understood separately from one another, this is clearly not the case in living cells. Rather, 'distinct' cellular functions are deeply interconnected in space and time. They may even make use of the same exact molecules, for instance where an actin cortex provides mechanical support of the plasma membrane, but at the same time must also drive cytokinesis. Here, bottom-up reconstitution studies must work towards integrating functional units with one another in order to re-build lifelike systems.

Cellular functions driven by the cytoskeleton are tightly connected to many of the other functional modules necessary for synthetic cell operation. Perhaps most obviously, both actin polymerization and myosin activity require ATP to function. This makes mechanical stability of synthetic cells, as well as synthetic cytokinesis, dependent on the cell's metabolism. In this thesis, we have used an enzymatic ATP-regenerating system to sustain ATP-dependent cytoskeletal processes, but autonomously dividing synthetic cells will require *de novo* synthesis of ATP. Recent work in the BaSyC research consortium has

demonstrated that ATP can be generated in sub-micron sized lipid vesicles by purified enzymes and membrane transporters [527]. While it will no doubt be technically challenging to transpose this knowledge to larger vesicles and ultimately lifelike cells, bringing together an energy-consuming cytoskeleton with an energy-generating enzymatic pathway is a natural next step for functional integration within a synthetic cell. The vesicle fusion strategy we presented in chapter 6 may help us overcome some technical challenges: while sensitive transmembrane proteins such as those needed for *in vesiculo* ATP production are incompatible with emulsion-based GUV formation methods, cytoskeletal encapsulation has been most successful using just such approaches (see chapter 4). Controlled membrane fusion may help bridge this divide, as it can potentially help integrate transmembrane proteins from small proteoliposomes into the membranes of GUVs produced by eDICE.

Similarly, cytoskeletal activity is deeply involved with chromosome segregation in mammalian cells, where the mitotic spindle, a complex cytoskeletal structure, mechanically separates DNA to distribute it equally into both daughter cells. Such a complex machinery is beyond the reach of full reconstitution at present, but it may not be necessary: Ongoing theoretical work suggests that DNA segregation in bacteria can be driven by entropic effects alone, based on the finding that two polymer strands will spontaneously de-mix, as long as they are confined to a small enough volume. The size and shape of the confining volume determine whether and how efficiently such de-mixing can take place, and it seems that dumbbell shaped confinement can bolster segregation (R. Creyghton, personal communication, 2021). Combining a cytoskeletal system that is templated on, or spontaneously produces, a dumbbell shape such as those we showed in chapter 4, may thus help establish a functional module for DNA segregation. Such synergies will need to be found and exploited in order to build a fully functional life-like cell from the bottom up.

Even when systems do not naturally synergize, considering the integration of different functional molecules early on (now!) can help design technological shortcuts in the most efficient way possible. In this outlook chapter, we showed how light can be used as a cue to drive targeted self-assembly of actomyosin networks. Other functional modules for synthetic cells may also be activated by the same cues, such as light-guided assembly of minimal spindles or DNA segregation machineries, which are currently in development (Y. Yawale and A. N. Maleki, personal communication, 2022). Similar mechanisms may also be developed to for instance drive DNA recruitment to membranes via photoswitchable protein or DNA linkers, to control membrane fusion in space and time.

Acknowledgements

We thank Jeffrey den Haan, Marjolein Vinkenoog, Irene Istúriz Petitjean, Nils Liebe (U Göttingen) and Kabir Razack for help with protein purification and labeling. Thank you to Michal Shemesh and Jérémie Capoulade for their advice on photoactivation experiments, and to Darius Köster for the kind gift of the curly protein and interesting discussions. Ramon Creyghton, Bela Mulder, Pauline Lefrançois, Christophe Danelon, Ali Nick Maleki and Yash Yawale are thanked for sharing their insights on other functional synthetic cell modules. We also gratefully acknowledge the members of the BaSyC consortium for open discussions on the purpose, status and future of synthetic cells.

Bibliography

References

[1] C. A. Hutchison, R. Y. Chuang, V. N. Noskov, N. Assad-Garcia, T. J. Deerinck, M. H. Ellisman, J. Gill, K. Kannan, B. J. Karas, L. Ma, J. F. Pelletier, Z. Q. Qi, R. A. Richter, E. A. Strychalski, L. Sun, Y. Suzuki, B. Tsvetanova, K. S. Wise, H. O. Smith, J. I. Glass, C. Merryman, D. G. Gibson, and J. C. Venter, "Design and synthesis of a minimal bacterial genome," *Science*, vol. 351, no. 6280, p. aad6253, 2016.

[2] C. Frischmon, C. Sorenson, M. Winikoff, and K. P. Adamala, "Build-a-cell: Engineering a synthetic cell community," *Life*, vol. 11, p. 1176, 2021.

[3] F. Lussier, O. Staufer, I. Platzman, and J. P. Spatz, "Can Bottom-Up Synthetic Biology Generate Advanced Drug-Delivery Systems?," *Trends in Biotechnology*, vol. 39, no. 5, pp. 445–459, 2021.

[4] D. K. Bhatt, M. E. Crooijmans, J. Coenradij, A. Macia Valero, M. Lubbers, E. Asin-Garcia, N. A. Yewdall, S. D'Adamo, N. J. Claassens, and S. Billerbeck, "A SynBio community comes of age: Political, academical, industrial, and societal developments in the Netherlands," *Biotechnology Notes*, vol. 3, pp. 62–69, 2022.

[5] J. O. Corliss, "Three centuries of protozoology: A brief tribute to its founding father, A. van Leeuwenhoek of Delft," *The Journal of Protozoology*, vol. 22, no. 1, pp. 3–7, 1975.

[6] P. Chugh and E. K. Paluch, "The actin cortex at a glance," *Journal of Cell Science*, vol. 131, no. 14, p. jcs186254, 2018.

[7] T. Hohmann and F. Dehghani, "The cytoskeleton - a complex interacting meshwork," *Cells*, vol. 8, p. 362, 2019.

[8] W. Kabsch and J. Vandekerckhove, "Structure and function of actin," *Annual Review of Biophysics and Biomolecular Structure*, vol. 21, pp. 49–76, 1992.

[9] V. E. Galkin, M. S. VanLoock, A. Orlova, and E. H. Egelman, "A new internal mode in F-actin helps explain the remarkable evolutionary conservation of actin's sequence and structure," *Current Biology*, vol. 12, pp. 570–575, 2002.

[10] A. R. Paredeza, Z. J. Assafa, D. Sept, L. Timofejeva, S. C. Dawsond, C. J. R. Wang, and W. Z. Cande, "An actin cytoskeleton with evolutionarily conserved functions in the absence of canonical actin-binding proteins," *PNAS*, vol. 108, no. 15, pp. 6151–6156, 2011.

[11] J. L. Symons, K. J. Cho, J. T. Chang, G. Du, M. N. Waxham, J. F. Hancock, I. Levental, and K. R. Levental, "Lipidomic atlas of mammalian cell membranes reveals hierarchical variation induced by culture conditions, subcellular membranes, and cell lineages," *Soft Matter*, vol. 17, pp. 288–297, 2021.

[12] H. I. Ingólfsson, M. N. Melo, F. J. Van Eerden, C. Arnarez, C. A. Lopez, T. A. Wassenaar, X. Periole, A. H. De Vries, D. P. Tieleman, and S. J. Marrink, "Lipid organization of the plasma membrane," *Journal of the American Chemical Society*, vol. 136, pp. 14554–14559, 2014.

[13] B. Alberts, A. Johnson, J. Lewis, M. Raff, K. Roberts, and P. Walter, "Membrane Proteins," in *Molecular Biology of the Cell* (B. Alberts, D. Bray, J. Lewis, M. Raff, K. Roberts, and J. D. Watson, eds.), New York: Garland Science, 2002.

[14] K. Olbrich, W. Rawicz, D. Needham, and E. Evans, "Water permeability and mechanical strength of polyunsaturated lipid bilayers," *Biophysical Journal*, vol. 79, pp. 321–327, 2000.

[15] H. V. Ly and M. L. Longo, "The influence of short-chain alcohols on interfacial tension, mechanical properties, area/molecule, and permeability of fluid lipid bilayers," *Biophysical Journal*, vol. 87, pp. 1013–1033, 2004.

[16] P. Bieling, T. Li, J. Weichsel, R. McGorty, P. Jreij, B. Huang, D. A. Fletcher, and R. D. Mullins, "Force feedback controls motor activity and mechanical properties of self-assembling branched actin networks," *Cell*, vol. 164, pp. 115–127, 2016.

[17] W. C. Wimley, "How does melittin permeabilize membranes?," *Biophysical Journal*, vol. 114, pp. 251–253, 2018.

[18] D. Sept and J. A. McCammon, "Thermodynamics and kinetics of actin filament nucleation," *Biophysical Journal*, vol. 81, pp. 667–674, 2001.

[19] P. Lappalainen, T. Kotila, A. Jegou, and G. Romet-Lemonne, "Biochemical and mechanical regulation of actin dynamics," *Nature Reviews Molecular Cell Biology*, 2022.

[20] C. S. Peskin, G. M. Odell, and G. F. Oster, "Cellular motions and thermal fluctuations: the Brownian ratchet," *Biophysical Journal*, vol. 65, pp. 316–324, 1993.

[21] T. D. Pollard and S. W. Craig, "Mechanism of actin polymerization," *Trends in Biochemical Sciences*, vol. 7, no. 2, pp. 55–58, 1982.

[22] M. F. Carlier and D. Pantaloni, "Control of actin dynamics in cell motility," *Journal of Molecular Biology*, vol. 269, pp. 459–467, 1997.

[23] E. G. Yarmola and M. R. Bubb, "Profilin: emerging concepts and lingering misconceptions," *Trends in Biochemical Sciences*, vol. 31, no. 4, pp. 197–205, 2006.

[24] B. L. Goode, D. G. Drubin, and P. Lappalainen, "Regulation of the cortical actin cytoskeleton in budding yeast by twinfilin, a ubiquitous actin monomer-sequestering protein," *Journal of Cell Biology*, vol. 142, no. 3, pp. 723–733, 1998.

[25] A. L. Goldstein, E. Hannappel, and H. K. Kleinman, "Thymosin β4: Actin-sequestering protein moonlights to repair injured tissues," *Trends in Molecular Medicine*, vol. 11, no. 9, pp. 421–429, 2005.

[26] M. Bovellan, Y. Romeo, M. Biro, A. Boden, P. Chugh, A. Yonis, M. Vaghela, M. Fritzsche, D. Moulding, R. Thorogate, A. Jégou, A. J. Thrasher, G. Romet-Lemonne, P. P. Roux, E. K. Paluch, and G. T. Charras, "Cellular control of cortical actin nucleation," *Current Biology*, vol. 24, pp. 1628–1635, 2014.

[27] H. N. Higgs, L. Blanchoin, and T. D. Pollard, "Influence of the C terminus of Wiskott-Aldrich syndrome protein (WASp) and the Arp2/3 complex on actin polymerization," *Biochemistry*, vol. 38, pp. 15212–15222, 1999.

[28] K. Hüfner, H. N. Higgs, T. D. Pollard, C. Jacobi, M. Aepfelbacher, and S. Linder, "The Verprolin-like Central (VC) region of Wiskott-Aldrich Syndrome Protein induces Arp2/3 complex-dependent actin nucleation," *Journal of Biological Chemistry*, vol. 276, no. 38, pp. 35761–35767, 2001.

[29] Robinson R.C., Turbedsky K., Kaiser D.A., Marchand J., Higgs H.N., Choe S., and Pollard T.D., "Crystal structure of Arp2/3 complex," *Science*, vol. 294, pp. 1679–1685, 2001.

[30] M. Rodnick-Smith, S. L. Liu, C. J. Balzer, Q. Luan, and B. J. Nolen, "Identification of an ATP-controlled allosteric switch that controls actin filament nucleation by Arp2/3 complex," *Nature Communications*, vol. 7, p. 12226, 2016.

[31] H. Gournier, E. D. Goley, H. Niederstrasser, T. Trinh, and M. D. Welch, "Reconstitution of human Arp2/3 complex reveals critical roles of individual subunits in complex structure and activity," *Molecular Cell*, vol. 8, pp. 1041–1052, 2001.

[32] Rohatgi R., Ma L., Miki H., Lopez M., Kirchhausen T., Takenawa T., and Kirschner M.W., "The interaction between N-WASP and the Arp2/3 complex links Cdc42-dependent signals to actin assembly," *Molecular Biology of the Cell*, vol. 97, pp. 221–231, 1999.

[33] S. H. Zigmond, "How WASP regulates actin polymerization," *Journal of Cell Biology*, vol. 150, no. 6, pp. F117–F119, 2000.

[34] M. A. Chesarone, A. G. Dupage, and B. L. Goode, "Unleashing formins to remodel the actin and microtubule cytoskeletons," *Nature Reviews Molecular Cell Biology*, vol. 11, pp. 62–74, 2010.

[35] A. M. Gautreau, F. E. Fregoso, G. Simanov, and R. Dominguez, "Nucleation, stabilization, and disassembly of branched actin networks," *Trends in Cell Biology*, vol. 32, no. 5, pp. 421–432, 2022.

[36] C. Le Clainche, D. Pantaloni, and M. F. Carlier, "ATP hydrolysis on actin-related protein 2/3 complex causes debranching of dendritic actin arrays," *PNAS*, vol. 100, no. 11, pp. 6337–6342, 2003.

[37] C. A. Ydenberg, B. A. Smith, D. Breitsprecher, J. Gelles, and B. L. Goode, "Cease-fire at the leading edge: New perspectives on actin filament branching, debranching, and cross-linking," *Cytoskeleton*, vol. 68, no. 11, pp. 596–602, 2011.

[38] Y. H. Tee, T. Shemesh, V. Thiagarajan, R. F. Hariadi, K. L. Anderson, C. Page, N. Volkmann, D. Hanein, S. Sivaramakrishnan, M. M. Kozlov, and A. D. Bershadsky, "Cellular chirality arising from the self-organization of the actin cytoskeleton," *Nature Cell Biology*, vol. 17, no. 4, pp. 445–457, 2015.

[39] S. Romero, C. Le Clainche, D. Didry, C. Egile, D. Pantaloni, and M. F. Carlier, "Formin is a processive motor that requires profilin to accelerate actin assembly and associated ATP hydrolysis," *Cell*, vol. 119, pp. 419–429, 2004.

[40] M. Fritzsche, C. Erlenkämper, E. Moeendarbary, G. Charras, and K. Kruse, "Actin kinetics shapes cortical network structure and mechanics," *Science Advances*, vol. 2, p. e1501337, 2016.

[41] D. S. Courson and R. S. Rock, "Actin cross-link assembly and disassembly mechanics for α-actinin and fascin," *Journal of Biological Chemistry*, vol. 285, no. 34, pp. 26350–26357, 2010.

[42] T. T. Falzone, M. Lenz, D. R. Kovar, and M. L. Gardel, "Assembly kinetics determine the architecture of α-actinin crosslinked F-actin networks," *Nature Communications*, vol. 3, p. 861, 2012.

[43] C. T. Skau, D. S. Courson, A. J. Bestul, J. D. Winkelman, R. S. Rock, V. Sirotkin, and D. R. Kovar, "Actin filament bundling by fimbrin is important for endocytosis, cytokinesis, and polarization in fission yeast," *Journal of Biological Chemistry*, vol. 286, no. 30, pp. 26964–26977, 2011.

[44] O. Lieleg, K. M. Schmoller, M. M. Claessens, and A. R. Bausch, "Cytoskeletal polymer networks: Viscoelastic properties are determined by the microscopic interaction potential of cross-links," *Biophysical Journal*, vol. 96, pp. 4725–4732, 2009.

[45] L. Blanchoin, R. Boujemaa-Paterski, C. Sykes, and J. Plastino, "Actin dynamics, architecture, and mechanics in cell motility," *Physiological Reviews*, vol. 94, pp. 235–263, 2014.

[46] M. Mavrakis, Y. Azou-Gros, F.-C. Tsai, J. Alvarado, A. Bertin, F. Iv, A. Kress, S. Brasselet, G. H. Koenderink, and T. Lecuit, "Septins promote F-actin ring formation by crosslinking actin filaments into curved bundles," *Nature Cell Biology*, vol. 16, no. 4, pp. 322–334, 2014.

[47] S. Palani, S. Ghosh, E. Ivorra-Molla, S. Clarke, A. Suchenko, M. K. Balasubramanian, and D. V. Köster, "Calponin-homology domain mediated bending of membrane-associated actin filaments," *eLife*, vol. 10, p. e61078, 2021.

[48] O. Kučera, V. Siahaan, D. Janda, S. H. Dijkstra, E. Pilátová, E. Zatecka, S. Diez, M. Braun, and Z. Lansky, "Anillin propels myosin-independent constriction of actin rings," *Nature Communications*, vol. 12, p. 4595, 2021.

[49] H. Ennomani, G. Letort, C. Guérin, J. L. Martiel, W. Cao, F. Nédélec, E. M. De La Cruz, M. Théry, and L. Blanchoin, "Architecture and connectivity govern actin network contractility," *Current Biology*, vol. 26, pp. 616–626, 2016.

[50] G. H. Koenderink and E. K. Paluch, "Architecture shapes contractility in actomyosin networks," *Current Opinion in Cell Biology*, vol. 50, pp. 79–85, 2018.

[51] M. Zhou and Y.-L. Wang, "Distinct pathways for the early recruitment of myosin II and actin to the cytokinetic furrow," *Molecular Biology of the Cell*, vol. 19, pp. 318–326, 2008.

[52] S. O. Dean, S. L. Rogers, N. Stuurman, R. D. Vale, and J. A. Spudich, "Distinct pathways control recruitment and maintenance of myosin II at the cleavage furrow during cytokinesis," *PNAS*, vol. 102, no. 38, pp. 13473–13478, 2005.

[53] M. Mishra, J. Kashiwazaki, T. Takagi, R. Srinivasan, Y. Huang, M. K. Balasubramanian, and I. Mabuchi, "In vitro contraction of cytokinetic ring depends on myosin II but not on actin dynamics," *Nature Cell Biology*, vol. 15, no. 7, pp. 853–859, 2013.

[54] T. E. Schroeder, "Preliminary notes. Cytokinesis: filaments in the cleavage furrow," *Experimental Cell Research*, vol. 53, pp. 272–3168, 1968.

[55] A.-C. Reymann, F. Staniscia, A. Erzberger, G. Salbreux, and S. W. Grill, "Cortical flow aligns actin filaments to form a furrow," *eLife*, vol. 5, p. e17807, 2016.

[56] P. Chugh, A. G. Clark, M. B. Smith, D. A. Cassani, K. Dierkes, A. Ragab, P. P. Roux, G. Charras, G. Salbreux, and E. K. Paluch, "Actin cortex architecture regulates cell surface tension," *Nature Cell Biology*, vol. 19, no. 6, pp. 689–697, 2017.

[57] S. M. Larson, H. J. Lee, P. H. Hung, L. M. Matthews, D. N. Robinson, and J. P. Evans, "Cortical mechanics and meiosis II completion in mammalian oocytes are mediated by myosin-II and Ezrin-Radixin-Moesin (ERM) proteins," *Molecular Biology of the Cell*, vol. 21, pp. 3182–3192, 2010.

[58] L. Wolpert, "The mechanical properties of the membrane of the sea urchin egg during cleavage," *Experimental Cell Research*, vol. 41, pp. 385–396, 1966.

[59] M. Kelkar, P. Bohec, and G. Charras, "Mechanics of the cellular actin cortex: From signalling to shape change," *Current Opinion in Cell Biology*, vol. 66, pp. 69–78, 2020.

[60] J. Sedzinski, M. Biro, A. Oswald, J. Y. Tinevez, G. Salbreux, and E. Paluch, "Polar actomyosin contractility destabilizes the position of the cytokinetic furrow," *Nature*, vol. 476, pp. 462–468, 2011.

[61] Y.-H. M. Chan, B. van Lengerich, and S. G. Boxer, "Lipid-anchored DNA mediates vesicle fusion as observed by lipid and content mixing," *Biointerphases*, vol. 3, no. 2, pp. FA17–FA21, 2008.

[62] O. Staufer, J. A. de Lora, E. Bailoni, A. Bazrafshan, A. S. Benk, K. Jahnke, Z. A. Manzer, L. Otrin, T. D. Pérez, J. Sharon, J. Steinkühler, K. P. Adamala, B. Jacobson, M. Dogterom, K. Göpfrich, D. Stefanovic, S. R. Atlas, M. Grunze, M. R. Lakin, A. P. Shreve, J. P. Spatz, and G. P. López, "Building a community to engineer synthetic cells and organelles from the bottom-up," *eLife*, vol. 10, p. e73556, 2021.

[63] Y. Mulla, A. Aufderhorst-Roberts, and G. H. Koenderink, "Shaping up synthetic cells," *Physical Biology*, vol. 15, p. 041001, 2018.

[64] W. K. Spoelstra, S. Deshpande, and C. Dekker, "Tailoring the appearance: what will synthetic cells look like?," *Current Opinion in Biotechnology*, vol. 51, pp. 47–56, 2018.

[65] N. J. Gaut and K. P. Adamala, "Reconstituting natural cell elements in synthetic cells," *Advanced Biology*, vol. 5, p. 2000188, 2021.

[66] T. Litschel and P. Schwille, "Protein reconstitution inside giant unilamellar vesicles," *Annual Review of Biophysics*, vol. 50, pp. 525–548, 2021.

[67] L. Olivi, M. Berger, R. N. Creyghton, N. De Franceschi, C. Dekker, B. M. Mulder, N. J. Claassens, P. R. ten Wolde, and J. van der Oost, "Towards a synthetic cell cycle," *Nature Communications*, vol. 12, p. 4531, 2021.

[68] S. Kretschmer, K. A. Ganzinger, H. G. Franquelim, and P. Schwille, "Synthetic cell division via membrane-transforming molecular assemblies," *BMC Biology*, vol. 17, p. 43, 2019.

[69] C. R. Mahone and E. D. Goley, "Bacterial cell division at a glance," *Journal of Cell Science*, vol. 133, no. 7, p. jcs237057, 2020.

[70] J. Wang and X. Guo, "Adsorption isotherm models: Classification, physical meaning, application and solving method," *Chemosphere*, vol. 258, p. 127279, 2020.

[71] T. D. Pollard, "Nine unanswered questions about cytokinesis," *Journal of Cell Biology*, vol. 216, no. 10, pp. 3007–3016, 2017.

[72] D. B. Cortes, A. Dawes, J. Liu, M. Nickaeen, W. Strychalski, and A. S. Maddox, "Unite to divide – How models and biological experimentation have come together to reveal mechanisms of cytokinesis," *Journal of Cell Science*, vol. 131, p. jcs203570, 2018.

[73] J. Leite, D. S. Osorio, A. F. Sobral, A. M. Silva, and A. X. Carvalho, "Network contractility during cytokinesis—from molecular to global views," *Biomolecules*, vol. 9, p. 194, 2019.

[74] K. Wang, H. Okada, and E. Bi, "Comparative analysis of the roles of non-muscle myosin-IIs in cytokinesis in budding yeast, fission yeast, and mammalian cells," *Frontiers in Cell and Developmental Biology*, vol. 8, p. 593400, 2020.

[75] M. L. Jongsma, I. Berlin, and J. Neefjes, "On the move: Organelle dynamics during mitosis," *Trends in Cell Biology*, vol. 25, no. 3, pp. 112–124, 2015.

[76] C. Addi, J. Bai, and A. Echard, "Actin, microtubule, septin and ESCRT filament remodeling during late steps of cytokinesis," *Current Opinion in Cell Biology*, vol. 50, pp. 27–34, 2018.

[77] P. Horváth and T. Müller-Reichert, "A structural view on ESCRT-mediated abscission," *Frontiers in Cell and Developmental Biology*, vol. 8, p. 586880, 2020.

[78] M. I. Anjur-Dietrich, C. P. Kelleher, and D. J. Needleman, "Mechanical mechanisms of chromosome segregation," *Cells*, vol. 10, p. 465, 2021.

[79] H. S. Roberts, "Mechanisms of cytokinesis: a critical review," *The Quarterly Review of Biology*, vol. 36, pp. 155–177, 1961.

[80] J. M. Mitchison and M. M. Swann, "The mechanical properties of the cell surface III. The sea-urchin egg from fertilization to cleavage," *Journal of Experimental Biology*, vol. 32, no. 4, pp. 734–750, 1955.

[81] J. M. Arnold, "Cleavage furrow formation in a telolecithal egg (loligo pealii): I. Filaments in Early Furrow Formation," *Journal of Cell Biology*, vol. 41, no. 3, pp. 894–904, 1969.

[82] K. Kruse, J. F. Joanny, F. Jülicher, J. Prost, and K. Sekimoto, "Generic theory of active polar gels: A paradigm for cytoskeletal dynamics," *European Physical Journal E*, vol. 16, pp. 5–16, 2005.

[83] G. Salbreux, J. Prost, and J. F. Joanny, "Hydrodynamics of cellular cortical flows and the formation of contractile rings," *Physical Review Letters*, vol. 103, no. 5, p. 058102, 2009.

[84] A. Zumdieck, M. C. Lagomarsino, C. Tanase, K. Kruse, B. Mulder, M. Dogterom, and F. Julicher, "Continuum description of the cytoskeleton: Ring formation in the cell cortex," *Physical Review Letters*, vol. 95, no. 25, p. 258103, 2005.

[85] H. Turlier, B. Audoly, J. Prost, and J.-F. F. Joanny, "Furrow constriction in animal cell cytokinesis," *Biophysical Journal*, vol. 106, pp. 114–123, 2014.

[86] E. Fischer-Friedrich, Y. Toyoda, C. J. Cattin, D. J. Müller, A. A. Hyman, and F. Jülicher, "Rheology of the active cell cortex in mitosis," *Biophysical Journal*, vol. 111, pp. 589–600, 2016.

[87] P. M. McCall, F. C. MacKintosh, D. R. Kovar, and M. L. Gardel, "Cofilin drives rapid turnover and fluidization of entangled F-actin," *PNAS*, vol. 116, no. 26, pp. 12629–12637, 2019.

[88] J. G. White and G. G. Borisy, "On the mechanisms of cytokinesis in animal cells," *Journal of Theoretical Biology*, vol. 101, no. 2, pp. 289–316, 1983.

[89] T. Hiraiwa and G. Salbreux, "Role of Turnover in Active Stress Generation in a Filament Network," *Physical Review Letters*, vol. 116, no. 18, p. 188101, 2016.

[90] T. G. Chew, J. Huang, S. Palani, R. Sommese, A. Kamnev, T. Hatano, Y. Gu, S. Oliferenko, S. Sivaramakrishnan, and M. K. Balasubramanian, "Actin turnover maintains actin filament homeostasis during cytokinetic ring contraction," *Journal of Cell Biology*, vol. 216, no. 9, pp. 2657–2667, 2017.

[91] B. O'Shaughnessy and S. Thiyagarajan, "Mechanisms of contractile ring tension production and constriction," *Biophysical Reviews*, vol. 10, pp. 1667–1681, 2018.

[92] M. M. Swann and J. M. Mitchison, "The mechanism of cleavage in animal cells," *Biological Reviews*, vol. 33, pp. 103–135, 1958.

[93] J. C. Dan, "On the mechanism of astral cleavage," *Physiological Zoology*, vol. XXI, no. 3, pp. 191–218, 1948.

[94] L. Wolpert, "The mechanics and mechanism of cleavage," in *International Review of Cytology*, pp. 163–216, Academic Press Inc., 1961.

[95] D. Marsland, "The mechanisms of cell division, temperature-pressure experiments on the cleaving eggs of arbacia punctulata," *Journal of Cellular and Comparative Physiology*, vol. 36, pp. 205–227, 1950.

[96] M. Yoneda and K. Dan, "Tension at the surface of the dividing sea-urchin egg," *Journal of Experimental Biology*, vol. 57, no. 3, pp. 575–587, 1972.

[97] R. A. Green, E. K. Paluch, and K. Oegema, "Cytokinesis in animal cells," *Annual Review of Cell and Developmental Biology*, vol. 28, no. 1, pp. 29–58, 2012.

[98] H. F. Gudejko, L. M. Alford, and D. R. Burgess, "Polar expansion during cytokinesis," *Cytoskeleton*, vol. 69, pp. 1000–1009, 2012.

[99] Y.-L. Wang, "The mechanism of cytokinesis: reconsideration and reconciliation," *Cell structure and function*, vol. 26, pp. 633–638, 2001.

[100] F. Frey and T. Idema, "More than just a barrier: using physical models to couple membrane shape to cell function," *Soft Matter*, vol. 17, pp. 3533–3549, 2021.

[101] B. Sinha, D. Köster, R. Ruez, P. Gonnord, M. Bastiani, D. Abankwa, R. V. Stan, G. Butler-Browne, B. Vedie, L. Johannes, N. Morone, R. G. Parton, G. Raposo, P. Sens, C. Lamaze, and P. Nassoy, "Cells respond to mechanical stress by rapid disassembly of caveolae," *Cell*, vol. 144, pp. 402–413, 2011.

[102] R. Albertson, B. Riggs, and W. Sullivan, "Membrane traffic: A driving force in cytokinesis," *Trends in Cell Biology*, vol. 15, no. 2, pp. 92–101, 2005.

[103] S. Asano, K. Hamao, and H. Hosoya, "Direct evidence for roles of phosphorylated regulatory light chain of myosin II in furrow ingression during cytokinesis in HeLa cells," *Genes to Cells*, vol. 14, pp. 555–568, 2009.

[104] D. Bray and D. J. White, "Cortical flow in animal cells," *Science*, vol. 282, no. 4842, pp. 883–888, 1988.

[105] F. R. Najafabadi, M. Leaver, and S. W. Grill, "Orchestrating nonmuscle myosin II filament assembly at the onset of cytokinesis," *Molecular Biology of the Cell*, vol. 33, p. ar74, 2022.

[106] I. Mendes Pinto, B. Y. Rubinstein, and R. Li, "Force to divide: Structural and mechanical requirements for actomyosin ring contraction," *Biophysical Journal*, vol. 105, pp. 547–554, 2013.

[107] M. P. Murrell, P. W. Oakes, M. Lenz, and M. L. Gardel, "Forcing cells into shape: The mechanics of actomyosin contractility," *Nature Reviews Molecular Cell Biology*, vol. 16, no. 8, pp. 486–498, 2015.

[108] H. Kang, M. J. Bradley, B. R. McCullough, A. Pierre, E. E. Grintsevich, E. Reisler, and E. M. De La Cruz, "Identification of cation-binding sites on actin that drive polymerization and modulate bending stiffness," *PNAS*, vol. 109, no. 42, pp. 16923–16927, 2012.

[109] M. P. Murrell and M. L. Gardel, "F-actin buckling coordinates contractility and severing in a biomimetic actomyosin cortex," *PNAS*, vol. 109, no. 51, pp. 20820–20825, 2012.

[110] M. Lenz, T. Thoresen, M. L. Gardel, and A. R. Dinner, "Contractile units in disordered actomyosin bundles arise from f-actin buckling," *Physical Review Letters*, vol. 108, no. 23, p. 238107, 2012.

[111] K. Kruse and F. Jülicher, "Actively contracting bundles of polar filaments," *Physical Review Letters*, vol. 85, no. 8, pp. 1778–1781, 2000.

[112] V. Wollrab, J. M. Belmonte, L. Baldauf, M. Leptin, F. Nédeléc, and G. H. Koenderink, "Polarity sorting drives remodeling of actin-myosin networks," *Journal of Cell Science*, vol. 132, p. jcs219717, 2019.

[113] H. Berthoumieux, J. L. Maître, C. P. Heisenberg, E. K. Paluch, F. Jülicher, and G. Salbreux, "Active elastic thin shell theory for cellular deformations," *New Journal of Physics*, vol. 16, p. 065005, 2014.

[114] M. Malik-Garbi, N. Ierushalmi, S. Jansen, E. Abu-Shah, B. L. Goode, A. Mogilner, and K. Keren, "Scaling behaviour in steady-state contracting actomyosin networks," *Nature Physics*, vol. 15, pp. 509–516, 2019.

[115] Sonal, K. A. Ganzinger, S. K. Vogel, J. Mücksch, P. Blumhardt, and P. Schwille, "Myosin-II activity generates a dynamic steady state with continuous actin turnover in a minimal actin cortex," *Journal of Cell Science*, vol. 132, p. jcs299899, 2019.

[116] M. Fritzsche, A. Lewalle, T. Duke, K. Kruse, and G. Charras, "Analysis of turnover dynamics of the submembranous actin cortex," *Molecular Biology of the Cell*, vol. 24, pp. 757–767, 2013.

[117] F. B. Robin, W. M. McFadden, B. Yao, and E. M. Munro, "Single-molecule analysis of cell surface dynamics in Caenorhabditis elegans embryos," *Nature Methods*, vol. 11, no. 6, pp. 677–682, 2014.

[118] S. Arzash, P. M. McCall, J. Feng, M. L. Gardel, and F. C. MacKintosh, "Stress relaxation in F-actin solutions by severing," *Soft Matter*, vol. 15, pp. 6300–6307, 2019.

[119] L. L. Pontani, J. Van Der Gucht, G. Salbreux, J. Heuvingh, J. F. Joanny, and C. Sykes, "Reconstitution of an actin cortex inside a liposome," *Biophysical Journal*, vol. 96, pp. 192–198, 2009.

[120] I. Linsmeier, S. Banerjee, P. W. Oakes, W. Jung, T. Kim, and M. P. Murrell, "Disordered actomyosin networks are sufficient to produce cooperative and telescopic contractility," *Nature Communications*, vol. 7, p. 12615, 2016.

[121] L. Cao, A. Yonis, M. Vaghela, E. H. Barriga, P. Chugh, M. B. Smith, J. Maufront, G. Lavoie, A. Méant, E. Ferber, M. Bovellan, A. Alberts, A. Bertin, R. Mayor, E. K. Paluch, P. P. Roux, A. Jégou, G. Romet-Lemonne, and G. Charras, "SPIN90 associates with mDia1 and the Arp2/3 complex to regulate cortical actin organization," *Nature Cell Biology*, vol. 22, pp. 803–814, 2020.

[122] D. Zimmermann, K. E. Homa, G. M. Hocky, L. W. Pollard, E. M. De La Cruz, G. A. Voth, K. M. Trybus, and D. R. Kovar, "Mechanoregulated inhibition of formin facilitates contractile actomyosin ring assembly," *Nature Communications*, vol. 8, p. 703, 2017.

[123] L. Cao, M. Kerleau, E. L. Suzuki, H. Wioland, S. Jouet, B. Guichard, M. Lenz, G. Romet-Lemonne, and A. Jegou, "Modulation of formin processivity by profilin and mechanical tension," *eLife*, vol. 7, p. e34176, 2018.

[124] C. Suarez, R. T. Carroll, T. A. Burke, J. R. Christensen, A. J. Bestul, J. A. Sees, M. L. James, V. Sirotkin, and D. R. Kovar, "Profilin regulates F-Actin network homeostasis by favoring formin over Arp2/3 complex," *Developmental Cell*, vol. 32, pp. 43–53, 2015.

[125] S. Shekhar, M. Kerleau, S. Kühn, J. Pernier, G. Romet-Lemonne, A. Jégou, and M. F. Carlier, "Formin and capping protein together embrace the actin filament in a ménage à trois," *Nature Communications*, vol. 6, p. 8730, 2015.

[126] R. D. Mullins, J. F. Kelleher, J. Xu, and T. D. Pollard, "Arp2/3 complex from Acanthamoeba binds profilin and cross-links actin filaments," *Molecular Biology of the Cell*, vol. 9, pp. 841–852, 1998.

[127] L. Blanchoin, T. D. Pollard, and R. D. Mullins, "Interactions of ADF/cofilin, Arp2/3 complex, capping protein and profilin in remodeling of branched actin filament networks," *Current Biology*, vol. 10, no. 20, pp. 1273–1282, 2000.

[128] V. I. Risca, E. B. Wang, O. Chaudhuri, J. J. Chia, P. L. Geissler, and D. A. Fletcher, "Actin filament curvature biases branching direction," *PNAS*, vol. 109, no. 8, pp. 2913–2918, 2012.

[129] J. V. Abella, C. Galloni, J. Pernier, D. J. Barry, S. Kjær, M. F. Carlier, and M. Way, "Isoform diversity in the Arp2/3 complex determines actin filament dynamics," *Nature Cell Biology*, vol. 18, no. 1, pp. 76–86, 2016.

[130] M. E. Quinlan, J. E. Heuser, E. Kerkhoff, and R. D. Mullins, "Drosophila Spire is an actin nucleation factor," *Nature*, vol. 433, pp. 382–388, 2005.

[131] C. Chan, C. C. Beltzner, and T. D. Pollard, "Cofilin Dissociates Arp2/3 Complex and Branches from Actin Filaments," *Current Biology*, vol. 19, pp. 537–545, 2009.

[132] T. Kotila, H. Wioland, G. Enkavi, K. Kogan, I. Vattulainen, A. Jégou, G. Romet-Lemonne, and P. Lappalainen, "Mechanism of synergistic actin filament pointed end depolymerization by cyclase-associated protein and cofilin," *Nature Communications*, vol. 10, p. 5320, 2019.

[133] S. Jansen, A. Collins, L. Golden, O. Sokolova, and B. L. Goode, "Structure and mechanism of mouse cyclase-associated protein (CAP1) in regulating actin dynamics," *Journal of Biological Chemistry*, vol. 289, no. 44, pp. 30732–30742, 2014.

[134] H. Wioland, A. Jegou, and G. Romet-Lemonne, "Torsional stress generated by ADF/cofilin on cross-linked actin filaments boosts their severing," *Proceedings of the National Academy of Sciences of the United States of America*, vol. 116, no. 7, pp. 2595–2602, 2019.

[135] N. G. Pandit, W. Cao, J. Bibeau, E. M. Johnson-Chavarria, E. W. Taylor, T. D. Pollard, and E. M. De La Cruz, "Force and phosphate release from Arp2/3 complex promote dissociation of actin filament branches," *PNAS*, vol. 117, no. 24, pp. 13519–13528, 2020.

[136] F.-C. Tsai and G. H. Koenderink, "Shape control of lipid bilayer membranes by confined actin bundles," *Soft Matter*, vol. 11, pp. 8834–8847, 2015.

[137] T. Litschel, C. F. Kelley, D. Holz, M. Adeli Koudehi, S. K. Vogel, L. Burbaum, N. Mizuno, D. Vavylonis, and P. Schwille, "Reconstitution of contractile actomyosin rings in vesicles," *Nature Communications*, vol. 12, p. 2254, 2021.

[138] L. Van De Cauter, F. Fanalista, L. Van Buren, N. De Franceschi, E. Godino, S. Bouw, C. Danelon, C. Dekker, G. H. Koenderink, and K. A. Ganzinger, "Optimized cDICE for efficient reconstitution of biological systems in giant unilamellar vesicles," *ACS Synthetic Biology*, vol. 10, pp. 1690–1702, 2021.

[139] Y. Bashirzadeh, N. Wubshet, T. Litschel, P. Schwille, and A. P. Liu, "Rapid encapsulation of reconstituted cytoskeleton inside giant unilamellar vesicles," *Journal of Visualized Experiments*, vol. 177, p. e63332, 2021.

[140] M. P. Murrell, L. L. Pontani, K. Guevorkian, D. Cuvelier, P. Nassoy, and C. Sykes, "Spreading dynamics of biomimetic actin cortices," *Biophysical Journal*, vol. 100, no. 6, pp. 1400–1409, 2011.

[141] K. Dürre, F. C. Keber, P. Bleicher, F. Brauns, C. J. Cyron, J. Faix, and A. R. Bausch, "Capping protein-controlled actin polymerization shapes lipid membranes," *Nature Communications*, vol. 9, p. 1630, 2018.

[142] Y. Bashirzadeh, H. Moghimianavval, and A. P. Liu, "Encapsulated actomyosin patterns drive cell-like membrane shape changes," *iScience*, vol. 25, no. 5, p. 104236, 2022.

[143] K. Carvalho, F.-C. C. Tsai, E. Lees, R. Voituriez, G. H. Koenderink, and C. Sykes, "Cell-sized liposomes reveal how actomyosin cortical tension drives shape change," *PNAS*, vol. 110, no. 41, pp. 16456–16461, 2013.

[144] E. Loiseau, J. A. Schneider, F. C. Keber, C. Pelzl, G. Massiera, G. Salbreux, and A. R. Bausch, "Shape remodeling and blebbing of active cytoskeletal vesicles," *Science Advances*, vol. 2, p. e1500465, 2016.

[145] T. Sakamoto, J. Limouze, C. A. Combs, A. F. Straight, and J. R. Sellers, "Blebbistatin, a myosin II inhibitor, is photoinactivated by blue light," *Biochemistry*, vol. 44, pp. 584–588, 2005.

[146] M. Schuppler, F. C. Keber, M. Krüger, and A. R. Bausch, "Boundaries steer the contraction of active gels," *Nature Communications*, vol. 7, p. 13120, 2016.

[147] K. Yamamoto, H. Miura, M. Ishida, Y. Mii, N. Kinoshita, S. Takada, N. Ueno, S. Sawai, Y. Kondo, and K. Aoki, "Optogenetic relaxation of actomyosin contractility uncovers mechanistic roles of cortical tension during cytokinesis," *Nature Communications*, vol. 12, p. 7145, 2021.

[148] F. Fanalista, A. Birnie, R. Maan, F. Burla, K. Charles, G. Pawlik, S. Deshpande, G. H. Koenderink, M. Dogterom, and C. Dekker, "Shape and size control of artificial cells for bottom-up biology," *ACS Nano*, vol. 13, pp. 5439–5450, 2019.

[149] J. M. Barrows and E. D. Goley, "FtsZ dynamics in bacterial division: What, how, and why?," *Current Opinion in Cell Biology*, vol. 68, pp. 163–172, 2021.

[150] A. W. Lau, A. Prasad, and Z. Dogic, "Condensation of isolated Semi-flexible filaments driven by depletion interactions," *Europhysics Letters*, vol. 87, p. 48006, 2009.

[151] J. X. Tang, J. A. Käs, J. V. Shah, and P. A. Janmey, "Counterion-induced actin ring formation," *European Biophysics Journal*, vol. 30, pp. 477–484, 2001.

[152] M. Kinoshita, C. M. Field, M. L. Coughlin, A. F. Straight, and T. J. Mitchison, "Self- and actin-templated assembly of mammalian septins," *Developmental Cell*, vol. 3, pp. 791–802, 2002.

[153] C. M. Field, M. Coughlin, S. Doberstein, T. Marty, and W. Sullivan, "Characterization of anillin mutants reveals essential roles in septin localization and plasma membrane integrity," *Development*, vol. 132, pp. 2849–2860, 2005.

[154] A. J. Piekny and M. Glotzer, "Anillin is a scaffold protein that links RhoA, actin, and myosin during cytokinesis," *Current Biology*, vol. 18, pp. 30–36, 2008.

[155] A. J. Piekny and A. S. Maddox, "The myriad roles of anillin during cytokinesis," *Seminars in Cell and Developmental Biology*, vol. 21, pp. 881–891, 2010.

[156] C. Garno, Z. H. Irons, C. M. Gamache, Q. McKim, G. Reyes, X. Wu, C. B. Shuster, and J. H. Henson, "Building the cytokinetic contractile ring in an early embryo: Initiation as clusters of myosin II, anillin and septin, and visualization of a septin filament network," *PLoS ONE*, vol. 16, no. 12, p. e0252845, 2021.

[157] M. Biro, Y. Romeo, S. Kroschwald, M. Bovellan, A. Boden, J. Tcherkezian, P. P. Roux, G. Charras, and E. K. Paluch, "Cell cortex composition and homeostasis resolved by integrating proteomics and quantitative imaging," *Cytoskeleton*, vol. 70, pp. 741–754, 2013.

[158] M. Miyazaki, M. Chiba, H. Eguchi, T. Ohki, and S. S. Ishiwata, "Cell-sized spherical confinement induces the spontaneous formation of contractile actomyosin rings in vitro," *Nature Cell Biology*, vol. 17, no. 4, pp. 480–489, 2015.

[159] A. A. Bridges, M. S. Jentzsch, P. W. Oakes, P. Occhipinti, and A. S. Gladfelter, "Micron-scale plasma membrane curvature is recognized by the septin cytoskeleton," *Journal of Cell Biology*, vol. 213, no. 1, pp. 23–32, 2016.

[160] K. A. Ganzinger, A. Merino-Salomón, D. A. García-Soriano, A. N. Butterfield, T. Litschel, F. Siedler, and P. Schwille, "FtsZ reorganization facilitates deformation of giant vesicles in microfluidic traps," *Angewandte Chemie International Edition*, vol. 59, pp. 21556–21560, 2020.

[161] G. Morrison and D. Thirumalai, "Semiflexible chains in confined spaces," *Physical Review E - Statistical, Nonlinear, and Soft Matter Physics*, vol. 79, p. 011924, 2009.

[162] M. Soares E Silva, J. Alvarado, J. Nguyen, N. Georgoulia, B. M. Mulder, and G. H. Koenderink, "Self-organized patterns of actin filaments in cell-sized confinement," *Soft Matter*, vol. 7, no. 22, pp. 10631–10641, 2011.

[163] M. M. Claessens, R. Tharmann, K. Kroy, and A. R. Bausch, "Microstructure and viscoelasticity of confined semiflexible polymer networks," *Nature Physics*, vol. 2, pp. 186–189, 2006.

[164] L. Limozin and E. Sackmann, "Polymorphism of Cross-Linked Actin Networks in Giant Vesicles," *Physical Review Letters*, vol. 89, no. 16, p. 168103, 2002.

[165] Y. Bashirzadeh, S. A. Redford, C. Lorpaiboon, A. Groaz, H. Moghimianavval, T. Litschel, P. Schwille, G. M. Hocky, A. R. Dinner, and A. P. Liu, "Actin crosslinker competition and sorting drive emergent GUV size-dependent actin network architecture," *Communications Biology*, vol. 4, p. 1136, 2021.

[166] E. Schäfer, M. Vache, T. T. Kliesch, and A. Janshoff, "Mechanical response of adherent giant liposomes to indentation with a conical AFM-tip," *Soft Matter*, vol. 11, pp. 4487–4495, 2015.

[167] M. Adeli Koudehi, D. M. Rutkowski, and D. Vavylonis, "Organization of associating or crosslinked actin filaments in confinement," *Cytoskeleton*, vol. 76, pp. 532–548, 2019.

[168] T. E. Schroeder, "The contractile ring II. Determining its brief existence, volumetric changes, and vital role in cleaving Arabica eggs," *Journal of Cell Biology*, vol. 53, pp. 419–434, 1972.

[169] X. Ma, M. Kovaćs, M. A. Conti, A. Wang, Y. Zhang, J. R. Sellers, R. S. Adelstein, M. Kovacs, M. A. Conti, A. Wang, Y. Zhang, J. R. Sellers, and R. S. Adelstein, "Nonmuscle myosin II exerts tension but does not translocate actin in vertebrate cytokinesis," *PNAS*, vol. 109, no. 12, pp. 4509–4514, 2012.

[170] E. M. Reichl, Y. Ren, M. K. Morphew, M. Delannoy, J. C. Effler, K. D. Girard, S. Divi, P. A. Iglesias, S. C. Kuo, and D. N. Robinson, "Interactions between myosin and actin crosslinkers control cytokinesis contractility dynamics and mechanics," *Current Biology*, vol. 18, pp. 471–480, 2008.

[171] D. J. Fishkind and Y. L. Wang, "Orientation and three-dimensional organization of actin filaments in dividing cultured cells," *Journal of Cell Biology*, vol. 123, no. 4, pp. 837–848, 1993.

[172] A. M. Fenix, N. Taneja, C. A. Buttler, J. Lewis, S. B. Van Engelenburg, R. Ohi, and D. T. Burnette, "Expansion and concatenation of nonmuscle myosin IIA filaments drive cellular contractile system formation during interphase and mitosis," *Molecular Biology of the Cell*, vol. 27, pp. 1465–1478, 2016.

[173] J. H. Henson, C. E. Ditzler, A. Germain, P. M. Irwin, E. T. Vogt, S. Yang, X. Wu, and C. B. Shuster, "The ultrastructural organization of actin and myosin II filaments in the contractile ring: New support for an old model of cytokinesis," *Molecular Biology of the Cell*, vol. 28, pp. 613–623, 2017.

[174] M. Lenz, "Geometrical origins of contractility in disordered actomyosin networks," *Physical Review X*, vol. 4, p. 041002, 2014.

[175] C. Schwayer, M. Sikora, J. Slováková, R. Kardos, and C. P. Heisenberg, "Actin Rings of Power," *Developmental Cell*, vol. 37, pp. 493–506, 2016.

[176] D. J. Odde, "Mitosis, diffusible crosslinkers, and the ideal gas law," *Cell*, vol. 160, pp. 1041–1043, 2015.

[177] S. Chen, T. Markovich, and F. C. MacKintosh, "Motor-free contractility in active gels," *Physical Review Letters*, vol. 125, p. 208101, 2020.

[178] F. Rizzelli, M. G. Malabarba, S. Sigismund, and M. Mapelli, "The crosstalk between microtubules, actin and membranes shapes cell division," *Open Biology*, vol. 10, p. 190314, 2020.

[179] O. M. Lancaster and B. Baum, "Shaping up to divide: Coordinating actin and microtubule cytoskeletal remodelling during mitosis," *Seminars in Cell and Developmental Biology*, vol. 34, pp. 109–115, 2014.

[180] F. C. Tsai, A. Bertin, H. Bousquet, J. Manzi, Y. Senju, M. C. Tsai, L. Picas, S. Miserey-Lenkei, P. Lappalainen, E. Lemichez, E. Coudrier, and P. Bassereau, "Ezrin enrichment on curved membranes requires a specific conformation or interaction with a curvature-sensitive partner," *eLife*, vol. 7, p. e37262, 2018.

[181] G. A. Quinones, J. Jin, and A. E. Oro, "I-BAR protein antagonism of endocytosis mediates directional sensing during guided cell migration," *Journal of Cell Biology*, vol. 189, no. 2, pp. 353–367, 2010.

[182] W. Bae, S. Kocabey, and T. Liedl, "DNA nanostructures in vitro, in vivo and on membranes," *Nano Today*, vol. 26, pp. 98–107, 2019.

[183] A. Czogalla, D. J. Kauert, H. G. Franquelim, V. Uzunova, Y. Zhang, R. Seidel, and P. Schwille, "Amphipathic DNA origami nanoparticles to scaffold and deform lipid membrane vesicles," *Angewandte Chemie International Edition*, vol. 54, pp. 6501–6505, 2015.

[184] J. Steinkühler, R. L. Knorr, Z. Zhao, T. Bhatia, S. M. Bartelt, S. Wegner, R. Dimova, and R. Lipowsky, "Controlled division of cell-sized vesicles by low densities of membrane-bound proteins," *Nature Communications*, vol. 11, p. 905, 2020.

[185] N. D. Franceschi, W. Pezeshkian, A. Fragasso, B. M. Bruininks, S. Tsai, S. J. Marrink, and C. Dekker, "A synthetic membrane shaper for controlled liposome deformation," *bioRxiv*, p. 2021.12.22.473854, 2021.

[186] H. T. McMahon and E. Boucrot, "Membrane curvature at a glance," *Journal of Cell Science*, vol. 128, pp. 1065–1070, 2015.

[187] A. Beber, C. Taveneau, M. Nania, F. C. Tsai, A. Di Cicco, P. Bassereau, D. Lévy, J. T. Cabral, H. Isambert, S. Mangenot, and A. Bertin, "Membrane reshaping by micrometric curvature sensitive septin filaments," *Nature Communications*, vol. 10, p. 420, 2019.

[188] A. V. Taubenberger, B. Baum, and H. K. Matthews, "The Mechanics of Mitotic Cell Rounding," *Frontiers in Cell and Developmental Biology*, vol. 8, p. 687, 2020.

[189] M. T. Prospéri, P. Lépine, F. Dingli, P. Paul-Gilloteaux, R. Martin, D. Loew, H. J. Knölker, and E. Coudrier, "Myosin 1b functions as an effector of EphB signaling to control cell repulsion," *Journal of Cell Biology*, vol. 210, no. 2, pp. 347–361, 2015.

[190] G. Russo and M. Krauss, "Septin remodeling during mammalian cytokinesis," *Frontiers in Cell and Developmental Biology*, vol. 9, p. 768309, 2021.

[191] K. A. Michie, A. Bermeister, N. O. Robertson, S. C. Goodchild, and P. M. Curmi, "Two sides of the coin: Ezrin/Radixin/Moesin and Merlin control membrane structure and contact inhibition," *International Journal of Molecular Sciences*, vol. 20, p. 1996, 2019.

[192] M. P. Clausen, H. Colin-York, F. Schneider, C. Eggeling, and M. Fritzsche, "Dissecting the actin cortex density and membrane-cortex distance in living cells by super-resolution microscopy," *Journal of Physics D: Applied Physics*, vol. 50, p. 064002, 2017.

[193] M. T. Swulius, L. T. Nguyen, M. S. Ladinsky, D. R. Ortega, S. Aich, M. Mishra, and G. J. Jensen, "Structure of the fission yeast actomyosin ring during constriction," *PNAS*, vol. 115, no. 7, pp. E1455–E1464, 2018.

[194] N. A. McDonald, A. L. Lind, S. E. Smith, R. Li, and K. L. Gould, "Nanoscale architecture of the Schizosaccharomyces pombe contractile ring," *eLife*, vol. 6, p. e28865, 2017.

[195] B. A. Truong Quang, R. Peters, D. A. Cassani, P. Chugh, A. G. Clark, M. Agnew, G. Charras, and E. K. Paluch, "Extent of myosin penetration within the actin cortex regulates cell surface mechanics," *Nature Communications*, vol. 12, p. 6511, 2021.

[196] A. Das, A. Bhat, R. Sknepnek, D. Köster, S. Mayor, and M. Rao, "Stratification relieves constraints from steric hindrance in the generation of compact actomyosin asters at the membrane cortex," *Science Advances*, vol. 6, p. eaay6093, 2020.

[197] M. P. Sheetz, "Cell control by membrane-cytoskeleton adhesion," *Nature Reviews Molecular Cell Biology*, vol. 2, no. 5, pp. 392–396, 2001.

[198] A. Paraschiv, T. J. Lagny, C. V. Campos, E. Coudrier, P. Bassereau, and A. Šarić, "Influence of membrane-cortex linkers on the extrusion of membrane tubes," *Biophysical Journal*, vol. 120, pp. 598–606, 2021.

[199] D. Raucher, T. Stauffer, W. Chen, K. Shen, S. Guo, J. D. York, M. P. Sheetz, and T. Meyer, "Phosphatidylinositol 4,5-bisphosphate functions as a second messenger that regulates cytoskeleton-plasma membrane adhesion," *Cell*, vol. 100, pp. 221–228, 2000.

[200] P. A. Janmey, W. Xian, and L. A. Flanagan, "Controlling cytoskeleton structure by phosphoinositide-protein interactions: Phosphoinositide binding protein domains and effects of lipid packing," *Chemistry and Physics of Lipids*, vol. 101, pp. 93–107, 1999.

[201] C. E. Snider, A. H. Willet, J. S. Chen, G. Arpag, M. Zanic, and K. L. Gould, "Phosphoinositide-mediated ring anchoring resists perpendicular forces to promote medial cytokinesis," *Journal of Cell Biology*, vol. 216, no. 10, pp. 3041–3050, 2017.

[202] C. Simon, V. Caorsi, C. Campillo, and C. Sykes, "Interplay between membrane tension and the actin cytoskeleton determines shape changes," *Physical Biology*, vol. 15, p. 065004, 2018.

[203] R. Shrivastava, D. V. Köster, S. Kalme, S. Mayor, and M. Neerathilingam, "Tailor-made ezrin actin binding domain to probe its interaction with actin in-vitro," *PLoS ONE*, vol. 10, no. 4, p. e0123428, 2015.

[204] F. Rico, A. Russek, L. González, H. Grubmüller, and S. Scheuring, "Heterogeneous and rate-dependent streptavidin–biotin unbinding revealed by high-speed force spectroscopy and atomistic simulations," *PNAS*, vol. 116, no. 14, pp. 6594–6601, 2019.

[205] J. A. Nye and J. T. Groves, "Kinetic control of histidine-tagged protein surface density on supported lipid bilayers," *Langmuir*, vol. 24, pp. 4145–4149, 2008.

[206] G. Raghunath and R. B. Dyer, "Kinetics of Histidine-tagged protein association to nickel-decorated liposome surfaces," *Langmuir*, vol. 35, pp. 12550–12561, 2019.

[207] E. Korkmazhan and A. R. Dunn, "The membrane-cortex crosslinker ezrin acts as a sliding anchor on F-actin," *Science Advances*, vol. 8, p. eabo2779, 2022.

[208] R. Grover, J. Fischer, F. W. Schwarz, W. J. Walter, P. Schwille, and S. Diez, "Transport efficiency of membrane-anchored kinesin-1 motors depends on motor density and diffusivity," *Proceedings of the National Academy of Sciences of the United States of America*, vol. 113, no. 46, pp. E7185–E7193, 2016.

[209] J. Pernier, R. Kusters, H. Bousquet, T. Lagny, A. Morchain, J. F. Joanny, P. Bassereau, and E. Coudrier, "Myosin 1b is an actin depolymerase," *Nature Communications*, vol. 10, p. 5200, 2019.

[210] F. Schneider, D. Waithe, M. P. Clausen, S. Galiani, T. Koller, G. Ozhan, C. Eggeling, and E. Sezgin, "Diffusion of lipids and GPI-anchored proteins in actin-free plasma membrane vesicles measured by STED-FCS," *Molecular Biology of the Cell*, vol. 28, pp. 1507–1518, 2017.

[211] F. Heinemann, S. K. Vogel, and P. Schwille, "Lateral membrane diffusion modulated by a minimal actin cortex," *Biophysical Journal*, vol. 104, no. 7, pp. 1465–1475, 2013.

[212] S. K. Vogel, F. Greiss, A. Khmelinskaia, and P. Schwille, "Control of lipid domain organization by a biomimetic contractile actomyosin cortex," *eLife*, vol. 6, p. e24350, 2017.

[213] D. V. Köster, K. Husain, E. Iljazi, A. Bhat, P. Bieling, R. D. Mullins, M. Rao, and S. Mayor, "Actomyosin dynamics drive local membrane component organization in an in vitro active composite layer," *PNAS*, vol. 113, no. 12, pp. E1645–E1654, 2016.

[214] A. Honigmann, S. Sadeghi, J. Keller, S. W. Hell, C. Eggeling, and R. Vink, "A lipid bound actin meshwork organizes liquid phase separation in model membranes," *eLife*, vol. 3, p. e01671, 2014.

[215] M. Rao and S. Mayor, "Active organization of membrane constituents in living cells," *Current Opinion in Cell Biology*, vol. 29, pp. 126–132, 2014.

[216] K. Gowrishankar, S. Ghosh, S. Saha, C. Rumamol, S. Mayor, and M. Rao, "Active remodeling of cortical actin regulates spatiotemporal organization of cell surface molecules," *Cell*, vol. 149, pp. 1353–1367, 2012.

[217] A. P. Liu and D. A. Fletcher, "Actin polymerization serves as a membrane domain switch in model lipid bilayers," *Biophysical Journal*, vol. 91, pp. 4064–4070, 2006.

[218] M. Schön, I. Mey, and C. Steinem, "Influence of cross-linkers on ezrin-bound minimal actin cortices," *Progress in Biophysics and Molecular Biology*, vol. 144, pp. 91–101, 2019.

[219] H. Nöding, M. Schön, C. Reinermann, N. Dörrer, A. Kürschner, B. Geil, I. Mey, C. Heussinger, A. Janshoff, and C. Steinem, "Rheology of membrane-attached minimal actin cortices," *Journal of Physical Chemistry B*, vol. 122, pp. 4537–4545, 2018.

[220] L. S. Mosby, N. Hundt, G. Young, A. Fineberg, M. Polin, S. Mayor, P. Kukura, and D. V. Köster, "Myosin II filament dynamics om actin networks revealed with interferometric scattering microscopy," *Biophysical Journal*, vol. 118, pp. 1946–1957, 2020.

[221] A. Szuba, F. Bano, G. Castro Linares, F. Iv, M. Mavrakis, R. P. Richter, A. Bertin, and G. H. Koenderink, "Membrane binding controls ordered self-assembly of animal septins," *eLife*, vol. 10, p. e63349, 2021.

[222] K. S. Cannon, B. L. Woods, J. M. Crutchley, and A. S. Gladfelter, "An amphipathic helix enables septins to sense micrometer-scale membrane curvature," *Journal of Cell Biology*, vol. 218, no. 4, pp. 1128–1137, 2019.

[223] L. Sun, R. Guan, I. J. Lee, Y. Liu, M. Chen, J. Wang, J. Q. Wu, and Z. Chen, "Mechanistic Insights into the Anchorage of the Contractile Ring by Anillin and Mid1," *Developmental Cell*, vol. 33, pp. 413–426, 2015.

[224] C. F. Schroer, L. Baldauf, L. van Buren, T. A. Wassenaar, M. N. Melo, G. H. Koenderink, and S. J. Marrink, "Charge-dependent interactions of monomeric and filamentous actin with lipid bilayers," *PNAS*, vol. 117, no. 11, pp. 5861–5872, 2020.

[225] S. H. Zigmond, "Formin-induced nucleation of actin filaments," *Current Opinion in Cell Biology*, vol. 16, pp. 99–105, 2004.

[226] K. Guevorkian, J. Manzi, L. L. Pontani, F. Brochard-Wyart, and C. Sykes, "Mechanics of biomimetic liposomes encapsulating an actin shell," *Biophysical Journal*, vol. 109, pp. 2471–2479, 2015.

[227] P. Bleicher, A. Sciortino, and A. R. Bausch, "The dynamics of actin network turnover is self-organized by a growth-depletion feedback," *Scientific Reports*, vol. 10, p. 6215, 2020.

[228] M. M. Ng, F. Chang, and D. R. Burgess, "Movement of membrane domains and requirement of membrane signaling molecules for cytokinesis," *Developmental Cell*, vol. 9, pp. 781–790, 2005.

[229] C. Cauvin and A. Echard, "Phosphoinositides: Lipids with informative heads and mastermind functions in cell division," *Biochimica et Biophysica Acta*, vol. 1851, pp. 832–843, 2015.

[230] M. R. Logan and C. A. Mandato, "Regulation of the actin cytoskeleton by PIP2 in cytokinesis," *Biology of the Cell*, vol. 98, pp. 377–388, 2006.

[231] K. Emoto and M. Umeda, "Membrane lipid control of cytokinesis," *Cell Structure and Function*, vol. 26, pp. 659–665, 2001.

[232] P. Bassereau, R. Jin, T. Baumgart, M. Deserno, R. Dimova, V. A. Frolov, P. V. Bashkirov, H. Grubmüller, R. Jahn, H. J. Risselada, L. Johannes, M. M. Kozlov, R. Lipowsky, T. J. Pucadyil, W. F. Zeno, J. C. Stachowiak, D. Stamou, A. Breuer, L. Lauritsen, C. Simon, C. Sykes, G. A. Voth, and T. R. Weikl, "The 2018 biomembrane curvature and remodeling roadmap," *Journal of Physics D: Applied Physics*, vol. 51, p. 343001, 2018.

[233] R. Dasgupta, M. S. Miettinen, N. Fricke, R. Lipowsky, and R. Dimova, "The glycolipid GM1 reshapes asymmetric biomembranes and giant vesicles by curvature generation," *PNAS*, vol. 115, no. 22, pp. 5756–5761, 2018.

[234] M. Karimi, J. Steinkühler, D. Roy, R. Dasgupta, R. Lipowsky, and R. Dimova, "Asymmetric ionic conditions generate large membrane curvatures," *Nano Letters*, vol. 18, pp. 7816–7821, 2018.

[235] C. B. Shuster and D. R. Burgess, "Targeted new membrane addition in the cleavage furrow is a late, separate event in cytokinesis," *PNAS*, vol. 99, no. 6, pp. 3633–3638, 2002.

[236] J. A. Schiel and R. Prekeris, "Membrane dynamics during cytokinesis," *Current Opinion in Cell Biology*, vol. 25, pp. 92–98, 2013.

[237] H. Robson Marsden, N. A. Elbers, P. H. H. Bomans, N. A. J. M. Sommerdijk, and A. Kros, "A reduced SNARE model for membrane fusion," *Angewandte Chemie*, vol. 121, pp. 2366–2369, 2009.

[238] R. B. Lira and R. Dimova, "Fusion assays for model membranes: a critical review," in *Advances in Biomembranes and Lipid Self-Assembly*, vol. 30, pp. 229–270, Academic Press, 2019.

[239] S. Deshpande, S. Wunnava, D. Hueting, and C. Dekker, "Membrane Tension–Mediated Growth of Liposomes," *Small*, vol. 15, no. 38, p. 1903898, 2019.

[240] Y. Dreher, K. Jahnke, E. Bobkova, J. P. Spatz, and K. Göpfrich, "Division and Regrowth of Phase-Separated Giant Unilamellar Vesicles," *Angewandte Chemie International Edition*, vol. 60, pp. 10661–10669, 2021.

[241] K. Kurihara, M. Tamura, K. I. Shohda, T. Toyota, K. Suzuki, and T. Sugawara, "Self-reproduction of supramolecular giant vesicles combined with the amplification of encapsulated DNA," *Nature Chemistry*, vol. 3, pp. 775–781, 2011.

[242] M. Exterkate, A. Caforio, M. C. Stuart, and A. J. Driessen, "Growing membranes in vitro by continuous phospholipid biosynthesis from free fatty acids," *ACS Synthetic Biology*, vol. 7, pp. 153–165, 2018.

[243] D. Blanken, D. Foschepoth, A. C. Serrão, and C. Danelon, "Genetically controlled membrane synthesis in liposomes," *Nature Communications*, vol. 11, p. 4317, 2020.

[244] T. E. Schroeder, "The origin of cleavage forces in dividing eggs - A mechanism in two steps," *Experimental Cell Research*, vol. 134, pp. 231–240, 1981.

[245] G. K. Wong, P. G. Allen, and D. A. Begg, "Dynamics of filamentous actin organization in the sea urchin egg cortex during early cleavage divisions: Implications for the mechanism of cytokinesis," *Cell Motility and the Cytoskeleton*, vol. 36, pp. 30–42, 1997.

[246] T. Bhatia, J. Agudo-Canalejo, R. Dimova, and R. Lipowsky, "Membrane Nanotubes Increase the Robustness of Giant Vesicles," *ACS Nano*, vol. 12, pp. 4478–4485, 2018.

[247] T. Bhatia, S. Christ, J. Steinkühler, R. Dimova, and R. Lipowsky, "Simple sugars shape giant vesicles into multispheres with many membrane necks," *Soft Matter*, vol. 16, pp. 1246–1258, 2020.

[248] N. Wang, L. D. Clark, Y. Gao, M. M. Kozlov, T. Shemesh, and T. A. Rapoport, "Mechanism of membrane-curvature generation by ER-tubule shaping proteins," *Nature Communications*, vol. 12, p. 568, 2021.

[249] D. N. Robinson and J. A. Spudich, "Mechanics and regulation of cytokinesis," *Current Opinion in Cell Biology*, vol. 16, pp. 182–188, 2004.

[250] F. Paquin, J. Rivnay, A. Salleo, N. Stingelin, and C. Silva, "Role of the supracellular actomyosin cable during epithelial wound healing," *Soft Matter*, vol. 14, no. 23, pp. 4866–4873, 2018.

[251] A. F. Huxley and R. Niedergerke, "Structural changes in muscle during contraction," *Nature*, vol. 174, no. 4412, pp. 971–973, 1954.

[252] J. R. Sellers, "Myosins: A diverse superfamily," *Biochimica et Biophysica Acta*, vol. 1496, no. 1, pp. 3–22, 2000.

[253] J. S. Berg, B. C. Powell, and R. E. Cheney, "A millennial myosin census," *Molecular Biology of the Cell*, vol. 12, pp. 780–794, 2001.

[254] C. Brito and S. Sousa, "Non-Muscle Myosin 2A (NM2A): Structure, Regulation and Function," *Cells*, vol. 9, p. 1590, 2020.

[255] D. Ricketson, C. A. Johnston, and K. E. Prehoda, "Multiple tail domain interactions stabilize nonmuscle myosin II bipolar filaments," *PNAS*, vol. 107, no. 49, pp. 20964–20969, 2010.

[256] X. Liu, S. Shu, and E. D. Korn, "Polymerization pathway of mammalian nonmuscle myosin 2s," *PNAS*, vol. 115, no. 30, pp. E7101–E7108, 2018.

[257] M. Linari, E. Brunello, M. Reconditi, L. Fusi, M. Caremani, T. Narayanan, G. Piazzesi, V. Lombardi, and M. Irving, "Force generation by skeletal muscle is controlled by mechanosensing in myosin filaments," *Nature*, vol. 528, no. 7581, pp. 276–279, 2015.

[258] A. Carmena, "Non-muscle myosin II activation: adding a classical touch to ROCK," *Small GTPases*, vol. 12, no. 3, pp. 161–166, 2021.

[259] C. B. O'Connell, M. J. Tyska, and M. S. Mooseker, "Myosin at work : Motor adaptations for a variety of cellular functions," *Biochimica et Biophysica Acta*, vol. 1773, pp. 615–630, 2007.

[260] J. R. Moore, E. B. Krementsova, K. M. Trybus, and D. M. Warshaw, "Myosin V exhibits a high duty cycle and large unitary displacement," *Journal of Cell Biology*, vol. 155, no. 4, pp. 625–635, 2001.

[261] K. Homma and M. Ikebe, "Myosin X is a high duty ratio motor," *Journal of Biological Chemistry*, vol. 280, no. 32, pp. 29381–29391, 2005.

[262] S. M. Heissler and J. R. Sellers, "Kinetic adaptations of myosins for their diverse cellular functions," *Traffic*, vol. 17, pp. 839–859, 2016.

[263] H. E. Huxley, "Electron microscope studies on the structure of natural and synthetic protein filaments from striated muscle," *Journal of Molecular Biology*, vol. 7, pp. 281–308, 1963.

[264] J. M. Barral and H. F. Epstein, "Protein machines and self assembly in muscle organization," *BioEssays*, vol. 21, pp. 813–823, 1999.

[265] T. D. Pollard, "Electron microscopy of synthetic myosin filaments: Evidence for cross-bridge flexibility and copolymer formation," *Journal of Cell Biology*, vol. 67, pp. 93–104, 1975.

[266] H. Hinssen, J. D'Haese, J. V. Small, and A. Sobieszek, "Mode of filament assembly of myosins from muscle and nonmuscle cells," *Journal of Ultrasructure Research*, vol. 64, pp. 282–302, 1978.

[267] R. Niederman and T. D. Pollard, "Human platelet myosin II. In vitro assembly and structure of myosin filaments," *The Journal of Cell Biology*, vol. 67, pp. 72–92, 1975.

[268] J. F. Koretz, "Structural studies of synthetic filaments prepared from column-purified myosin," *Biophysical Journal*, vol. 27, pp. 423–432, 1979.

[269] N. Billington, A. Wang, J. Mao, R. S. Adelstein, and J. R. Sellers, "Characterization of three full-length human nonmuscle myosin II paralogs," *Journal of Biological Chemistry*, vol. 288, no. 46, pp. 33398–33410, 2013.

[270] E. Reisler, C. Smith, and G. Seegan, "Myosin minifilaments," *Journal of Molecular Biology*, vol. 143, pp. 129–145, 1980.

[271] J. F. Koretz, "Hybridization and reconstitution of thick-filament structure," in *Methods in Enzymology*, vol. 85, pp. 20–55, Academic Press Inc., 1982.

[272] T. D. Pollard, "Structure and polymerization of acanthamoeba myosin-II filaments," *Journal of Cell Biology*, vol. 95, pp. 816–825, 1982.

[273] R. C. Thompson, M. Buvoli, A. Buvoli, and L. A. Leinwand, "Myosin filament assembly requires a cluster of four positive residues located in the rod domain," *FEBS Letters*, vol. 586, pp. 3008–3012, 2012.

[274] A. D. McLachlan and J. Karn, "Periodic charge distributions in the myosin rod amino acid sequence match cross-bridge spacings in muscle," *Nature*, vol. 299, pp. 226–231, 1982.

[275] R. Straussman, J. M. Squire, A. Ben-Ya'acov, and S. Ravid, "Skip residues and charge interactions in myosin II coiled-coils: Implications for molecular packing," *Journal of Molecular Biology*, vol. 353, pp. 613–628, 2005.

[276] R. Craig and J. L. Woodhead, "Structure and function of myosin filaments," *Current Opinion in Structural Biology*, vol. 16, pp. 204–212, 2006.

[277] J. Grewe and U. S. Schwarz, "Mechanosensitive self-assembly of myosin II minifilaments," *Physical Review E*, vol. 101, p. 022402, 2020.

[278] B. Kaminer and A. L. Bell, "Myosin filamentogenesis: Effects of pH and ionic concentration," *Journal of Molecular Biology*, vol. 20, pp. 391–401, 1966.

[279] L. Melli, N. Billington, S. A. Sun, J. E. Bird, A. Nagy, T. B. Friedman, Y. Takagi, and J. R. Sellers, "Bipolar filaments of human nonmuscle myosin 2-A and 2-B have distinct motile and mechanical properties," *eLife*, vol. 7, p. e32871, 2018.

[280] D. P. Kiehart and R. Feghali, "Cytoplasmic myosin from Drosophila melanogaster," *Journal of Cell Biology*, vol. 103, pp. 1517–1525, 1986.

[281] W. Kühne, *Untersuchungen über das Protoplasma und die Contractilität*. Leipzig: Wilhelm Engelmann, 1864.

[282] S. J. Kron and J. A. Spudich, "Fluorescent actin filaments move on myosin fixed to a glass surface," *PNAS*, vol. 83, pp. 6272–6276, 1986.

[283] C. Toepfer and J. R. Sellers, "Use of fluorescent techniques to study the in vitro movement of myosins.," in *Fluorescent methods for molecular motors* (C. P. Toseland and N. Fili, eds.), pp. 193–210, Basel: Springer, 2014.

[284] J. R. Sellers, "In vitro motility assays with actin," in *Cell Biology*, vol. 2, pp. 387–392, Elsevier Science (USA), 2006.

[285] Y. Y. Toyoshima, S. J. Kron, E. M. McNally, K. R. Niebling, C. Toyoshima, and J. A. Spudich, "Myosin subfragment-1 is sufficient to move actin filaments in vitro," *Nature*, vol. 328, pp. 536–539, 1987.

[286] T. Q. Uyeda, H. M. Warrick, S. J. Kron, and J. A. Spudich, "Quantized velocities at low myosin densities in an in vitro motility," *Nature*, vol. 352, pp. 307–311, 1991.

[287] K. Y. Kim, M. Kovács, S. Kawamoto, J. R. Sellers, and R. S. Adelstein, "Disease-associated mutations and alternative splicing alter the enzymatic and motile activity of nonmuscle myosins II-B and II-C," *Journal of Biological Chemistry*, vol. 280, no. 24, pp. 22769–22775, 2005.

[288] M. P. Sheetz and J. A. Spudich, "Movement of myosin-coated structures on actin cables," *Cell Motility*, vol. 303, no. 5, pp. 485–489, 1983.

[289] M. Scholz, K. L. Weirich, M. L. Gardel, A. R. Dinner, M. Scholz, K. L. Weirich, M. L. Gardel, A. R. Dinner, M. L. Gardel, A. R. Dinner, and M. Scholz, "Tuning molecular motor transport through cytoskeletal filament network organization," *Soft Matter*, vol. 16, pp. 2135–2140, 2020.

[290] K. Strange, *C. elegans - Methods and Applications*. Totowa: Humana Press, methods in ed., 2006.

[291] V. T. Yan, A. Narayanan, F. Julicher, and S. W. Grill, "A condensate dynamic instability orchestrates oocyte actomyosin cortex activation," *Nature*, 2022.

[292] C. R. Cowan and A. A. Hyman, "Acto-myosin reorganization and PAR polarity in C . elegans," *Development*, vol. 134, pp. 1035–1043, 2007.

[293] S. Guo and K. J. Kemphues, "A non-muscle myosin required for embryonic polarity in Caenorhabditis elegans," *Nature*, vol. 382, pp. 455–458, 1996.

[294] C. Gally, F. Wissler, H. Zahreddine, S. Quintin, F. Landmann, and M. Labouesse, "Myosin II regulation during C . elegans embryonic elongation : LET-502 / ROCK , MRCK-1 and PAK-1 , three kinases with different roles," *Development*, vol. 136, pp. 3109–3119, 2009.

[295] R. L. Sohn, K. L. Vikstrom, M. Strauss, C. Cohen, A. G. Szent-Gyorgyi, and L. A. Leinwand, "A 29 residue region of the sarcomeric myosin rod is necessary for filament formation," *Journal of Molecular Biology*, vol. 266, pp. 317–330, 1997.

[296] H. Fischer, I. Polikarpov, and A. F. Craievich, "Average protein density is a molecular-weight-dependent function," *Protein Science*, vol. 13, pp. 2825–2828, 2004.

[297] J. M. Squire, "Muscle myosin filaments: Cores, crowns and couplings," *Biophysical Reviews*, vol. 1, pp. 149–160, 2009.

[298] J. S. Wall and J. F. Hainfeld, "Mass mapping with the scanning transmission electron microscope," in *Annual Review of Biophysics and Chemistry* (D. M. Engelman, ed.), vol. 15, pp. 355–376, Palo Alto: Annual Reviews Inc., 1986.

[299] C. Martinez-Torres, F. Burla, C. Alkemade, and G. H. Koenderink, "Revealing the assembly of filamentous proteins with scanning transmission electron microscopy," *PLoS ONE*, vol. 14, no. 12, p. e0226277, 2019.

[300] S. A. Müller and A. Engel, "Structure and mass analysis by scanning transmission electron microscopy," *Micron*, vol. 32, pp. 21–31, 2001.

[301] J. J. Connell and I. M. Mackie, "Molecular weight of rabbit and cod myosins," *Nature*, vol. 201, pp. 78–79, 1964.

[302] M. P. López, F. Huber, I. Grigoriev, M. O. Steinmetz, A. Akhmanova, G. H. Koenderink, and M. Dogterom, "Actin-microtubule coordination at growing microtubule ends," *Nature Communications*, vol. 5, p. 4778, 2014.

[303] S. Köhler, O. Lieleg, and A. R. Bausch, "Rheological characterization of the bundling transition in F-actin solutions induced by methylcellulose," *PLoS ONE*, vol. 3, no. 7, p. e2736, 2008.

[304] J. D. Winkelman, C. Suarez, G. M. Hocky, A. J. Harker, A. N. Morganthaler, J. R. Christensen, G. A. Voth, J. R. Bartles, and D. R. Kovar, "Fascin- and α-Actinin-Bundled Networks Contain Intrinsic Structural Features that Drive Protein Sorting," *Current Biology*, vol. 26, pp. 2697–2706, 2016.

[305] S. L. Freedman, C. Suarez, J. D. Winkelman, D. R. Kovar, G. A. Voth, A. R. Dinner, and G. M. Hocky, "Mechanical and kinetic factors drive sorting of F-actin cross-linkers on bundles," *PNAS*, vol. 116, no. 33, pp. 16192–16197, 2019.

[306] M. Lenz, "Reversal of contractility as a signature of self-organization in cytoskeletal bundles," *eLife*, vol. 9, p. e51751, 2020.

[307] D. B. Allan, T. Caswell, N. C. Keim, C. M. van der Wel, and R. W. Verweij, "Trackpy v0.5.0," 2021.

[308] J. Crocker and D. Grier, "Methods of Digital Video Microscopy for Colloidal Studies | Elsevier Enhanced Reader," *Journal of Colloid and Interface Science*, vol. 179, pp. 298–310, 1996.

[309] B. Liu, B. Poolman, and A. J. Boersma, "Ionic Strength Sensing in Living Cells," *ACS Chemical BIology*, vol. 12, pp. 2510–2514, 2017.

[310] J. I. Lehtimäki, A. M. Fenix, T. M. Kotila, G. Balistreri, L. Paavolainen, M. Varjosalo, D. T. Burnette, and P. Lappalainen, "UNC-45a promotes myosin folding and stress fiber assembly," *Journal of Cell Biology*, vol. 216, no. 12, pp. 4053–4072, 2017.

[311] S. Lechuga, A. X. Cartagena-Rivera, A. Khan, B. I. Crawford, V. Narayana, D. E. Conway, J. I. Lehtimäki, P. Lappalainen, F. Rieder, M. S. Longworth, and A. I. Ivanov, "A myosin chaperone , UNC- 45A , is a novel regulator of intestinal epithelial barrier integrity and repair," *The FASEB Journal*, vol. 36, p. e22290, 2022.

[312] P. Ecsedi, N. Billington, G. Palfy, G. Gogl, B. Kiss, E. Bulyaki, A. Bodor, J. R. Sellers, and L. Nyitray, "Multiple S100 protein isoforms and C-terminal phosphorylation contribute to the paralog-selective regulation of nonmuscle myosin 2 filaments," *Journal of Cell Biologyl*, vol. 293, no. 38, pp. 14850–14867, 2018.

[313] R. Craig, R. Padrón, and J. Kendrick-Jones, "Structural changes accompanying phosphorylation of tarantula musclemyosin filaments," *Journal of Cell Biology*, vol. 105, pp. 1319–1327, 1987.

[314] S. Hu, K. Dasbiswas, Z. Guo, Y. H. Tee, V. Thiagarajan, P. Hersen, T. L. Chew, S. A. Safran, R. Zaidel-Bar, and A. D. Bershadsky, "Long-range self-organization of cytoskeletal myosin II filament stacks," *Nature Cell Biology*, vol. 19, no. 2, pp. 133–141, 2017.

[315] A. E. Brown, A. Hategan, D. Safer, Y. E. Goldman, and D. E. Discher, "Cross-correlated TIRF/AFM reveals asymmetric distribution of force-generating heads along self-assembled, "synthetic" myosin filaments," *Biophysical Journal*, vol. 96, pp. 1952–1960, 2009.

[316] M. M. Claessens, C. Semmrich, L. Ramos, and A. R. Bausch, "Helical twist controls the thickness of F-actin bundles," *PNAS*, vol. 105, no. 26, pp. 8819–8822, 2008.

[317] D. Sept, J. Xu, T. D. Pollard, and J. A. McCammon, "Annealing accounts for the length of actin filaments formed by spontaneous polymerization," *Biophysical Journal*, vol. 77, pp. 2911–2919, 1999.

[318] K. Matsuda, M. Sugawa, M. Yamagishi, N. Kodera, and J. Yajima, "Visualizing dynamic actin cross-linking processes driven by the actin-binding protein anillin," *FEBS Letters*, vol. 594, pp. 1237–1247, 2020.

[319] L. Haviv, N. S. Gov, Y. Ideses, and A. Bernheim-Groswasser, "Thickness distribution of actin bundles in vitro," *European Biophysics Journal*, vol. 37, pp. 447–454, 2008.

[320] B. Barua, A. Nagy, J. R. Sellers, and S. E. Hitchcock-Degregori, "Regulation of non-muscle myosin II by tropomyosin," *Biochemistry*, vol. 53, pp. 4015–4024, 2014.

[321] T. Q. Uyeda, S. J. Kron, and J. A. Spudich, "Myosin step size. Estimation from slow sliding movement of actin over low densities of heavy meromyosin," *Journal of Molecular Biology*, vol. 214, pp. 699–710, 1990.

[322] K. I. Okazaki, T. Sato, and M. Takano, "Temperature-enhanced association of proteins due to electrostatic interaction: A coarse-grained simulation of actin-myosin binding," *Journal of the American Chemical Society*, vol. 134, pp. 8918–8925, 2012.

[323] S. K. Vogel, Z. Petrasek, F. Heinemann, and P. Schwille, "Myosin motors fragment and compact membrane-bound actin filaments," *eLife*, vol. 2, p. e00116, 2013.

[324] G. Cuda, E. Pate, R. Cooke, and J. R. Sellers, "In vitro actin filament sliding velocities produced by mixtures of different types of myosin," *Biophysical Journal*, vol. 72, pp. 1767–1779, 1997.

[325] J. R. Sellers, "In vitro motility assay to study translocation of actin by myosin," in *Current Protocols in Cell Biology*, pp. 13.2.1–13.2.10, Wiley, 1998.

[326] A. M. Fenix and D. T. Burnette, "Assembly of myosin-II filament arrays: network contraction vs. expansion," *Cytoskeleton*, vol. 75, no. 12, pp. 545–549, 2018.

[327] L. S. Mosby, M. Polin, and D. V. Köster, "A Python based automated tracking routine for myosin II filaments," *Journal of Physics D: Applied Physics*, vol. 53, p. 304002, 2020.

[328] S. S. Margossian and S. Lowey, "Preparation of myosin and its subfragments from rabbit skeletal muscle," in *Methods in Enzymology*, vol. 85, ch. 7, pp. 55–71, Academic Press Inc., 1982.

[329] J. Alvarado and G. H. Koenderink, "Reconstituting cytoskeletal contraction events with biomimetic actin-myosin active gels," in *Methods in Cell Biology*, vol. 128, pp. 83–103, Elsevier Inc., 2015.

[330] M. A. Rahman, A. Salhotra, and A. Månsson, "Comparative analysis of widely used methods to remove nonfunctional myosin heads for the in vitro motility assay," *Journal of Muscle Research and Cell Motility*, vol. 39, pp. 175–187, 2019.

[331] O. E. Technologies, "baculoCOMPLETE: a laboratory guide to the Baculovirus Expression System and Insect Cell Culture," tech. rep., 2019.

[332] S. Shekhar and M. F. Carlier, "Enhanced depolymerization of actin filaments by ADF/cofilin and monomer funneling by capping protein cooperate to accelerate barbed-end growth," *Current Biology*, vol. 27, pp. 1–9, 2017.

[333] J. Xu, W. H. Schwarz, J. A. Käs, T. P. Stossel, P. A. Janmey, and T. D. Pollard, "Mechanical properties of actin filament networks depend on preparation, polymerization conditions, and storage of actin monomers," *Biophysical Journal*, vol. 74, pp. 2731–2740, 1998.

[334] T. A. Burke, A. J. Harker, R. Dominguez, and D. R. Kovar, "The bacterial virulence factors VopL and VopF nucleate actin from the pointed end," *Journal of Cell Biology*, vol. 216, no. 5, pp. 1267–1276, 2017.

[335] B. S. Gentry, S. Van Der Meulen, P. Noguera, B. Alonso-Latorre, J. Plastino, and G. H. Koenderink, "Multiple actin binding domains of Ena/VASP proteins determine actin network stiffening," *European Biophysics Journal*, vol. 41, pp. 979–990, 2012.

[336] G. van Rossum and F. L. Drake, *Python 3 Reference Manual*. Scotts Valley, CA: CreateSpace, 2009.

[337] T. pandas development Team, "pandas-dev/pandas: Pandas," 2020.

[338] W. McKinney, "Data structures for statistical computing in python," in *Proceedings of the 9th Python in Science Conference* (S. van der Walt and J. Millman, eds.), pp. 56–61, 2010.

[339] F. Pedregosa, G. Varoquaux, A. Gramfort, V. Michel, B. Thirion, O. Grisel, M. Blondel, P. Prettenhofer, R. Weiss, V. Dubourg, J. Vanderplas, A. Passos, D. Cournapeau, M. Brucher, M. Perrot, and E. Duchesnay, "Scikit-learn: machine learning in python," *Jorunal of Machine Learning Research*, vol. 12, pp. 2825–2830, 2011.

[340] J. Schindelin, I. Arganda-Carreras, E. Frise, V. Kaynig, M. Longair, T. Pietzsch, S. Preibisch, C. Rueden, S. Saalfeld, B. Schmid, J. Y. Tinevez, D. J. White, V. Hartenstein, K. Eliceiri, P. Tomancak, and A. Cardona, "Fiji: An open-source platform for biological-image analysis," *Nature Methods*, vol. 9, no. 7, pp. 676–682, 2012.

[341] S. Preibisch, S. Saalfeld, J. Schindelin, and P. Tomancak, "Software for bead-based registration of selective plane illumination microscopy data," *Nature Methods*, vol. 7, no. 6, pp. 418–419, 2010.

[342] M. Fritzsche, R. Thorogate, and G. Charras, "Quantitative analysis of ezrin turnover dynamics in the actin cortex," *Biophysical Journal*, vol. 106, pp. 343–353, 2014.

[343] L. Blanchoin, K. J. Amann, H. N. Higgs, J. B. Marchand, D. A. Kaiser, and T. D. Pollard, "Direct observation of dendritic actin filament networks nucleated by Arp2/3 complex and WASP/Scar proteins," *Nature*, vol. 404, no. 6781, pp. 1007–1011, 2000.

[344] V. Achard, J. L. Martiel, A. Michelot, C. Guérin, A. C. Reymann, L. Blanchoin, and R. Boujemaa-Paterski, "A "Primer"-Based Mechanism Underlies Branched Actin Filament Network Formation and Motility," *Current Biology*, vol. 20, pp. 423–428, 2010.

[345] E. G. Fedorov and T. Shemesh, "Physical Model for Stabilization and Repair of Trans-endothelial Apertures," *Biophysical Journal*, vol. 112, pp. 388–397, 2017.

[346] M. Clarke, U. Engel, J. Giorgione, A. Müller-Taubenberger, J. Prassler, D. Veltman, and G. Gerisch, "Curvature recognition and force generation in phagocytosis," *BMC Biology*, vol. 8, p. 154, 2010.

[347] T. Chen, A. Callan-Jones, E. Fedorov, A. Ravasio, A. Brugués, H. T. Ong, Y. Toyama, B. C. Low, X. Trepat, T. Shemesh, R. Voituriez, and B. Ladoux, "Large-scale curvature sensing by directional actin flow drives cellular migration mode switching," *Nature Physics*, vol. 15, pp. 393–402, 2019.

[348] H. R. Thiam, P. Vargas, N. Carpi, C. L. Crespo, M. Raab, E. Terriac, M. C. King, J. Jacobelli, A. S. Alberts, T. Stradal, A. M. Lennon-Dumenil, and M. Piel, "Perinuclear Arp2/3-driven actin polymerization enables nuclear deformation to facilitate cell migration through complex environments," *Nature Communications*, vol. 7, p. 10997, 2016.

[349] B. J. Peter, H. M. Kent, I. G. Mills, Y. Vallis, P. J. G. Butler, P. R. Evans, and H. T. McMahon, "BAR domains as sensors of membrane curvature: The amphiphysin BAR structure," *Science*, vol. 303, pp. 495–499, 2004.

[350] K. Tsujita, S. Suetsugu, N. Sasaki, M. Furutani, T. Oikawa, and T. Takenawa, "Coordination between the actin cytoskeleton and membrane deformation by a novel membrane tubulation domain of PCH proteins is involved in endocytosis," *Journal of Cell Biology*, vol. 172, no. 2, pp. 269–279, 2006.

[351] P. J. Carman and R. Dominguez, "BAR domain proteins—a linkage between cellular membranes, signaling pathways, and the actin cytoskeleton," *Biophysical Reviews*, vol. 10, pp. 1587–1604, 2018.

[352] C. Simon, R. R. Kusters, V. Caorsi, A. Allard, M. Abou-Ghali, J. Manzi, A. Di Cicco, D. Lévy, M. Lenz, J.-F. F. Joanny, C. C. Campillo, J. Plastino, P. Sens, C. Sykes, A. D.

Cicco, D. Levy, M. Lenz, J.-F. F. Joanny, C. C. Campillo, J. Plastino, P. Sens, and C. Sykes, "Actin dynamics drive cell-like membrane deformation," *Nature Physics*, vol. 15, pp. 602–609, 2019.

[353] G. Fläschner, C. I. Roman, N. Strohmeyer, D. Martinez-Martin, and D. J. Müller, "Rheology of rounded mammalian cells over continuous high-frequencies," *Nature Communications*, vol. 12, p. 2922, 2021.

[354] R. Maan, E. Loiseau, and A. R. Bausch, "Article Adhesion of Active Cytoskeletal Vesicles," *Biophysical Journal*, vol. 115, pp. 2395–2402, 2018.

[355] J. P. Reeves and R. M. Dowben, "Formation and properties of thin-walled phospholipid vesicles," *Journal of Cellular Physiology*, vol. 73, pp. 49–60, 1969.

[356] P. Walde, K. Cosentino, H. Engel, and P. Stano, "Giant Vesicles: Preparations and Applications," *ChemBioChem*, vol. 11, pp. 848–865, 2010.

[357] K. S. Horger, D. J. Estes, R. Capone, and M. Mayer, "Films of agarose enable rapid formation of giant liposomes in solutions of physiologic ionic strength," *Journal of the American Chemical Society*, vol. 131, pp. 1810–1819, 2009.

[358] N. López Mora, J. S. Hansen, Y. Gao, A. A. Ronald, R. Kieltyka, N. Malmstadt, and A. Kros, "Preparation of size tunable giant vesicles from cross-linked dextran(ethylene glycol) hydrogels," *Chemical Communications*, vol. 50, pp. 1953–1955, 2014.

[359] J. Pazzi, M. Xu, and A. B. Subramaniam, "Size distributions and yields of giant vesicles assembled on cellulose papers and cotton fabric," *Langmuir*, vol. 35, pp. 7798–7804, 2019.

[360] M. I. Angelova and D. S. Dimitrov, "Liposome Electro formation," *Faraday Discussions of the Chemical Society*, vol. 81, pp. 303–311, 1986.

[361] L. R. Montes, A. Alonso, F. M. Goñi, and L. A. Bagatolli, "Giant unilamellar vesicles electroformed from native membranes and organic lipid mixtures under physiological conditions," *Biophysical Journal*, vol. 93, pp. 3548–3554, 2007.

[362] T. Pott, H. Bouvrais, and P. Méléard, "Giant unilamellar vesicle formation under physiologically relevant conditions," *Chemistry and Physics of Lipids*, vol. 154, pp. 115–119, 2008.

[363] M. Weiss, J. P. Frohnmayer, L. T. Benk, B. Haller, J. W. Janiesch, T. Heitkamp, M. Börsch, R. B. Lira, R. Dimova, R. Lipowsky, E. Bodenschatz, J. C. Baret, T. Vidakovic-Koch, K. Sundmacher, I. Platzman, and J. P. Spatz, "Sequential bottom-up assembly of mechanically stabilized synthetic cells by microfluidics," *Nature Materials*, vol. 17, pp. 89–95, 2018.

[364] A. R. Abate, T. Hung, P. Marya, J. J. Agresti, and D. A. Weitz, "High-throughput injection with microfluidics using picoinjectors using picoinjectors," *PNAS*, vol. 107, no. 45, pp. 19163–19166, 2010.

[365] S. Pautot, B. J. Frisken, and D. A. Weitz, "Production of unilamellar vesicles using an inverted emulsion," *Langmuir*, vol. 19, pp. 2870–2879, 2003.

[366] S. Deshpande and C. Dekker, "On-chip microfluidic production of cell-sized liposomes," *Nature Protocols*, vol. 13, pp. 856–874, 2018.

[367] N. Yandrapalli, J. Petit, O. Bäumchen, and T. Robinson, "Surfactant-free production of biomimetic giant unilamellar vesicles using PDMS-based microfluidics," *Communications Chemistry*, vol. 4, p. 100, 2021.

[368] R. Tivony, M. Fletcher, K. Al Nahas, and U. F. Keyser, "A microfluidic platform for sequential assembly and separation of synthetic cell models," *ACS Synthetic Biology*, vol. 10, pp. 3105–3116, 2021.

[369] N. N. Deng, M. Yelleswarapu, and W. T. Huck, "Monodisperse Uni- and Multicompartment Liposomes," *Journal of the American Chemical Society*, vol. 138, pp. 7584–7591, 2016.

[370] M. Abkarian, E. Loiseau, and G. Massiera, "Continuous droplet interface crossing encapsulation (cDICE) for high throughput monodisperse vesicle design," *Soft Matter*, vol. 7, pp. 4610–4614, 2011.

[371] C. Claudet, M. In, and G. Massiera, "Method to disperse lipids as aggregates in oil for bilayers production," *European Physical Journal E*, vol. 39, p. 9, 2016.

[372] K. Göpfrich, B. Haller, O. Staufer, Y. Dreher, U. Mersdorf, I. Platzman, and J. P. Spatz, "One-pot assembly of complex giant unilamellar vesicle-based synthetic cells," *ACS Synthetic Biology*, vol. 8, pp. 937–947, 2019.

[373] A. Moga, N. Yandrapalli, R. Dimova, and T. Robinson, "Optimization of the Inverted Emulsion Method for High-Yield Production of Biomimetic Giant Unilamellar Vesicles," *ChemBioChem*, vol. 20, pp. 2674–2682, 2019.

[374] T. Luo, V. Srivastava, Y. Ren, and D. N. Robinson, "Mimicking the mechanical properties of the cell cortex by the self-assembly of an actin cortex in vesicles," *Applied Physics Letters*, vol. 104, p. 153701, 2014.

[375] J. Deek, R. Maan, E. Loiseau, and A. R. Bausch, "Reconstitution of composite actin and keratin networks in vesicles," *Soft Matter*, vol. 14, pp. 1897–1902, 2018.

[376] C. Egile, T. P. Loisel, V. Laurent, R. Li, D. Pantaloni, P. J. Sansonetti, and M.-f. Carlier, "Protein promotes actin nucleation by Arp2/3 complex and bacterial actin-based motility," *Journal of Cell Biology*, vol. 146, no. 6, pp. 1319–1332, 1999.

[377] F. Jülicher and R. Lipowsky, "Domain-induced budding of vesicles," *Physical Review Letters*, vol. 70, no. 19, pp. 2964–2967, 1993.

[378] F. Julicher and R. Lipowsky, "Shape transformations," *Physical Review E*, vol. 53, no. 3, pp. 2670–2683, 1996.

[379] T. Baumgart, S. T. Hess, and W. W. Webb, "Imaging coexisting fluid domains in biomembrane models coupling curvature and line tension," *Nature*, vol. 425, pp. 821–824, 2003.

[380] J. M. Allain and M. Ben Amar, "Budding and fission of a multiphase vesicle," *European Physical Journal E*, vol. 20, pp. 409–420, 2006.

[381] H. Yamaguchi, H. Miki, S. Suetsugu, L. Ma, M. W. Kirschner, and T. Takenawa, "Two tandem verprolin homology domains are necessary for a strong activation of Arp2/3 complex-induced actin polymerization and induction of microspike formation by N-WASP," *PNAS*, vol. 97, no. 23, pp. 12631–12636, 2000.

[382] K. Guevorkian and J. L. Maître, "Micropipette aspiration: A unique tool for exploring cell and tissue mechanics in vivo," in *Methods in Cell Biology*, vol. 139, pp. 187–201, Elsevier Inc., 2017.

[383] M. Rinaldin, P. Fonda, L. Giomi, and D. J. Kraft, "Geometric pinning and antimixing in scaffolded lipid vesicles," *Nature Communications*, vol. 11, p. 4314, 2020.

[384] F. Y. Chan, A. M. Silva, J. Saramago, J. Pereira-Sousa, H. E. Brighton, M. Pereira, K. Oegema, R. Gassmann, and A. X. Carvalho, "The ARP2/3 complex prevents excessive formin activity during cytokinesis," *Molecular Biology of the Cell*, vol. 30, pp. 96–107, 2019.

[385] B. Zhu, Q. Lu, J. Yin, J. Hu, and Z. Wang, "Alignment of osteoblast-like cells and cell-produced collagen matrix induced by nanogrooves," *Tissue Engineering*, vol. 11, no. 5, pp. 825–834, 2005.

[386] M. Galic, S. Jeong, F. C. Tsai, L. M. Joubert, Y. I. Wu, K. M. Hahn, Y. Cui, and T. Meyer, "External push and internal pull forces recruit curvature-sensing N-BAR domain proteins to the plasma membrane," *Nature Cell Biology*, vol. 14, pp. 874–881, 2012.

[387] C. E. Aitken, R. A. Marshall, and J. D. Puglisi, "An oxygen scavenging system for improvement of dye stability in single-molecule fluorescence experiments," *Biophysical Journal*, vol. 94, pp. 1826–1835, 2008.

[388] M. M. Claessens, F. A. Leermakers, F. A. Hoekstra, and M. A. Stuart, "Osmotic shrinkage and reswelling of giant vesicles composed of dioleoylphosphatidylglycerol and cholesterol," *Biochimica et Biophysica Acta*, vol. 1778, pp. 890–895, 2008.

[389] L. van Buren, G. H. Koenderink, and C. Martinez-Torres, "DisGUVery: a versatile open-source software for high-throughput image analysis of Giant Unilamellar Vesicles," *bioRxiv*, p. 2022.01.25.477663, 2022.

[390] H. Mary and G. J. Brouhard, "Kappa (κ): Analysis of Curvature in Biological Image Data using B-splines," *bioRxiv*, p. 852772, 2019.

[391] T. Baumgart, S. Das, W. W. Webb, and J. T. Jenkins, "Membrane elasticity in giant vesicles with fluid phase coexistence," *Biophysical Journal*, vol. 89, pp. 1067–1080, 2005.

[392] S. G. Baldursdottir, M. S. Fullerton, S. H. Nielsen, and L. Jorgensen, "Adsorption of proteins at the oil/water interface-Observation of protein adsorption by interfacial shear stress measurements," *Colloids and Surfaces B: Biointerfaces*, vol. 79, pp. 41–46, 2010.

[393] V. Mitropoulos, A. Mütze, and P. Fischer, "Mechanical properties of protein adsorption layers at the air/water and oil/water interface: A comparison in light of the thermodynamical stability of proteins," *Advances in Colloid and Interface Science*, vol. 206, pp. 195–206, 2014.

[394] L. Hobley, A. Ostrowski, F. V. Rao, K. M. Bromley, M. Porter, A. R. Prescott, C. E. MacPhee, D. M. Van Aalten, and N. R. Stanley-Wall, "BslA is a self-assembling bacterial hydrophobin that coats the Bacillus subtilis biofilm," *PNAS*, vol. 110, no. 33, pp. 13600–13605, 2013.

[395] K. M. Bromley and C. E. Macphee, "BslA-stabilized emulsion droplets with designed microstructure," *Interface Focus*, vol. 7, p. 20160124, 2017.

[396] C. Gicquaud, J. P. Chauvet, G. Grenier, P. Tancrède, and G. Coulombe, "Adsorption of actin at the air-water interface: A monolayer study," *Biopolymers*, vol. 70, pp. 289–296, 2003.

[397] C. Gicquaud, J. P. Chauvet, and P. Tancrède, "Surface film pressure of actin: Interactions with lipids in mixed monolayers," *Biochemical and Biophysical Research Communications*, vol. 308, no. 4, pp. 995–1000, 2003.

[398] S. A. Vitale and J. L. Katz, "Liquid droplet dispersions formed by homogeneous liquid-liquid nucleation: "The ouzo effect"," *Langmuir*, vol. 19, pp. 4105–4110, 2003.

[399] K. J. Vendel, C. Alkemade, N. Andrea, G. H. Koenderink, and M. Dogterom, "In vitro reconstitution of dynamic co-organization of microtubules and actin filaments in emulsion droplets," in *Methods in Molecular Biology* (M. Helder, ed.), vol. 2101, ch. 5, pp. 53–75, Humana Press, 2020.

[400] S. Tcholakova, N. D. Denkov, and T. Banner, "Role of surfactant type and concentration for the mean drop size during emulsification in turbulent flow," *Langmuir*, vol. 20, pp. 7444–7458, 2004.

[401] H. Wioland, B. Guichard, Y. Senju, S. Myram, P. Lappalainen, A. Jégou, and G. Romet-Lemonne, "ADF/Cofilin accelerates actin dynamics by severing filaments and promoting their depolymerization at both ends," *Current Biology*, vol. 27, no. 13, pp. 1956–1967.e7, 2017.

[402] U. Lindberg, C. E. Schutt, E. Hellsten, A. C. Tjäder, and T. Hult, "The use of poly(L-proline)-Sepharose in the isolation of profilin and profilactin complexes," *BBA - General Subjects*, vol. 967, pp. 391–400, 1988.

[403] A. Weinberger, F. C. Tsai, G. H. Koenderink, T. F. Schmidt, R. Itri, W. Meier, T. Schmatko, A. Schröder, and C. Marques, "Gel-assisted formation of giant unilamellar vesicles," *Biophysical Journal*, vol. 105, pp. 154–164, 2013.

[404] J. A. Cooper, S. B. Walker, and T. D. Pollard, "Pyrene actin: documentation of the validity of a sensitive assay for actin polymerization," *Journal of Muscle Research and Cell Motility*, vol. 4, pp. 253–262, 1983.

[405] L. K. Doolittle, M. K. Rosen, and S. B. Padrick, "Measurement and analysis of in vitro actin polymerization," in *Methods in Molecular Biology* (A. S. Coutts, ed.), vol. 1046, pp. 273–293, Springer Science and Business Media LLC, 2013.

[406] J. Widengren and R. Rigler, "Fluorescence correlation spectroscopy of triplet states in solution: a theoretical and experimental study," *Journal of Physical Chemistry*, vol. 99, pp. 13368–13379, 1995.

[407] E. P. Petrov, T. Ohrt, R. G. Winkler, and P. Schwille, "Diffusion and segmental dynamics of double-stranded DNA," *Physical Review Letters*, vol. 97, p. 258101, 2006.

[408] L. Cao, F. Ghasemi, M. Way, A. Jégou, and G. Romet-lemonne, "Nucleation and stability of branched versus linear Arp2/3-generated actin filaments," *biorxiv preprint*, pp. 1–21, 2022.

[409] V. Laplaud, N. Levernier, J. Pineau, M. San Roman, L. Barbier, P. J. S ez, A. M. Lennon-Dum nil, P. Vargas, K. Kruse, O. D. Roure, M. Piel, and J. Heuvingh, "Pinching the cortex of live cells reveals thickness instabilities caused by myosin II motors," *Science Advances*, vol. 7, no. 27, p. eabe3640, 2021.

[410] A. Mogilner and B. Rubinstein, "The physics of filopodial protrusion," *Biophysical Journal*, vol. 89, pp. 782–795, 2005.

[411] D. Vignjevic, S. I. Kojima, Y. Aratyn, O. Danciu, T. Svitkina, and G. G. Borisy, "Role of fascin in filopodial protrusion," *Journal of Cell Biology*, vol. 174, no. 6, pp. 863–875, 2006.

[412] G. Sekerková, L. Zheng, P. A. Loomis, E. Mugnaini, and J. R. Bartles, "Espins and the actin cytoskeleton of hair cell stereocilia and sensory cell microvilli," *Cellular and Molecular Life Sciences*, vol. 63, pp. 2329–2341, 2006.

[413] T. M. Svitkina, E. A. Bulanova, O. Y. Chaga, D. M. Vignjevic, S. ichiro Kojima, J. M. Vasiliev, and G. G. Borisy, "Mechanism of filopodia initiation by reorganization of a dendritic network," *Journal of Cell Biology*, vol. 160, no. 3, pp. 409–421, 2003.

[414] C. Yang, L. Czech, S. Gerboth, S. I. Kojima, G. Scita, and T. Svitkina, "Novel roles of formin mDia2 in lamellipodia and filopodia formation in motile cells," *PLoS Biology*, vol. 5, no. 11, pp. 2624–2645, 2007.

[415] A. B. Bohil, B. W. Robertson, and R. E. Cheney, "Myosin-X is a molecular motor that functions in filopodia formation," *PNAS*, vol. 103, no. 33, pp. 12411–12416, 2006.

[416] L. Haviv, Y. Brill-Karniely, R. Mahaffy, F. Backouche, A. Ben-Shaul, T. D. Pollard, and A. Bernheim-Groswasser, "Reconstitution of the transition from lamellipodium to filopodium in a membrane-free system," *PNAS*, vol. 103, no. 13, pp. 4906–4911, 2006.

[417] A. Upadhyaya, J. R. Chabot, A. Andreeva, A. Samadani, and A. Van Oudenaarden, "Probing polymerization forces by using actin-propelled lipid vesicles," *PNAS*, vol. 100, no. 8, pp. 4521–4526, 2003.

[418] G. Salbreux, G. T. Charras, and E. K. Paluch, "Actin cortex mechanics and cellular morphogenesis," *Trends in Cell Biology*, vol. 22, no. 10, pp. 536–545, 2012.

[419] C. Wu, S. B. Asokan, M. E. Berginski, E. M. Haynes, N. E. Sharpless, J. D. Griffith, S. M. Gomez, and J. E. Bear, "Arp2/3 is critical for lamellipodia and response to extracellular matrix cues but is dispensable for chemotaxis," *Cell*, vol. 148, pp. 973–987, 2012.

[420] D. Raz-Ben Aroush, N. Ofer, E. Abu-Shah, J. Allard, O. Krichevsky, A. Mogilner, and K. Keren, "Actin turnover in lamellipodial fragments," *Current Biology*, vol. 27, pp. 2963–2973, 2017.

[421] L. Baldauf, F. Frey, M. A. Perez, T. Idema, and G. H. Koenderink, "Reconstituted branched actin networks sense and generate micron-scale membrane curvature," *biorxiv preprint*, p. 2022.08.31.505969, 2022.

[422] S. Suetsugu, "Activation of nucleation promoting factors for directional actin filament elongation: Allosteric regulation and multimerization on the membrane," *Seminars in Cell and Developmental Biology*, vol. 24, pp. 267–271, 2013.

[423] P. Echave, I. J. Conlon, and A. C. Lloyd, "Cell size regulation in mammalian cells," *Cell Cycle*, vol. 6, no. 2, pp. 218–224, 2007.

[424] G. Romet-Lemonne and A. Jégou, "The dynamic instability of actin filament barbed ends," *Journal of Cell Biology*, vol. 220, no. 4, p. e202102020, 2021.

[425] U. Seifert, K. Berndl, and R. Lipowsky, "Shape transformation of vesicles: Phase diagram for spontaneous-curvature and bilayer-coupling models," *Physical Review A*, vol. 44, no. 2, pp. 1182–1202, 1991.

[426] T. Vignaud, C. Copos, C. Leterrier, M. Toro-Nahuelpan, Q. Tseng, J. Mahamid, L. Blanchoin, A. Mogilner, M. Théry, and L. Kurzawa, "Stress fibres are embedded in a contractile cortical network," *Nature Materials*, vol. 20, pp. 410–420, 2021.

[427] M. Mayer, M. Depken, J. S. Bois, F. Jülicher, and S. W. Grill, "Anisotropies in cortical tension reveal the physical basis of polarizing cortical flows," *Nature*, vol. 467, pp. 617–621, 2010.

[428] C. Guillot and T. Lecuit, "Adhesion disengagement uncouples intrinsic and extrinsic forces to drive cytokinesis in epithelial tissues," *Developmental Cell*, vol. 24, pp. 227–241, 2013.

[429] P. Sampath and T. D. Pollard, "Effects of cytochalasin, phalloidin, and pH on the elongation of actin filaments," *Biochemistry*, vol. 30, pp. 1973–1980, 1991.

[430] J. Steinkühler, P. De Tillieux, R. L. Knorr, R. Lipowsky, and R. Dimova, "Charged giant unilamellar vesicles prepared by electroformation exhibit nanotubes and transbilayer lipid asymmetry," *Scientific Reports*, vol. 8, p. 11838, 2018.

[431] N. S. Gov, "Dynamics and morphology of microvilli driven by actin polymerization," *Physical Review Letters*, vol. 97, p. 018101, 2006.

[432] N. S. Gov and A. Gopinathan, "Dynamics of membranes driven by actin polymerization," *Biophysical Journal*, vol. 90, pp. 454–469, 2006.

[433] R. D. Mullins, P. Bieling, and D. A. Fletcher, "From solution to surface to filament: actin flux into branched networks," *Biophysical Reviews*, vol. 10, pp. 1537–1551, 2018.

[434] S. Ghosh, S. Gutti, and D. Chaudhuri, "Pattern formation, pulsation and traveling wave on active spherical membranes," *Soft Matter*, vol. 47, pp. 10583–10778, 2021.

[435] C. Co, D. T. Wong, S. Gierke, V. Chang, and J. Taunton, "Mechanism of actin network attachment to moving membranes: Barbed end capture by N-WASP WH2 domains," *Cell*, vol. 128, pp. 901–913, 2007.

[436] I. Weisswange, T. P. Newsome, S. Schleich, and M. Way, "The rate of N-WASP exchange limits the extent of ARP2/3-complex-dependent actin-based motility," *Nature*, vol. 458, pp. 87–91, 2009.

[437] N. Selve and A. Wegner, "Rate of treadmilling of actin filaments in vitro," *Journal of Molecular Biology*, vol. 187, pp. 627–631, 1986.

[438] A. E. Carlsson, "The effect of branching on the critical concentration and average filament length of actin," *Biophysical Journal*, vol. 89, pp. 130–140, 2005.

[439] J. Rosenblatt, B. J. Agnew, H. Abe, J. R. Bamburg, and T. J. Mitchison, "Xenopus actin depolymerizing factor/cofilin (XAC) is responsible for the turnover of actin filaments in Listeria monocytogenes tails," *Journal of Cell Biology*, vol. 136, no. 6, pp. 1323–1332, 1997.

[440] C. Galloni, D. Carra, J. V. Abella, S. Kjær, P. Singaravelu, D. J. Barry, N. Kogata, C. Guérin, L. Blanchoin, and M. Way, "MICAL2 enhances branched actin network disassembly by oxidizing arp3b-containing arp2/3 complexes," *Journal of Cell Biology*, vol. 220, no. 8, p. e202102043, 2021.

[441] A. M. Weaver, A. V. Karginov, A. W. Kinley, S. A. Weed, Y. Li, J. T. Parsons, and J. A. Cooper, "Cortactin promotes and stabilizes Arp2/3-induced actin filament network formation," *Current Biology*, vol. 11, pp. 370–374, 2001.

[442] L. Song, M. R. Hobaugh, C. Shustak, S. Celey, H. Bayley, and J. E. Gouaux, "Structure of staphylococcal a-hemolysin, a heptameric transmembrane pore," *Science*, vol. 274, pp. 1859–1866, 1996.

[443] A. Rørvig-Lund, A. Bahadori, S. Semsey, P. M. Bendix, and L. B. Oddershede, "Vesicle fusion triggered by optically heated gold nanoparticles," *Nano Letters*, vol. 15, pp. 4183–4188, 2015.

[444] T. Wittmann, A. Dema, and J. van Haren, "Lights, cytoskeleton, action: Optogenetic control of cell dynamics," *Current Opinion in Cell Biology*, vol. 66, pp. 1–10, 2020.

[445] N. Leijnse, Y. F. Barooji, M. R. Arastoo, S. L. Sønder, B. Verhagen, L. Wullkopf, J. T. Erler, S. Semsey, J. Nylandsted, L. B. Oddershede, A. Doostmohammadi, and P. M. Bendix, "Filopodia rotate and coil by actively generating twist in their actin shaft," *Nature Communications*, vol. 13, p. 1636, 2022.

[446] A. P. Liu, D. L. Richmond, L. Maibaum, S. Pronk, P. L. Geissler, and D. A. Fletcher, "Membrane-induced bundling of actinfilaments," *Nature Physics*, vol. 4, pp. 789–793, 2008.

[447] J. Weichsel and P. L. Geissler, "The more the tubular: Dynamic bundling of actin filaments for membrane tube formation," *PLoS Computational Biology*, vol. 12, no. 7, p. e1004982, 2016.

[448] A. Mallavarapu and T. Mitchison, "Regulated actin cytoskeleton assembly at filopodium tips controls their extension and retraction," *Journal of Cell Biology*, vol. 146, no. 5, pp. 1097–1106, 1999.

[449] L. Trichet, C. Sykes, and J. Plastino, "Relaxing the actin cytoskeleton for adhesion and movement with Ena/VASP," *Journal of Cell Biology*, vol. 181, no. 1, pp. 19–25, 2008.

[450] P. Bieling, S. D. Hansen, O. Akin, T. Li, C. C. Hayden, D. A. Fletcher, and R. D. Mullins, "WH2 and proline-rich domains of WASP-family proteins collaborate to accelerate actin filament elongation," *The EMBO Journal*, p. e201797039, 2017.

[451] B. A. Smith, K. Daugherty-Clarke, B. L. Goode, and J. Gelles, "Pathway of actin filament branch formation by Arp2/3 complex revealed by single-molecule imaging," *PNAS*, vol. 110, no. 4, pp. 1285–1290, 2013.

[452] A. Y. Pollitt and R. H. Insall, "WASP and SCAR/WAVE proteins: The drivers of actin assembly," *Journal of Cell Science*, vol. 122, no. 15, pp. 2575–2578, 2009.

[453] P. Sens, "Stick-slip model for actin-driven cell protrusions, cell polarization, and crawling," *PNAS*, vol. 117, no. 40, pp. 24670–24678, 2020.

[454] J. Neuhold, K. Radakovics, A. Lehner, F. Weissmann, M. Q. Garcia, M. C. Romero, N. S. Berrow, and P. Stolt-Bergner, "GoldenBac: A simple, highly efficient, and widely applicable system for construction of multi-gene expression vectors for use with the baculovirus expression vector system," *BMC Biotechnology*, vol. 20, p. 26, 2020.

[455] K. Miura and J. Schindelin, "Temporal Colorcode," 2018.

[456] H. A. Faizi, C. J. Reeves, V. N. Georgiev, P. M. Vlahovska, and R. Dimova, "Fluctuation spectroscopy of giant unilamellar vesicles using confocal and phase contrast microscopy," *Soft Matter*, vol. 16, pp. 8996–9001, 2020.

[457] M. D. Flanagan and S. Lin, "Cytochalasins block actin filament elongation by binding to high affinity sites associated with F-actin.," *Journal of Biological Chemistry*, vol. 255, no. 3, pp. 835–838, 1980.

[458] P. Forscher and S. J. Smith, "Actions of cytochalasins on the organization of actin filaments and microtubules in a neuronal growth cone.," *The Journal of cell biology*, vol. 107, pp. 1505–1516, 1988.

[459] E. Bailoni and B. Poolman, "ATP Recycling Fuels Sustainable Glycerol 3-Phosphate Formation in Synthetic Cells Fed by Dynamic Dialysis," *ACS Synthetic Biology*, vol. 11, no. 7, pp. 2348–2360, 2022.

[460] G. Van Meer, D. R. Voelker, and G. W. Feigenson, "Membrane lipids: Where they are and how they behave," *Nature Reviews Molecular Cell Biology*, vol. 9, pp. 112–124, 2008.

[461] Y. Kuruma, P. Stano, T. Ueda, and P. L. Luisi, "A synthetic biology approach to the construction of membrane proteins in semi-synthetic minimal cells," *Biochimica et Biophysica Acta*, vol. 1788, pp. 567–574, 2009.

[462] A. Scott, M. J. Noga, P. De Graaf, I. Westerlaken, E. Yildirim, and C. Danelon, "Cell-free phospholipid biosynthesis by gene-encoded enzymes reconstituted in liposomes," *PLoS ONE*, vol. 11, no. 10, p. e0163058, 2016.

[463] R. Jahn and T. Sudhof, "Membrane Fusion and Exocytosis," *Annual Reviews in Biochemistry*, vol. 68, pp. 863–911, 1999.

[464] R. Jahn, "Principles of exocytosis and membrane fusion," *Annals of the New York Academy of Sciences*, vol. 1014, pp. 170–178, 2004.

[465] T. Y. Yoon, B. Okumus, F. Zhang, Y. K. Shin, and T. Ha, "Multiple intermediates in SNARE-induced membrane fusion," *PNAS*, vol. 103, no. 52, pp. 19731–19736, 2006.

[466] L. V. Chernomordik and M. M. Kozlov, "Mechanics of membrane fusion," *Nature Structural and Molecular Biology*, vol. 15, no. 7, pp. 675–683, 2008.

[467] L. K. Tamm, J. Crane, and V. Kiessling, "Membrane fusion: A structural perspective on the interplay of lipids and proteins," *Current Opinion in Structural Biology*, vol. 13, pp. 453–466, 2003.

[468] S. J. Marrink, A. H. de Vries, and D. P. Tieleman, "Lipids on the move: Simulations of membrane pores, domains, stalks and curves," *Biochimica et Biophysica Acta - Biomembranes*, vol. 1788, pp. 149–168, 2009.

[469] E. I. Pécheur, O. Maier, and D. Hoekstra, "On the mechanism of intracellular membrane fusion: In search of the genuine fusion factor," *Bioscience Reports*, vol. 20, no. 6, pp. 613–631, 2000.

[470] M. Arribas Perez and P. A. Beales, "Biomimetic Curvature and Tension-Driven Membrane Fusion Induced by Silica Nanoparticles," *Langmuir*, vol. 37, pp. 13917–13931, 2021.

[471] B. Van Lengerich, R. J. Rawle, P. M. Bendix, and S. G. Boxer, "Individual vesicle fusion events mediated by lipid-anchored DNA," *Biophysical Journal*, vol. 105, pp. 409–419, 2013.

[472] B. R. Lentz, "PEG as a tool to gain insight into membrane fusion," *European Biophysics Journal*, vol. 36, pp. 315–326, 2007.

[473] J. Wilschut, N. Düzgüneş, R. Fraley, and D. Papahadjopoulos, "Studies on the mechanism of membrane fusion: kinetics of calcium ion induced fusion of phosphatidylserine vesicles followed by a new assay for mixing of aqueous vesicle contents," *Biochemistry*, vol. 19, pp. 6011–6021, 1980.

[474] R. B. Lira, T. Robinson, R. Dimova, and K. A. Riske, "Highly Efficient Protein-free Membrane Fusion: A Giant Vesicle Study," *Biophysical Journal*, vol. 116, pp. 79–91, 2019.

[475] T. Weber, B. V. Zemelman, J. A. McNew, B. Westermann, M. Gmachl, F. Parlati, T. H. Söllner, and J. E. Rothman, "SNAREpins: Minimal machinery for membrane fusion," *Cell*, vol. 92, pp. 759–772, 1998.

[476] G. Stengel, L. Simonsson, R. A. Campbell, and F. Höök, "Determinants for membrane fusion induced by cholesterol-modified DNA zippers," *Journal of Physical Chemistry B*, vol. 112, pp. 8264–8274, 2008.

[477] N. J. Gaut, J. Gomez-Garcia, J. M. Heili, B. Cash, Q. Han, A. E. Engelhart, and K. P. Adamala, "Programmable fusion and differentiation of synthetic minimal cells," *ACS Synthetic Biology*, vol. 11, pp. 855–866, 2022.

[478] K. M. Flavier and S. G. Boxer, "Vesicle fusion mediated by solanesol-anchored DNA," *Biophysical Journal*, vol. 113, pp. 1260–1268, 2017.

[479] G. Stengel, R. Zahn, and F. Höök, "DNA-induced programmable fusion of phospholipid vesicles," *Journal of the American Chemical Society*, vol. 129, pp. 9584–9585, 2007.

[480] I. Pfeiffer and F. Höök, "Quantification of oligonucleotide modifications of small unilamellar lipid vesicles," *Analytical Chemistry*, vol. 78, pp. 7493–7498, 2006.

[481] S. A. Van Der Meulen, G. V. Dubacheva, M. Dogterom, R. P. Richter, and M. E. Leunissen, "Quartz crystal microbalance with dissipation monitoring and spectroscopic ellipsometry measurements of the phospholipid bilayer anchoring stability and kinetics of hydrophobically modified DNA oligonucleotides," *Langmuir*, vol. 30, pp. 6525–6533, 2014.

[482] I. Pfeiffer and F. Höök, "Bivalent cholesterol-based coupling of oligonucletides to lipid membrane assemblies," *Journal of the American Chemical Society*, vol. 126, pp. 10224–10225, 2004.

[483] A. Sonnleitner, G. J. Schütz, and T. Schmidt, "Free Brownian motion of individual lipid molecules in biomembranes," *Biophysical Journal*, vol. 77, pp. 2638–2642, 1999.

[484] M. Przybylo, J. Sýkora, J. Humpolíčová, A. Benda, A. Zan, and M. Hof, "Lipid diffusion in giant unilamellar vesicles is more than 2 times faster than in supported phospholipid bilayers under identical conditions," *Langmuir*, vol. 22, pp. 9096–9099, 2006.

[485] H. P. Wacklin, "Composition and asymmetry in supported membranes formed by vesicle fusion," *Langmuir*, vol. 27, pp. 7698–7707, 2011.

[486] K. Kastl, A. Herrig, E. Lüthgens, A. Janshoff, and C. Steinem, "Scrutiny of annexin A1 mediated membrane-membrane interaction by means of a thickness shear mode resonator and computer simulations," *Langmuir*, vol. 20, pp. 7246–7253, 2004.

[487] T. Porstmann and S. T. Kiessig, "Enzyme immunoassay techniques," *Journal of Immunological Methods*, vol. 150, pp. 5–21, 1992.

[488] R. D. Hills and N. McGlinchey, "Model parameters for simulation of physiological lipids," *Journal of Computational Chemistry*, vol. 37, pp. 1112–1118, 2016.

[489] D. Papahadjopoulos, S. Nir, and S. Ohki, "Permeability properties of phospholipid membranes: Effect of cholesterol and temperature," *Biochimica et Biophysica Acta*, vol. 266, pp. 561–583, 1971.

[490] G. Szabo, "Dual mechanism for the action of cholesterol on membrane permeability," *Nature*, vol. 252, pp. 47–49, 1974.

[491] C. Campillo, P. Sens, D. Köster, L. L. Pontani, D. Lévy, P. Bassereau, P. Nassoy, and C. Sykes, "Unexpected membrane dynamics unveiled by membrane nanotube extrusion," *Biophysical Journal*, vol. 104, no. 6, pp. 1248–1256, 2013.

[492] S. J. Lord, K. B. Velle, R. Dyche Mullins, and L. K. Fritz-Laylin, "SuperPlots: Communicating reproducibility and variability in cell biology," *Journal of Cell Biology*, vol. 219, no. 6, p. e202001064, 2020.

[493] J. Goedhart, "SuperPlotsOfData - A web app for the transparent display and quantitative comparison of continuous data from different conditions," *Molecular Biology of the Cell*, vol. 32, no. 6, pp. 470–474, 2021.

[494] Y. Gong, M. Ma, Y. Luo, and D. Bong, "Functional determinants of a synthetic vesicle fusion system," *Journal of the American Chemical Society*, vol. 130, pp. 6196–6205, 2008.

[495] K. Carvalho, L. Ramos, C. Roy, and C. Picart, "Giant unilamellar vesicles containing phosphatidylinositol(4,5) bisphosphate: Characterization and functionality," *Biophysical Journal*, vol. 95, pp. 4348–4360, 2008.

[496] N. L. Mora, A. L. Boyle, B. J. van Kolck, A. Rossen, Š. Pokorná, A. Koukalová, R. Šachl, M. Hof, and A. Kros, "Controlled peptide-mediated vesicle fusion assessed by simultaneous dual-color time-lapsed fluorescence microscopy," *Scientific Reports*, vol. 10, p. 3087, 2020.

[497] J. L. Rigaud, B. Pitard, and D. Levy, "Reconstitution of membrane proteins into liposomes: application to energy-transducing membrane proteins," *BBA - Bioenergetics*, vol. 1231, pp. 223–246, 1995.

[498] L. G. Wang and L. G. Tonggu, "Membrane protein reconstitution for functional and structural studies," *Science China Life Sciences*, vol. 58, no. 1, pp. 66–74, 2015.

[499] M. Garten, S. Aimon, P. Bassereau, and G. E. Toombes, "Reconstitution of a transmembrane protein, the voltage-gated ion channel, KvAP, into giant unilamellar vesicles for microscopy and patch clamp studies," *Journal of Visualized Experiments*, vol. 95, p. e52281, 2015.

[500] A. Granéli, J. Rydström, B. Kasemo, and F. Höök, "Formation of supported lipid bilayer membranes on SiO2 from proteoliposomes containing transmembrane proteins," *Langmuir*, vol. 19, pp. 842–850, 2003.

[501] M. Dezi, A. Di Cicco, P. Bassereau, and D. Lévy, "Detergent-mediated incorporation of transmembrane proteins in giant unilamellar vesicles with controlled physiological contents," *PNAS*, vol. 110, no. 18, pp. 7276–7281, 2013.

[502] M. L. Carlson, J. W. Young, Z. Zhao, L. Fabre, D. Jun, J. Li, J. Li, H. S. Dhupar, I. Wason, A. T. Mills, J. T. Beatty, J. S. Klassen, I. Rouiller, and F. Duong, "The peptidisc, a simple method for stabilizing membrane proteins in detergent-free solution," *eLife*, vol. 7, p. e34085, 2018.

[503] P. Girard, J. Pécréaux, G. Lenoir, P. Falson, J. L. Rigaud, and P. Bassereau, "A new method for the reconstitution of membrane proteins into giant unilamellar vesicles," *Biophysical Journal*, vol. 87, pp. 419–429, 2004.

[504] Y.-H. M. Chan, B. Van Lengerich, and S. G. Boxer, "Effects of linker sequences on vesicle fusion mediated by lipid-anchored DNA oligonucleotides," *PNAS*, vol. 106, no. 4, pp. 979–984, 2009.

[505] P. Schwille and B. P. Frohn, "Hidden protein functions and what they may teach us," *Trends in Cell Biology*, vol. 32, no. 2, pp. 102–109, 2022.

[506] G. Li, Q. Wen, and J. X. Tang, "Single filament electrophoresis of F-actin and filamentous virus fd," *Journal of Chemical Physics*, vol. 122, p. 104708, 2005.

[507] L. Limozin, M. Bärmann, and E. Sackmann, "On the organization of self-assembled actin networks in giant vesicles," *European Physical Journal E*, vol. 10, pp. 319–330, 2003.

[508] K. A. Taylor and D. W. Taylor, "Formation of 2-D paracrystals of F-actin on phospholipid layers mixed with quarternary ammonium surfactants," *Journal of Structural Biology*, vol. 108, pp. 140–147, 1992.

[509] B. Demé, D. Hess, M. Tristl, L. T. Lee, and E. Sackmann, "Binding of actin filaments to charged lipid monolayers: Film balance experiments combined with neutron reflectivity," *European Physical Journal E*, vol. 2, pp. 125–136, 2000.

[510] A. Renault, P. F. Lenne, C. Zakri, A. Aradian, C. Vénien-Bryan, and F. Amblard, "Surface-induced polymerization of actin," *Biophysical Journal*, vol. 76, pp. 1580–1590, 1999.

[511] A. Laliberte and C. Gicquaud, "Polymerization of actin by positively charged liposomes," *Journal of Cell Biology*, vol. 106, pp. 1221–1227, 1988.

[512] T. L. Hill, "Charge distribution in protein molecules," *Journal of the American Chemical Society*, vol. 78, pp. 1577–1580, 1956.

[513] M. L. Grant, "Nonuniform charge effects in protein-protein interactions," *Journal of Physical Chemistry B*, vol. 105, pp. 2858–2863, 2001.

[514] A. X. Li, X. Q. Cui, F. Yang, and X. R. Yang, "Interaction between F-actin and negatively charged lipids membrane," *Chinese Journal of Analytical Chemistry*, vol. 37, no. 1, pp. 25–29, 2009.

[515] S. Garg, J. X. Tang, J. Rühe, and C. A. Naumann, "Actin-induced perturbation of PS lipid-cholesterol interaction: A possible mechanism of cytoskeleton-based regulation of membrane organization," *Journal of Structural Biology*, vol. 168, pp. 11–20, 2009.

[516] S. J. Marrink, A. H. De Vries, and A. E. Mark, "Coarse grained model for semiquantitative lipid simulations," *Journal of Physical Chemistry B*, vol. 108, pp. 750–760, 2004.

[517] P. C. Souza, R. Alessandri, J. Barnoud, S. Thallmair, I. Faustino, F. Grünewald, I. Patmanidis, H. Abdizadeh, B. M. Bruininks, T. A. Wassenaar, P. C. Kroon, J. Melcr, V. Nieto, V. Corradi, H. M. Khan, J. Domański, M. Javanainen, H. Martinez-Seara, N. Reuter, R. B. Best, I. Vattulainen, L. Monticelli, X. Periole, D. P. Tieleman, A. H. de Vries, and S. J. Marrink, "Martini 3: a general purpose force field for coarse-grained molecular dynamics," *Nature Methods*, vol. 18, pp. 382–388, 2021.

[518] A. G. Lee, "How lipids affect the activities of integral membrane proteins," *Biochimica et Biophysica Acta*, vol. 1666, pp. 62–87, 2004.

[519] H. H. Shen, T. Lithgow, and L. L. Martin, "Reconstitution of membrane proteins into model membranes: Seeking better ways to retain protein activities," *International Journal of Molecular Sciences*, vol. 14, pp. 1589–1607, 2013.

[520] T. Andersen, D. Wörthmüller, D. Probst, I. Wang, P. Moreau, V. Fitzpatrick, T. Boudou, U. S. Schwarz, and M. Balland, "Cell size and actin architecture determine force generation in optogenetically activated adherent cells," *bioRxiv*, p. 2022.03.15.484408, 2022.

[521] T. D. Schindler, L. Chen, P. Lebel, M. Nakamura, and Z. Bryant, "Engineering myosins for long-range transport on actin filaments," *Nature Nanotechnology*, vol. 9, pp. 33–38, 2014.

[522] Z. Zhang, N. Denans, Y. Liu, O. Zhulyn, H. D. Rosenblatt, M. Wernig, and M. Barna, "Optogenetic manipulation of cellular communication using engineered myosin motors," *Nature Cell Biology*, vol. 23, pp. 198–208, 2021.

[523] M. Kovács, J. Tóth, C. Hetényi, A. Málnási-Csizmadia, and J. R. Seller, "Mechanism of blebbistatin inhibition of myosin II," *Journal of Biological Chemistry*, vol. 279, no. 34, pp. 35557–35563, 2004.

[524] Y. E. Goldman, M. G. Hibberd, J. A. McCray, and D. R. Trentham, "Relaxation of muscle fibres by photolysis of caged ATP," *Nature*, vol. 300, pp. 701–705, 1982.

[525] C. Ciobanasu, B. Faivre, and C. Le Clainche, "Actomyosin-dependent formation of the mechanosensitive talin-vinculin complex reinforces actin anchoring," *Nature communications*, vol. 5, p. 3095, 2014.

[526] J. A. Epp and J. Chant, "An IQGAP-related protein controls actin-ring formation and cytokinesis in yeast," *Current Biology*, vol. 7, no. 12, pp. 921–929, 1997.

[527] T. Pols, H. R. Sikkema, B. F. Gaastra, J. Frallicciardi, W. M. Śmigiel, S. Singh, and B. Poolman, "A synthetic metabolic network for physicochemical homeostasis," *Nature Communications*, vol. 10, p. 4239, 2019.

Curriculum Vitæ

Lucia Baldauf

25.05.1994	Born in Freiburg, Germany

Education

2012	Abitur (with honours) *Humboldt-Gymnasium Berlin*
2015	Bachelor of Science (with honours): Technische Physik *Technische Universität Ilmenau*
2017	Master of Science (with honours): Technische Physik *Technische Universität Ilmenau*
2018-2022	PhD research *AMOLF, Delft University of Technology*

Honours and Awards

2022	Travel grant for research at UC Berkeley (Fletcher lab) *Marine Biological Laboratory, University of Chicago*
2022	Travel grants for MBL Physiology 2022 *Stichting Catharine van Tussenbroek, MBL*
2020, 2019, 2017	Poster prizes (1st place) at scientific conferences *Dutch Biophysics 2020, NWO Life 2019,* *DPG Physikerinnentagung 2017*
2020	Science communication award *Durham ECR Biophysics Symposium 2020*
2019	Dutch Face of Science *KNAW, De Jonge Academie and NEMO Kennislink*
2016 and 2018	Student engagement prize, *TU Ilmenau*
2015, 2016 - 2017	Research scholarships *Studienstiftung des Deutschen Volkes, ERASMUS+*
2015 - 2017	Academic scholarship, *Studienstiftung des Deutschen Volkes*
2012	Book Prize, *German Physical Society*

List of Publications

Included in this thesis

L. Baldauf, F. Frey, M. Arribas Perez, M. Mladenov, M. Way, T. Idema, G. Koenderink
Biomimetic actin cortices shape cell-sized lipid vesicles
in preparation

L. Baldauf*, F. Frey*, M. Arribas Perez, T. Idema, G. Koenderink
Branched actin cortices reconstituted in vesicles sense membrane curvature
in revision, preprint doi: 10.1101/2022.08.31.505969

L. Baldauf*, L. van Buren*, F. Fanalista, G. Koenderink
Actin-mediated synthetic cell division
ACS Synthetic Biology (2022), doi: 10.1021/acssynbio.2c00287

C. Schroer, **L. Baldauf**, L. van Buren , T. Wassenaar , M. Melo , G. Koenderink , S. Marrink
Charge-dependent interactions of monomeric and filamentous actin with lipid bilayers
PNAS (2020), doi: 10.1073/pnas.1914884117

Other

L. Baldauf*, E. Teich*, P. Schall, G. van Anders, L. Rossi
Shape and interaction decoupling for colloidal pre-assembly
Science Advances (2022), doi: 10.1126/sciadv.abm0548

Y. Mulla, M. Avellaneda-Sarrio, A. Roland, **L. Baldauf**, W. Jung, T. Kim, S. Tans, G. Koenderink
Weak catch-bonds make strong networks
Nature Materials (2022), doi: 10.1038/s41563-022-01288-0

S. Schyck*, J.-M. Meijer*, **L. Baldauf**, P. Schall, A. Petukhov, L. Rossi
Self-assembly of colloidal superballs under spherical confinement of a drying droplet
JCIS Open (2021), doi: 10.1016/j.jciso.2021.100037

V. Wollrab, J. Belmonte, **L. Baldauf**, M. Leptin, F. Nédeléc, G. Koenderink
Polarity sorting drives remodeling of actin-myosin networks
Journal of Cell Science (2019), doi: 10.1242/jcs.219717

R. Morris, M. Schor, R. Gillespie, A. Ferreira, **L. Baldauf**, C. Earl, A. Ostrowski, L. Hobley, K. Bromley, T. Sukhodub, S. Arnaouteli, N. Stanley-Wall, C. MacPhee
Natural variations in the biofilm-associated protein BslA from the genus Bacillus
Scientific Reports (2017), doi: 10.1038/s41598-017-06786-9

Acknowledgments

In your hands you have a book that contains many hours of my life. For me, these hours held giddy excitement in equal measure with desparate frustration, and hard work as well as serendipity. While my name is on the cover, this book is also the result of the many influences that shaped my work and my thoughts over the last years. If you are one of those influences, this chapter is for you.

Gijsje, where do I even start? When I applied to you at AMOLF in the summer of 2017, I could not have predicted any of the outcomes in my thesis, nor the circumstances in which it was created. Back then, I felt a little stupid for even asking how you got stuff into GUVs, and was confident that we could make that pesky synthetic cell division work within a year. Since then, I have become significantly more knowledgeable, learned a whole bunch of new skills, and have gotten a good deal more cynical - the latter sometimes to your dismay, but you countered it well with your unrelenting optimism. All of this was possible because you entrusted me with this complex research project, encouraged my curiosity and embraced the many collaborations that have shaped my PhD. While this time came with some unusual challenges *(Lab move? Boring! Let's add a bit of excitement with a global pandemic!)* and there were certainly a fair share of other ups and downs for me, I was always secure in the knowlegde that I had you in my corner when tackling them. Beyond 'just' lab life you always encouraged my other interests and pursuits. Our discussions on synthetic cells, scientific integrity, academic careers and much more were always a joy. Thank you for all of this and more!

To my co-promotor Timon, you seemed more than a little surprised when I walked into your office shortly after arriving in Delft, and asked you - a theoretician - to be my promotor in my very experimental thesis work. I explained that I wanted someone with an outside perspective, and someone who would help push me to better conceptualize my work in a physics context. You agreed, and I have to say my hopes were fulfilled wonderfully. In particular in my joint work with Felix, but also more broadly in my last thesis writing stages, you were a great source of inspiration and different perspectives on the questions that were driving me. I also really enjoyed our more casual chats which confirmed that gifted scientists can also be dedicated teachers, prolific users of sarcasm, and proud all-round nerds. Thank you!

Staying with the senior scientists for a moment, I would like to extend warm thanks to my thesis committee. Dear Kristina, Darius, Cees, Guillaume, Hylkje and Chirlmin, I am honored that you took the time and effort to read my thesis, and even gave me comments to strengthen it further. Thank you also for your personal encouragement, I appreciated it greatly!

Of course, a lot of my time in the past few years was spent in the lab, making it extra important that this should be a nice place. Dearest Biosofties past and present, you honestly deserve a medal. Even (especially?) when the lab was the only place I could go during peak covid times, you made sure that it was always a pleasant one.

While I can't put an order to the many great people in this category, I do have to start with my wonderful paranimfs. Gerard, how can I ever be without you and your stickers? You embody a truly unique combination of fun, competence, kindness, integrity, and not-giving-a-shittitude that I cannot help but love. What a journey we've been on from your first shy forays into my office, learning how to operate the TIRF, to you and Paula basically mobbing Andreas into marrying me. Thank you for all of it! Your faible for short wiggly things (be that septins, churros, worms, or sentences) will surely serve you well in whatever you decide to pursue, and I look forward to seeing it in action. Irene, I can not get over how much of a positive presence you are, even when the world is making an effort to screw you personally. Every single time we talked I feel more thoughtful, smarter, more entertained or just happier. It's a shame that the project we pursued together was so incredibly doomed, but honestly I think doing it together has been a huge blessing in disguise, since it taught me so much as a scientist, manager, and human. Thank you for sharing so liberally your insights, experiences, food, heart, and of course the hottest bachata tunes.

Lennard, you know I'm not a spiritual person but if I was, I would say fate brought us to the Biosofties together. It was a great pleasure to be with you throughout both our PhD journeys, and I reserve an extra special thanks for you for being my ranting partner whenever either of us needed it. I greatly enjoyed our many chats, ideas, one-off experiments and full-blown project together, and I am really proud of what we achieved. Thank you for your generosity with everything from your time, code, dark chocolate and tolerance for beer-rejection. James, it's been an absolute pleasure to have you around and I am so glad you got out of The Box, so both you and the rest of us could enjoy your sunny mind. Your appreciation for good food, art, nature and surrealism (not least in our own science) is just fabulous, and other political commentators will forever fall short in my mind because they can never capture sheer exasperation just like you do. Marcos, I was so happy that you joined us and carried forth the torch of actin GUVs. Your competence and care alone would make this a great development, but your enthusiasm, kindness and helpfulness in wrapping up my work with me has been nothing less than a blessing. It's also refreshing to meet someone with even less faith in published works than me - thank you for everything! Iain, your rigorous and unashamed physics treatment of biological systems is truly something to aspire to. Thank you for bringing and sharing your competence, as well as introducing me to Cuthbert, together with James setting out to prove that none of us in fact speak English, and lots of fun cynicism in an accent that properly does it justice. Ilina, while you're only half a Biosoftie, you have always been more than kind enough for a whole person (or two). Thank you for making the most tedious labwork fun, and sharing your thoughtful takes on places, moves, science and cakes. Michal, what a joy it is to meet someone so curious, passionate, and at the same time just really really good at what they do. Thank you for sharing your wisdom not only on microscopy, but on life, motherhood, bread, and politics across all scales. Anouk, I thought I had my shit somewhat together, but you have proven me wrong. I am so happy to see how your skill and knowledge makes everyone around

you level up. And to find inside this incredibly competent and well-organized woman a mean wit and fantastic sense of humor - chef's kiss! Jeff, I bet you are taking a deep breath now that I am no longer there to demand fifteen different proteins and complain about labbooks, sinks, and everything in between. Thank you for putting up with it, being the sweet guy that you are, and providing frankly unreasonable amounts of fun with food (mosterd anyone? or maybe some kwark?). I'll miss our many biertjes and, oddly enough, even the shared travel time. Celine, from my first days in the lab I was in awe of your care, knowledge and communicative talent. It didn't take long to learn that this came packaged in an incredibly fun person who spreads around good vibes like nobody's business. More than anything, your openness and resilience in bad times is an example that I can only hope to have learned from. Cristina, I wonder if there is a single sentence that has captured so much of my PhD as your personal catchphrase: *What an unexpected surprise!* Thank you for sharing this gem and many other things, from beautiful software to disdain for tequila with hats on. Anders and Viktoria, thank you both for welcoming me so warmly into the lab, sharing your favourite Amsterdam spots, and introducing me to some of my pet proteins and assays at the very start of my PhD. Your dry humor and excitement about even the smallest nerdy things made me feel at home from the very beginning. Federica and Yuval, you both are ridiculously impressive as scientists, and equally awesome as people. Thank you for sharing your knowledge and the limits thereof (perhaps an even rarer quality), and for letting me into the joys of your life whether that is in French wine, bouldering or starting a family. Bart, from beamtime in Grenoble to the many hours of Eldritch Horror in my kitchen, it was never boring to hang out with you. Thank you for sharing gossip, fibrin drama, excellent food, and your incredible enthusiasm for almost everything. Marjolein, thank you for taking the utter noob-me under your wing and teaching her that biology - at least some of it - is in fact not scary at all. Agata, your dedication to doing your own thing was an education in itself. Thank you for doing it so unapologetically, and sharing your knowledge, joys and thoughts along the way. Gitta and Federico, I did not get to spend a lot of time with either of you, but the time I did have was great. Thank you for a lovely send-off from AMOLF and welcome in Delft. With both of you, I enjoyed our discussions on synthetic cells and real happiness. SaFyre, Nikki and Bert, sadly I only had a few weeks with you before I left, but I am excited to see how you get on. Parts of your projects are very dear to me, and I am happy to see them in such good hands.

I had the honour and pleasure of supervising a whole flock (!) of students. Designing, guiding and advising their projects was one of the most nervewracking, but also most fulfilling and frankly most fun parts of my entire PhD. Many of the projects were collaborative in nature, and I feel lucky to have worked with all of my co-supervisors - Jeffrey, Lennard, Irene and Gerard, thank you for making every project special and all of them exciting. Even more importantly though, thank you to my wonderful ~~ducklings~~ students. Erik, thank you for trusting noobs like Jeff and me with your bachelor project. Your skill and determination in the lab was fantastic, and to the last day of writing my thesis I still blessed you for the attention you dedicated to documenting your work. Miglė, even in the very early stages of our GUV work, you managed to produce crazy deformations and tentacled vesicle monsters. Thank you also for introducing me to the fanciest-looking soup in the world! Iris, only you could talk of love at first sight in a physics thesis and make it

not cheesy. At the height of covid in late 2020, you managed to inject so much brightness into the lab as a whole and my work in particular, I don't know how to thank you. Let's not even mention how two of my thesis chapters really got kickstarted thanks to your fearless eDICE efforts. And of course thank you and Benjamin for being such sunshines outside the lab as well! Kabir, I am not sure what the three of us did to deserve the sheer density of unprovoked clusterfucks that we got. Nonetheless, your determination, skill and perseverence led to a fabulous light-control assay, a wealth of great software, and a thesis you can be very proud of. I couldn't have hoped for a better partner in trouble, and whenever I burn my mouth unexpectedly I still fondly remember your chili cakes. Djim, king of the artefacts! Your determination to make high-resolution imaging work on challenging systems was unparalleled, and it was a real pleasure to see you grow through all of it. Thank you for your roadtripping tips, university politics gossip and general guide to Delft. May the electrons be ever in your favour! Nigel, you were another great duckling, agent of chaos and bright ray of sunshine. I honestly don't know how one person can have so much energy within them, but I can only thank you for sharing it so liberally. Best of luck for your new adventures! Tom, how lucky can two supervisors get when they come up with an important but somewhat vague idea? As lucky as to recruit you as their student, thats how! You did incredibly well in your project, and I am still impressed by how organized but also just-do-it you are. Even if we have had to re-think the results recently, I still believe your work is really important for the broader SynCell efforts and will hopefully lead the way towards more realistic cell growth. Thank you for the great collaboration and for your always smart and wonderfully sweet presence. Finally, Sophie, my last duckling to hatch! Your BSc project offered so little time to get used to anything, and yet you bravely plunged into the depths of actin reconstitution and GUV mechanics. I wish I had had a few more months to experiment, so I could have given your work the follow-up it deserved, but either way I was blessed to see your skills and confidence progress. *Quack quack!*

A lot of people outside my lab were instrumental in making thinks work, facilitating interesting discussions, providing general support, and all the other important things that allow science to flow at least somewhat smoothly. If I dedicated to all of them as many words as I would need to do them justice, this thesis would be twice as long. So instead, let me be brief: Thank you to Marko and Jan Bonne at AMOLF, and to Jérémie, Wiel, Roland and Cécilia in Delft, for your absolutely invaluable microscopy support. Sacha, I don't know how BN is coping without you, but I feel lucky to have had you there as my favourite alround wizard who could always be depended upon for parts, tech support, lovely chats and Russian candy. Similarly, dear Hinco at AMOLF: thank you for your kind and ever-reliable help with practically everything, and also for your patience and encouragement with my Dutch-learning efforts! Esengul, Eli, Ilja, Ashmiani, Ramon, Cátia, Theo, Jan, Anke, Vanda, Yvonne and Simone, thank you for always being there when I needed materials, knowledge, an extra pair of hands or just someone to vent to about proteins and cells. Tracey, Esther, Stefania, Floortje and all the other wonderful managment and secretarial staff, thank you for keeping the lights on for all of us, and helping me out whenever things were not working or suddenly became very urgent. Martine and Petra, thank you for your loving support for my outreach efforts, and Juliette and Ad, thank you for brightening the start of every day at AMOLF.

Speaking of brightening, among a whole bunch of nice people both at AMOLF and TU Delft, I'd like to highlight a few true angels. Harmen, thank you for welcoming me so warmly into your office and bestowing upon me the honour of being your paranimf. Your birthday garland is still gracing the window of my Delft workplace, and who knows, maybe some future archeologist will eventually dig up that stuiterbal... Thank you for sticking with me in my pursuit of Dutch well beyond any reasonable limits of patience, and thank you for the many happy occasions inside the lab and out. Thank you Mareike and Gerard granting us asylum in your office when we got kicked out of ours, and initiating the cult of the Delta Daltons. Mareike, you're always such a blast to be with and I wish we had had more time together. Thank you for sharing your enthusiasm for science, curries, travel, art, dance, design, everything really! Leaving behind AMOLF, I was still blessed with wonderful office mates: Gerard, Cristina, Irene, Michal, and SaFyre, you always made the office an interesting place to be, and provided knowledge, deep insight into the human psyche, chocolate, fun, and support throughout. My apologies to George, who had to suffer for this. Thank you to Esengul, Eli, Anne, Roland, Susanne, and others for embracing us in Delft as a fully formed group, and making the transition as pleasant as possible. Daniel, you had an unerring talent to meet me at my worst, and then through your sweetness lift me up and make even the shittest days brighter. Thank you and hope to see you soon in London! Wouter, George, Felix, Rachel, Hidde, Elisa, Sabrina, Alberto, Ana, Ali, Vladimir, and many more who have made Delft a good place to be - thank you.

Throughout my PhD, I was lucky enough to work together with some prolific scientists and wonderful people.

Felix, thank you for being the best collaborator anyone could hope for, but beyond that an incredibly sweet and kind person. I really valued our long science chats and your intelligent and always surprising approach to questions I would have never come up with. My thesis truly would not be the same without you, and inshallah we might get the chance to do this again some day. Beyond the science, I thank you for our many and prolonged discussions on the point of synthetic biology, academia, marriage, and life. During the times when I felt the most insecure about future decisions, your presence and encouragement were an immense help.

Nils and the rest of the Steinem lab, thank you for having me and sharing with me the magic of ezrin. Unfortunately it did not end up agreeing with me, but you gave me the best chance I could have asked for. Thanks to you I also know the true purpose of cold rooms, and how beer can unveil the secrets of statistical physics.

Ruth, we picked the absolute worst time to get a travel grant - nonetheless, I am so happy that you spent the last two normal weeks of 2020 in Delft with me. While our actin stretching success was rather limited, the time we spent on it was a success in its own right, and I feel like I have found my lost and slightly mental twin. Thank you!

Michael, your beautiful Arp2/3 proteins allowed me to do the most awesome experiments of my entire thesis, and your clear views on writing really helped me shape the work on GUV deformations. Thank you for taking the time and energy to improve our manuscript immeasurably!

Kristina, Lori, Yash and Marileen, thank you for many insightful and helpful discussions on actin dynamics, GUV formation, holes in the literature, and much more. Kristina, your

lived approach to science is a shining example which gives me concrete hope that practices in academia are changing for the better.

Dan and Nicole, as a stand-in for many others, thank you for a fantastic Physiology experience. We may have been disappointing at softball, and spent rather more time sick and quarantining than we had all hoped, but I am incredibly grateful for my weeks in Woods Hole. Thank you to the many fantastic scientists who took the time to let me pick their brains - special thanks to Dyche, Dan, Matthieu and Stephan for insight and inspiration in the very final stages of writing my thesis. Florian, Neil and Joe, your skill, fun and passion for your fields are truly inspiring. Dear Physio students and TAs, you made this time so special. Since I can't list everyone, I'd just like to give thanks to the trogdog dreamteam (see you soon!), my covid saviour Chunzi, the ever-inspiring Mugdha and Jana, and the wonderful dino appreciation society, Gil, Arthur, Yahor and Manny.

Many a BaSyC discussion would have been quite pointess without the fundamental and provocative points that were brought up there. Out of the many people who made them I would like to thank in particular Bela, Ramon, Christophe, Matthias, Mareike, Bert and Mahesh. Thanks also to the book club's iron core of Daphne, Bettina, Ludo, Mareike and Ramon - even though I am sad we didn't manage to meet more often, it was always a pleasure.

My final co-author will have to be quoted literally. Here is her contribution to my thesis: qawwwwwwwwwwwwwwwwwwwwwwwwwwwwwwwwwwwwwwwwwwwwwwwwwwwsp;'. Thank you, fluffy neighbor, for brightening my writing days, and only occasionally stepping on my keyboard.

Just like during my PhD, I was privileged to have some great mentors before starting this project. From my highschool physics teachers Dominique Barthel and Guido Narberhaus, through my undergraduate professors Martina Hentschel and Sigfried Stapf, to my scientific mentors Keith Bromley, Cait MacPhee, Peter Schall and Laura Rossi: Thank you all for teaching, challenging, and encouraging me, and believing in me throughout.

Conversely, a few other scientists provided me with a different type of valuable learning opportunity. Thank you for teaching me what I don't want to become.

I could not have navigated the ups and downs of science without the joys outside it. Thank you to my beloved friends, especially Mohsin, Paul, Rebecca and Thijs, for keeping me sane and happy. Thank you also to Constantin, Patrick, Raphael and Priscilla for always being there with me. Erna, Laura and Koen - dank voor het wobbelen!

Dancing has always been my passion and refuge, and through it I have much to be thankful for. Jennifer, thank you for single-handedly breathing life into the Amsterdam WCS community and making our time there fantastic. Maarten and Judith in Utrecht, as well as the lovely Nijmegen Westie crowd, thank you for the good times. Evi, you are incredible for keeping the passion alive via zoom. Thank you for welcoming us home every time we are passing through. Taryn and Neil, thank you for the last big festival in a long time - I would not have missed it for the world. Geno and Steffie, thank you for cultivating a lovely Bachata community, and giving me the chance to leave my brain and just enjoy. Beccy and Jeroen, thank you for awakening my love for Lindy Hop. Lastly, thank you to the many wonderful leaders and followers who have challenged and inspired me.

Finally, my family. Kuni, Ulrike, Petra and Peter, thank you for your interest, encouragement and belief. Julia, thank you for many therapeutic hours of sharing rants and joys alike. To my parents - you never let me believe for a minute that I could not do something, scientific or otherwise, and you made sure that this was so. Thank you for everything.

Andreas, my love, my champion and my rock. I don't know how I would have done any of this without you - you have always been there with me and for me, and not even my worst puns have managed to push you away. I am proud of becoming Dr. Baldauf, and extra happy to be Dr. Baldauf-Behringer.

Lucia
London, November 2022